



# PACIFIC EARTHQUAKE ENGINEERING RESEARCH CENTER

## **Influence of Kinematic SSI on Foundation Input Motions for Bridges on Deep Foundations**

**Benjamin J. Turner**

**Scott J. Brandenberg**

**Jonathan P. Stewart**

Department of Civil and Environmental Engineering  
University of California, Los Angeles

PEER Report No. 2017/08  
Pacific Earthquake Engineering Research Center  
Headquarters at the University of California, Berkeley

November 2017

#### Disclaimer

The opinions, findings, and conclusions or recommendations expressed in this publication are those of the author(s) and do not necessarily reflect the views of the study sponsor(s), the Pacific Earthquake Engineering Research Center, or the Regents of the University of California.

# **Influence of Kinematic SSI on Foundation Input Motions for Bridges on Deep Foundations**

**Benjamin J. Turner**  
**Scott. J. Brandenberg**  
**Jonathan P. Stewart**

Department of Civil and Environmental Engineering  
University of California, Los Angeles

PEER Report No. 2017/08  
Pacific Earthquake Engineering Research Center  
Headquarters at the University of California, Berkeley

November 2017



## ABSTRACT

Seismic design of bridges and other pile-supported structures often utilizes a substructure method of dynamic analysis in which the foundation elements are not explicitly modeled but are replaced by springs and dashpots representing the foundation impedance. The ground motion appropriate for input to the free end of the springs, known as the “foundation input motion” (FIM), differs from the free-field motion (FFM) due to the difference in stiffness and deformation characteristics between the pile(s) and soil, which is typically overlooked in practice. Results of a parametric study of the influence of kinematic pile–soil interaction on FIM are presented. One-dimensional nonlinear ground response analyses were used to define free-field motions, which were subsequently imposed on a beam-on-nonlinear-dynamic-Winkler-foundation pile model. The free-field ground surface motion and top-of-pile FIM computed from these results were then used to compute transfer functions and spectral ratios for use with the substructure method of seismic analysis. A total of 1920 parametric combinations of different pile sizes, soil profiles, and ground motions were analyzed.

Results of the study show that significant reductions of the FFM occur for stiff piles in soft soil, which could result in a favorable reduction in design demands for short-period structures. Group effects considering spatially-variable (incoherent) ground motions are found to be minor over the footprint of a typical bridge bent, resulting in an additional reduction of FFM by 10% or less compared to an equivalent single pile.

This study aims to overcome limitations of idealistic assumptions that have been employed in previous studies such as linear-elastic material behavior, drastically simplified stratigraphy, and harmonic oscillations in lieu of real ground motions. In order to capture the important influence of more realistic conditions such as material nonlinearity, subsurface heterogeneity, and variable frequency-content ground motions, a set of models for predicting transfer functions and spectral ratios has been developed through statistical regression of the results from this parametric study. These allow foundation engineers to predict kinematic pile–soil interaction effects without performing dynamic pile analyses.

While previously available elastic analytical models are shown to be capable of predicting the average results of this study, they do not adequately reflect the amount of variability in the results that arises from consideration of more realistic conditions. The new model is also used to re-examine available case history data that could not be explained by existing models.



## **ACKNOWLEDGMENTS**

This work was supported by the Pacific Earthquake Engineering Research Center's (PEER) Program of Applied Earthquake Engineering Research of Lifelines Systems supported by the California Department of Transportation (Caltrans) and the Pacific Gas and Electric Company. Any opinions, findings, and conclusions or recommendations expressed in this material are those of the authors and do not necessarily reflect those of the sponsors.

The authors would like to acknowledge the feedback and support from Tom Shantz of Caltrans acting as research coordinator of the PEER Lifelines Program, as well as the input of Professors John Wallace, Anne Lemnitzer, George Mylonakis, and George Anoyatis.



# CONTENTS

ABSTRACT.....	iii
ACKNOWLEDGMENTS .....	v
TABLE OF CONTENTS .....	vii
LIST OF TABLES .....	xi
LIST OF FIGURES .....	xiii
LIST OF SYMBOLS .....	xix
<b>1 INTRODUCTION.....</b>	<b>1</b>
<b>1.1 Organization .....</b>	<b>2</b>
<b>1.2 Fundamentals .....</b>	<b>3</b>
<b>1.3 Previous Studies .....</b>	<b>10</b>
1.3.1 Winkler Analysis and $p$ - $y$ Curves .....	10
1.3.2 Analytical and Numerical Solutions for Pile Dynamics .....	12
1.3.3 Normalization Schemes .....	15
1.3.4 Limitations of Elastic and Analytical Solutions .....	19
1.3.5 Experimental Investigations.....	20
1.3.6 Empirical Observations of Kinematic Pile–Soil Interaction.....	21
<b>1.4 Kinematic SSI in Building Codes .....</b>	<b>29</b>
<b>1.5 Notes on Terminology and Notation .....</b>	<b>30</b>
<b>2 ELASTIC ANALYTICAL AND NUMERICAL SOLUTIONS.....</b>	<b>31</b>
<b>2.1 Elastic Analytical Solution .....</b>	<b>31</b>
<b>2.2 Elastic Numerical Solution.....</b>	<b>37</b>
<b>2.3 Elastic Winkler Modulus.....</b>	<b>39</b>
2.3.1 Terminology and Units .....	39
2.3.2 Previous Definitions of $K_e$ .....	40
2.3.3 Diameter Effects .....	44
<b>2.4 Questions of Pile Mass and Inertia.....</b>	<b>46</b>
<b>2.5 Pile–Soil System Fundamental Frequency and Resonance.....</b>	<b>47</b>
<b>3 ANALYSIS .....</b>	<b>49</b>
<b>3.1 Approach .....</b>	<b>49</b>

3.2	<b>Parametric Study Bounds .....</b>	<b>50</b>
3.3	<b><i>PySimple3</i>—Motivation and Model Updates .....</b>	<b>50</b>
3.3.1	Motivation.....	51
3.3.2	Governing Equations and OpenSees Implementation .....	53
3.4	<b><i>PySimple3</i>—Parameter Values.....</b>	<b>55</b>
3.4.1	Initial Elastic Stiffness $K_e$ .....	55
3.4.2	Ultimate Resistance .....	57
3.4.3	Curvature Parameter and Yield Force.....	57
3.4.4	Radiation Damping .....	61
3.5	<b>Pile Modeling.....</b>	<b>65</b>
3.5.1	Pile Moment-Curvature Behavior.....	65
3.5.2	Pile Head Fixity Condition .....	67
3.5.3	Pile Shear Deformations .....	68
3.5.4	Pile Groups.....	69
3.6	<b>Soild Profiles for Analyses.....</b>	<b>70</b>
3.7	<b>Ground Motions .....</b>	<b>71</b>
3.7.1	Baker et al. [2011] Ground Motion Suite .....	71
3.7.2	Ground Response Analyses .....	75
3.7.3	Ground Motion Incoherence .....	76
3.8	<b>OpenSees Analysis .....</b>	<b>79</b>
4	<b>RESULTS .....</b>	<b>81</b>
4.1	<b>Single Piles .....</b>	<b>81</b>
4.2	<b>Normalized Results using Dimensionless Frequency.....</b>	<b>93</b>
4.3	<b>Controlling Parameters and Comparison to Elastic Solutions.....</b>	<b>97</b>
4.4	<b>Generalized Models for Predicting Transfer Functions.....</b>	<b>103</b>
4.4.1	Functional Form.....	105
4.4.2	Approach.....	106
4.4.3	Models for Predicting Fixed-Head Transfer Function Coefficients .....	108
4.4.4	Models for Predicting Free-Head Displacement Transfer Function Coefficients .....	114
4.4.5	Models for Predicting Free-Head Rotation Transfer Function Coefficients .....	118
4.5	<b>Generalized Models for Predicting Spectral Ratios .....</b>	<b>123</b>
4.5.1	Functional Form.....	123
4.5.2	Models for Predicting Fixed-Head Spectral Ratio Coefficients .....	125

4.5.3	Models for Predicting Free-Head Spectral Ratio Coefficients .....	130
<b>4.6</b>	<b>Pile-Group Results .....</b>	<b>134</b>
<b>5</b>	<b>COMBINATION OF INERTIAL AND KINEMATIC PILE–SOIL INTERACTION .....</b>	<b>137</b>
<b>5.1</b>	<b>Combining Inertial and Kinematic SSI .....</b>	<b>137</b>
5.1.1	Linear-Elastic SDOFO-Pile–Soil System .....	139
5.1.2	Effects of SDOFO Properties.....	146
5.1.3	Effect of Pile-Soil Kinematic Interaction Corner Frequency versus SDOFO Fundamental Frequency.....	148
5.1.4	Effect of Pile–Soil interaction Nonlinearity .....	149
<b>6</b>	<b>EXAMPLE APPLICATIONS OF TRANSFER FUNCTION AND SPECTRAL RATIO PREDICTION MODELS .....</b>	<b>155</b>
<b>6.1</b>	<b>Empirical Case Studies.....</b>	<b>155</b>
6.1.1	Sendai, Japan, Site after Givens et al. [2012] .....	155
6.1.2	Lancaster, California, Site after Kim and Stewart [2003]. .....	159
<b>6.2</b>	<b>Example Application of Spectral Ratio Prediction Model for Pile-Supported Bridge .....</b>	<b>163</b>
<b>7</b>	<b>CONCLUSIONS AND RECOMMENDATIONS FOR ENGINEERING PRACTICE.....</b>	<b>169</b>
<b>7.1</b>	<b>Predictive Models and Limitations.....</b>	<b>171</b>
<b>7.2</b>	<b>Reinterpretation of Empirical Case Studies.....</b>	<b>172</b>
<b>7.3</b>	<b>Future Research Needs.....</b>	<b>173</b>
	<b>REFERENCES.....</b>	<b>175</b>
<b>APPENDIX A</b>	<b>SITE PROFILES FOR KINEMATIC PILE–SOIL INTERACTION ANALYSIS.....</b>	<b>183</b>
<b>APPENDIX B</b>	<b>A FRAMEWORK FOR FULL-SCALE EXPERIMENTAL MEASUREMENTS OF KINEMATIC PILE–SOIL INTERACTION.....</b>	<b>197</b>



## LIST OF TABLES

### Chapter 2

Table 2.1	Ground motions for elastic numerical analyses; numbering follows Baker et al. [2011]. .....	39
Table 2.2	$\delta$ expressions from previous researchers derived by matching results of BDWF analyses to continuum analyses.....	44

### Chapter 3

Table 3.1	Parametric study bounds for single piles. ....	50
Table 3.2	Site time-averaged shear-wave velocity characteristics for Sites 1–6. ....	71
Table 3.3	Ground-motion records used for analyses (after Baker et al. [2011]). ....	73
Table 3.4	Intensity measures for ground-motion set.....	74
Table 3.5	Summary of ground-motion intensity measures. ....	75
Table 3.6	Site fundamental frequencies.....	76
Table 3.7	Segment duration ( $L$ ) and frequency bands ( $b$ ) used in the FDW routine. ....	78

### Chapter 4

Table 4.1	Fixed-head transfer function coefficient prediction model metrics.....	110
Table 4.2	Metrics for free-head displacement transfer function coefficient prediction models. ....	115
Table 4.3	Metrics for free-head rotation transfer function coefficient prediction models. ....	119
Table 4.4	Fixed-head spectral ratio coefficient prediction model metrics.....	127
Table 4.5	Metrics for free-head spectral ratio coefficient prediction models.....	131



# LIST OF FIGURES

## Chapter 1

Figure 1.1	Substructure method of analysis for bridge bent supported on a pile group. Note that vertical impedance is not shown but could also be considered.....	4
Figure 1.2	Profiles of soil and free-head pile displacement for three frequencies of harmonic free-field excitation.....	6
Figure 1.3	Profiles of soil and fixed-head pile displacement for three frequencies of harmonic free-field excitation.....	6
Figure 1.4	Kinematic pile–soil interaction transfer functions computed for idealized linear-elastic conditions. ....	7
Figure 1.5	Time- and frequency-domain representations of pile seismic response for computation of kinematic transfer function.....	9
Figure 1.6	Time-domain and response spectrum representations of pile seismic response for computation of kinematic spectral ratios. ....	10
Figure 1.7	Kinematic pile-soil transfer functions from Fan et al. [1991] study for single pile with length-to-diameter ratio of 20. ....	15
Figure 1.8	Static kinematic pile–soil interaction transfer functions using improved dimensionless frequency definition from Anoyatis et al. [2013]. Applies for a free-tip pile with $\lambda L \geq 5$ and homogeneous elastic soil of any stiffness. ....	18
Figure 1.9	Comparison of observed versus model prediction transfer functions for a 5-story hospital building in Lancaster, California, during the 1994 Northridge, California, earthquake (after Kim and Stewart [2003]). ....	23
Figure 1.10	Comparison of observed versus model prediction transfer functions for a 4-story building at Tohoku Institute of Technology in Sendai, Japan, during the 2011 Tohoku, Japan, earthquake (after Givens et al. [2012]). ....	23
Figure 1.11	Influence of small changes between input and output signals on system transfer functions. Relative to input signal, the output signal (a) is identical, (b) is perfectly out-of-phase, (c) is out of phase by 0.1, and (d) exhibits slight baseline drift.....	28

## Chapter 2

Figure 2.1	Soil and pile response under imposed 10 Hz harmonic ground motion using elastic analytical solutions.....	35
Figure 2.2	Transfer function for kinematic soil–structure interaction effects for three diameters of 25-m long, fixed-head reinforced concrete piles in soft- and stiff-soil profiles.....	36

Figure 2.3	Transfer functions from Figure 2.2 plotted versus dimensionless frequency and compared to Anoyatis et al. [2013]. All solutions lie within the same narrow band. ....	36
Figure 2.4	Analytical and numerical solution transfer functions for sine-sweep input motion. ....	38
Figure 2.5	Fourier amplitude spectra for free-field and foundation-input motions (top) and corresponding transfer functions (bottom). ....	38
Figure 2.6	(a) Normal and (b) shear stress contours around a laterally-loaded pile. Color key indicates change in stress from initial condition. ....	41
Figure 2.7	Values of Winkler coefficient $\delta$ proposed in previous pile SSI research. ....	43
Figure 2.8	Normalized elastic transfer functions computed with and without pile mass. ....	47
Figure 2.9	Effect of resonance at pile–soil system fundamental frequency on kinematic transfer functions. ....	48

### Chapter 3

Figure 3.1	Numerical modeling approach. ....	49
Figure 3.2	Basic features of <i>PySimple3</i> material under monotonic loading (after Choi et al. [2015]). ....	51
Figure 3.3	Comparison of Boulanger et al. [1999] dynamic <i>p-y</i> material and later implementation in <i>OpenSees</i> . ....	52
Figure 3.4	<i>PySimple3</i> viscoelastic-plastic material model formulation. ....	52
Figure 3.5	Comparison of <i>PySimple1</i> and <i>PySimple3</i> material models. ....	53
Figure 3.6	Effect of initial elastic stiffness $K_e$ on <i>PySimple3</i> behavior for typical soft-clay properties. ....	56
Figure 3.7	Transfer functions (left) and <i>p-y</i> curve initial stiffness parameter versus depth plots (right) for free-head pile with uniform and variable values of Winkler coefficient $\phi$ over the depth of the pile. ....	56
Figure 3.8	Effect of <i>PySimple3</i> curvature parameter $C$ . ....	57
Figure 3.9	<i>Phase2</i> finite element domain for plane-strain analyses of laterally loaded pile. The pile is displaced from left to right during the analyses. ....	60
Figure 3.10	Comparison of normalized $y_{50}$ values using (a) existing <i>p-y</i> relationships and (b) from results of plane-strain finite element simulations of laterally-loaded piles in <i>Phase2</i> using Duncan-Chang nonlinear-elastic (D-C) and Mohr-Coulomb (M-C) soil constitutive models. ....	60
Figure 3.11	Effect of radiation damping in <i>PySimple3</i> material. ....	64
Figure 3.12	Normalized dashpot coefficient for $v = 0.25$ m, $\rho_s = 1.7$ Mg/m <sup>3</sup> and $E_p/E_s \approx 690$ . ....	64

Figure 3.13	Moment curvature analyses conducted at axial load $P = 0.05 * A_g * f'_c$ for (a) 2-m- and (b) 0.5-m-diameter pile sections.....	66
Figure 3.14	Pile-group layout considered for analyses.....	70
Figure 3.15	Shear-wave velocity and reference strain ( $\gamma_r$ ) profiles for Sites 1–6. ....	71
Figure 3.16	Acceleration (top) and displacement (bottom) time series for seed motion (1971 San Fernando, California, earthquake, Lake Hughes #4 recording station) and simulated spatially-variable ground motions at locations corresponding to other piles in group layout shown in Figure 3.14. ....	79

## Chapter 4

Figure 4.1	Transfer functions for Site 1 fixed-head piles.....	82
Figure 4.2	Transfer functions for Site 2 fixed-head piles.....	83
Figure 4.3	Transfer functions for Site 3 fixed-head piles.....	84
Figure 4.4	Transfer functions for Site 4 fixed-head piles.....	85
Figure 4.5	Transfer functions for Site 5 fixed-head piles.....	86
Figure 4.6	Transfer functions for Site 6 fixed-head piles.....	87
Figure 4.7	Transfer functions for Site 1 free-head piles.....	88
Figure 4.8	Transfer functions for Site 2 free-head piles.....	89
Figure 4.9	Transfer functions for Site 3 free-head piles.....	90
Figure 4.10	Transfer functions for Site 4 free-head piles.....	91
Figure 4.11	Transfer functions for Site 5 free-head piles.....	92
Figure 4.12	Transfer functions for Site 6 free-head piles.....	93
Figure 4.13	Normalized horizontal displacement transfer function results for fixed-head piles. ....	95
Figure 4.14	Normalized horizontal displacement transfer function results for free-head piles. ....	96
Figure 4.15	Normalized rotation transfer function results for free-head piles. ....	97
Figure 4.16	Mean fixed-head transfer function results for each pile/site combination.....	98
Figure 4.17	Influence of changes in stiffness over pile length for $B = 2.0$ m, $L = 30$ m pile subjected to (a) 1971 San Fernando, California, earthquake (NGA record sequence number 72); (b) 1994 Northridge, California, earthquake (NGA record 1011); and (c) 1999 Chi-Chi, Taiwan, earthquake (NGA record 2661). ....	100
Figure 4.18	Competing effects of radiation damping and stiffness degradation due to pile–soil interaction.....	100

Figure 4.19	Mean fixed-head transfer function results for each pile/site combination plotted versus dimensionless frequency: (a) shows variability in results due to pile stiffness, and (b) shows lack of variability in results due to pile slenderness ratio $L/B$ . .....	101
Figure 4.20	Example of nonlinear least-squares regression to determine coefficients for free-head pile functional form [Equation (4.7)] using computed data for $B = 2$ m, $L = 60$ m pile embedded in Site 4 and subjected to 1999 Hector Mine earthquake (NGA record sequence number 1786). .....	108
Figure 4.21	Residuals versus predicted values plots (left) and normal Q-Q plots (right) for fixed-head transfer function coefficient prediction models. Lines on residuals plots show trend and $\pm$ one standard deviation. ....	111
Figure 4.22	Variability in fixed-head transfer function results for the two pile diameters considered in this study. ....	112
Figure 4.23	Mean fixed-head transfer function model prediction for $B = 0.5$ m compared to computed results. ....	113
Figure 4.24	Mean fixed-head transfer function model prediction for $B = 2.0$ m compared to computed results. ....	114
Figure 4.25	Residuals versus predicted values plots (left) and normal Q-Q plots (right) for free-head displacement transfer function coefficient prediction models. Lines on residuals plots show trend and $\pm$ one standard deviation. ....	116
Figure 4.26	Mean free-head displacement transfer function model prediction for $B = 0.5$ m compared to computed results. ....	117
Figure 4.27	Mean free-head displacement transfer function model prediction for $B = 2.0$ m compared to computed results. ....	118
Figure 4.28	Residuals versus predicted values plots (left) and normal Q-Q plots (right) for free-head rotation transfer function coefficient prediction models. Lines on residuals plots show trend and $\pm$ one standard deviation. ....	120
Figure 4.29	Variability in free-head rotation transfer function results for the two pile diameters considered in this study. ....	121
Figure 4.30	Mean free-head rotation transfer function model prediction for $B = 0.5$ m results. ....	122
Figure 4.31	Mean free-head rotation transfer function model prediction for $B = 2.0$ m results. ....	123
Figure 4.32	Fixed-head pile spectral ratio functional form after Di Laora and Sanctis [2013]. ....	124
Figure 4.33	Free-head pile spectral ratio functional form. ....	125
Figure 4.34	Residuals versus predicted values plots (left) and normal Q-Q plots (right) for fixed-head spectral ratio coefficient prediction models. Lines on residuals plots show trend and $\pm$ one standard deviation. ....	128
Figure 4.35	Fixed-head spectral ratio results. ....	129

Figure 4.36	Fixed-head pile spectral ratio predictive model residuals.....	130
Figure 4.37	Residuals versus predicted values plots (left) and normal Q-Q plots (right) for free-head spectral ratio coefficient prediction models. ....	132
Figure 4.38	Free-head pile spectral ratio results. ....	133
Figure 4.39	Free-head pile spectral ratio predictive model residuals.....	133
Figure 4.40	Group versus single-pile results for $B = 2.0$ m. $L = 30$ m pile, Site 1, subjected to 1994 Northridge, California, earthquake (NGA record sequence number 957). ....	135
Figure 4.41	Group versus single-pile results for $B = 2.0$ m. $L = 30$ m pile, Site 1, subjected to 1971 San Fernando, California, earthquake (NGA record sequence number 72). ....	135
Figure 4.42:	Group versus single-pile results for $B = 2.0$ m. $L = 30$ m pile, Site 4, subjected to 1971 San Fernando, California, earthquake (NGA record sequence number 72). ....	136

## Chapter 5

Figure 5.1	(a) Schematic of pile-soil kinematic interaction, which produces foundation-input motion (FIM) to free-field motion (FFM) transfer function (b), and (c) application of kinematic transfer function using substructure approach to represent a structure supported by a fixed-head pile; (d) the foundation motion (FM) transfer function differs from the FIM transfer function because of additional foundation displacements resulting from superstructure inertial forces. ....	138
Figure 5.2	Idealized system used for direct analysis method.....	139
Figure 5.3	Comparison of transfer functions computed for pile–soil system and combined SDOF oscillator and pile–soil systems using direct and substructure analysis methods.....	140
Figure 5.4	Comparison of transfer functions computed with and without consideration of kinematic pile–soil interaction. ....	142
Figure 5.5	(a) Phase angle frequency-response curves for SDOFO–pile–soil system (inset) and (b)-(e) response history of system components at different frequencies of harmonic free-field excitation. ....	144
Figure 5.6	Response of SDOFO–pile–soil system to harmonic free-field excitation.....	145
Figure 5.7	Transfer functions computed for variable SDOFO properties. Note fixed-base fundamental frequency $f_{l,SDOFO} = 7$ Hz for all cases.....	147
Figure 5.8	Effect of varying fixed-base fundamental frequency of SDOFO–pile–soil system relative to kinematic pile–soil interaction transfer function corner frequency.....	149

Figure 5.9	Effect of nonlinear pile–soil interaction on SDOFO–pile–soil system transfer functions for homogeneous soil subjected to sine-sweep free-field excitation.....	151
Figure 5.10	Formulation of nonlinear and equivalent-linear impedance spring macro-elements to replace pile in substructure method of analysis.....	152
Figure 5.11	Effect of nonlinear pile–soil interaction on SDOFO–pile–soil system transfer functions for Site 1 subjected to 1971 San Fernando, California, earthquake Lake Hughes #4 recording. ....	153

## Chapter 6

Figure 6.1	Tohoku Institute of Technology building layout after Givens et al. [2012] and idealized single-degree-of-freedom oscillator representation.....	156
Figure 6.2	Subsurface information for Sendai site after Givens et al. [2012]. Subsurface data originally reported by OYO Corporation [2007].....	156
Figure 6.3	Model predictions versus empirical data for Tohoku Institute of Technology building during 2011 Tohoku earthquake after Givens et al. [2012]......	158
Figure 6.4	Lancaster, California, hospital building layout and idealized single-degree-of-freedom oscillator representation after Stewart and Stewart [1997].....	160
Figure 6.5	Subsurface conditions at Lancaster site after Stewart and Stewart [1997]......	161
Figure 6.6	Predicted kinematic pile–soil interaction transfer function for the Lancaster site plotted versus (a) plain frequency and (b) dimensionless frequency.....	162
Figure 6.7	Model predictions versus empirical data for the Lancaster building during 1994 Northridge, California, earthquake after Kim and Stewart [2003]......	163
Figure 6.8	Longitudinal elevation view of proposed Linden Street Overcrossing replacement (after Caltrans [2016])......	164
Figure 6.9	Transverse elevation view of interior bent for proposed Linden Street Overcrossing replacement (after Caltrans [2016])......	164
Figure 6.10	Acceleration response spectrum used for proposed Linden Street Overcrossing replacement (after construction plans, Caltrans [2016]). ....	165
Figure 6.11	Shear-wave velocity profile measured using P-S suspension logging (after Caltrans [2016]). ....	165
Figure 6.12	Predicted spectral ratios for Linden Street Overcrossing. ....	167
Figure 6.13	Kinematic pile–soil interaction effect on acceleration response spectrum. ....	167

## LIST OF SYMBOLS

**LATIN SYMBOLS (default units listed in parenthesis unless otherwise noted in text)**

$a_0^p$	Dimensionless frequency for pile dynamics
$A_g$	Pile gross cross-sectional area (m <sup>2</sup> )
$B$	Pile diameter, or beam transverse width for beam-on-springs methods (m)
$c$	Dashpot coefficient (kN·s/m)
$c_0$	Phase speed of flexural waves in cylindrical rod (m/s)
$E$	Young's modulus (kPa)
$E_s$	Soil elastic Young's modulus (kPa)
$E_p$	Pile elastic Young's modulus (kPa)
$EI_{SDOFO}$	Flexural rigidity of single-degree-of-freedom oscillator column (kN·m <sup>2</sup> )
$f$	Frequency (Hz)
$f_{1,SDOFO}$	First-mode fundamental frequency of fixed-base single-degree-of-freedom oscillator (Hz)
$\tilde{f}_{1,SDOFO}$	First-mode fundamental frequency of flexible-base single-degree-of-freedom oscillator, <i>i.e.</i> considering foundation flexibility (Hz)
$f_c$	Corner frequency of kinematic pile–soil interaction transfer function, defined as frequency beyond which significant deamplification of the free-field motion occurs due to kinematic pile–soil interaction (Hz)
$f'_c$	Concrete 28-day nominal compressive strength (kPa)
$f_m$	Ground motion mean frequency; inverse of $T_m$ (Hz)
$G$	Shear modulus (kPa)
$H$	Thickness of soil profile from ground surface to bedrock (m)
$H_{SDOFO}$	Height of single-degree-of-freedom oscillator from ground surface to lumped mass centroid (m)
$H_u$	Transfer function ordinate
$I_p$	Pile gross moment of inertia (m <sup>4</sup> )
$k$	Linear-elastic soil $p$ - $y$ curve stiffness [(kN/m)/m = kPa]
$k_{msr}$	Modulus of subgrade reaction [kN/m <sup>2</sup> /m = kPa/m = kN/m <sup>3</sup> ]
$k_{SDOFO}$	Horizontal swaying stiffness of single-degree-of-freedom oscillator (kN/m)
$K_e$	Soil $p$ - $y$ curve elastic stiffness [(kN/m)/m = kPa]

$K_{e,10B}$	Average value $K_e$ computed over upper ten pile diameters [(kN/m)/m = kPa]
$K_{xx}$	Foundation impedance for horizontal translation degree of freedom (kN/m)
$K_0$	At-rest coefficient of lateral earth pressure
$L$	Pile length (m)
$l_c$	Pile active length (m)
$m_{SDOFO}$	Mass of single-degree-of-freedom oscillator (kg)
$M$	Moment (kN·m)
<b>M</b>	Earthquake moment magnitude
$M_{cr}$	Moment corresponding to cracking of concrete in tension for reinforced-concrete section (kN·m)
$M_y$	Moment corresponding to yielding of longitudinal reinforcing steel in tension for reinforced-concrete section (kN·m)
$M_y$	Yield moment for reinforced-concrete section (kN·m)
$p$	Soil $p$ - $y$ curve force, per unit length of pile (kN/m)
$P$	Pile axial load (kN)
$s_u$	Soil undrained shear strength (kPa)
$S_{DS}$	Short-period spectral acceleration as defined in ASCE 7 (ASCE 2010); (g)
$S_{ij}$	Cross power spectral density between signals $i$ and $j$
$S_{ii}$	Auto power spectral density for signal $i$
$T_m$	Ground motion mean period computed using Rathje et al. (2004); (s)
$u_g$	Ground surface displacement (m)
$u_p$	Pile head displacement (m)
$u(t)$	Displacement signal in time domain (m)
$U(\omega)$	Frequency-domain representation of the time domain signal $u(t)$
$V_S$	Soil shear wave velocity (m/s)
$V_{S,10B}$	Time-averaged shear wave velocity computed over upper ten pile diameters (m/s)
$V_{S,30}$	Time-averaged shear wave velocity computed over upper 30 m of site profile (m/s)
$V_{S,H}$	Time-averaged shear wave velocity computed over full thickness of soil profiles used for ground response analyses, $H$ (m/s)
$V_{S,L}$	Time-averaged shear wave velocity computed over length of pile, $L$ (m/s)
$y$	Soil $p$ - $y$ curve relative horizontal displacement between pile and soil (m)
$z$	Depth below ground surface measured as a positive number (m)

## GREEK SYMBOLS AND OPERATORS

$\alpha$	Static stiffness modifier for pile lateral translation
$\beta$	Damping, expressed as percentage of critical damping.
$\delta$	Ratio of Winkler modulus $K_e$ to soil elastic modulus $E_s$
$\Delta t$	Time increment for discrete time signal (s)
$\varepsilon_{50}$	Strain mobilized at one-half of maximum stress during laboratory strength tests on soil
$\mathbf{F}$	Fourier transform operator
$\gamma_{avg}$	Average soil shear strain in pile–soil interaction zone of influence for laterally-loaded pile
$\gamma_r$	Reference strain corresponding to 50% modulus reduction
$\gamma^2$	Coherence
$\kappa$	Wavenumber
$\lambda$	Characteristic term or “Winkler parameter” for laterally loaded pile ( $m^{-1}$ )
$\lambda_{ff}$	Wavelength of free-field soil column under harmonic excitation (m)
$\nu$	Poisson’s ratio
$\omega$	Angular frequency (rad./s)
$\phi$	Curvature ( $m^{-1}$ )
$\phi_{pk}$	Soil peak friction angle (deg.)
$\theta$	Pile head rotation (radians)
$\rho_p$	Mass density of pile ( $Mg/m^3$ )
$\rho_s$	Mass density of soil ( $Mg/m^3$ )



# 1 Introduction

Seismic design of bridges and other structures supported on bored or driven piles often utilizes a substructure method of dynamic analysis in which the foundation elements are not explicitly modeled but are replaced by springs and dashpots representing the foundation impedance. The ground motion appropriate for input to the free end of the springs, known as the *foundation input motion* (FIM) differs from the free-field motion (FFM) due to the difference in stiffness and deformation characteristics between the pile(s) and soil, which is the concept of kinematic soil–structure interaction (SSI). As with many other aspects of SSI, the difference between the FIM and FFM often results in a favorable reduction in demand placed on the structure, yet it is typically ignored in practice. In some cases, however, the FIM could actually be greater than the FFM, which is also typically overlooked.

Within the substructure method, the problem of relating the FFM to the FIM is solved separately from the dynamic analysis of the superstructure. Ground motions from a seismic hazard analysis represent shaking in the free field and must be modified to account for kinematic SSI. For example, the PEER ground-motion database [Ancheta et al. 2014], a commonly used source for accelerograms used for dynamic analyses, excludes records influenced by SSI. Similarly, response spectra representative of the FFM rather than the FIM are typically used for pseudo-static response spectrum analysis. Pseudo-spectral accelerations (PSA) on seismic hazard maps and site amplification factors used in building codes and seismic design guidelines (e.g., ASCE-7 [2010]) do not include the influence of SSI.

Whereas kinematic SSI for shallow foundations is relatively well understood, and tools are available for implementation in routine practice (e.g., NIST [2012]), similar tools are not yet available for piles. Since the 1960s, several researchers have studied the response of piles and pile groups using simplifying assumptions such as linear elasticity, homogeneous soil properties, and harmonic ground motions, including Tajimi [1969], Flores-Berones and Whitman [1982], Gazetas and Dobry [1984a], Fan et al. [1991], Kaynia and Novak [1992], and many others. More recent developments such as Anoyatis et al. [2013], Sica et al. [2013], and Di Laora and Rovithis [2014] have incorporated the effects of inhomogeneous and layered soil profiles and different pile boundary conditions. However, the previous studies to-date have yet to produce tools such as formulas for transfer functions and response spectrum scaling factors that reliably account for the complexity of realistic pile, soil, and ground motion conditions—in particular, nonlinear material behavior—yet are simple enough for implementation in routine practice. The purpose of this study is to develop such tools with consideration of realistic dynamic material behavior and subsurface conditions using the type of information known for a typical project. Emphasis is placed on evaluating the influence of the following factors:

- Nonlinearity due to (i) free-field site response, (ii) interaction at the pile–soil interface, and (iii) nonlinear pile structural behavior.
- Inhomogeneous soil profiles, which for this study are developed from the results of real subsurface investigations.
- The complexity of real ground motions, including variable frequency content, intensity, and incoherence (i.e., spatial variability).
- Pile group behavior, in particular the influence of ground-motion incoherence over the spatial extent of the pile group in light of the preceding factors.

Previous computational studies using elastic material properties and other highly idealized conditions have generally concluded that reductions between the FIM and FFM are insignificant and can be ignored in practice. This study demonstrates that large-diameter piles used in soft-soil conditions can result in reductions to design ground motions that are significant and could result in appreciable cost savings.

The few documented case studies of measured kinematic pile–soil interaction effects provide conflicting evidence as to whether or not it is a significant phenomenon that should be of interest to foundation engineers. This research seeks to explain these case studies and clearly demonstrate the conditions under which pile kinematic SSI should be considered, and likewise when it can safely be ignored.

The outcome of this work is a set of “generalized models” for predicting transfer functions and spectral ratios for use in routine practice. The terminology “generalized model” is used here to refer to a mathematical model (i.e., equation with a specified functional form) intended to cover a wide range of conditions encountered in routine practice. The generalized model is implemented for specific project conditions by computing coefficients based on known project parameters such as pile size and soil shear-wave velocity. The coefficients have been determined by statistical regression of the results of a parametric analysis covering typical foundation, subsurface, and ground motions conditions.

## 1.1 ORGANIZATION

This report is organized as follows:

- The remainder of Chapter 1 introduces the fundamentals of kinematic pile–soil interaction, followed by a literature review of previous work on the subjects of pile dynamics and lateral load analyses using the  $p$ - $y$  method. Since most of the available pile kinematic solutions rely on simplifying assumptions of linear elasticity and highly idealized subsurface conditions, a critique is given in the context of the limitations of these assumptions and the motivation to overcome them with the present study. The limited amount of available empirical and experimental evidence of pile kinematic SSI is also presented.
- Chapter 2 presents a derivation of an elastic analytical solution for kinematic pile–soil interaction. The closed-form solution that results is used for validating the numerical modeling approach that will subsequently be used for nonlinear analyses.

- Chapter 3 defines the bounds of the parametric study performed to investigate the kinematic pile problem, and lays out the means by which the input parameters for the nonlinear analyses were formulated.
- Chapter 4 presents the results of the parametric study, followed by development of generalized models for predicting those results in a forward-design scenario. The forward prediction models consist of a specified functional form with coefficients that are predicted via equations developed through statistical regression. Comparisons are made between the nonlinear analysis results and idealized elastic solutions, which show that the elastic solutions generally are capable of predicting the average response of the nonlinear system. However, the elastic solutions fail to capture the large variability exhibited by the nonlinear analysis results, which is caused by the complexity of realistic subsurface conditions and ground motions, and soil nonlinearity.
- Chapter 5 investigates issues related to the combination of inertial and kinematic SSI effects. An understanding of the combined effects is necessary for the re-examination of case history data presented in the following chapter.
- Chapter 6 provides example applications of the generalized models through (i) re-examination of existing case history data, and (ii) a hypothetical bridge design scenario.
- Chapter 7 provides conclusions and recommendations for implementation of the generalized results in engineering practice.
- Appendix A contains profiles of soil properties that define the sites used for nonlinear analyses.
- Appendix B discusses a pilot field study done as part of this project to measure kinematic pile–soil interaction transfer functions for full-scale conditions. The framework used for this pile study is documented with the intent that it will be repeated in the future for further validation of computational approaches.

## 1.2 FUNDAMENTALS

Soil–structure interaction (SSI) can be broadly classified into two effects<sup>1</sup>:

- *Inertial interaction*, which describes how inertial forces generated in the structure induce foundation displacements and rotations that would not occur if the structure had a fixed base, resulting in additional displacements in the structure and a change of fundamental frequency or “period lengthening”
- *Kinematic interaction*, which describes how waves propagating in the free field differ from the motion of the foundation(s) due to differential foundation–soil stiffness, ground-motion incoherence, and wave-scattering effects

---

<sup>1</sup> Professor Robert V. Whitman is credited with coining the terms inertial and kinematic during the 1970s [Roesset 1994; Kausel 2010].

In the context of the substructure method, foundation “impedance” (defined below) depends primarily on inertial SSI, and kinematic SSI determines the appropriate FIM to be used for the analysis. For pile-supported structures, kinematic SSI will be referred to as “kinematic pile–soil interaction” in this text.

Two effects resulting from kinematic pile–soil interaction are of interest to foundation engineers. The first, which is the primary subject of this study, is the difference between the FIM and the FFM. The second topic of interest is quantifying demands placed on the pile directly as a result of excitation of the surrounding soil. Pile foundations are typically designed only to resist force effects from the superstructure, including inertial demands during earthquake loading in seismic regions. Kinematic loads coming from the ground are often ignored, except for cases of large permanent ground displacement such as lateral spreading. However, kinematic pile–soil interaction can impose large demands on piles even in the absence of permanent ground deformation, particularly where a significant soil stiffness contrast exists over the length of the pile. While kinematic demands are not the focus of this study, the analysis method described herein sheds lights on the problem and could be used for future studies.

The substructure method of SSI analysis (e.g., Roesset et al. [1973]) for a pile-supported structure can be summarized in three steps:

1. Determine the kinematic response of the pile foundation with the mass of the supported structure set equal to zero; this provides an estimate of the demand on the pile resulting from the ground vibration as well as the motion at the top of the pile (the FIM);
2. Determine the dynamic impedance at the pile head, consisting of frequency-dependent springs and dashpots that relate an applied force or moment at the pile head to a unit displacement or rotation, respectively; and
3. Evaluate the response of the structure supported on the springs and dashpots from step 2 and excited by the FIM from step 1.

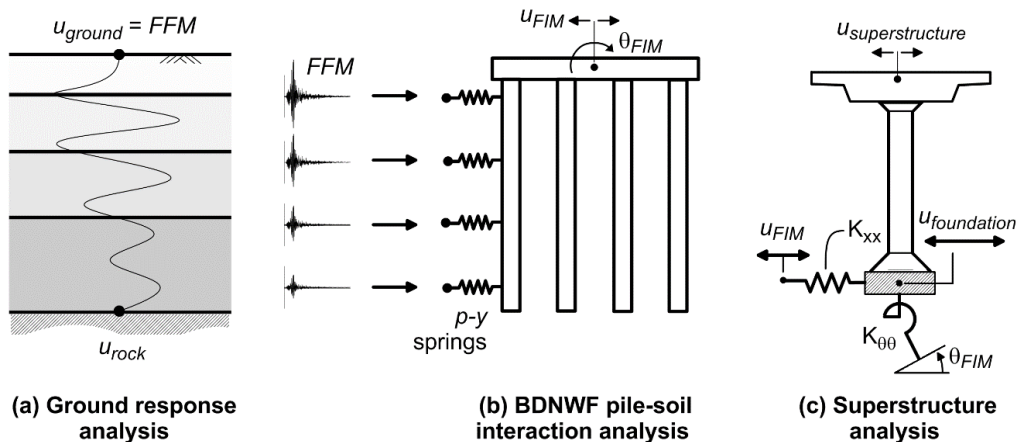


**Figure 1.1** Substructure method of analysis for bridge bent supported on a pile group. Note that vertical impedance is not shown but could also be considered.

The substructure method for a pile-supported bridge bent is depicted in Figure 1.1. The alternative to the substructure method is to analyze the complete structure–pile–soil system simultaneously, known as the “direct” method of analysis. While this approach overcomes certain issues associated with combining the different steps of the substructure method, it is computationally expensive, difficult to perform using existing commercial software, and requires advanced expertise in both geotechnical and structural engineering. Hence for routine practice, tools and associated guidance for facilitating use of the substructure method are preferred.

The stiffness contrast between a pile and surrounding soil is the primary mechanism driving kinematic pile–soil interaction. A stiff pile in a relatively soft-soil profile will generally undergo less deformation than the free-field soil, whereas the deformed shape of a flexible pile in stiff soil will be closer to the deformation of the surrounding ground.

Frequency of the free-field excitation has a strong influence on kinematic pile–soil interaction because the wavelength of the free-field motion determines the extent to which the ground movement varies over the length of the pile. Wavelength of the free-field motion is defined as  $\lambda_{ff} = V_S / f$ , where  $V_S$  is soil shear-wave velocity, and  $f$  is the excitation frequency. This is illustrated in Figure 1.2 for a “floating” pile with free-head and free-tip boundary conditions of length  $L = 20$  m, subjected to harmonic free-field excitation representing idealized vertically-propagating shear waves. The pile flexural rigidity  $E_p I_p = 1325 \text{ MN}\cdot\text{m}^2$  ( $E_p$  and  $I_p$  are the pile Young’s modulus and moment of inertia, respectively) corresponds to a  $B = 1$ -m-diameter circular reinforced concrete (RC) section. Figure 1.3 depicts the response of the same system, but for a fixed-head pile boundary condition in which the pile head is restrained against rotation to simulate connection to a pile cap or other stiff structural element.

For low-frequency excitation, the pile moves in concert with the ground since the ground displacement is relatively uniform over  $L$ . For high-frequency, short-wavelength excitation, the ground displacement reverses directions many times over  $L$ . The pile flexural stiffness prevents it from conforming exactly to the ground displacement, instead averaging the variable ground displacements imposed over its length. This average displacement approaches zero at high frequencies corresponding to low ratios of  $\lambda_{ff}/L$ . This is similar to the concept of base–slab averaging for shallow foundations (e.g., see Veletsos and Prasad [1988]), in which the stiffness and strength of the foundation average the spatially variable ground motions imposed across its footprint. As for shallow foundations, spatial variability (incoherence) of real ground motions has the potential to further increase the averaging effect for pile groups that cover a large area, such as the footprint of a building.

Between these extremes, intermediate-frequency excitation places the largest flexural demands on the pile for the example parameters considered here. Notice that the free-field excitation has the same displacement amplitude for each of the frequencies shown.

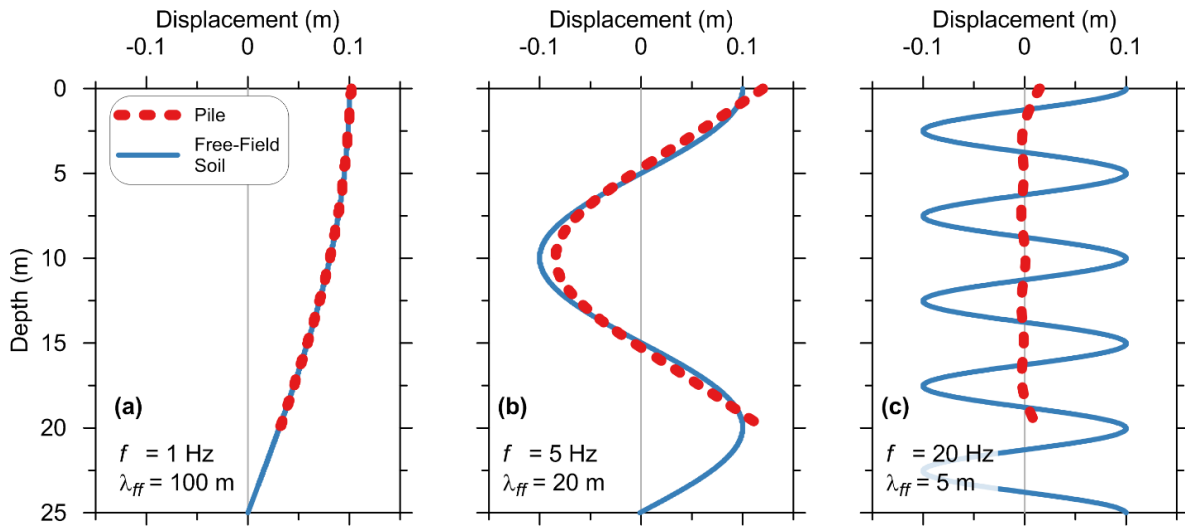


**Figure 1.2** Profiles of soil and free-head pile displacement for three frequencies of harmonic free-field excitation.

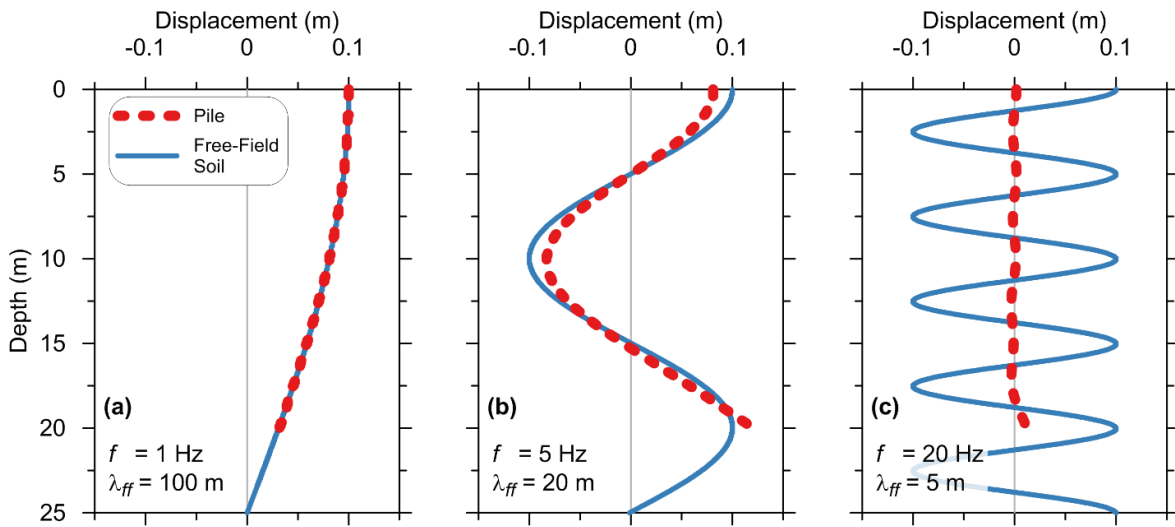


**Figure 1.3** Profiles of soil and fixed-head pile displacement for three frequencies of harmonic free-field excitation.

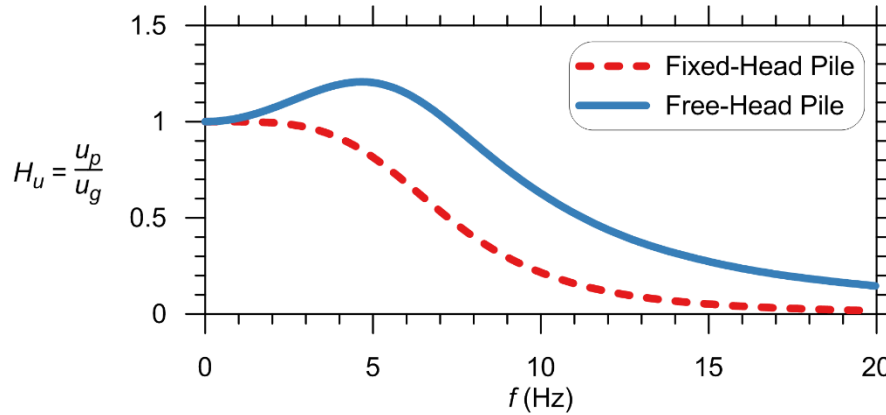


**Figure 1.4 Kinematic pile–soil interaction transfer functions computed for idealized linear-elastic conditions.**

Taking the pile head motion  $u_p$  as the FIM and the ground surface displacement  $u_g$  as the FFM, the ratio FIM/FFM can be expressed as a frequency-dependent transfer function by computing FIM/FFM at several frequencies over a range of interest. The transfer function can be thought of as a filter, which describes how the pile–soil system modifies an input signal (the FFM) to produce an output signal (FIM). A transfer function ordinate  $H_u$  of unity indicates that the soil and pile move in unison, such as depicted in Figure 1.2(a), while  $H_u \approx 1.2$  and 0.15 for the conditions depicted in Figure 1.2(b) and (c), respectively. Transfer functions for the free- and fixed-head piles are depicted in Figure 1.4. Notice that for the free-head pile,  $H_u$  exceeds 1.0 for frequencies up to about 7 Hz, indicating that the pile amplifies the ground motion ( $u_p > u_g$ ), while the fixed-head pile displaces less than the free field at all frequencies. The phenomenon of  $H_u > 1.0$  for free-head piles, which occurs when  $\lambda_{ff} \approx L$  as depicted in Figure 1.2(b), will be referred to as “kinematic amplification” in this study.

For both fixed- and free-head piles, the FIM is reduced from the FFM at high frequencies, implying that a structure supported by the piles will experience a beneficial reduction in demand at these frequencies if the FIM is used for design. The frequency beyond which  $H_u$  descends below unity will be referred to as the “corner frequency” ( $f_c$ ) of the transfer function in this text. Since  $H_u$  is technically less than unity for any  $f > 0$  for elastic fixed-head transfer functions, an arbitrary definition of  $f_c$  will be adopted as the frequency at which  $H_u \approx 0.95$ , for example about 3.5 Hz for the fixed-head case in Figure 1.4. Whether or not the corner frequency falls within the frequency range of engineering interest (approximately 0.2–20 Hz for typical structures) depends on factors such as the relative stiffness contrast between the pile and soil, changes in soil stiffness over the length of the pile, and whether or not restraint against rotation is provided at the pile head.

In addition to the differences in displacement between the pile and soil, Figure 1.2 shows that a free-head pile also undergoes rotation at the pile head due to the kinematic response. To compute the response of a structure supported by free-head piles using the substructure method, the pile head rotation  $\theta_{FIM}$  must be input to the base of the structural model in addition to  $u_{FIM}$ . Since rotation of the free-field soil column is zero at the ground surface for vertically propagating shear waves (since shear strain has to be zero for a zero stress condition), the transfer function for free-head pile rotation is instead normalized by the free-field displacement, and is usually multiplied by pile diameter such that is dimensionless (i.e.,  $H_\theta = \theta_{FIM} \cdot B / u_{FFM}$ ).

The transfer functions depicted in Figure 1.4 were computed using an analytically-derived linear-elastic solution that is presented in detail in Chapter 2. For more realistic pile, soil, and ground motion conditions typical of a real project, numerical techniques such as the finite-element method can be used to compute the dynamic response of the system, which is the approach used in this study. Because real earthquakes cause the free field and structure to respond at multiple frequencies simultaneously, and because of nonlinearity in the system response, the results of dynamic analyses cannot be used directly to compute  $u_p/u_g$  at a single isolated frequency. Instead, the response history of the pile-head and ground-surface motions must be transformed to the frequency domain, e.g., using a Fourier transform. This allows  $H_u$  to be computed as the ratio of Fourier amplitude spectra (FAS) at each frequency over the range of interest as depicted in Figure 1.5. The following notation is used to denote these operations:

$$\mathbf{F}(u(t)) = U(\omega) \quad (1.1)$$

$$H_u(\omega) = |U_{FIM}(\omega)| / |U_{FFM}(\omega)| \quad (1.2)$$

In Equations (1.1) and (1.2),  $u(t)$  is the time-domain signal of either the FIM ( $u_p$ ) or FFM ( $u_g$ ), and  $\mathbf{F}$  denotes a Fourier transform operation that produces a complex-valued frequency-domain signal denoted by capital letter  $U(\omega)$ . The amplitude and phase of the signal are computed from its real and imaginary parts [ $Re(U(\omega))$  and  $Im(U(\omega))$ ] as:

$$|U(\omega)| = \sqrt{Re[U(\omega)]^2 + Im[U(\omega)]^2} \quad (1.3)$$

$$\phi_u(\omega) = \arctan\left(\frac{Im[U(\omega)]}{Re[U(\omega)]}\right) \quad (1.4)$$

For simplicity, the abbreviation FAS is sometimes used as a shorthand for the magnitude of the FAS, that is  $FAS = |U(\omega)|$ . The frequency domain signal can be represented equivalently in terms of either frequency  $f$  or angular frequency  $\omega$ .

Although transfer functions may be unfamiliar to foundation engineers outside the realm of pile dynamics, they are a very useful tool for seismic design. Once a kinematic pile–soil interaction transfer function has been defined for a given pile–soil system, it can be used to compute a FIM given a FFM without repeating the actual dynamic analysis of the pile subjected to the FFM. This is accomplished by convolving the transfer function with the FFM in the frequency domain (i.e., multiplying the FAS ordinates of the FFM and transfer function at each frequency), then performing an inverse-Fourier transform to recover the FIM signal in the time-domain—essentially performing the process depicted in Figure 1.5(b)–(d) in reverse. These operations can easily be performed with commonly used mathematical software. Hence, if a reliable predictive model is made available to define a transfer function using parameters known for a typical project—pile and soil properties and estimates of ground-motion intensity measures from a seismic hazard analysis—then foundation engineers can skip the dynamic pile analysis yet still provide the structural designer an estimated FIM instead of FFM for more realistic dynamic analysis of the superstructure.

While response history analysis may be used for major bridges or other critical infrastructure, for routine projects, seismic design is usually performed via pseudo-static response

spectrum analysis. By computing response spectra from a FIM and FFM, the ratio of spectral ordinates at each period can be computed as depicted in Figure 1.6. These “spectral ratios” (also referred to as ratio-of-response-spectra or RRS) can then be used in a forward-design scenario to modify FFM response spectra generated from the building code or site-specific seismic hazard analysis to represent a FIM. Hence, just as in the case of the transfer functions for dynamic analysis, if foundation engineers can reliably estimate spectral ratios using known project parameters, FIM response spectra can be generated for design purposes without performing dynamic pile analyses.

Although the spectral ratio plot in Figure 1.6(d) appears to be equal to the transfer function plot in Figure 1.5(d) with the horizontal axes flipped, spectral ratios should not be interpreted simply as the inverse of the kinematic transfer function. A response spectrum represents the response of a single-degree-of-freedom oscillator (SFOFO) to an input ground motion and therefore depends on the properties of both the ground motion and the oscillator. Whereas the response spectrum ordinate at longer natural periods (low natural frequency) is heavily dependent on the flexibility of the oscillator, at short natural periods (high natural frequency) the spectral ordinate is controlled by the largest amplitude peak in the ground motion, which is usually dominated by intermediate frequency energy.

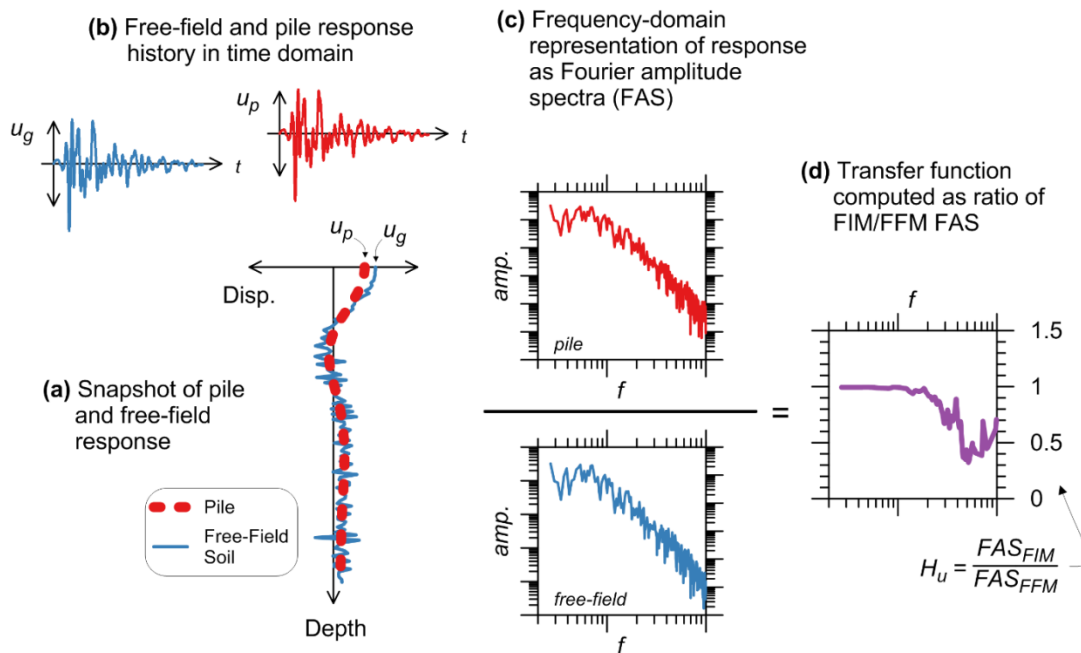


**Figure 1.5** Time- and frequency-domain representations of pile seismic response for computation of kinematic transfer function.

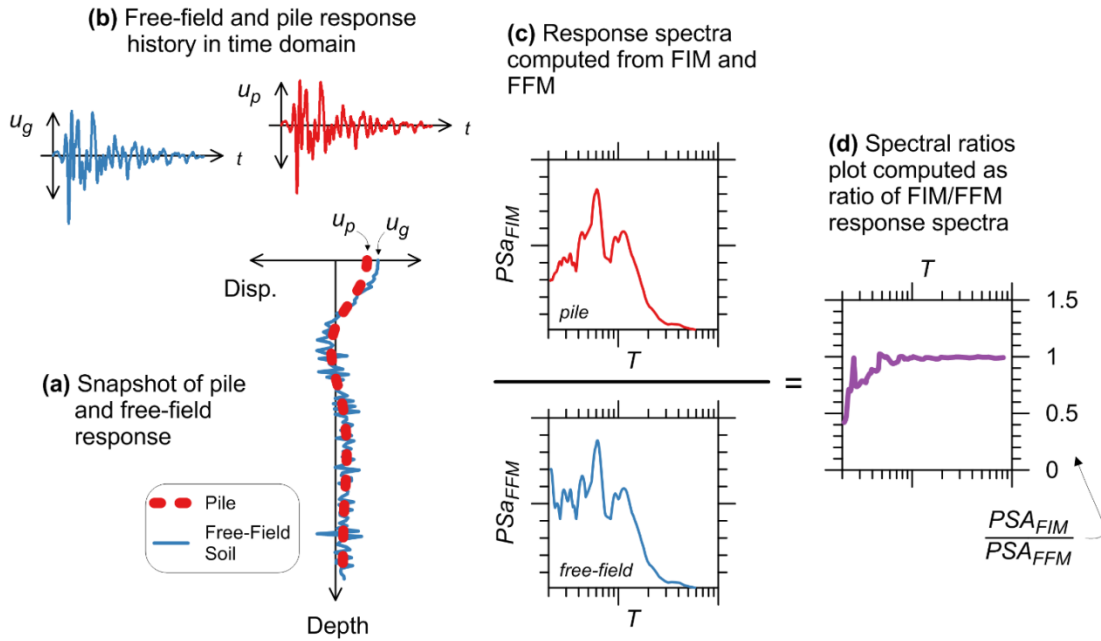


**Figure 1.6 Time-domain and response spectrum representations of pile seismic response for computation of kinematic spectral ratios.**

### 1.3 PREVIOUS STUDIES

#### 1.3.1 Winkler Analysis and $p$ - $y$ Curves

The approach used in this study is the beam-on-dynamic-nonlinear-Winkler-foundation (BDNWF) model solved numerically with the finite-element method. The Winkler method refers to the response of a beam supported on a bed of springs characterized by a constant elastic stiffness or “modulus of subgrade reaction,” the term favored by Terzaghi and Peck [1948]. Winkler’s [1867] hypothesis is that the pressure exerted by the subgrade on a loaded beam at a given point is proportional to the deflection of the beam at that point and independent of the response at other locations. Hetenyi [1946] and Vesic [1961] demonstrated that the error between Winkler models and elastic continuum models is small for many realistic scenarios involving flexible beams, and that when used within the appropriate bounds, the Winkler method can generate reliable results for foundation design. For analysis of piles, the Winkler family of methods considers a discretized foundation element attached to the ground through springs representative of horizontal and/or vertical pile–soil interaction, and has been extended to include nonlinear pile–soil interaction through  $p$ - $y$ ,  $t$ - $z$ , and  $q$ - $z$  curves.

While the majority of previous studies of dynamic pile–soil interaction using the Winkler method have utilized linear-elastic Winkler foundation springs, this study utilizes nonlinear soil springs. Accounting for soil nonlinearity directly is a more robust approach than equivalent-linear methods that approximate nonlinearity through a strain-compatible degraded stiffness. This is particularly true when soil strains vary over the duration of a dynamic problem and over the length of a pile. Several variations of the Winkler method are possible ranging from static analysis with linear-elastic springs (BWF), to static analysis with nonlinear springs (BNWF), to the dynamic

analyses performed for this project. These methods will be collectively referred to as Winkler-type to distinguish them from continuum models.

Early nonlinear  $p$ - $y$  curves (e.g., McClelland and Focht [1958]) were developed by matching the results of full-scale load tests to simple functional forms that were based on the theoretical state of stress around a laterally loaded pile. The offshore oil drilling industry funded seminal work by Matlock [1970] for soft clays, Reese and Welch [1975] for stiff clay above groundwater, Reese et al. [1975] for submerged stiff clays, and Reese et al. [1974] for sand. Reese et al. [2006] provides an overview of the theoretical and experimental development of these  $p$ - $y$  curves. Much of this original work has been improved upon and adapted for specific conditions; e.g., Reese et al. [1974] was updated by O’Neill and Murchison [1983] and is often known as the “API sand” curve [API 1993]. Boulanger et al. [2003] recommended further modifications to the API [1993] curve to reflect the fact that the modulus of sand tends to increase approximately in proportion to the square root of confining pressure rather than increasingly linearly with depth.

The first-widely available computer-based implementation of the  $p$ - $y$  method was a finite-difference solution called *COM624* [Reese and Sullivan 1980]. This code later became the basis for the commercial program *LPILE* [Reese et al. 2005] and other similar software that is widely used in practice. For many projects, the extent of “seismic” foundation design is that the project structural engineer provides the foundation engineer with top-of-pile force effects (shear, axial, and moment), and the foundation designer sizes the pile in terms of diameter and length to adequately resist these loads. Even in cases when the design loads are pseudo-static representations of seismic inertial forces, *LPILE* or an equivalent program is often used to design for seismic lateral loads as if they were static, without consideration of the fact that the default  $p$ - $y$  curves available in the software are not intended for dynamic problems. While top-of-pile spring stiffness matrices (impedance functions) are sometimes provided back to the structural designer for further analyses, kinematic pile–soil interaction is rarely considered.

While the  $p$ - $y$  curves described above have seen widespread use in practice, they were initially developed for static or slow-monotonic loading conditions. In some instances, effects of cyclic degradation over time were taken into account, but these were meant to represent repeated cyclic loading from wave action for offshore applications—not rapid, high-intensity cyclic loading from earthquakes. Existing  $p$ - $y$  curve definitions have several shortcomings, including (after Khalili-Tehrani et al. [2014]):

- Inaccurate small-strain stiffness.
- A functional dependence on diameter that is not thoroughly validated since the curves are based on a limited number of tests.
- A lack of functional dependence on the pile head boundary condition.

For dynamic analyses, the initial stiffness problem is of greatest concern. There are two issues to consider:

1. Some of the functional forms (e.g., Matlock [1970] and Reese and Welch [1975]) have an initial tangent stiffness of infinity. While this may be trivial for conventional problems in which loads applied at the pile head induce significant head displacement and thus reach the nonlinear range of the  $p$ - $y$  curve, infinite stiffness is problematic for dynamic problems where small relative displacements may occur between the pile

and soil, especially at depth. Small trial displacements during numerical solution routines will result in erroneously large forces, causing convergence problems. Furthermore, infinite initial stiffness is problematic when performing modal analyses to compute natural frequencies of the pile-soil or structure-pile-soil system.

2. Because of the rudimentary equipment used in the early tests, accurate measurements of pile strains could not be achieved in the range of truly elastic soil behavior [Choi et al. 2015]. This error is further propagated when the strains are numerically double integrated to compute displacement and double differentiated to compute soil reaction, which are necessary steps to generate  $p$ - $y$  curves from load test results. Hence, even if the functional form of the  $p$ - $y$  curve allows specification of the initial stiffness, the available load test results are not adequate for accurately defining it. A more attractive approach would relate the initial stiffness of the soil-pile interaction to the elastic soil stiffness measured *in situ* using geophysical methods (e.g., maximum shear modulus  $G_{max}$ ), which is described further in §3.4.1.

Lam [2009] questioned the applicability of initial stiffness corresponding to  $G_{max}$  for practical applications of  $p$ - $y$  curves, noting that several lateral load tests of full- and model-scale piles have shown that the measured initial  $p$ - $y$  stiffness is significantly softer— by a factor of as much as ten—than the elastic stiffness computed from the results of small-strain geophysical site investigation methods. In reality, however, the instrumentation used during the load test is not capable of measuring the true initial stiffness. Hence, the experimental measurements to which Lam [2009] refers are actually in the nonlinear, albeit small-strain, range.

Numerical implementation of  $p$ - $y$  curves to accommodate cyclic loading via unload/reload rules is described by Wang et al. [1998] and Boulanger et al. [1999]. With some exceptions that will be discussed further in §3.3, the  $p$ - $y$  macro-element described by Boulanger et al. is implemented in *OpenSees* [McKenna 1997; McKenna et al. 2010] as the material *PySimple1*. The backbone curve defined by the *PySimple1* material is formulated to match the shapes of the Matlock [1970] and API [1993] curves for clay and sand, respectively. The infinite initial stiffness problem of Matlock [1970] is overcome in *PySimple1* by using a finite elastic stiffness computed using the method of Vesic [1961] up to a value of 35% of the ultimate resistance of the spring ( $p_{ult}$ ).

### 1.3.2 Analytical and Numerical Solutions for Pile Dynamics

Computational studies of pile dynamics can generally be divided into two groups: (i) simulated loading is applied at the pile head by machine vibrations or seismically-induced inertial forces in the structure, thereby inducing inertial SSI; or (ii) loading is applied by excitation of the free field, typically from seismic sources, inducing kinematic SSI. Studies falling into the latter category may or may not include inertial effects in addition to kinematic effects, depending on whether or not a superstructure mass is included. Studies can be further classified based on (i) the computational method used to arrive at the solution—analytical versus numerical; (ii) whether the domain is represented as a continuum or is discretized into thin layers using, for example, Winkler’s assumption; and (iii) whether linear or nonlinear material properties are used. While even further subcategories could be defined (two- versus three-dimensional domains, homogeneous versus

layered soil, mixed linear/nonlinear materials, etc.), the preceding classification broadly outlines the existing body of work on pile dynamics and will guide the following literature review.

Two of the earliest studies of pile dynamics, Penzien et al. [1964] and Tajimi [1969], considered a complete soil–pile–superstructure system excited by seismic waves. Penzien et al. performed one-dimensional ground response analysis of a clay layer using a lumped mass model and applied these free-field excitations to the pile foundations via viscoelastic Winkler springs, which in turn excited the superstructure. Soil nonlinearity was approximated using bilinear rather than linear springs, and connection details within the bridge superstructure were modeled explicitly. The entire system was solved simultaneously using a numerical time-stepping approach, a considerable achievement given computational power in the 1960s. Penzien [1970] describes application of this method for design of the Elkhorn Slough Bridge in California, with a detailed account of how the soil properties were selected based on results of a rigorous field investigation and laboratory testing program. Tajimi [1969] derived an elasticity-based analytical solution for a rigid structure supported by a flexible pile in a three-dimensional elastic continuum. While an exact solution is not reached, approximate solutions are given for the amplification of the structure displacement relative to the free-field ground displacement and for the pile head impedance.

In much of the pile dynamics work that followed, and especially over the following decade, emphasis was placed on inertial SSI with less attention given to kinematic effects. In inertial SSI studies, loading is applied at the pile head, and the goal is to generate impedance functions to represent foundation stiffness and damping for use in the substructure method. This includes studies utilizing Winkler models by Novak [1974], Matlock et al. [1978], Kagawa and Kraft [1981], Dobry et al. [1982], Gazetas and Dobry [1984a], Nogami and Konagi [1988], Nogami et al. [1992], and Chau and Yang [2005], as well as continuum model approaches by Novak et al. [1978], Kuhlemeyer [1979], Kaynia and Kausel [1982; 1991], Sen et al. [1985], Wolf [1985], Pak and Jennings [1987], Tronchanis et al. [1991], and Mamoon and Banerjee [1992]. While the inertial SSI results are not directly applicable to this study, the analytical framework developed by these researchers was often used subsequently to investigate kinematic effects. Additionally, studies that focused on inertial SSI provide the only available references for quantifying certain parameters, such as the dashpot coefficient used to model radiation damping for Winkler-type analyses.

Blaney et al. [1976] generated perhaps the first kinematic transfer functions for free-head piles from results of a finite-element continuum model considering a limited parametric range of pile and soil profile properties. At roughly the same time, R. Flores-Berrones' research [1974], who was completing a Ph.D. at the time, focused on the pile kinematic problem but utilized a Winkler model. In their seminal 1982 paper, Flores-Berrones and Whitman provide a chart-based solution for predicting the amplification or de-amplification of the pile head relative to the free-field soil displacement as a function of excitation frequency and the soil-profile fundamental frequency. The kinematic response is isolated by using a massless superstructure; the work also considers combination of inertial and kinematic effects. Other studies including kinematic response include Gazetas [1984], Gazetas and Dobry [1984a], Banerjee et al. [1987], Fan et al. [1991], Makris and Gazetas [1992], Makris et al. [1996], Giannakou et al. [2010] for battered piles, Di Laora et al. [2012], Di Laora and Sanctis [2013], Anoyatis et al. [2013], and Di Laora and Rovithis [2014]. The most recent references provide analytical solutions for increasingly complex soil profiles (e.g., stiffness increasing as a nonlinear function of depth) and new insight into normalization of the results.

While most of these studies modeled seismic excitation by vertically-propagating shear waves, similar solutions for inclined waves have been presented by Barghouthi [1984], Mamoon and Banerjee [1992], and Kaynia and Novak [1992]. Kaynia and Novak [1992] and Makris [1994] also provided solutions for Rayleigh waves, and solutions are available for axial kinematic response due to vertical  $P$ -wave excitation (e.g., Mylonakis and Gazetas [2002]).

Kaynia and Kausel [1982] formulated a boundary-integral solution to the Green's functions for a loaded circular disc in an elastic half-space meant to represent a pile. Their rigorous approach produced impedance functions and kinematic transfer functions for single piles and pile groups, and became the standard by which many other studies were judged throughout the 1980s and 1990s. Fan et al. [1991] implemented a computer-based solution of the Kaynia and Kausel [1982] formulation, which allowed computation of transfer functions for single piles and pile groups for a variety of pile/soil stiffness ratios, pile length/diameter ratios, and pile head-fixity conditions. Up until this point, most studies had failed to present generalized recommendations that could easily be applied in a forward design sense. Fan et al. [1991] thus became the standard against which future pile KSSI studies were judged. Transfer functions from the Fan et al. [1991] study are shown in Figure 1.7.

The results of these studies showed that pile kinematic SSI effects depend primarily on (i) the stiffness contrast between the pile and soil, often expressed as a ratio of pile to soil modulus ( $E_p/E_s$ ); (ii) the variation of soil stiffness over the length of the pile, e.g. homogeneous soil versus layered or increasing stiffness with depth; (iii) the pile head-fixity condition; and (iv) the pile length to diameter or "slenderness" ratio ( $L/d$ ). With regards to  $L/d$ , recent work by Anoyatis et al. [2013] as well as the results of this study show that for piles longer than the active length (i.e., flexible piles), as is typical for deep foundations, kinematic effects are not strongly dependent on the slenderness ratio as a standalone parameter. Fan et al. also considered pile groups, and concluded that the group response was similar to that for a single pile for typical pile spacing when coherent ground motions are considered.

For the studies that do center on kinematic effects, the focus is often placed on the flexural and/or shear demands imposed on the pile by the deforming soil (e.g., Banerjee et al. [1987]; Kavvadas and Gazetas [1993]; Kaynia and Mahzooni [1996]; Mylonakis [2001]; Nikolaou et al. [2001]; Saitoh [2005]; Maiorano et al. [2009]; Di Laora et al. [2012], and Sica et al. [2013]) rather than on modification of the FIM relative to the FFM. This is likely in part due to the prevailing opinion that piles in general do not have sufficient stiffness to significantly reduce the FIM over the frequency range of engineering interest. However, this may not be true considering that (i) large diameter drilled shafts and cast-in-steel-shell piles on the order of 2 m to 3 m diameter or more are now commonplace for supporting large bridges; (ii) soil nonlinearity effectively increases the stiffness contrast between pile and soil, and explicit consideration of nonlinearity has been missing from most previous studies; and (iii) the ability to reduce high-frequency motions may be of significant interest for certain structures, higher modes of conventional structures, and vibration-sensitive nonstructural components, even if there is no significant reduction near the first-mode period of the structure.

Beginning in the early 1990s and continuing to the present, the advent of personal computers and commercial and open-source finite-element/difference software has produced a number of studies that expand upon previous work by incorporating more realistic assumptions such as soil and pile nonlinearity, three-dimensional domains, and dynamic analysis with realistic

earthquake motions. This includes Nogami et al. [1992], Badoni and Makris [1996], Wu and Finn [1997a; 1997b], Boulanger et al. [1999], Bentley and El Naggar [2000], Klar and Frydman [2002], Maheshwari et al. [2004], Chau and Yang [2005], Kampitsis et al. [2013], Hussein et al. [2014], Pecker [2014], and others. In most cases, these studies attempted to recreate the results of model-scale dynamic tests and/or to compare to previous simplified approaches. While the findings provide valuable insight, especially on the importance of considering nonlinearity explicitly, in most cases results were not generalized for use with simplified design methods in forward analysis. One of the primary goals of this study is to fill that gap.

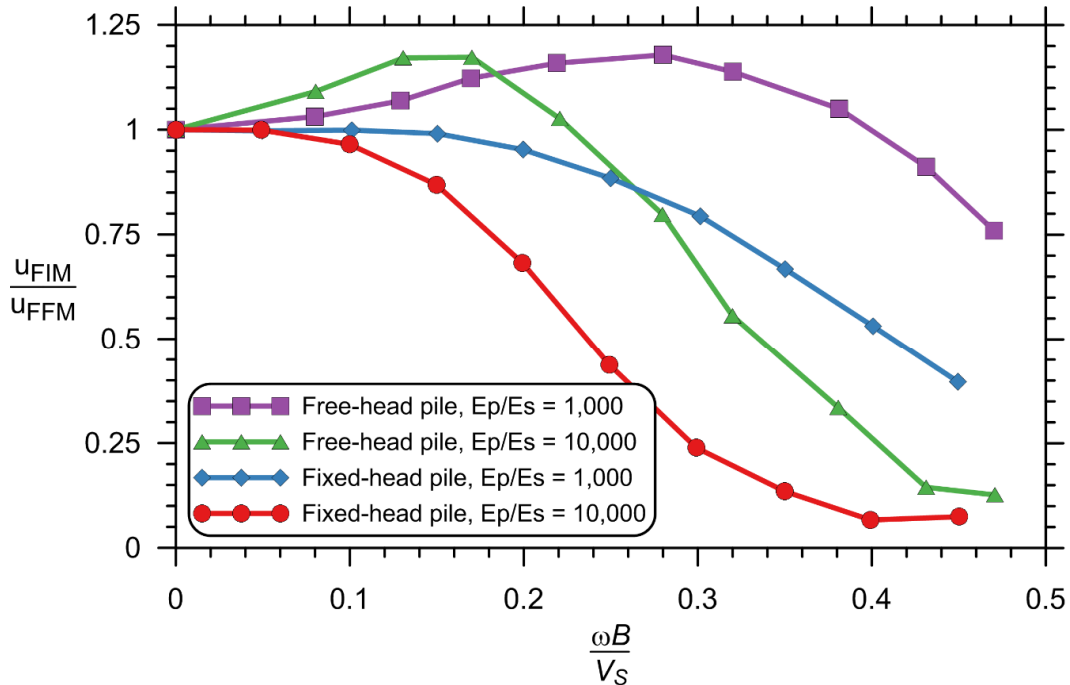


Figure 1.7 Kinematic pile-soil transfer functions from Fan et al. [1991] study for single pile with length-to-diameter ratio of 20.

### 1.3.3 Normalization Schemes

In order for the results of numerical pile kinematic SSI studies to be made useful for practical design applications, and indeed for SSI in general, it is desirable to find normalization schemes that describe kinematic pile response using variables that capture the physics of the problem and are themselves tractable to predict. For solutions based on linear-elasticity, closed-form solutions may be tractable because the solution does not depend on shaking intensity or other ground motion parameters, and involves a small number of input parameters. The task is more complicated for nonlinear problems and inhomogeneous soil domains because the solution becomes sensitive to shaking intensity and involves significantly more input parameters.

For pile dynamics problems, transfer functions are often presented versus dimensionless frequency  $\alpha_0^p$ , typically defined as (e.g., Kaynia and Kausel [1982] and Fan et al. [1991]):

$$a_0^p = \frac{\omega B}{V_s} \quad (1.5)$$

where  $\omega = 2\pi f$  is the angular frequency of excitation,  $B$  is the pile diameter (or radius for some studies, e.g., Novak et al. [1978] and Gazetas and Dobry [1984a]), and  $V_s$  is the soil shear-wave velocity. This dimensionless frequency was borrowed from the equivalent term for shallow foundations, where the  $B$  term represents the shallow foundation radius (e.g., Gazetas [1983]). While this form of  $a_0$  is essentially the only available choice for shallow foundations, pile behavior can be better characterized by terms other than diameter, which is a poor standalone representation of stiffness and characteristic patterns of deformation.

To incorporate the effect of pile-to-soil stiffness ratio, results of early studies are often presented as families of transfer function curves for various ratios of pile-to-soil modulus  $E_p/E_s$ . For example, the Fan et al. [1991] results in Figure 1.7 indicate that the same result is achieved for any size pile and soil stiffness as long as the slenderness ratio  $L/B$  and  $E_p/E_s$  are held constant. While the ratio of pile-to-soil stiffness is a very significant parameter in terms of its influence on the kinematic pile–soil interaction, the simple quantity  $E_p/E_s$  is a poor representation of this mechanism for practical applications because it does not contain any information on the geometric properties of the pile cross section. An “effective” pile modulus can be computed that equates a hollow section such as a steel pipe to an equivalent solid section, but this calculation is cumbersome and unfamiliar in routine foundation engineering. A more informative and familiar quantity to describe the pile stiffness is its flexural rigidity, which is the product of the pile material elastic modulus  $E_p$  and its moment of inertia  $I_p$ . By using flexural rigidity, explicit consideration can be made of (i) any pile geometry (e.g., rectangular, circular, hollow, octagonal, etc.); (ii) composite sections such as cast-in-steel-shell concrete piles; and (iii) material nonlinearity such as cracking of concrete in tension or yielding of reinforcing steel. Likewise, the use of  $B$  in Equation (1.5) serves only as a proxy for pile stiffness because it does not contain information about the material modulus. Accordingly, a more desirable dimensionless frequency parameter would be one that contains the pile flexural rigidity directly along with a measure of the soil stiffness. A useful parameter that combines these quantities is [Hetenyi 1946]:

$$\lambda = \sqrt[4]{\frac{k}{4E_p I_p}} \quad (1.6)$$

Hetenyi referred to  $\lambda$  as the “characteristic” term because it appears in the roots of the characteristic equation of the homogeneous form of the governing differential equation for a laterally-loaded pile (presented in §2.1). Hetenyi also noted that since  $\lambda$  has the units [ $\text{length}^{-1}$ ], the quantity  $1/\lambda$  has units of length and hence he dubbed it “characteristic length.” More recent researchers sometimes refer to  $\lambda$  as the “Winkler parameter,” which is not to be confused with the Winkler coefficient  $\delta$  as defined for this study in §2.3.

Randolph [1981] used the term “critical length” (and, interchangeably, “active length”) to refer to the portion of a laterally-loaded pile that effectively resists a lateral load, approximated as:

$$L_a \approx 4 \left( \sqrt[4]{\frac{E_p I_p}{k}} \right) \quad (1.7)$$

For piles that are longer than the active length, further increases in length will not affect the response to lateral loads at the pile head; thus, the piles are classified as “long” or “flexible” in comparison to “short” piles that are shorter than the active length. Close inspection of Equation (1.7) reveals that it is not equal to the inverse of Equation (1.6). The ratio of  $1/\lambda$  to Equation (1.7) is  $4^{-3/4} \approx 0.35$ ; therefore, the definitions of “characteristic” and “critical” length used by Hetenyi and Randolph, respectively, are different. To avoid confusion, “active length” will be used in this text to refer to the portion of the pile that effectively resists the lateral load such as defined by Equation (1.7).

Di Laora and Sanctis [2013], expanding on the work of Rovithis et al. [2009] and recognizing the aforementioned shortcomings of the typical definition of  $a_0^p$  given by Equation (1.5), proposed a revised dimensionless frequency that incorporated the characteristic length directly. Similarly, Anoyatis et al. [2013] proposed the following dimensionless frequency:

$$a_0^p = \frac{\omega}{\lambda V_s} \quad (1.8)$$

where  $\lambda$  is consistent with the definition given by Equation (1.6). This term improves upon the previous form given by Equation (1.5) because it contains (i) the ratio of pile stiffness expressed as flexural rigidity to soil stiffness contained in the  $\lambda$  term, and (ii) the ratio of pile characteristic length ( $1/\lambda$ ) to the wavelength of soil free-field excitation ( $\lambda_{ff} = V_s/\omega$ ). The latter quantity captures a fundamental aspect of the problem at hand, which is that a stiff pile will not conform to the deformed shape of the free field under high-frequency excitation as shown in Figure 1.2. Because the new normalization scheme better captures the underlying physics of the problem, the static results (radiation damping and pile inertia not considered) for a flexible pile ( $L > L_a$ ) with any combination of soil and pile stiffness conveniently collapse into a narrow band as shown in Figure 1.8, which can be represented by a simple best-fit equation. Similarly, transfer functions for free-head pile rotation collapse into a narrow band when the transfer function ordinate is defined as  $H_\theta = \theta_{FIM} / \lambda \cdot u_{FFM}$ , where  $1/\lambda$  is used to normalize the result in lieu of  $B$ . This finding is perhaps the most significant advancement in elastic analytical solutions for pile kinematic SSI in recent years.

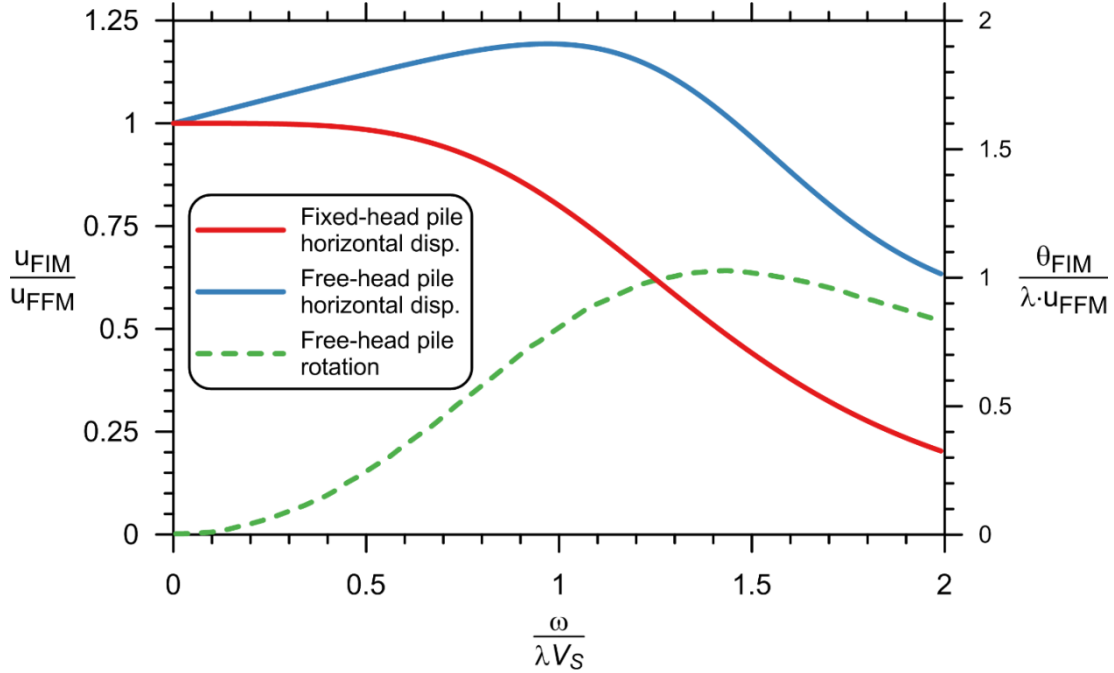


**Figure 1.8** Static kinematic pile–soil interaction transfer functions using improved dimensionless frequency definition from Anoyatis et al. [2013]. Applies for a free-tip pile with  $\lambda L \geq 5$  and homogeneous elastic soil of any stiffness.

The Anoyatis et al. [2013] study considered a uniform, homogeneous viscoelastic soil profile such that the  $\lambda$  and  $V_s$  terms in Equation (1.8) are constant over the length of the pile. To extend these results to more realistic soil profiles in which the soil stiffness varies as a function of depth, Di Laora and Rovithis [2014] proposed a dimensionless frequency with the same form as Equation (1.8) except with  $\lambda$  and  $V_s$  computed as average values over a depth interval equal to the uppermost active pile length. They described increases in soil stiffness versus depth using a generalized power law function such that analytical solutions could still be derived in closed form for the pile kinematic response. This approach provides a convenient framework to account for the fact that the soil profiles considered for this study, and real soil profiles in general, do not have uniform shear-wave velocity or modulus. To compute  $\lambda$  for use in Equation (1.8) for this study, the following will be used:

$$\lambda_{L_a} = \sqrt[4]{\frac{K_{e,L_a}}{4E_p I_p}} \quad (1.9)$$

where  $K_{e,L_a}$  is the average value of  $p$ - $y$  curve initial elastic stiffness ( $K_e$ ) computed over the upper active length of the pile. Likewise,  $V_s$  for use in Equation (1.8) will be computed as the time-averaged shear-wave velocity computed over the upper pile active length,  $V_{s,L_a}$ . From this point forward, any plots or discussion of normalizing by dimensionless frequency use the definition of Equation (1.8) unless noted otherwise.

The pile active length  $L_a$  is usually on the order of  $10B$  to  $15B$  [Randolph 1981; Gazetas and Dobry 1984a], depending on the pile-to-soil stiffness ratio. In general, increasing soil stiffness results in a decreasing  $L_a$  if the pile properties are held constant. While this is a useful first-order

approximation, a more precise value will be computed for this study as the length for which  $\lambda \cdot L = 4$  [Timoshenko 1948; Reese et al. 2006], where  $\lambda$  is computed using the average values [as in Equation (1.9)] over the trial pile length  $L$ . Because the soil properties vary with depth, a simple iterative calculation is required to determine  $L_a$  in this manner.

Because the concept of active length refers specifically to the upper portion of a pile that responds to a lateral load imposed at the pile head, it is not directly applicable to the pile kinematic SSI case in which kinematic demands are imposed over the full length of pile. Nonetheless, the results of this study have shown that the pile–soil interaction near the surface has the greatest influence on the foundation input motion; therefore, considering some portion of the pile length near the surface is a useful descriptor of system response.

### 1.3.4 Limitations of Elastic and Analytical Solutions

The previous studies described above generally considered highly idealized soil–pile domains, such as uniform or simple layered combinations of uniform elastic soil layers, rigid bedrock, rigid and/or infinitely long piles, and simple harmonic excitation in lieu of realistic earthquake ground motions. Linear-elastic solutions are useful for elucidating the driving mechanisms behind complex SSI problems and have some advantages over nonlinear approaches. The primary attraction is that they require low computational effort, and in many cases chart-based or closed-form solutions are available. This makes them amenable to preliminary analysis when full details of a project or soil conditions are not yet known, and the solutions can quickly be updated as more information becomes available. Also, the principle of superposition is exactly valid for use with the substructure method when linear elasticity is used to model all system components, and because the elastic solutions are exact, they should be reproducible for verification. However, to quote the late professor A.S. Vesic [1977], “...analyses of this kind assume that the surrounding soil acts as an elastic-isotropic solid defined by a constant modulus of deformation and a Poisson’s ratio. This assumption represents a serious departure from reality...” Put simply, this is because lateral pile–soil interaction is nonlinear, and real subsurface conditions are inhomogeneous.

Highly idealized assumptions can have unintended and unrealistic consequences on the dynamic behavior of the system. For example:

- Pile radiation damping cannot occur for a pile embedded in an elastic soil layer underlain by rigid bedrock at frequencies below the fundamental frequency of the soil profile (e.g., see Gazetas [1991], Syngros [2004], and Anoyatis et al. [2013]), which is unrealistic for real systems.
- Theoretical transfer functions for fixed-head piles suggest that the pile head motion is always less than the free-field motion for any pile and soil properties and at all frequencies. Not only is this shown to be false when realistic stratigraphy is considered, but it is erroneous in the unsafe direction, potentially resulting in an underestimate of actual demands imposed on the structure.

A primary issue with elastic SSI solutions is that a single value of strain-compatible soil stiffness must be specified to approximate nonlinearity. Simplified methods are available for estimating the average shear modulus reduction induced in the free field by a ground motion of a given amplitude (e.g., Table 2-1 in NIST [2012]). However, no similar method is available for

estimating a reduced modulus to represent pile–soil interaction that considers the non-uniform relative pile–soil displacement occurring over the length of the pile. An accurate equivalent-linear modulus must combine the effects of modulus degradation due to pile–soil interaction and shearing by the ground motion during free-field site response<sup>2</sup>.

Furthermore, even in the simplest case of an approximately uniform soil layer such as stiff over-consolidated clay, because the amount of relative pile–soil displacement will vary over the depth of the layer [e.g., see Figure 1.2(b)], the equivalent-linear soil stiffness needed to accurately capture the response changes with depth. This has been recognized since the early work on pile dynamics began; see Kagawa and Kraft [1980]. Although the stiffness specified in an equivalent-linear analysis could be varied with depth, this further complicates the selection of appropriate equivalent-linear properties and makes most closed-form solutions unsolvable.

Relative to the total number of publications concerning pile dynamics for elastic material properties, the amount of guidance on selection of equivalent-linear properties for actual implementation is comparatively sparse. While back-analyses of single case studies or model studies may be able to determine a single value of reduced modulus that can be used in equivalent-linear analysis to match the desired response, doing so in a generalized manner for forward design cases presents significant challenges and uncertainty.

A shortcoming of continuum solutions, whether solved analytically or numerically, is that the interaction between the pile and soil is often distilled to a simple condition of displacement compatibility (e.g., Tajimi [1969], Novak et al. [1978], and Kaynia and Kausel [1982]). Even if the independent behavior of soil and pile materials could be captured by constitutive models, a pile-soil system cannot be accurately modeled without capturing interaction at the interface. While the assumption of displacement compatibility (i.e., no slip) may be appropriate for relatively small amplitude loading, such as produced by vibrating machinery, design-level earthquakes will induce significant nonlinearity at the pile–soil interface.

While the simplifications adopted for theoretical, elasticity-based solutions may have been state-of-the-art and the “best available” tools for practicing engineers in the decades before modern personal computing power became widely available, this is simply no longer the case. Tools such as dynamic  $p$ - $y$  analysis using nonlinear finite elements that enable significantly more accurate modeling of realistic pile, soil, and ground motion characteristics are now at the disposal of our profession. Nonetheless, use of these tools is beyond the scope of most projects and the expertise of most practitioners. The present work is meant to address these disparities by providing simplified tools that capture realistic complexities of soil and pile dynamics in a more rigorous manner than previous efforts.

### 1.3.5 Experimental Investigations

Experimental studies of pile dynamics are limited relative to the number of computational studies described in the previous section. Of the experiments that have been conducted, most use dynamic loading applied at the pile head to generate inertial SSI as opposed to loading the pile via free-field

---

<sup>2</sup> Stewart et al. [2000] referred to these as “secondary” and “primary” nonlinearities, respectively. These terms could be misleading for pile-soil interaction because the nonlinearity induced by pile-soil interaction can exceed that due to site response for large earthquakes.

excitation. From a practical standpoint, it is much easier to apply load directly to a test structure via actuators or shakers than to load the structure indirectly by loading the adjacent ground. To measure a purely kinematic response, (i) no superstructure mass can be supported by the pile, and (ii) it must be excited by the free field. Hence, experimental results for purely kinematic pile SSI are very limited.

One  $g$  model-scale tests of piles undergoing dynamic loading at the pile head by Gaul [1958], Novak and Grigg [1976], Novak and El Sharnouby [1984], Blaney and O'Neill [1986], Han and Novak [1988], and El-Marsafawi et al. [1992] along with centrifuge tests by Prevost et al. [1981] were useful for validating early analytical procedures. More recent full-scale tests by Vaziri and Han [1992], centrifuge tests by Ashlock and Pak [2009], and model-scale tests by Burr et al. [1997], Tokimatsu et al. [2005], and Manna and Baidya [2010] have been compared favorably to nonlinear analyses. Durante et al. [2015] describe a series of  $1g$  tests that provide an opportunity to validate combined kinematic and inertial analysis techniques.

Only a handful of full-scale dynamic tests have been reported and only for inertia loading. Vaziri and Han [1992] conducted ground-level forced vibration tests on a group of six 7.5-m-long, 0.32-m-diameter drilled shafts connected by a concrete pile cap. McManus and Alabaster [2004] performed cyclic loading on a group of four 5.5-m-long, 0.75-m-diameter piles. Appendix B documents an attempt made as part of this study to measure transfer functions for full-scale piles by exciting the free field and establishes a repeatable method for this type of testing in the future. Apart from this effort, the authors are not aware of any full-scale experiments of purely kinematic SSI for piles. Further experimental testing to validate the results of this study is an important future research need.

A common finding of the experimental tests listed here, especially for the full-scale tests, is that the stiffness and damping of the piles are highly strain-dependent. This makes it difficult to choose a single value of stiffness or damping that is appropriate for design, supporting the notion that nonlinear analyses are superior to analytical or theoretical methods utilizing a single value of equivalent-linear stiffness or damping.

### **1.3.6 Empirical Observations of Kinematic Pile–Soil Interaction**

Due to the same challenges that make experimental measurements of purely kinematic pile–soil interaction difficult—namely, the necessary absence of a superstructure mass atop the pile—empirical observations of pile kinematic SSI during past earthquakes are also limited. A few well-documented cases of pile-supported buildings instrumented with accelerographs at the foundation-level and in the adjacent free field undergoing strong earthquakes are available. However, interpretation of these cases is complicated by the fact that the foundation-level response includes not only the influence of pile kinematic SSI, but also inertial SSI due to the superstructure response. The issue of combined kinematic and inertial SSI effects is examined in more detail in Chapter 5.

#### **1.3.6.1 Empirical Transfer Functions**

Stewart et al. [1999a; 1999b] considered pairs of instrumented structure and adjacent free-field recordings to compare foundation-level and free-field intensity measures from earthquake recordings at 57 building sites in California and Taiwan, including 23 buildings supported on deep

foundations. The intensity measures considered were peak ground acceleration (PGA) and pseudo-spectral acceleration (PSA) at the flexible-base, first-mode building period. The results indicated that kinematic reduction of the foundation-level PGA was appreciable, whereas the reductions of first-mode PSA was relatively modest. However, this study did not present foundation/free-field transfer functions and hence provides limited insight into kinematic interaction effects.

Kim and Stewart [2003] focused specifically on kinematic interaction and considered recordings from 16 of the pile-supported buildings, all of which utilized grade beams or mat slabs to connect the piles. Figure 1.9 shows a comparison from the Kim and Stewart study between the Fan et al. [1991] kinematic pile model and the observed “transmissibility” function at one of the sites. (A transmissibility function represents the same concept as a transfer function, but is computed from ratios of power spectral density functions rather than spectral amplitude; the motivation for this alternative approach is discussed below.) The Fan et al. model generally underpredicts the reduction seen in the observed transfer function, while a base-slab averaging model representing shallow foundation kinematic SSI by Veletsos et al. [1997], using a site-specific value of a parameter controlling ground motion incoherence ( $\kappa_a$ ), provided a closer match. Kim and Stewart concluded that kinematic interaction between the ground and surface foundation elements likely dominated the response of the pile-supported buildings in their study. However, Kim and Stewart noted that the Fan et al. model and other existing kinematic pile models fail to include the effects of ground motion incoherence (spatial variability), thus posing a lingering question as to whether or not consideration of incoherence in a pile kinematic model would provide a closer match to observed behavior.

Mikami et al. [2006; 2008] and Givens et al. [2012] describe recordings from a pile-supported building in Sendai, Japan, during the 2003 Off-Miyagi and 2011 Tohoku earthquakes that show a stronger reduction of foundation-level motion to FFM than the California and Taiwan recordings reported above. Three modeling approaches were applied in an attempt to match the observed transfer function: (i) a shallow foundation base-slab averaging model [Veletsos et al. 1997; Kim and Stewart 2003] similar to that ultimately published in NIST [2012]; (ii) a linear-elastic model including piles in the computer program SASSI [Ostadan 2005] subjected to coherent ground motions; and (iii) a second SASSI model without piles but with incoherent ground motions. The results are shown in Figure 1.10.

The NIST model and SASSI model with coherent ground motions and piles both fail to capture the significant reduction in the observed transfer function between about 2–7 Hz. The SASSI model with incoherent ground motions but no piles comes closer to capturing the reduction but misses the sharp drop-off occurring around 2 Hz. Mikami et al. and Givens et al. speculate that the misfit of these models may be due to inadequate consideration of incoherence in combination with the pile kinematic interaction or failure to capture the end-bearing resistance of the piles. Recent discussion with Professor Atsushi Mikami [*personal communication*, 2015] and a re-examination of this case in Chapter 6 make it clear that the influence of inertial SSI is the dominant factor causing the significant reduction in the observed transfer function.

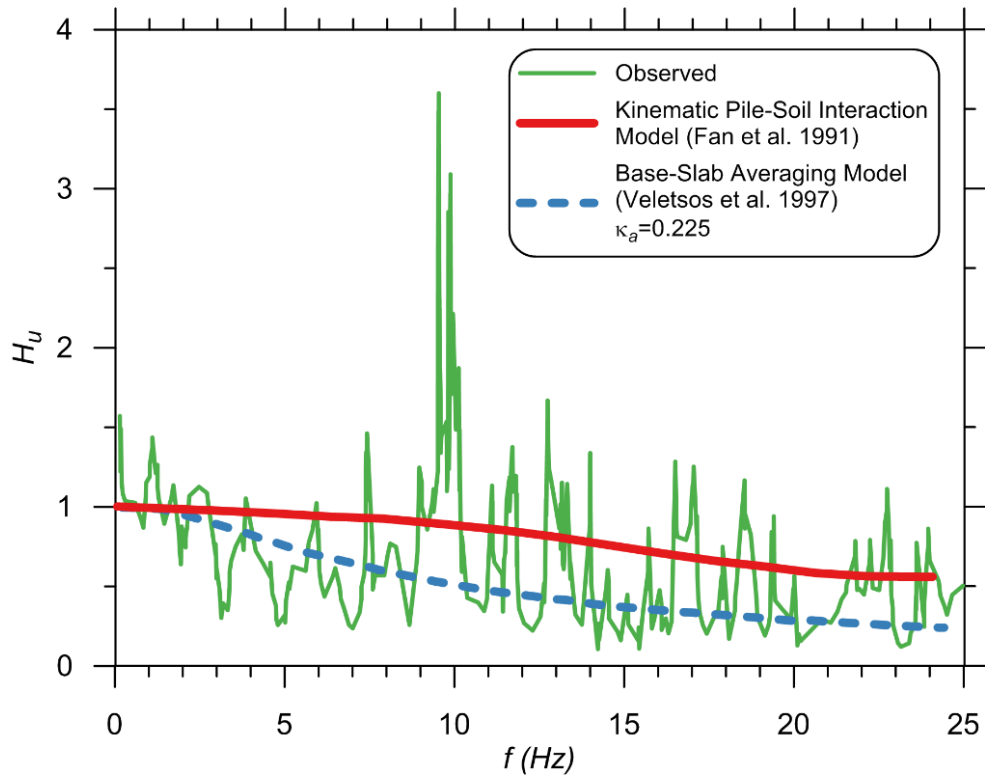


**Figure 1.9** Comparison of observed versus model prediction transfer functions for a 5-story hospital building in Lancaster, California, during the 1994 Northridge, California, earthquake (after Kim and Stewart [2003]).

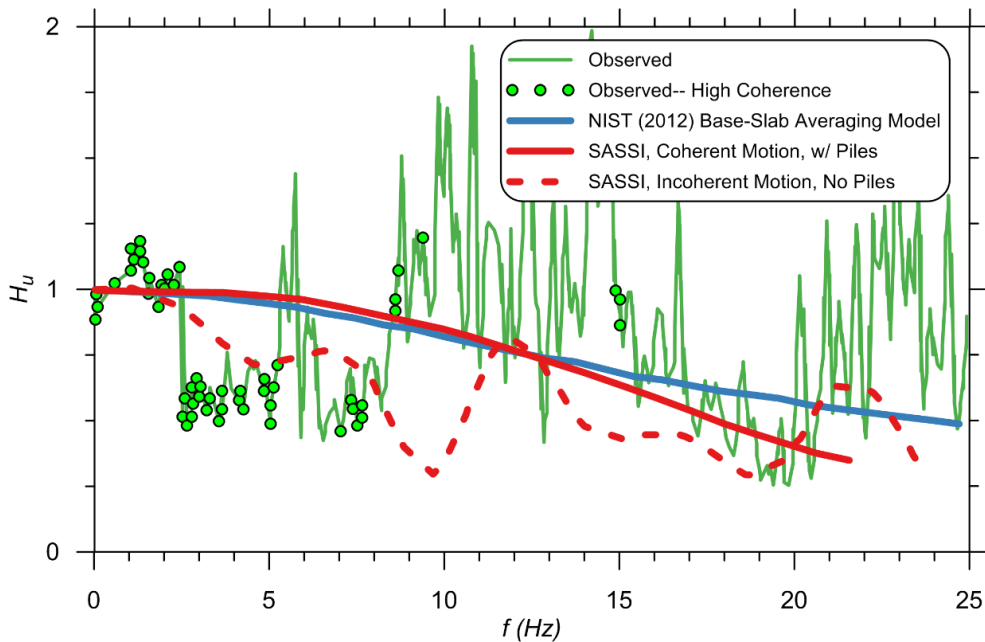


**Figure 1.10** Comparison of observed versus model prediction transfer functions for a 4-story building at Tohoku Institute of Technology in Sendai, Japan, during the 2011 Tohoku, Japan, earthquake (after Givens et al. [2012]).

### 1.3.6.2 Signal Processing Techniques

Empirical transfer functions computed from recorded earthquake motions exhibit sudden changes in amplitude over short frequency ranges as seen in Figure 1.9 and Figure 1.10. Especially at high frequencies where the motion amplitude is typically low, this is due in part to the fact that the ratio of two very small numbers is being computed, such that small oscillations in either the free field or foundation-level motion can result in spurious peaks in the transfer functions. The level of displacement required to produce such a spike may be close to the recording accuracy of the accelerographs and therefore representative of “noise” in the signal rather than a meaningful representation of the system response. Noise could also result from energy sources other than seismic waves that affect either the free field or foundation-level accelerographs, but not both, such as vibrating machinery near one of the recording stations.

Kim and Stewart [2003], and Mikami et al. [2008] describe signal processing techniques to separate the meaningful transfer function ordinates from noise by utilizing an alternative transfer function definition:

$$H_u(\omega) = \sqrt{S_{pp}(\omega) / S_{gg}(\omega)} \quad (1.10)$$

where  $S_{pp}$  and  $S_{gg}$  are the smoothed auto power spectral density functions of the foundation-level and FFM, respectively<sup>3</sup>. Auto ( $S_{pp}$  and  $S_{gg}$ ) and cross ( $S_{gp}$ ) power spectral density functions are defined as:

$$S_{pp}(\omega) = U_{pp}(\omega)U_{pp}^*(\omega) \quad (1.11)$$

$$S_{gg}(\omega) = U_{gg}(\omega)U_{gg}^*(\omega) \quad (1.12)$$

$$S_{gp}(\omega) = U_{gg}(\omega)U_{pp}^*(\omega) \quad (1.13)$$

where  $U^*(\omega)$  is the complex conjugate of  $U(\omega)$ :

$$U^*(\omega) = Re(U(\omega)) - Im(U(\omega)) \cdot i \quad (1.14)$$

and  $i$  is the imaginary number defined by  $i^2 = -1$ . In signal processing terms,  $H_u$  computed using Equation (1.10) is called a transmissibility function, while Equation (1.2) produces a transfer function. The concept is the same—describing the manner in which a system modifies an input signal to produce an output signal—so the term “transfer function” will be used from this point forward.

There are two benefits to using Equation (1.10) rather than defining the transfer function directly as the ratio of the FAS:

- Coherence can be computed, which allows quantitative identification of the transfer function ordinates with the highest signal-to-noise ratio.

---

<sup>3</sup> Kim and Stewart [2003] and Mikami et al. [2006; 2008] use the notation  $x$  and  $y$  to refer to the free-field and foundation-level, respectively;  $p$  and  $g$  will be used here to be consistent with the previous notation and to retain the physical interpretation as the pile and ground-surface motions.

- Smoothing of the power spectral density functions, a necessary step for computing coherence, further reduces the spurious nature of the transfer functions computed from raw signals.

Coherence ( $\gamma^2$ ) between the foundation-level and FFM signals is defined as [Pandit 1991]:

$$\gamma^2 = \frac{|S_{gp}(\omega)|^2}{S_{gg}(\omega)S_{pp}(\omega)} \quad (1.15)$$

Coherence indicates the strength of the relationship between an input and output signal; values near 1.0 indicate a strong dependence of the output on the input, while smaller values indicate a weak relationship. Hence, coherence can be used as a quantitative measure of whether certain frequency components of the foundation-level motion are likely a result of the system responding to excitation by the FFM or represent noise. By using a threshold value of coherence below which data are discarded, empirical transfer functions can effectively be filtered to discern the most meaningful data points. Points with coherence greater than 0.8 are shown in Figure 1.10, which is the cutoff used by Mikami et al. and Givens et al.

Prior to computing coherence with Equation (1.15), the power spectral density functions must be smoothed. Coherence computed between unsmoothed input and output signals over the full frequency bandwidth of the signals will be unity at every frequency and thus is not a useful metric. The smoothing operation is accomplished by replacing each ordinate of the unsmoothed power spectrum with a weighted average value of the unsmoothed ordinates over a frequency band (i.e., window) centered on the point of interest. Mikami et al. [2008] examined the influence of the parameters used to define the smoothing window, which ultimately affect the computed value of coherence, and found that an 11-point Hamming window provided qualitatively good results. Mikami et al. also recommended not only emphasizing empirical transfer function points with high coherence, but bandwidths that have high coherence at multiple successive frequencies. This is an important secondary criterion, because even pairs of white noise signals will occasionally have coherence greater than 0.8 despite having a mean value of approximately 0.15 to 0.25 (the exact value depends on the shape and bandwidth of the windowing function used for smoothing).

As the terminology implies, *incoherent* or spatially-variable ground motions resulting from stochastic effects such as wave scattering and subsurface variability will result in differences in the foundation-level and FFM that are not due to foundation kinematic interaction; this ground motion incoherence will manifest as low coherence in the computed empirical transfer function. Since the incoherence of real ground motions tends to increase with increasing frequency, this mechanism is especially significant at higher frequencies. Mikami et al. [2008] concluded that empirical transfer function ordinates at high frequencies are usually dominated by incoherence, and thus should be deemphasized relative to low-frequency ordinates when quantifying kinematic SSI. For the examples described in their paper, the usable frequency range is typically below about 10 Hz.

Although interpretation of empirical transfer functions is not the main focus of this study, the signal processing techniques described above turn out to be very useful, if not necessary, for interpreting the results of the numerical simulations. Ground motions used as input to the pile–soil interaction analyses are sourced from earthquake recordings at a single location, and the foundation is modeled as occupying the same physical location. Therefore, the incoherence of real

ground motions between the physical locations of the free field and foundation-level recording stations that can cause low coherence for high-frequency empirical transfer function ordinates does not apply, at least for single pile models. Nonetheless, variability between the computed FIM and FFM when represented in the frequency domain can mimic the variability between empirical foundation-level and FFM signals because:

- Numerical oscillations in the finite-element solution on the order of the tolerance that satisfies the convergence criterion are significant relative to the Fourier amplitude of the computed FIM, particularly at higher frequencies, and
- Transfer functions are an imperfect representation of seismic response due to the finite-duration and non-stationary nature of the signals used to compute them (discussed further below).

As a result, transfer functions computed from the numerical simulations look similar to the empirical transfer functions described above, in particular exhibiting large variability at higher frequencies. This is true even when the numerical solution approach is used to compute transfer functions for elastic pile and soil conditions subjected to harmonic free-field ground motions, and thus is not solely an artifact of nonlinearity in the system response. To facilitate extraction of meaningful trends from the simulations performed in this study, the same signal processing techniques described by Mikami et al. [2008] are applied, specifically:

- Transfer functions are computed using Equation (1.10),
- Power spectral density functions are smoothed with an 11-point Hamming window,
- A minimum coherence threshold of 0.8 is applied to the computed transfer functions, while in some instances a more stringent value of 0.9 is used to clarify the trend exhibited by the results, particularly for stiffer soil sites for which the transfer function corner frequency is relatively high, and
- Transfer functions are only defined up to the frequency at which a smoothed version of the coherence-versus-frequency curve is above the minimum threshold (0.8 or 0.9).

Although other approaches could be taken for smoothing the results, for example simply smoothing the computed transfer functions directly, the approach used for interpretation of empirical data is adopted here because of its demonstrated applicability to the mechanisms governing kinematic SSI.

The last criterion in the above list is intended to satisfy the recommendation by Mikami et al. [2008] that not only should high coherence points be emphasized, but a further restriction should be implemented of focusing on bandwidths over which high coherence occurs for a series of successive frequencies. The coherence versus frequency curve is smoothed using a 25-point median smoothing window, which replaces each value with the median of the 25 points centered on that frequency. This allows automated processing of the thousands of results from the parametric study.

In addition to the insights provided in the context of interpreting empirical transfer function data, the concept of using transfer functions as a means of quantifying SSI has additional limitations, and some discussion is warranted here.

Strictly speaking, the concept of a transfer function applies only to an infinitely-repeating stationary process, which is defined as an entirely stochastic (random) process that displays no trends in mean or variance with time. While certain aspects of SSI are approximately stochastic, time signals of earthquake ground motions and the response of structures to these ground motions exhibit strong trends with time, and are of a finite duration. While advanced signal processing techniques are available to transform the time response of some physical systems from non-stationary to approximately stationary (e.g., White and Boahash [1990]), they are generally not applicable to ground motions.

In particular, the ordinates of FAS can be unintentionally altered by the non-repeating nature of ground motions, and by the simple fact that the Fast-Fourier transform (FFT) algorithm used to perform the Fourier transform generates very small numbers at frequencies away from the predominant energy of the signal. Consider the following simple examples to illustrate these points.

A signal defined as a sine wave with amplitude of unity and frequency 1 Hz is passed through a system that has the ability to modify the input signal and produce an output signal. Since the FFT algorithm applied to a discrete time signal requires that the signal have  $2^n$  points, where  $n$  is an integer, the input signal for this example is chosen to have  $2^{11} = 2,048$  points. The time step  $\Delta t$  is taken as four times the inverse of  $n$  ( $4/2,048$  sec) so that the vector of frequencies at which the FFT is defined includes  $f = 1$  Hz without the need for interpolation. The amplitude is zero at time  $t = 0$ , and the amplitude of the 2,048<sup>th</sup> point is  $\sin[2\pi f \Delta t (n-1)] \approx -0.012$  such that the 2049<sup>th</sup> point would have an amplitude of zero and the signal could repeat indefinitely.

The time- and frequency-domain representations of the input and output signals are presented in Figure 1.11, along with the transfer functions computed between them using Equation (1.2). First consider that the system makes no modification to the input signal, such that the input and output are identical [Figure 1.11(a)]. The FFT captures the amplitude of the signal at 1 Hz exactly. Theoretically, the amplitude at all other frequencies is zero since the signals are perfect 1 Hz sine waves, but the FFT returns a non-zero, albeit very small, amplitude ranging between  $1.0\text{E-}13$  and  $1.0\text{E-}15$ . Nonetheless, the values are exactly the same for the input and output, thus the transfer function ordinate is exactly unity at all frequencies. Figure 1.11(b) shows the results when the output signal is perfectly out of phase by  $\pm\pi$  radians. Even though the transfer function amplitude is defined only as the ratio of Fourier amplitude spectra and should not be affected by phase, the small, yet non-zero oscillations in computed Fourier amplitude now vary between the input and output signals, such that the transfer function is erratic away from  $f = 1$  Hz. This highlights an important point—the transfer function amplitude does not reflect the amplitude of the input and output signals over different frequencies, only the ratio of their amplitudes. Hence by simply examining a transfer function without viewing the corresponding FAS, it cannot be known which transfer function ordinates correspond to the predominant energy in the system and are therefore most meaningful.

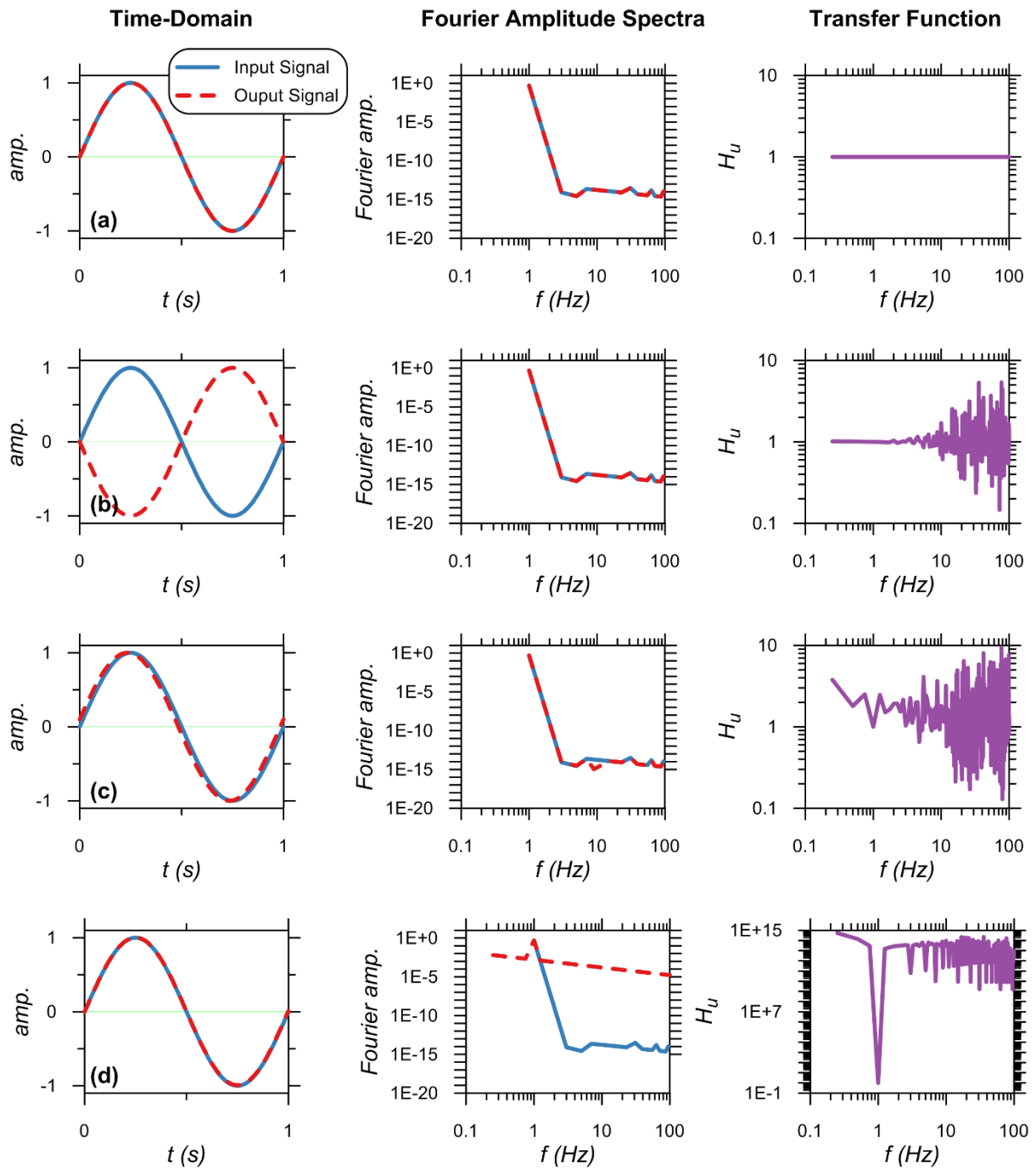


**Figure 1.11** Influence of small changes between input and output signals on system transfer functions. Relative to input signal, the output signal (a) is identical, (b) is perfectly out-of-phase, (c) is out of phase by 0.1, and (d) exhibits slight baseline drift.

Figure 1.11(c) shows the effect of a small phase offset, which produces similar high-frequency noise in the transfer function. Again, the amplitude of the output signal is identical to the input signal for (b) and (c). Figure 1.11(d) shows the effect of a small baseline drift in the output signal (linear change of 0.01 over 1 sec), which also has a drastic effect on the transfer function away from  $f = 1$  Hz.

These example of changes between input and output signals were chosen because, to some extent, they all appear in signals representing the free field and a structure during seismic excitation. The intent in pointing out their influence on the computed transfer functions is not to suggest that the transfer function approach should not be used; on the contrary, it is an excellent tool for earthquake engineering. These issues simply need to be kept in mind when trying to discern the meaningful trends from noise.

### **1.3.6.3 Pile Damage due to Kinematic Demands**

Many of the same earthquakes that inspired the seminal work in geotechnical earthquake engineering on topics such as soil liquefaction and ground-motion estimation also provided evidence that kinematic demands caused damage to pile foundations. The documented cases include damage to concrete piles supporting bridges during the 1964 Alaska Earthquake [Kachadoorian 1968] and a building during the 1964 Niigata Earthquake [Nishizawa et al. 1984]. Mizuno [1987] documented pile performance during several Japanese earthquakes that occurred between 1923 and 1983, including several cases of piles damaged by kinematic demands, although most appear to be cases with large permanent ground displacement. Tazoh et al. [1987] instrumented the Ohba-Ohashi Bridge in Japan and recorded the structural response during several earthquakes, including a **M** 6.0. They found that the peak strains recorded by longitudinal strain gauges in the piles supporting one of the main piers occurred deep in the soil profile at the interface between the bearing stratum and softer overlying soil.

Studies by Nikolaou et al. [2001] and others cite this evidence as motivation for considering kinematic demands in design, which eventually became a building code requirement as discussed in the following section. It is worth noting that the number of documented cases in which ground failure (e.g., liquefaction), permanent ground displacement, and inertial loads could be ruled out as the cause of damage is relatively low. This does not necessarily imply that this damage mechanism is not common; but it is likely more attributable to the difficulty and cost associated with post-earthquake inspections of piles at significant depths.

## **1.4 KINEMATIC SSI IN BUILDING CODES**

The influence of kinematic pile–soil interaction on FIM receives little or no attention in U.S. building codes. On the other hand, demands resulting from pile–soil interaction must be considered according to most building codes. For example, ASCE 7-10 (ASCE 2013) §12.13.6.7 “Pile Soil Interaction” requires that piles be designed for the moment, shear, and deflections “considering the interaction of the shaft and soil.” Unlike the specifications in Chapter 19 of ASCE 7-10 “Soil-Structure Interaction for Seismic Design,” which are optional and can be ignored at the designer’s discretion, the requirement that piles be designed to resist kinematic demands in addition to

superstructure demands is required in all cases. Nonetheless, in the authors' experience it is often neglected in practice.

## 1.5 NOTES ON TERMINOLOGY AND NOTATION

Because the terms used to describe various types of deep foundations tend to evolve over time, a few clarifications are noteworthy in the context of this study.

During the timeframe of the early work on this subject (1960s-1980s), the term “pile” was most commonly used to refer specifically to driven piles. Drilled shafts were often referred to as “caissons” or “piers.” This distinction is important, because driven piles were categorically assumed to be more flexible than their drilled counterparts. Early work on this subject often applied specifically to relatively flexible driven piles for which kinematic SSI effects are less significant in comparison to larger-diameter, stiffer drilled shafts. For example, in the seminal 1982 paper by Flores-Berrones and Whitman, “Seismic Response of End-Bearing Piles,” the authors conclude that:

*... Piles located in seismic zones are subjected to two very important effects; one is the action of the soil along the pile length [kinematic SSI] and the other one is related to the supported mass at the pile's head [inertial SSI]. Regarding the first of these effects, very often neglected in dynamic analysis for piles subjected to seismic forces, there are two extremes... (1) Piles behave as flexible elements and follow the ground displacements; and (2) piles behave as rigid elements, and their tendency is to remain still while the soil moves around them... Most “piles” fall into the first of these categories while piers and caissons might fall in the second one... Generally speaking, piles do not reduce significantly the horizontal movements of a structure...*

Consistent with this conclusion, much of the work on the topic of kinematic pile–soil interaction has focused on the shear and moment demands imposed on relatively flexible piles, while less attention has been paid to the beneficial reduction in FIM that large, stiff piles can provide. Because large-diameter piles in soft-soil conditions are now commonplace, especially for the support of bridges, this topic is worth revisiting.

For simplicity, the term “pile” foundation will be used herein to refer to both driven piles and drilled, cast-in-place deep foundations, also known as drilled shafts or piers, bored piles (the predominant term outside the U.S.), cast-in-drilled-hole piles (Caltrans), etc. The distinction between driven and drilled shaft-type piles will be noted when relevant; otherwise the content of this study is intended to apply to both.

Early work (1960s–1990s) on pile KSSI and much of the contemporary work using analytical solutions use the term  $I_u$ , short for interaction factor, to represent the transfer function ordinate. This study adopts the term  $H_u$  based on the work of Kim and Stewart [2003], who applied signal processing techniques borrowed from the field of electrical engineering where  $H$  is typically used to represent the transfer function between input and output signals.

## 2 Elastic Analytical and Numerical Solutions

Elastic solutions for kinematic pile–soil interaction are useful for elucidating the fundamental mechanisms that control the physics of the problem and for formulating the bounds of the nonlinear numerical analyses performed subsequently. In this chapter, a closed-form elastic analytical solution is derived, compared to previous solutions by other researchers, and then used to validate the proposed numerical modeling approach.

In addition, for the nonlinear numerical analyses that follow, pile–soil interaction is characterized by elastic behavior at very small strains. Hence, issues related to the small-strain elastic behavior of the nonlinear system are explored in the second half of this chapter.

### 2.1 ELASTIC ANALYTICAL SOLUTION

Derivation of the closed-form static solution for a vertical elastic pile in elastic soil begins with the following fourth-order differential equation for a laterally-loaded pile (after Hetenyi [1946]):

$$\frac{d^4 u_p}{dz^4} E_p I_p + \frac{d^2 u_p}{dz^2} P - k \cdot u_p = 0 \quad (2.1)$$

in which  $u_p$  is the horizontal pile displacement,  $z$  is the depth measured downwards from the pile head,  $E_p I_p$  is the pile flexural rigidity,  $P$  is axial load, and  $k$  is the soil–pile interaction stiffness intensity, all defined in a consistent set of units. Equation (2.1) states that the force applied externally by the soil reaction ( $k \cdot u_p$  term) is in equilibrium with the internal forces in the pile described by the 4<sup>th</sup> derivative of the transverse displacement multiplied by the pile flexural rigidity, plus second-order (“ $P$ - $\mathcal{L}$ ”) effects. The pile is treated as an Euler-Bernoulli beam in this formulation. For the purpose of this derivation going forward, axial load is taken as zero such that second-order effects are dropped<sup>4</sup>.

For a kinematic pile–soil interaction dynamic solution, the pile–soil interaction modulus  $k$  is replaced with the complex-valued  $k^* = k + i\omega c$ , where  $c$  is the dashpot coefficient for equivalent viscous damping, the displacement term is replaced with the relative displacement between the pile and free-field soil, and an additional term is added to capture the inertial force generated by acceleration of the pile mass per unit length  $\tilde{m}_p$ :

---

<sup>4</sup> Second-order moments are included in the nonlinear numerical analyses performed for this study.

$$\frac{d^4 u_p}{dz^4} E_p I_p + k^* [u_p - u_{g0}] + \tilde{m}_p \frac{d^2 u_p}{dt^2} = 0 \quad (2.2)$$

If the free-field ground motion is represented as harmonic excitation by vertically propagating shear waves (after Kramer [1996]):

$$u_g(z) = u_{g0} \cdot \cos(\kappa \cdot z) \quad (2.3)$$

where  $u_{g0}$  is the ground displacement at the surface due to the harmonic seismic excitation, and  $\kappa^*$  is the complex-valued wave number defined as the ratio of excitation angular frequency ( $\omega$ ) to soil complex-valued shear-wave velocity ( $V_s^* = V_s \sqrt{1 + 2i\beta_s}$ , where  $\beta_s$  is the soil hysteretic damping ratio), then Equation (2.3) can be substituted into (2.2) to give:

$$\frac{d^4 u_p}{dz^4} E_p I_p + k^* [u_p - u_{g0} \cos(\kappa z)] + \tilde{m}_p \frac{d^2 u_p}{dt^2} = 0 \quad (2.4)$$

Although a solution is available to the dynamic Equation (2.4) (e.g., Anoyatis et al. [2013]), the static solution without consideration of damping or pile inertia is still a reasonable means of investigating the controlling mechanisms of kinematic pile–soil interaction. The static version of Equation (2.4) is:

$$\frac{d^4 u_p}{dz^4} E_p I_p + k [u_p - u_{g0} \cos(\kappa z)] = 0 \quad (2.5)$$

The solution to Equation (2.5) is the sum of complementary and particular solutions. Finding the complementary solution begins by solving the homogeneous form of Equation (2.5), which does not include the ground displacement term since it is not a function of pile displacement  $u_p$ :

$$\frac{d^4 u_p}{dz^4} E_p I_p + k (u_p) = 0 \quad (2.6)$$

The characteristic equation for the homogeneous form is:

$$r^4 + \frac{k}{E_p I_p} = 0 \quad (2.7)$$

The roots of Equation (2.7) are equal to the 4<sup>th</sup> roots of the  $k/E_p I_p$  term:

$$r = \sqrt[4]{\frac{-k}{E_p I_p}} = \sqrt[4]{\frac{k}{E_p I_p}} \exp \left[ \left( \frac{\pi}{4} + \frac{\pi \cdot j}{2} \right) i \right]_{j=1,2,3,4} = \sqrt[4]{\frac{k}{4E_p I_p}} \pm i \left( \sqrt[4]{\frac{k}{4E_p I_p}} \right) \quad (2.8)$$

Recalling that a complex root of the characteristic equation results in two terms in the complementary solution, the complementary solution to Equation (2.4) can be written as:

$$u = e^{\beta z} \cos(\beta z) \chi_1 + e^{\beta z} \sin(\beta z) \chi_2 + e^{-\beta z} \cos(-\beta z) \chi_3 + e^{-\beta z} \sin(-\beta z) \chi_4 \quad (2.9)$$

where  $\chi_1$  through  $\chi_4$  are constants and the characteristic term  $\beta$  is a substitution variable defined as:

$$\beta = \sqrt[4]{\frac{k}{4E_p I_p}} \quad (2.10)$$

This is the origin of the familiar ‘‘Winkler’s parameter’’, and the inverse of Equation (2.10) is often called the characteristic length.

The particular solution is found using the method of undetermined coefficients as:

$$u = \frac{k \cdot u_{g0}}{E_p I_p \cdot \kappa^4 + k} \cos(\kappa \cdot z) \quad (2.11)$$

and the sum of Equations (2.9) and (2.11) is the complete solution to Equation (2.4) for the pile horizontal displacement at any depth  $z$ :

$$u_p(z) = e^{\beta z} \cos(\beta z) \chi_1 + e^{\beta z} \sin(\beta z) \chi_2 + e^{-\beta z} \cos(-\beta z) \chi_3 + e^{-\beta z} \sin(-\beta z) \chi_4 + \frac{k \cdot u_{g0}}{EI \cdot \kappa^4 + k} \cos(\kappa \cdot z) \quad (2.12)$$

A similar derivation can be found in Flores-Berrones and Whitman [1981] for pile–soil kinematic interaction, and in Hetenyi [1946] for conventional lateral loading at the pile head in the absence of free-field excitation.

Successive derivatives of Equation (2.12) provide expressions for slope ( $S$ ), curvature ( $\phi$ ), moment ( $M$ ), shear ( $V$ ), and soil reaction ( $p$ ):

$$S(z) = \frac{du_p}{dz} = \beta \left[ e^{\beta z} (A\chi_1 + B\chi_2) - e^{-\beta z} (B\chi_3 + A\chi_4) \right] - \kappa \cdot C \sin(\kappa z) \quad (2.13)$$

$$\begin{aligned} M(z) &= \frac{d^2 u_p}{dz^2} E_p I_p \\ &= E_p I_p \left( 2\beta^2 \left\{ e^{\beta z} [-\sin(\beta z) \chi_1 + \cos(\beta z) \chi_2] \right. \right. \\ &\quad \left. \left. + e^{-\beta z} [\sin(\beta z) \chi_3 + \cos(\beta z) \chi_4] \right\} - \kappa^2 C \cos(\kappa z) \right) \end{aligned} \quad (2.14)$$

$$\begin{aligned} V(z) &= \frac{d^3 u_p}{dz^3} E_p I_p \\ &= E_p I_p \left( 2\beta^3 \left[ e^{\beta z} (-B\chi_1 + A\chi_2) + e^{-\beta z} (A\chi_3 - B\chi_4) \right] + \kappa^3 C \sin(\kappa z) \right) \end{aligned} \quad (2.15)$$

$$\begin{aligned} p(z) &= \frac{d^4 u_p}{dz^4} E_p I_p \\ &= E_p I_p \left( 4\beta^4 \left\{ e^{\beta z} [-\cos(\beta z) \chi_1 - \sin(\beta z) \chi_2] \right. \right. \\ &\quad \left. \left. + e^{-\beta z} [-\cos(\beta z) \chi_3 + \sin(\beta z) \chi_4] \right\} - \kappa^4 C \cos(\kappa z) \right) \end{aligned} \quad (2.16)$$

The following substitutions were used to abbreviate Equations (2.13) through (2.16):

$$A = \cos(\beta z) - \sin(\beta z) ; \quad B = \cos(\beta z) + \sin(\beta z) ; \quad C = \frac{k \cdot u_{g0}}{E_p I_p \cdot \kappa^4 + k} \quad (2.17)$$

To solve for the constants  $\chi_1$  through  $\chi_4$ , a set of four permissible boundary conditions must be imposed. Typically the boundary conditions are prescribed at the pile head and tip since these can be determined on the basis of details such as embedment into a pile cap or a stiff bearing stratum. For example, in the absence of superstructure force or moment demands (required for a kinematic pile–soil interaction analysis) the boundary conditions for a fixed-head, free-tip pile of length  $L$  are:

$$V_{z=0} = 0 ; \quad S_{z=0} = 0 ; \quad V_{z=L} = 0 ; \quad M_{z=L} = 0 \quad (2.18)$$

An example of the solution in terms of pile-versus-soil displacement, moment, and shear is shown in Figure 2.1 for the following input parameters:

- $E = 27 \text{ GPa}$ ,  $I = 0.0031 \text{ m}^4$  (corresponding to a 0.5-m-diameter RC pile), length ( $L$ ) = 10 m
- $V_s = 100 \text{ m/sec}$  (soft soil),  $k = 47 \text{ MPa}$
- $u_{g0} = 0.1 \text{ m}$ ,  $f = 10 \text{ Hz}$
- Boundary condition at pile head = zero slope and zero shear; i.e., a fixed-head pile with no superstructure demands so that the kinematic pile–soil interaction can be evaluated independently
- Boundary condition at pile tip = zero shear and zero moment; i.e., the pile tip is unrestrained

To produce an analytical transfer function, the pile head displacement determined from Equation (2.12) at depth  $z = 0$  is normalized by the amplitude of the harmonic ground motion,  $u_{g0}$ , and computed over the frequency range of interest (recall that the solution is frequency-dependent even for the simplified static version because it contains the wavenumber term  $\kappa$ ). Parametric studies using elastic solutions can provide valuable insight into the range of pile and soil stiffness for which kinematic pile–soil interaction is significant over the frequency range of engineering interest. Figure 2.2 shows kinematic pile–soil interaction transfer functions computed using the elastic analytical solution for three diameters of a 25-m-long pile in two homogeneous soil profiles representative of relatively soft and relatively stiff soil. The boundary conditions for the pile are the same as shown in Figure 2.1—the pile tip is free (zero shear, zero moment), and the pile head is restrained against rotation to model a fixed-head condition with zero applied shear. The ranges of pile and soil properties considered are as follows:

- Pile flexural rigidity ( $E_p I_p$ ) between  $82 \text{ MN}\cdot\text{m}^2$  and  $21,200 \text{ MN}\cdot\text{m}^2$ . These values approximately correspond to a 50-cm-diameter RC pile, such as might be used in a pile group, and a 2.0-m-diameter pile that would likely be used as a mono-shaft to support a single column or in a pile group for a very large suspension or cable-stayed bridge.
- Pile–soil interaction stiffness  $k$  of 60 MPa, corresponding to the initial elastic stiffness for a  $V_s = 100 \text{ m/sec}$  soft-soil site, and 1050 MPa, corresponding to a  $V_s = 400 \text{ m/sec}$  stiff-soil site.

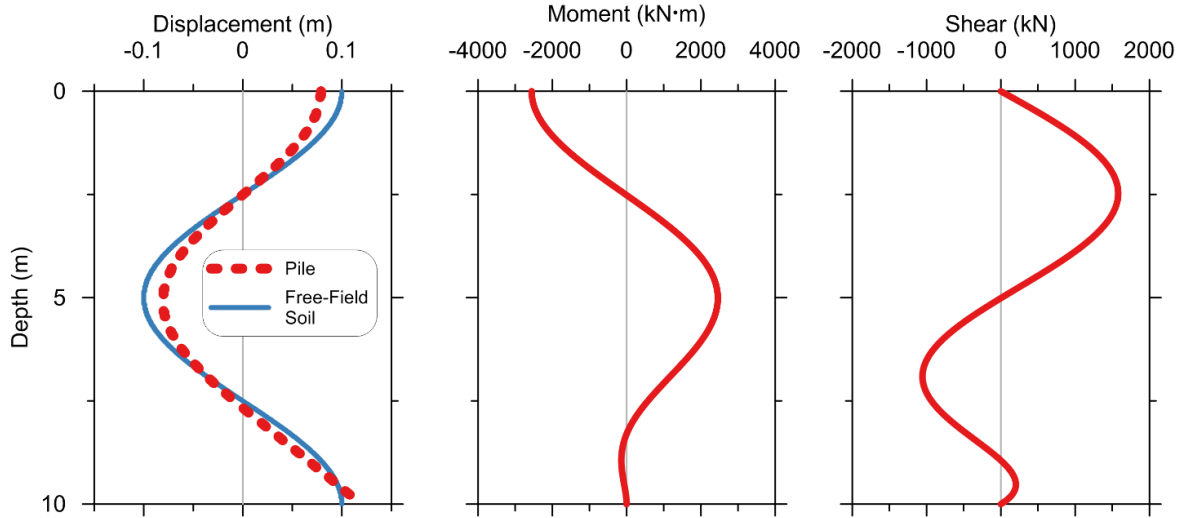
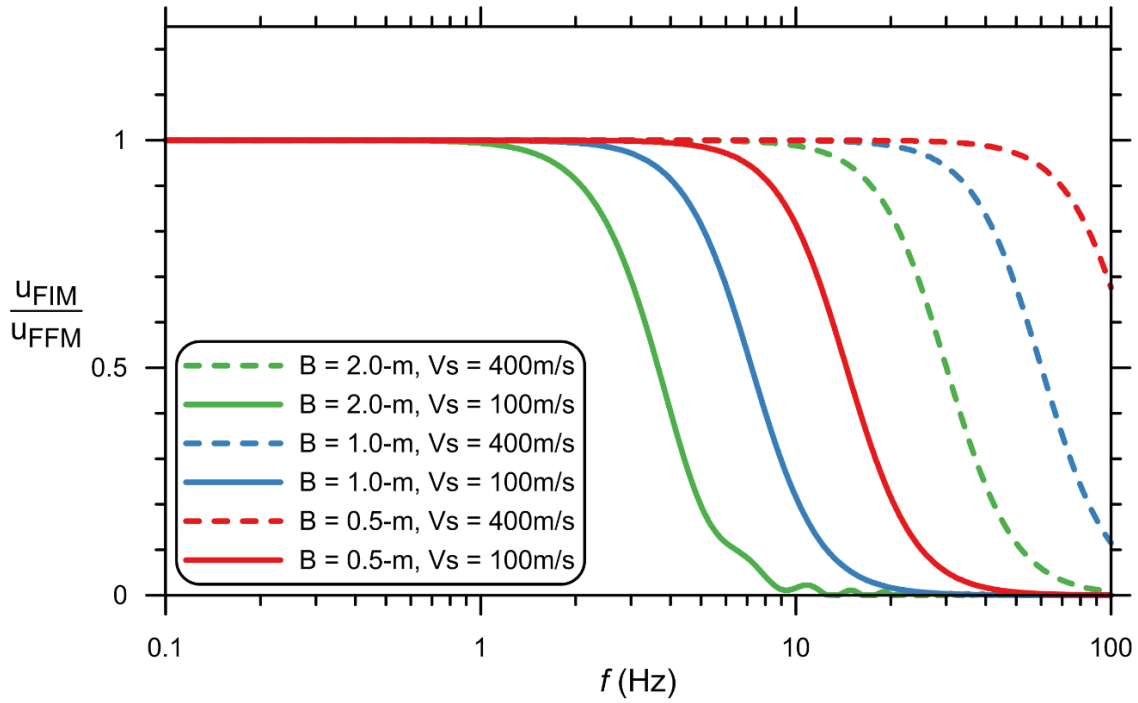


**Figure 2.1 Soil and pile response under imposed 10 Hz harmonic ground motion using elastic analytical solutions.**

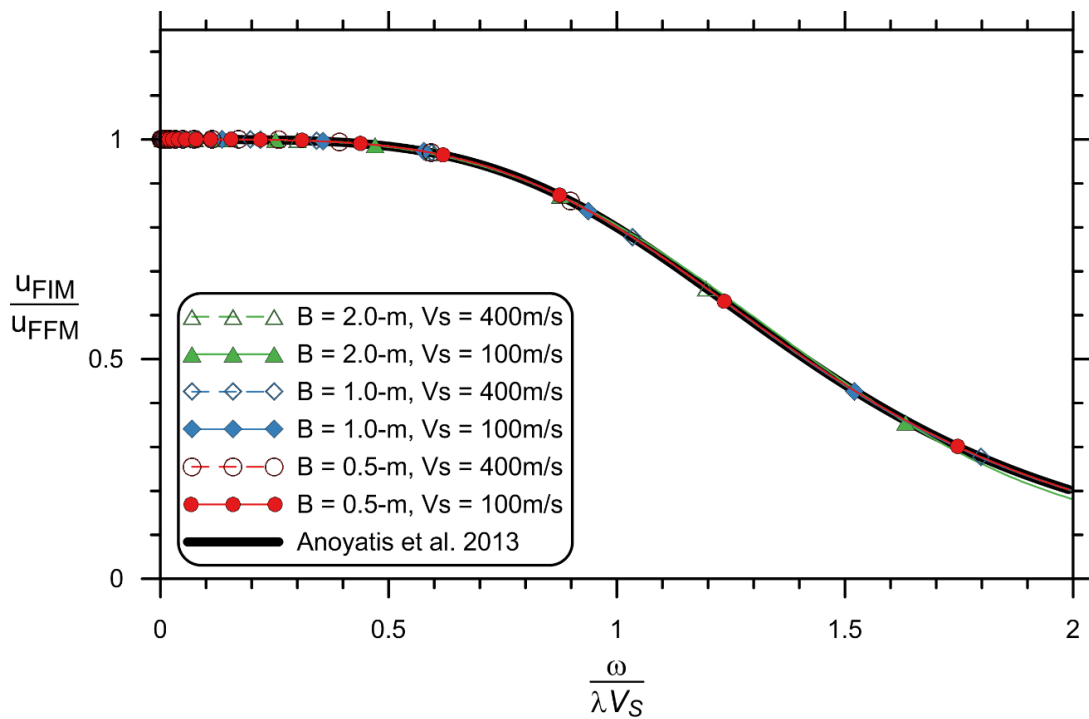
The transfer functions shown in Figure 2.2 represent the bounds of these ranges of soil and pile properties over a frequency range of 0.1 to 100 Hz. The first-mode period for most bridges and building structures typically falls in the range of about 0.1 to 2 sec, so the value of the transfer function ordinate  $H_u$  over this range is of most significance. This corresponds to a frequency range of 0.5 to 10 Hz.

Figure 2.2 shows that the pile/soil combination with the greatest reduction in  $H_u$  within the frequency range of interest is the larger diameter 1.0-m and 2.0-m piles embedded in the soft-soil profile. In contrast to the stiff-pile/soft-soil cases, there is little reduction in  $H_u$  for the piles embedded in the stiff soil profile over the frequency range of interest, even for the 2.0-m-diameter shaft. Significant reduction is predicted only for frequencies greater than about 20 Hz (corresponding to a period less than 0.05 sec). Such high-frequency energy usually does not have a large influence on the behavior of a structure relative to the energy content at the structure fundamental frequency. Structures supported on stiff soil with significant participation from higher modes may still be affected in some cases. These findings are consistent with the previous elastic studies by Flores-Berrones and Whitman [1982] and Fan et al. [1991].

As discussed in the previous chapter, transfer functions are usually presented in a normalized manner by plotting versus dimensionless frequency. The version of dimensionless frequency given in Equation (1.8), proposed by Di Laora and Sanctis [2013] and Anoyatis et al. [2013], is demonstrated in Figure 2.3 to provide “perfect normalization” (i.e., the results all collapse onto a single line) for the parametric bounds considered here.



**Figure 2.2** Transfer function for kinematic soil–structure interaction effects for three diameters of 25-m long, fixed-head reinforced concrete piles in soft- and stiff-soil profiles.



**Figure 2.3** Transfer functions from Figure 2.2 plotted versus dimensionless frequency and compared to Anoyatis et al. [2013]. All solutions lie within the same narrow band.

## 2.2 ELASTIC NUMERICAL SOLUTION

The numerical modeling approach used for this study consists of discretized pile segments attached to soil springs at each node as depicted in Figure 1.1(b). The elastic analytical solution from the preceding section provides an opportunity to verify that the proposed numerical modeling approach provides an accurate solution, since the elastic analytical solution is explicit and the numerical solution should converge to a high degree of accuracy for elastic conditions. While each component of the numerical modeling approach is discussed in detail in Chapter 3, this section will focus only on the results of elastic simulations. The pile and soil are modeled using elastic beam–column and elastic zero-length uniaxial materials, respectively, in *OpenSees*.

Two categories of input excitation are considered, sine-sweep motions consisting of uniform-displacement amplitude broadband frequency content from 0.1 to 50 Hz, and recorded ground motions with variable bandwidth. The free-field input motions were specified at the ground surface and motions at the depth of each soil spring were computed using Equation (2.3). By specifying the input motion at the ground surface rather than the base of the soil profile, the problem of infinite amplification at resonant site frequencies is avoided. The amplitude of the input excitation does not affect the computed transfer functions since the model is linear-elastic.

Soil and pile properties for the numerical analyses match the properties used in the analytical solution so that a direct comparison of the computed transfer functions can be made. The soil–pile interaction stiffness ( $k$ ) at depth  $z$  is defined as [Gazetas and Dobry 1984]:

$$k = 1.69 E_s \left( \frac{E_p}{E_s(z)} \right)^{-0.137} ; \quad E_s(z) = 2\rho V_s^2 (1 + \nu) \quad (2.19)$$

where  $E_p$  is the pile elastic modulus, taken as 2.7E7 kPa for RC, and  $E_s$  is depth-dependent elastic soil modulus computed from  $V_s$  based on classical elasticity theory with assumed soil density  $\rho = 1.6 \text{ Mg/m}^3$  and Poisson's ratio  $\nu = 0.3$ . The uniaxial spring stiffness is defined as  $k$  divided by the tributary length of the pile element to which it is attached. The soil springs connected to the pile head and tip are assigned a tributary length equal to half of the pile segment discretization length.

Transfer functions for the analytical solution are compared to the numerical solution results for a sine-sweep input motion in Figure 2.4 and for recorded earthquake ground motions in Figure 2.5. Two sizes of circular concrete piles were considered, 0.5-m and 2.0-m diameter, for a site with  $V_s=150\text{m/sec}$ . Both fixed-head and free-head restraint conditions were considered. The sine-sweep input motion transfer functions showed near-perfect agreement with the analytical solution for both pile sizes over the entire frequency range considered.

For the nonlinear parametric study described in the following chapter, ground motions were sourced from a set of 40 records with broad frequency content and statistical variability compiled by Baker et al. [2011]. These motions and their characteristics are described in detail in §3.7.1. For the current comparison, three of the 40 the motions were selected that have variable frequency content as seen in the Fourier amplitude spectra (FAS) in Figure 2.5. The three motions are described in Table 2.1.

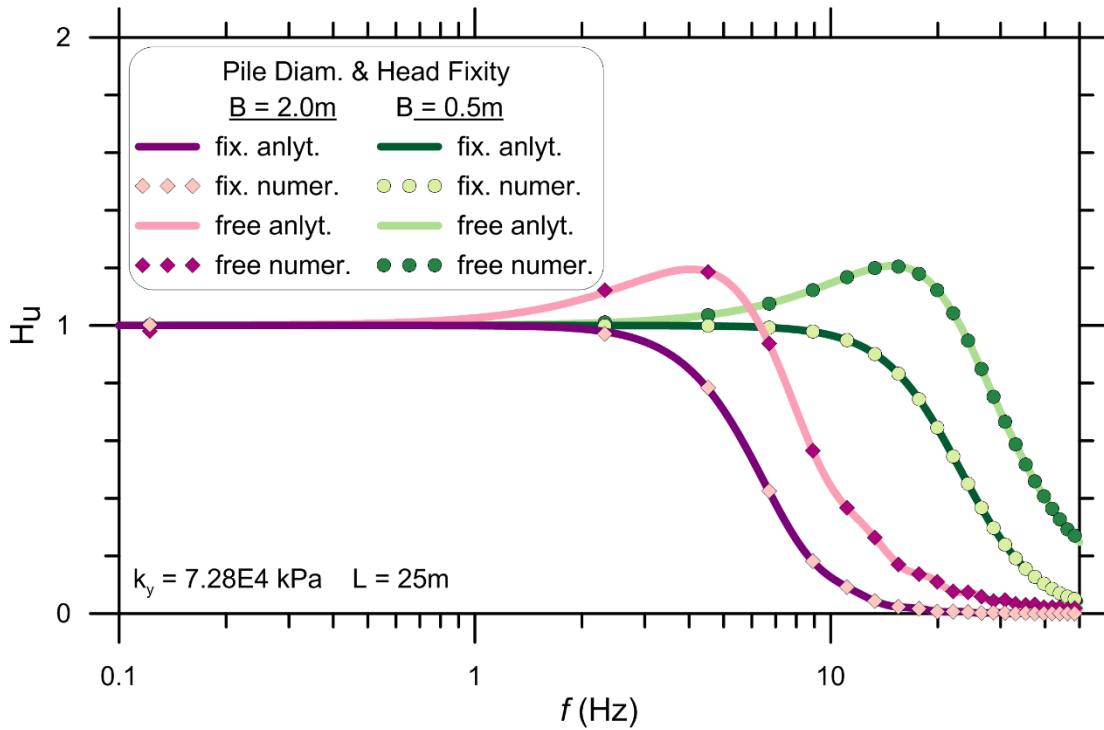


**Figure 2.4 Analytical and numerical solution transfer functions for sine-sweep input motion.**

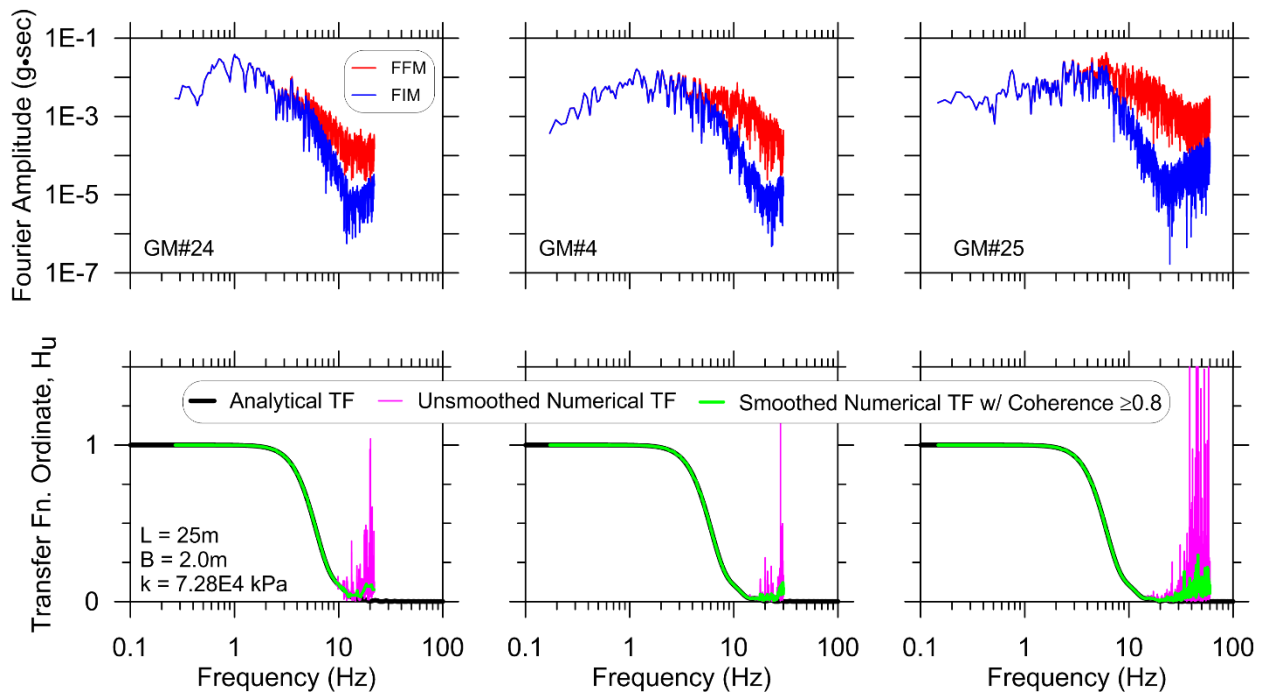


**Figure 2.5 Fourier amplitude spectra for free-field and foundation-input motions (top) and corresponding transfer functions (bottom).**

**Table 2.1** Ground motions for elastic numerical analyses; numbering follows Baker et al. [2011].

Motion #	Earthquake	Recording Station	M	PGA (s)
25	1989 Loma Prieta	UCSC	6.9	0.34
4	1994 Northridge	LA – Wonderland Ave.	6.7	0.13
24	1989 Loma Prieta	Golden Gate Bridge	6.9	0.16

Figure 2.5 shows acceleration FAS for the pile head motion (FIM) and ground surface motion (FFM) for each of the three input ground motions. Note that each ground motion FAS is only plotted over the useable frequency range of the ground motion, which depends on the processing applied to the original recording [Ancheta et al. 2014]. The ratio of the displacement FAS is the unsmoothed transfer function shown along with the high-coherence transfer function computed using Equation (1.10) in the lower portion of the figure. At frequencies up to about 20 Hz, the analytical solution matches the numerically-computed transfer functions exactly. At higher frequencies, the numerical transfer functions are dominated by noise, although the smoothed, high-coherence transfer function reduces the noise significantly.

The finding that the transfer functions computed for the three ground motions with variable frequency content all agree perfectly with the analytical solution (and therefore with each other) highlights the underlying assumption of elastic material behavior and superposition of the response at each frequency. For realistic nonlinear conditions, the response of the system will change for input motions with different frequency content.

In light of the findings that the numerical results provide a near-perfect match to the analytical solution (Figure 2.4 and Figure 2.5), and that the analytical solution matches previous solutions by others (e.g., Figure 2.3), it has been verified that the proposed numerical modeling approach is valid, at least for elastic material properties.

The remaining sections in this chapter discuss elastic behavior that applies to the small-strain, initial stiffness range of pile–soil interaction for the nonlinear analyses that follow.

## 2.3 ELASTIC WINKLER MODULUS

### 2.3.1 Terminology and Units

In the past, terms such as modulus of subgrade reaction, coefficient of subgrade reaction, Winkler stiffness, Winkler modulus, normalized Winkler modulus, and other similar combinations of these phrases have been used somewhat interchangeably to refer to two concepts that are distinct and must be clearly differentiated. Some clarification is warranted here to avoid confusion.

The concept of “modulus of subgrade reaction” refers to the soil settlement that occurs beneath a uniformly loaded area, and hence has units of  $[(\text{force}/\text{length}^2)/\text{length} = \text{force}/\text{length}^3]$ . Herein the symbol  $k_{msr}$  refers to this definition. It is formulated in this way because of its usefulness in structural models for estimating settlement resulting from the bearing pressure exerted by a

structure; it has limited usefulness as a standalone descriptor of soil behavior (true soil modulus  $E_s$  is more meaningful). Values of modulus of subgrade reaction can be crudely measured in the field using the “plate load test” [ASTM D 1194]) by applying a measured force to a steel plate of known area (stress = force/area) and measuring the downward deflection. Terzaghi and Peck [1955] provided tabulated values of  $k_{msr}$  for different relative densities of sand that were widely used for lateral pile analyses until full-scale pile testing began in the 1970s.

When used with a beam-on-springs Winkler approach, the soil stiffness term must be modified to account for the out-of-plane (transverse) width of the beam over which the soil pressure acts, since Winkler models consider only two dimensions—the longitudinal axis of the beam and the orthogonal direction in which load is applied, parallel to the beam height. For example, if a measured value of  $k_{msr}$  was to be used for a Winkler analysis, it would be multiplied by beam width to obtain  $K_e = k_{msr}B$ , where  $K_e$  is the Winkler modulus with units of distributed load per unit deflection [force/length/length], which is equivalent to the units of stress [force/length<sup>2</sup>]. The symbol  $K_e$  will be used in this text in reference to both (1) Winkler stiffness for elastic analyses and (2) the initial elastic stiffness of  $p$ - $y$  springs for nonlinear analyses.

Confusion may arise because  $K_e$  and soil Young’s modulus  $E_s$  share the same units and are sometimes presented as being related by a dimensionless coefficient for pile analysis. A discussion of the basis for this assumption is provided in the following sections, but it should be noted that  $E_s$  cannot be exactly defined from a measured value of  $k_{msr}$ . To define  $E_s$ , a measurement of strain parallel to the direction of loading is needed. In a laboratory test this is trivial because the specimen height and boundary conditions are known. To measure strain during a plate load test would require knowing the height of the soil column ( $h$ ) that is influenced by the load applied at the surface, which for an elastic half-space is theoretically infinite. While finite values of  $h$  are more reasonable and could be estimated by taking into account the three-dimensional attenuation of stress below the plate, the computed value of  $E_s$  scales linearly with  $h$  and is therefore highly sensitive to the estimate. Hence any tabulated values relating  $k_{msr}$  to  $E_s$  (e.g., Table 9-1 in Bowles [1997]) contain an inherent assumption about the plate load test depth of influence and how this will scale with size between the test and real foundations. Likewise any relation between measured or tabulated  $k_{msr}$  and Winkler modulus for lateral pile analysis contain a similar embedded assumption, or represent the results of specific load test(s).

### 2.3.2 Previous Definitions of $K_e$

Existing  $p$ - $y$  relationships such as the widely-used API [1993] curve for sand and Matlock’s [1970] curves for clay were derived by fitting equations that have a theoretically-derived functional form to the results of full-scale load tests. While load tests may provide a reasonable estimate of the near-surface ultimate lateral soil resistance  $p_{ult}$ , the instrumentation used to measure pile strain in the original tests was not capable of accurately measuring small enough deformations to capture the truly elastic soil behavior [Choi et al. 2015]. Since  $E_s$  can be related to the small-strain shear modulus measured using geophysical methods, and since geophysical tests are an increasingly common part of site investigations for projects in seismic regions, a more attractive approach would relate the soil elastic Young’s modulus  $E_s$  directly to the initial stiffness of the  $p$ - $y$  curve,  $K_e$ . Soil shear modulus  $G$ , shear-wave velocity  $V_s$ , and Young’s modulus are related through the following well known equations from elasticity theory:

$$G = \rho_s V_s^2 \quad (2.20)$$

$$E_s = 2G(1+\nu) \quad (2.21)$$

where  $\nu$  and  $\rho_s$  are the soil Poisson's ratio and mass density, respectively.

Vesic [1961] provided the following expression for  $K_e$ :

$$k_{msr} B = K_e = 0.65 \left( \frac{E_s}{1-\nu^2} \right)^{1/2} \sqrt{\frac{E_s B^4}{E_p I_p}} \quad (2.22)$$

which explicitly recognizes that beam width  $B$  must be taken into account when formulating a Winkler modulus from  $k_{msr}$ . This is straightforward for the case that Winkler (1867), Hetenyi [1946], and Vesic [1961] were considering—an infinitely-long rectangular or wide-flange beam that only exerts normal stress at the contact between the flat base of the beam and the ground surface. For the case of a laterally-loaded circular pile, the stress field at the pile-soil interface is a combination of shear and normal stresses, and the relative contribution and direction of each component changes around the circumference of the pile as shown in Figure 2.6. Equation (2.22) has been used in the past to define  $p$ - $y$  curve elastic stiffness (e.g., Boulanger et al. [1999]) despite not being derived for these conditions.

Several researchers performing elastic pile KSSI analyses have quantified a Winkler spring coefficient  $\delta$ , where the linear-elastic Winkler spring stiffness is defined as the product of the dimensionless parameter  $\delta$  and the soil modulus  $E_s$ :

$$K_e = \delta E_s \quad (2.23)$$

In other words,  $\delta$  is the ratio of the  $p$ - $y$  elastic stiffness to the soil elastic stiffness:

$$\delta = \frac{K_e}{E_s} \quad (2.24)$$

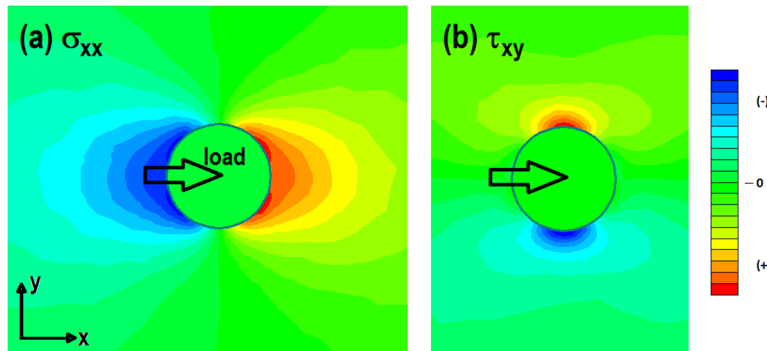


**Figure 2.6** (a) Normal and (b) shear stress contours around a laterally-loaded pile. Color key indicates change in stress from initial condition.

Values and equations for  $\delta$  for fixed- and free-head piles and for various soil properties (homogeneous, layered, stiffness increasing linearly with depth, etc.) have been proposed by many researchers including Kagawa and Kraft [1980], Roesset [1980a], Dobry et al. [1982], Gazetas and Dobry [1984b], Kavvadas and Gazetas [1993], and Syngros [2004]. In these studies, a single value of  $\delta$  was applied over the length of the pile in an elastic BDWF model; the value of  $\delta$  was then adjusted until the pile head displacement matched the displacement computed with finite-element or boundary-element continuum solutions under the same applied lateral force at the pile head. In other words, the pile-head lateral impedances were matched between the two numerical modeling approaches. Regression models to determine best-fits to parametric results were then used to determine coefficients for the expressions. A selection of these expressions and notes on their derivation are given in Table 2.2 and plotted in Figure 2.7.

Even in the case of a homogeneous soil profile, relative pile–soil displacement varies with depth for both inertial and kinematic loading due to the deformation pattern of the pile. Since a single value of  $\delta$  was applied over the entire pile length in these comparative studies, the mechanics controlling the interaction at a single depth are not directly reflected in the result, which represents an average response. This is counterproductive for practical applications because real soil profiles are inhomogeneous, and foundation designers need reliable methods for specifying accurate  $p$ - $y$  curve parameters at a single depth within a given soil layer. Furthermore since this approach simply equates one numerical study with another, the outcome is perhaps less a reflection of reality than it is of the difference between the modeling approaches. A more rigorous derivation of  $\delta$  based on theory and rigorous numerical modeling complemented by validation from accurate small strain measurements during physical modeling studies is a future research need.

Since loading was applied at the pile head in these studies, the resulting values of  $\delta$  were not derived for the fundamental mechanics governing kinematic interaction from free-field excitation. Anoyatis et al. [2013] showed that the commonly used value of  $\delta = 1.2$ , initially proposed by Roesset [1980a], does not provide a good match to finite-element solutions for kinematic loading for certain pile and soil stiffness combinations. Furthermore, the parametric results of Anoyatis et al. showed that even for the same pile and soil conditions, different values of  $\delta$  are required to match the BDWF results to the continuum finite-element results depending on which result is being matched (e.g., curvature ratios between the pile and soil at the pile head versus pile tip, maximum pile bending moment, etc.), which has also been reported by Kavvadas and Gazetas [1993]. This is again a reflection of the fact that the approach of obtaining  $\delta$  by matching impedances from BDWF and continuum analyses does not faithfully capture the underlying pile–soil interaction mechanics; if it did then a single expression would work for a variety of boundary conditions. A useful finding of Anoyatis et al. is that the  $\delta$  parameter is not strongly frequency-dependent, which is convenient because of the difficulties involved in performing frequency-domain analyses.

Despite the shortcomings of the impedance-matching approach, the difference between  $\delta$  values for fixed- and free-head piles in Figure 2.7 clearly shows that pile rotation or the lack thereof has a significant influence on the magnitude of the mobilized soil resistance, and there is a physical basis for this trend. Near the head of a free-head pile where rotation is significant, the pile encounters greater soil resistance than a fixed-head pile because pile rotation mobilizes soil shear resistance in addition to the predominantly compressive stress induced by translation. Ideally,  $p$ - $y$  curves should be formulated as  $p$ - $y$ - $\theta$  curves, where  $\theta$  is pile rotation. This is another future research need and will not be addressed in the current study.

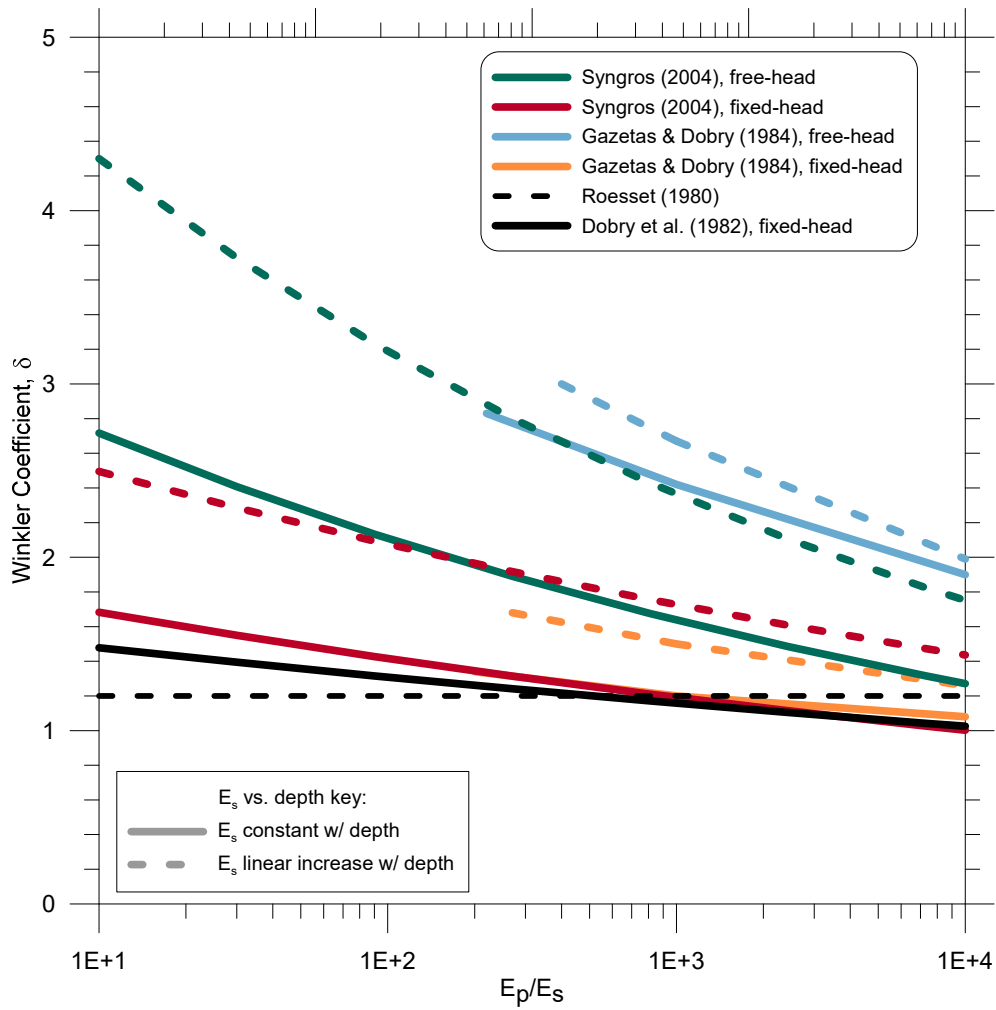


Figure 2.7 Values of Winkler coefficient  $\delta$  proposed in previous pile SSI research.

**Table 2.2**  $\delta$  expressions from previous researchers derived by matching results of BDWF analyses to continuum analyses.

Applicable soil condition	Pile head-fixity condition	Source:	Roesset [1980a]	Dobry et al. [1982]	Kavvasdas and Gazetas [1993] <sup>b</sup>	Syngros [2004] <sup>c</sup>
Any, or not specified	Any, or not specified	$\delta =$	1.2	-	-	-
Constant stiffness w/ depth	Fixed		-	$1.67 \left( \frac{E_p}{E_s} \right)^{-0.053}$	-	$2.0 \left( \frac{E_p}{E_s} \right)^{-0.075}$
	Free		-	$1.67 \left( \frac{E_p}{E_s} \right)^{-0.053}$	$\frac{3}{1-\nu^2} \left( \frac{E_s}{E_p} \right)^{1/8} \left( \frac{L}{B} \right)^{1/8}$	$3.5 \left( \frac{E_p}{E_s} \right)^{-0.11}$
Linearly increasing stiffness w/ depth <sup>a</sup>	Fixed		-	-	-	$3.0 \left( \frac{E_p}{E_s} \right)^{-0.08}$
	Free		-	-	-	$5.8 \left( \frac{E_p}{E_s} \right)^{-0.13}$

<sup>a</sup>Soil stiffness  $E_s$  defined as the stiffness at the pile tip, decreases linearly to zero at the ground surface.

<sup>b</sup>Main emphasis of study was matching peak bending moments between BDWF and finite-element (FEM) continuum analyses

<sup>c</sup>FEM studies performed using *K-PAX* software, described in Syngros [2004] dissertation. The axisymmetric domain is two-dimensional and formulated in radial coordinates. Soil-pile interaction represented by a strain compatibility condition at interface.

### 2.3.3 Diameter Effects

The relationships for  $\delta$  in Table 2.2 generally lack a functional dependence on pile diameter, suggesting that pile–soil interaction initial stiffness is independent of diameter. While this holds true for plane-strain elastic solutions considering a homogeneous full-space domain, solutions using more realistic boundary conditions along with experimental results (e.g., see Carter 1984 and Pender [2004]) indicate that initial stiffness does depend on pile diameter. Conversely, experimental work by Ashford and Juirnarongrit [2003] showed that a diameter-independent estimate of  $K_e$  provided the best match to full-scale experimental results, but only for piles with active length contained within a uniform-stiffness stiff clay layer.

A dependence on diameter is intuitive—it would seem that a pile undergoing lateral displacement will encounter greater soil resistance than a smaller diameter pile undergoing the same displacement due simply to the fact that it is wider than the small-diameter pile. Pile rotation and changes in soil stiffness with depth also affect the resistance encountered by the pile as a function of its diameter [Pender 2004]. These effects are due to the dependence of the pile’s flexural response on  $EI$  (and hence  $B$ ), and because a larger diameter pile mobilizes soil resistance over an increasingly larger depth increment and hence “feels” an increase in stiffness with depth. Pender [2004] and others have suggested that previous experimental campaigns failed to identify these trends because only a small number of pile diameters were tested—in some cases, one.

Nonetheless, the majority of elastic pile dynamics work and many nonlinear  $p$ - $y$  studies (e.g., Kagawa and Kraft [1981] and Boulanger et al. [1999]) have proceeded with the assumption of  $K_e$  being independent of pile diameter. The underlying assumption for this approach is that a small-diameter pile will induce greater average soil strain than a large-diameter pile for the same lateral displacement by a factor proportional to the difference of the two piles diameters. This is consistent with Terzaghi's [1955] assumption that the zone in which significant strain is mobilized beneath a loaded footing scales in proportion to the size of the footing.

Kagawa and Kraft [1980] adapted a formulation by Matlock [1970] as the basis for applying this assumption to pile dynamics<sup>5</sup>, suggesting that the average shear strain  $\gamma_{ave}$  which develops around a laterally loaded pile is a linear function of the ratio of displacement to pile diameter ( $y/B$ ), such that as  $B$  increases, the relationship between stress and strain, and hence  $p/y$ , scales at the same rate:

$$\gamma_{ave} = \frac{(1+\nu)y}{2.5B} \quad (2.25)$$

To test this hypothesis, a series of simple plane-strain elastic analyses were run for this study in the finite-element program *Phase2* [Rocscience 2013]. The results showed that  $\delta$  is independent of diameter, but only if the domain size is scaled to match changes in pile size—a significant caveat. This is in agreement with previous two- and three-dimensional elastic analyses (e.g., see Pender [2004]), so further details will not be provided here.

The potential error introduced by using a diameter-independent  $K_e$  is likely minor for many applications in which large relative pile–soil displacements are expected, since the tangent modulus of a nonlinear  $p$ - $y$  curve depends on both the initial stiffness and the ultimate resistance. The results of Ashford and Juirnarongrit [2003] also suggest that the error is minor for small-strain dynamic loading if the soil stiffness is approximately constant with depth.

Despite its shortcomings, the framework of Equation (2.25) is convenient because it allows the relative pile–soil displacement defining the onset of nonlinearity  $y_{yield}$  to be defined as a function of shear strain at the onset of soil nonlinearity, the latter of which has been studied extensively through laboratory testing (e.g., Vucetic and Dobry [1991]). Hence, a diameter-independent definition for  $K_e$  based on Equation (2.25) will be adopted for this study, with the

---

<sup>5</sup> It is worth noting that further examination of the underlying theory behind Equation (2.25) reveals that it has little relation to lateral pile-soil interaction. The basis for Equation (2.25) is Skempton's [1951] method for estimating the immediate settlement of an embedded strip footing on clay based on a combination of elasticity theory, limit-state concepts, and laboratory tests results. Skempton estimated that the ratio of  $E_s$  to undrained strength ( $s_u$ ) for typical clays is about 50 to 200, and assumed that the inverse of this range (0.005 to 0.02) could be used to approximate the strain occurring at one-half the measured strength ( $\varepsilon_{50}$ ). Using these values and an assumption of the size of the stress zone of influence below the footing, a simple approximation for settlement was provided. Matlock adopted this for piles by taking the average of the  $\varepsilon_{50}$  range ( $\approx 0.01$ ) and substituting pile diameter for footing width, resulting in the expression that average normal strain around the pile could be approximates as  $y/2.5B$ —hardly a rigorous consideration of pile-soil interaction mechanics. Kagawa and Kraft [1980] later adopted this approach for their theoretical pile dynamics study. Noting that the strain orthogonal to  $\varepsilon$  is  $-\nu\varepsilon$ , and thus the maximum shear strain is  $(1+\nu)\varepsilon$ , they came up with Equation (2.25).

opportunity to revise the findings in the future if more rigorous relationships between  $\delta$  and  $B$  (or  $\gamma_{ave}$  and  $B$ ) become available.

## 2.4 QUESTIONS OF PILE MASS AND INERTIA

For static loading, since acceleration is zero (or is ignored for pseudo-static analysis) no inertial force is associated with movements of the pile mass. During the rapid and potentially large-amplitude loading from an earthquake, however, pile inertia contributes to the overall response of the pile–soil system and should be included in dynamic analyses, as recognized early on by Novak [1974]. To produce more tractable and simplified solutions, previous researchers using Winkler models have often neglected the pile mass such that a static solution is being used to approximate the dynamic response (e.g., Dobry et al. [1982] and Anoyatis et al. [2013]). Others assigned a mass density greater than the true pile mass (e.g., Berger et al. [1977] and Marshall et al. [1977]) to account for the fact that some portion of the soil surrounding the pile moves in phase with the pile, amplifying its inertia. The volume of soil that moves with the pile likely varies depending on the frequency and amplitude of the excitation along with the pile and soil properties, and is therefore difficult to quantify.

The influence of pile mass is demonstrated in Figure 2.8, which compares normalized elastic transfer functions computed for two pile sizes with and without mass. In general, these elastic analyses indicate that the effect of pile mass is minor, which agrees with previous findings by Kagawa and Kraft [1980], and only deviates from the no-mass condition over a limited frequency range. The effect does not appear to scale with pile diameter, since the difference between the with-mass and without-mass curves is approximately equal for the two sizes considered when plotted versus dimensionless frequency. The effect of pile inertia may not be as consistent when system nonlinearity is considered. As discussed in the following section, including pile mass in numerical simulations can complicate interpretation of the kinematic transfer function because of inertial resonance near the fundamental frequency of the pile–soil system. Because of this, and in light of the finding that the influence of pile inertia is minor, piles will be modelled as massless for the numerical simulations that follow.

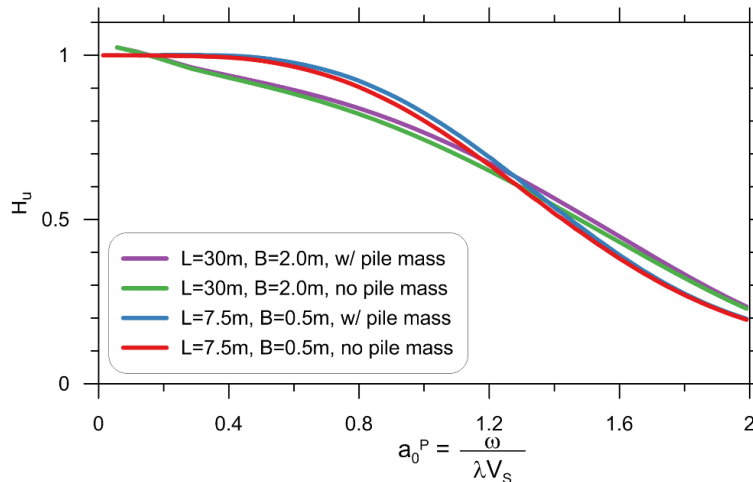


**Figure 2.8** Normalized elastic transfer functions computed with and without pile mass.

## 2.5 PILE–SOIL SYSTEM FUNDAMENTAL FREQUENCY AND RESONANCE

When pile mass is included in a Winkler model, the pile–soil system will have a defined fundamental frequency. It is important to recognize that this represents a somewhat fictitious mode of vibration in the context of a real structure, since in general the dynamic response of a system depends on the coupled response of the superstructure and foundation–soil components. Nonetheless, transfer functions computed for this study have the potential to be influenced by inertial resonance when pile mass is included. To investigate the potential influence of resonance, transfer functions were computed for pile–soil systems with and without pile mass, similar to the analyses presented in the previous section.

As shown in Figure 2.9, it is clear that the kinematic transfer function is strongly influenced by resonance near the first-mode period of the pile–soil system (at about 17 Hz), amplifying the free-field motion by a factor of nearly five. Also of note is that the bandwidth of the zone influenced by first-mode resonance is on the order of 5 Hz. In general this bandwidth will increase with increasing fundamental frequency of the system [Rathje et al. 2004; Chopra 2007]. Hence, it is possible for resonance to influence the kinematic transfer function over the frequency range of interest even if the fundamental frequency of the pile–soil system lies beyond this this range.

Inflation of transfer function ordinates due to inertial resonance further compounds the difficulties associated with accurately defining kinematic transfer functions at high frequencies as discussed in §1.3.6.2. In light of this, pile mass will be set to zero for the analyses that follow unless otherwise noted. This approach is especially helpful for nonlinear analyses in which the fundamental frequency of the system changes over the duration of the problem, which makes it difficult to discern which portions of the resulting transfer function are strongly affected by resonance.

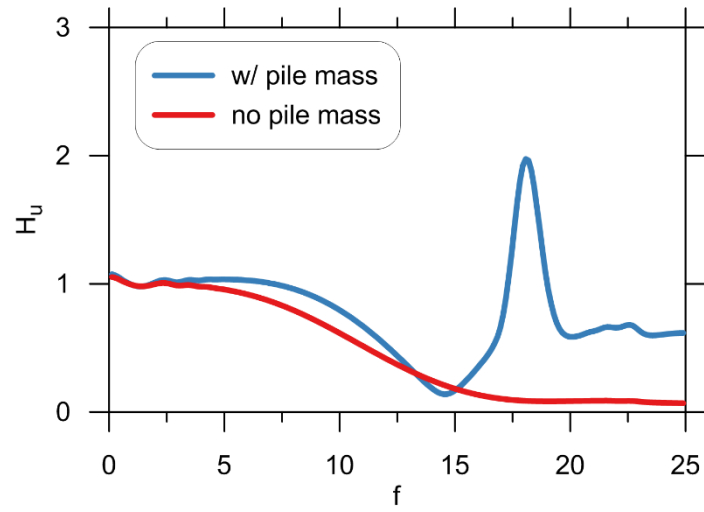


**Figure 2.9** Effect of resonance at pile–soil system fundamental frequency on kinematic transfer functions.

# 3 Analysis

## 3.1 APPROACH

The approach for investigating kinematic pile–soil interaction for this study is through numerical analyses using the finite element modeling platform *OpenSees*. A model of a single pile or pile group connected to nonlinear *p-y* springs is formulated as shown in Figure 3.1(b). Dynamic time-domain analyses are then conducted in which the free ends of the *p-y* springs are displaced to simulate free-field ground response due to earthquake excitation; the free-field ground motions are computed separately using one-dimensional nonlinear ground response analysis in *DEEPSOIL* [Hashash et al. 2015] as depicted in Figure 3.1(a). Transfer functions and spectral ratios are then computed using the pile head and free-field ground surface response histories.

In the following sections, the various components used in the beam-on-dynamic-nonlinear-Winkler-foundation (BDNWF) and ground response models for this study are discussed. Background on the parameters is first given in the context of previous efforts by other researchers studying pile dynamics, followed by an explanation of how the parameters were quantified for this study.

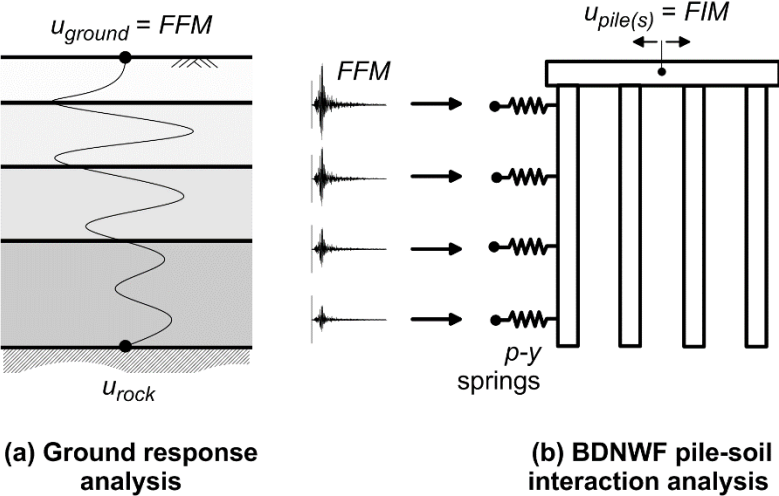


Figure 3.1 Numerical modeling approach.

### 3.2 PARAMETRIC STUDY BOUNDS

The range of pile and soil properties considered for this study are intended to span the conditions encountered in typical bridge design practice. The study bounds were further refined based on the combinations of pile and soil stiffness found to result in significant kinematic interaction based on elastic solutions in the previous chapter.

Table 3.1 presents the range of single pile properties considered. Models of each of the four piles in Table 3.1 have been analyzed for six different soil profiles each subjected to 40 ground motions for free- and fixed-head pile boundary conditions. This represents 960 analyses for each head-fixity, for a total of 1920 single pile analyses. Properties of sites 1 through 6 are discussed in §3.6, and the 40 ground motions are discussed in §3.7. In addition, a limited number of pile group analyses were performed to investigate group effects and the influence of ground-motion incoherence, and are discussed in §3.5.4 and §3.7.3, respectively

**Table 3.1 Parametric study bounds for single piles.**

Length (L)	Diameter (B)	Slenderness Ratio (L/B)	Cracked Section Stiffness (MN·m)
7.5 m	0.5 m	15	28
15 m	0.5 m	30	28
30 m	2.0 m	15	7220
60 m	2.0 m	30	7220

### 3.3 *PySimple3*—MOTIVATION AND MODEL UPDATES

It is well known in the geotechnical community that the generic  $p$ - $y$  springs typically used in practice do not sufficiently capture realistic soil behavior, especially for dynamic analysis. For this study, a modified version of the  $p$ - $y$  model developed by Choi et al. [2015] is used, known as *PySimple3* in *OpenSees*. The *PySimple3* model was developed specifically for dynamic analysis of laterally loaded piles and includes several features not found in previously available models, such as the ability to independently specify small stain stiffness, the force at which yielding/nonlinearity occurs, and hysteretic and radiation damping. The model consists of an initial linear portion followed by nonlinear behavior according to a bounding-surface plasticity formulation (e.g., Dafalias [1986]) as illustrated in Figure 3.2. The user specifies the initial elastic slope of the curve  $K_e$ , the ultimate resistance  $p_{ult}$ , the resistance at yielding  $p_y$ , and shape parameter  $C$  that describes curvature and hence affects the amount of soil hysteric damping. Radiation damping can also be modeled by specifying an optional viscous damping coefficient.

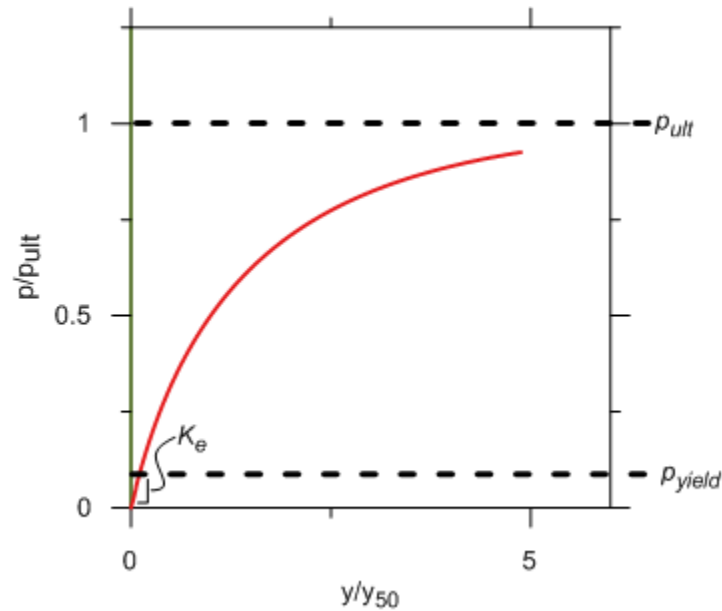
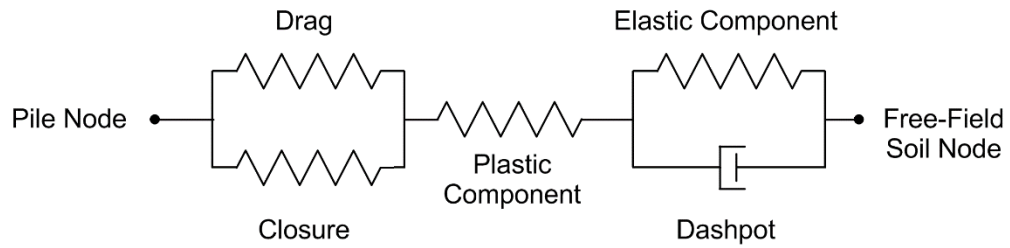


**Figure 3.2** Basic features of *PySimple3* material under monotonic loading (after Choi et al. [2015]).

### 3.3.1 Motivation

Prior to development of *PySimple3*, the primary tool available for pile SSI modeling with a BNWF approach was the *PySimple1* material model in *OpenSees*, which is based on a framework presented by Boulanger et al. [1999]. The implementation of *PySimple1* in *OpenSees* is formulated to approximate the shape of the API [1993] or Matlock [1970]  $p$ - $y$  curves for sand and clay, respectively. Because the material model is coded to match the shapes of these previous  $p$ - $y$  definitions, the user has limited control over specific aspects of the curve. For example, the initial stiffness cannot be specified directly, only adjusted indirectly by changing the other parameters. In addition, as shown in Figure 3.3, the viscous dashpot used to represent radiation damping is placed in parallel with the entire material instead of just the far-field elastic component as presented in Boulanger et al. [1999]. For the *OpenSees* implementation, the dashpot force is computed after force and displacement compatibility has been achieved between the gap, plastic, and elastic components based on the proportion of the total displacement that occurs in the elastic component relative to the total element. In other words, the dashpot force is not considered while solving for compatible forces and displacements in the other components, only after the fact. While this approach is computationally stable, it is more desirable to have a true viscoelastic-plastic implementation as shown in Figure 3.4(b). Note that placing the dashpot in parallel with the elastic component, also known as the Kelvin-Voigt viscoelasticity model, is distinct from placing the two components in series, known as the Maxwell model [Simo and Hughes 1998]. The *PySimple1* and *PySimple3* materials are compared for sand and clay in Figure 3.5.

(a) after Boulanger et al. (1999)



(b) *PySimple1* OpenSees implementation

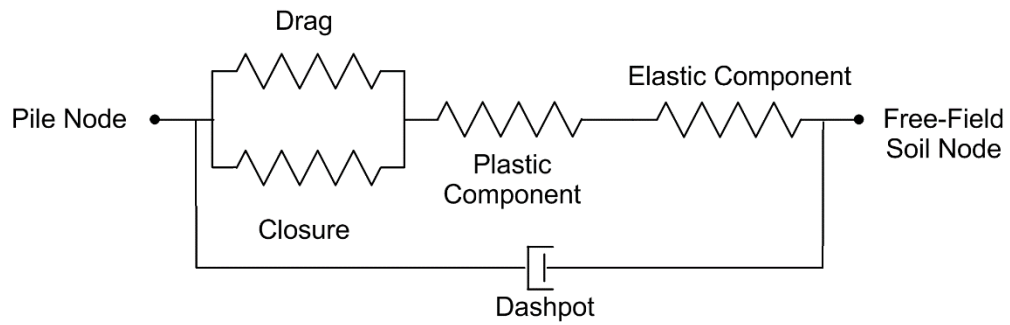
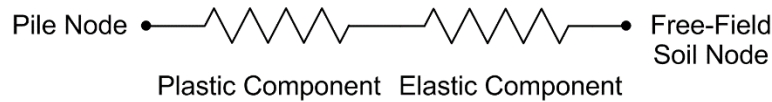


**Figure 3.3** Comparison of Boulanger et al. [1999] dynamic *p-y* material and later implementation in OpenSees.

(a) *PySimple3* (Choi et al. 2015, JGGE)



(b) Updated *PySimple3* (current study)

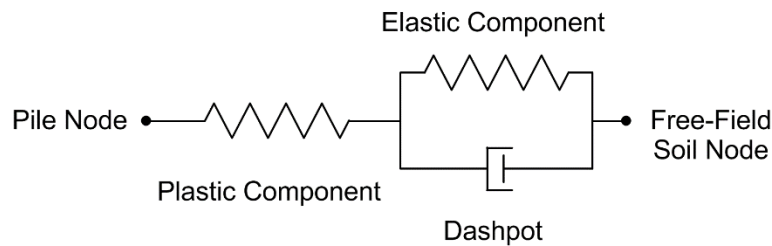


**Figure 3.4** *PySimple3* viscoelastic-plastic material model formulation.

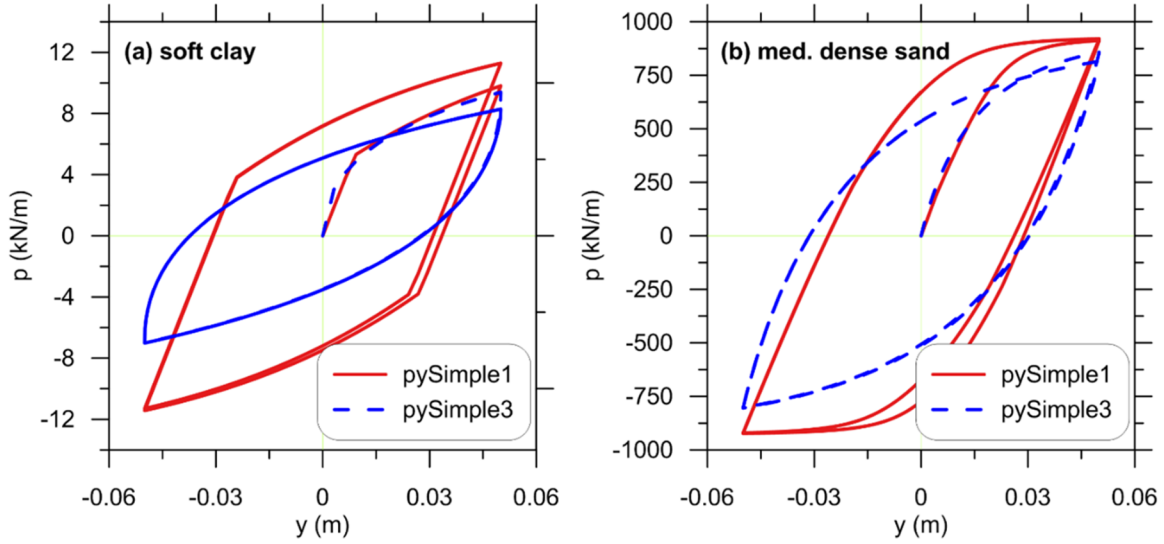


Figure 3.5 Comparison of *PySimple1* and *PySimple3* material models.

### 3.3.2 Governing Equations and OpenSees Implementation

The *PySimple3* constitutive model by Choi et al. [2015] is based on a bounding-surface plasticity formulation according to the following governing equations:

$$\dot{p} = K_e \dot{y}_e = K_e (\dot{y} - \dot{y}_p) \quad (3.1)$$

$$f = |p - p_\alpha| - p_y \quad (3.2)$$

$$K_p = C \cdot K_e \frac{[p_u \cdot \text{sign}(\dot{y})] - p}{|p - p_{in}|} \quad (3.3)$$

$$\dot{p}_\alpha = K_p \dot{y}_p \quad (3.4)$$

$$K = \frac{\dot{p}}{\dot{y}} = \frac{K_p K_e}{K_p + K_e} \quad (3.5)$$

Equation (3.1) is the elastic constitutive law relating the rate of change versus time (signified by the overdot) of force in the element  $\dot{p}$  to the elastic displacement rate  $\dot{y}_e$  based on the elastic stiffness  $K_e$ . The right-hand side of Equation (3.1) shows that the elastic displacement rate is equivalent to the total displacement rate minus the plastic displacement rate. Equation (3.2) is the yield function used to determine if yielding has occurred ( $f = 0$ ) or if the current state remains in the elastic region ( $f < 0$ ). When yielding has occurred, Equations (3.3)–(3.5) define the plastic modulus, kinematic hardening law, and elastoplastic (tangent) modulus. The force  $p_\alpha$  tracks the center of the elastic region, which evolves with the yield surface during continued post-yield loading. This is equivalent to the concept of backstress in classical plasticity formulations, but in this case is a “backforce.” The plastic modulus is determined by how close the current state  $p$  lies to the ultimate resistance (bounding surface) represented by  $p_{ult}$  and the force at the onset of yielding  $p_{in}$ . The formulation allows for a smooth transition between elastic and post-yield

behavior since the plastic modulus is infinite at the onset of yielding, such that the elastoplastic modulus is initially equal to the elastic modulus but undergoes degradation with continued displacement. Further details are available in Choi et al. [2015].

Three updates were made to *PySimple3* to meet the needs of this study and to improve the performance of the material for general use in other pile dynamics problems: (i) optional viscoelastic behavior was added to model radiation damping; (ii) a backforce-updating routine was added to prevent overestimates of force following an unload-reload cycle; and (iii) the implicit integration scheme used for solving the governing equations was updated to use the unconditionally-stable and efficient Ridder's method [1979].

An elastic spring in parallel with a viscous dashpot as shown in Figure 3.4(b) is known as the Kelvin-Voigt viscoelasticity model. The instantaneous force in a Kelvin-Voigt material is the sum of the force in the elastic component due to the material's elastic stiffness plus the force in the dashpot:

$$\dot{p} = K_e \dot{y}_e + c \ddot{y}_e \rightarrow \frac{dp}{dt} = K_e \left( \frac{dy_e}{dt} \right) + c \left( \frac{d^2 y_e}{dt^2} \right) \quad (3.6)$$

where  $c$  is the dashpot coefficient. This formulation defines the elastic (now viscoelastic) constitutive law for the updated *PySimple3* material. The viscoelastic-plastic tangent becomes:

$$K = \frac{dp}{dy} = \frac{\left( \frac{dp}{dy_e} \right) K_p}{\left( \frac{dp}{dy_e} \right) + K_p} \quad (3.7)$$

The term relating change in force to change in elastic displacement ( $dp/dy_e$ ) can be isolated from Equation (3.6) in incremental form as follows:

$$dp = K_e dy_e + c \left( \frac{dy_e}{dt} - \frac{dy_{e,last}}{dt} \right) \rightarrow \frac{dp}{dy_e} = K_e + c \left( \frac{dy_e}{dy_e dt} - \frac{dy_{e,last}}{dy_e dt} \right) = K_e + \frac{c}{dt} \left( 1 - \frac{dy_{e,last}}{dy_e} \right) \quad (3.8)$$

where  $dy_{e,last}/dt$  is the elastic displacement rate during the last converged step. Note that the following possible alternative formulation for  $dp/dy_e$ :

$$\frac{dp}{dt} = K_e \frac{dy_e}{dt} + c \left( \frac{d^2 y_e}{dt^2} \right) \rightarrow dp = K_e dy_e + c \left( \frac{dy_e}{dt} \right) \rightarrow \frac{dp}{dy_e} = K_e + \frac{c}{dt} \quad (3.9)$$

implies that the dashpot force would continue to be added to the total force in the viscoelastic component even if the elastic displacement rate stays constant. This is an incorrect formulation; if the elastic displacement rate (i.e., velocity) is constant, then the dashpot force should remain constant between successive increments. Only the force in the elastic spring component changes if the elastic displacement rate is constant; Equation (3.8) has been formulated to capture this.

The approach for solving the governing equations in the *OpenSees* implementation of the *PySimple3* material is as follows:

- A trial displacement step is passed to the material by the program; if yielding does not occur, the resulting force is determined from Equation (3.6) directly.
- If yielding occurs, an initial guess is made that divides the trial displacement increment into elastic and plastic sub-increments.
- The force in the plastic and viscoelastic components is computed based on the imposed trial displacements.
- Since the plastic and viscoelastic components are in series, the force in the two components must be equal. Hence the unbalanced force between the two components is cast as a residual equation, and the trial amount of elastic versus plastic displacement is adjusted until the residual unbalanced force falls below a specified tolerance. Ridder's method is used to solve this iteration scheme.

### 3.4 *PySimple3*—PARAMETER VALUES

The following sections describe how each of the parameters that define the *PySimple3* model are defined for this study.

#### 3.4.1 Initial Elastic Stiffness $K_e$

The initial horizontal interaction between a laterally-loaded pile and soil does not induce nonlinearity in the pile or soil. Although the nonlinear *PySimple3* model used for this study is linear only for very small displacements [on the order of  $y/B$  of  $2 \times 10^{-5}$  (after Choi et al. [2015]), the elastic slope has a significant impact on the shape of the  $p$ - $y$  curve and the resulting tangent stiffness and hysteresis at displacements large enough to induce nonlinearity. Figure 3.6 demonstrates that for all other parameters being equal, the amount of hysteretic damping during harmonic loading is significantly different when  $K_e$  is varied by a factor of two—even at displacements less than 1 cm. Hence, it is important to make an accurate estimate of  $K_e$  in order to capture nonlinear behavior at larger strains.

Values of the parameter  $\delta$  that relates  $K_e$  to the soil elastic modulus were discussed in §2.3.2. In general, these values apply to inertial interaction cases and have not been validated against real pile behavior. In the absence of more rigorous studies specifically targeting  $\delta$  for kinematic pile SSI applications, lower- and upper-bound values of 1.0 and 3.0 were used for this study. The lower-bound value 1.0 was used for fixed-head piles, including pile groups connected by a stiff pile cap that undergo translation with little corresponding rotation. The finite-element simulations discussed in the following section indicate that this value is reasonable. A value of  $\delta = 3.0$  was used in this study for free-head piles (such as extended-shaft bridge columns). These values fall within the range implied by the elastic solutions presented in Figure 2.7 and Table 2.2.

The effect of head-fixity condition on the pile response is most significant near the pile head within the uppermost pile active length  $L_a$ . Hence, it is possible that using a  $\delta$  value of 3.0 over the full length of a free-head pile results in an overestimate of the pile–soil interaction stiffness. To investigate whether or not this has a significant effect on the transfer functions computed for this study, a comparison was made between transfer functions computed using a uniform value of  $\delta = 3.0$  over the full length of a free-head pile versus using  $\delta = 3.0$  over a depth

increment from the surface to eight pile diameters, and  $\delta = 1.0$  below this depth. As indicated in Figure 3.7, there is a negligible influence of the value of  $\delta$  used over the lower portion of the pile on the computed transfer function. Hence, a uniform value of  $\delta = 3.0$  will be used for free-head piles for simplicity.

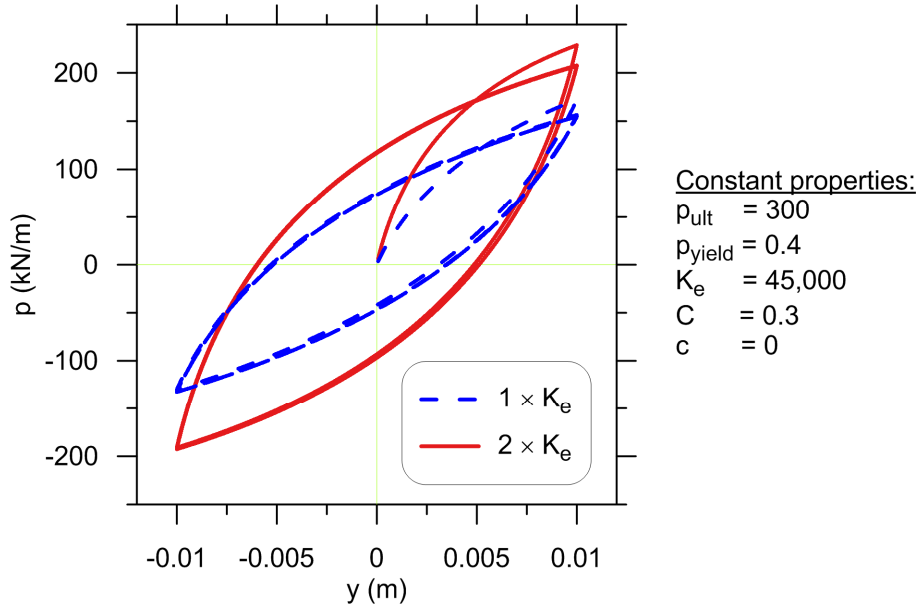


Figure 3.6 Effect of initial elastic stiffness  $K_e$  on *PySimple3* behavior for typical soft-clay properties.

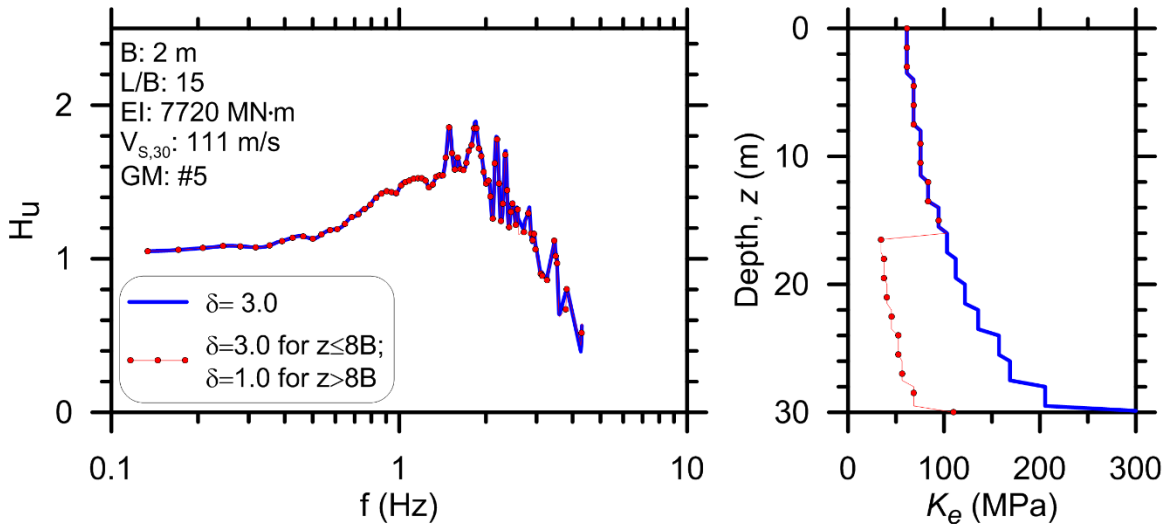


Figure 3.7 Transfer functions (left) and  $p$ - $y$  curve initial stiffness parameter versus depth plots (right) for free-head pile with uniform and variable values of Winkler coefficient  $\phi$  over the depth of the pile.

### 3.4.2 Ultimate Resistance

The API [1993] and Matlock [1970] values for  $p$ - $y$  spring ultimate resistance were adopted for this study for sand and clay, respectively. Although these relationships are semi-empirical and do not account for seismic loading conditions, they provide a convenient method for estimating ultimate resistance. Furthermore, since the relative displacement between the pile and the soil due to kinematic interaction is small over the majority of the length of the pile, the ultimate resistance of the  $p$ - $y$  springs will rarely be mobilized, and the initial stiffness  $K_e$  and yield force  $p_{yield}$  are more important terms. Further research is needed to better characterize the ultimate resistance for both static and dynamic loading conditions.

### 3.4.3 Curvature Parameter and Yield Force

The parameter  $C$  controls the shape of the  $PySimple3$  curve between the elastic region and the ultimate resistance, with smaller values of  $C$  resulting in more curvature if  $K_e$  and  $p_{ult}$  are held constant (Figure 3.8).  $C$  can be calibrated to fit the results of model- or full-scale load tests, or can be set such that the curve passes through a target point.

In this study,  $C$  was computed such that the curve passes through a target  $y_{50}$  point, where  $y_{50}$  is the deformation at which 50% of  $p_{ult}$  has been mobilized and, conveniently, is a parameter usually defined for existing  $p$ - $y$  curve models. Choi et al. [2015] derived the following expression for  $C$  as a function of  $y_{50}$  and the remaining  $PySimple3$  parameters from the governing Equations (3.1) through (3.5) presented above:

$$C = \frac{(p_{ult} - p_y) [\ln(p_{ult} - p_y) - \ln(p_{ult})] + p_{ult} [\ln(2) - 0.5] + p_y [1 - \ln(2)]}{K_e y_{50} - 0.5 p_{ult}} \quad (3.10)$$

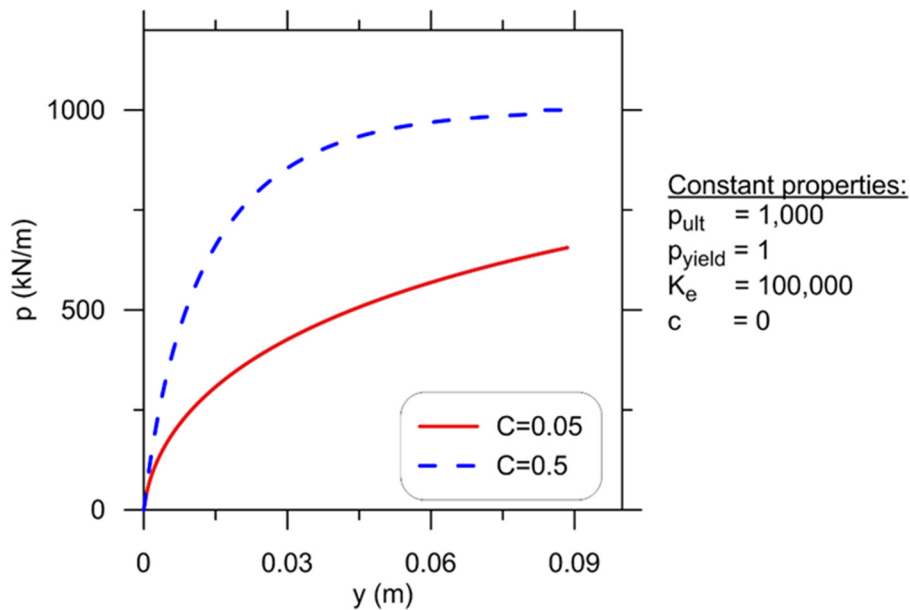


Figure 3.8 Effect of  $PySimple3$  curvature parameter  $C$ .

where  $p_y = K_e y_{yield}$  is the value of  $p$  at which yielding occurs. The relative pile–soil displacement  $y_{yield}$  is the value of  $y$  at the onset of soil nonlinearity. For this study,  $y_{yield}$  was estimated using Equation (2.25), the same approach taken in the Choi et al. [2015] study. Shear strain corresponding to the onset of soil nonlinearity was approximated as 0.001% based on laboratory direct simple shear test results performed by Darendeli [2001].

As the target  $y_{50}$  value becomes smaller and the denominator of Equation (3.10) approaches zero,  $C$  approaches infinity. Very large values of  $C$  result in approximately elastic perfectly-plastic  $p$ - $y$  behavior, which can lead to numerical instability in the finite element solution. (The trend towards this behavior is shown in Figure 3.8.) Permissible values of  $y_{50}$  must satisfy the expression:

$$y_{50} > \frac{0.5p_{ult}}{K_e} \quad (3.11)$$

One approach for establishing the target  $y_{50}$  is to use expressions from an existing  $p$ - $y$  relationship such as API [1993] or Matlock [1970]. For sand, the API relationship tends to predict  $y_{50}$  values that are close to the lower bound defined by Equation (3.11), especially for loose to medium-dense sands at confining pressures greater than about 400 kPa. This is partially due to the implicit assumption in the API formulation that the stiffness of sand increases linearly with depth; the stiffness of sand can more accurately be described as scaling in proportion to the square root of confining stress [Hardin and Drnevich 1972]. Hence, the API formulation tends to overpredict sand stiffness, with the magnitude of the overprediction increasing with depth. This results in a corresponding underestimate of  $y_{50}$ . The modified version of the API sand formulation described by Boulanger et al. [2003], in which soil stiffness is assumed to increase in proportion to the square root of confining pressure, also resulted in  $y_{50}$  values near the lower bound defined by Equation (3.11).

To address the shortcoming described above for estimating  $y_{50}$  for sand, a series of plane-strain finite element analyses of laterally-loaded piles were conducted using the program *Phase2* [Rocscience 2013]. The domain consists of a horizontal slice through the pile and the surrounding soil as shown in Figure 3.9. The plane-strain behavior is meant to capture the lateral pile–soil interaction below the depth at which a passive pressure wedge would form and displace upward near the ground surface. The sand was characterized as having minimum and maximum void ratios of 0.4 and 0.9, respectively, and a critical state friction angle of 32° [Bolton 1986]. For three relative densities corresponding to loose, medium-dense and dense sand (20%, 50%, and 80%) and assumptions of 100% saturation and a specific gravity of solids of 2.65, unit weights and corresponding vertical stresses were calculated at depths of 5, 10, 20, and 40 m. Shear strength and stiffness properties of the sand were then estimated using a consistent framework to ensure that the properties scaled uniformly with changes in stress.

Peak friction angles were calculated based on relative density, confining pressure, and mean effective stress at failure assuming a triaxial stress path after Bolton [1986]. The resulting values of  $\phi'$  ranged from 32 to 45°; these values were used to compute the coefficient of lateral earth pressure at-rest  $K_0$  using the expression for normally consolidated sand by Jaky [1948]:

$$K_0 = 1 - \sin \phi' \quad (3.12)$$

Values of Young's modulus for the sand were estimated using an expression proposed by Lewis [1990] with the coefficients representing the average results of laboratory testing on sands at

different relative densities and confining stresses. The expression captures the increase in stiffness of sand as a function of square root of confining pressure:

$$E_s = 1700(p')^{0.5} \frac{P_a^{(0.5)}}{(0.3 + 0.7e^2)} \quad (3.13)$$

where  $p'$  is mean effective stress,  $p_a$  is atmospheric pressure in the same units as  $p'$ , and  $e$  is void ratio. The parameters  $\phi'$  and  $E_s$  were used to define the Duncan-Chang [1970] nonlinear-elastic hyperbolic material model in *Phase2*. Soil Poisson's ratio  $\nu = 0.3$  and a failure ratio  $R_f = 0.9$  were used for the model. Although the Duncan-Chang model does not include plasticity, it provides a reasonable representation of the stress-strain behavior of soil up to the point of shear failure and is simple to define based on readily-quantifiable soil parameters.

Analyses were performed for the four depths listed previously for pile diameters of 0.5 and 2.0 m. The loose soil ( $D_r = 20\%$ ) was not considered at the 40-m depth. The plane-strain behavior results in  $p$ - $y$  curves that do not reach an asymptotic value of  $p_{ult}$  since increasing pile displacement mobilizes resistance in an increasingly larger zone of soil (which is likely a realistic behavior, although current  $p$ - $y$  curves are not formulated this way). As such,  $p_{ult}$  was defined somewhat arbitrarily as the value of  $p$  for which the secant slope of the  $p$ - $y$  curve decreased to 5% of the initial slope.

The results of the simulations are presented in normalized form in Figure 3.10(b) along with the normalized values predicted by API [1993] and the modified API relationship presented by Boulanger et al. [2003] in Figure 3.10(a). The 1:1 slope line in Figure 3.10 represents the minimum value of  $y_{50}/B$  that satisfies Equation (3.11) for a given pile diameter; values of  $y_{50}/B$  plotting to the left of this line are inadmissible and values plotting near the line indicate approximately elastic perfectly-plastic behavior that can result in numerical instability. The best-fit linear trend line passing through the *Phase2* results can be simplified to the following expression:

$$y_{50} = \frac{0.82p_{ult}}{K_e} \quad (3.14)$$

Equation (3.14) was used to define  $y_{50}$  for sand layers in this study.

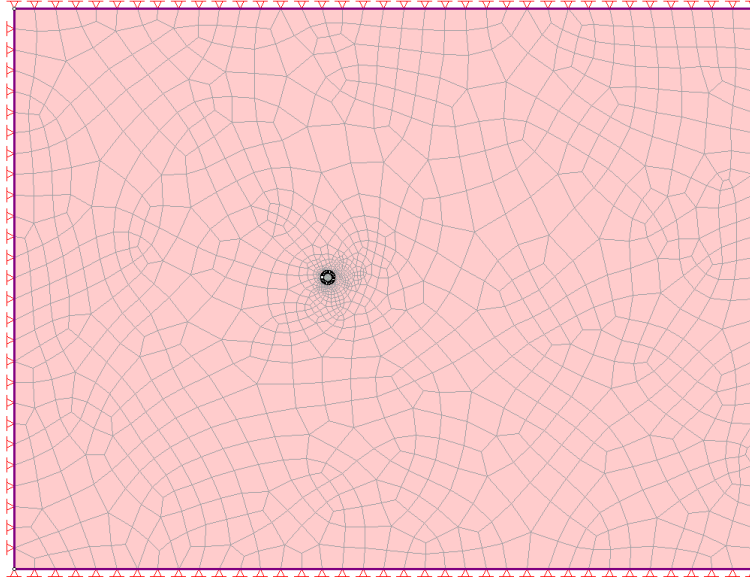


**Figure 3.9** *Phase2* finite element domain for plane-strain analyses of laterally loaded pile. The pile is displaced from left to right during the analyses.

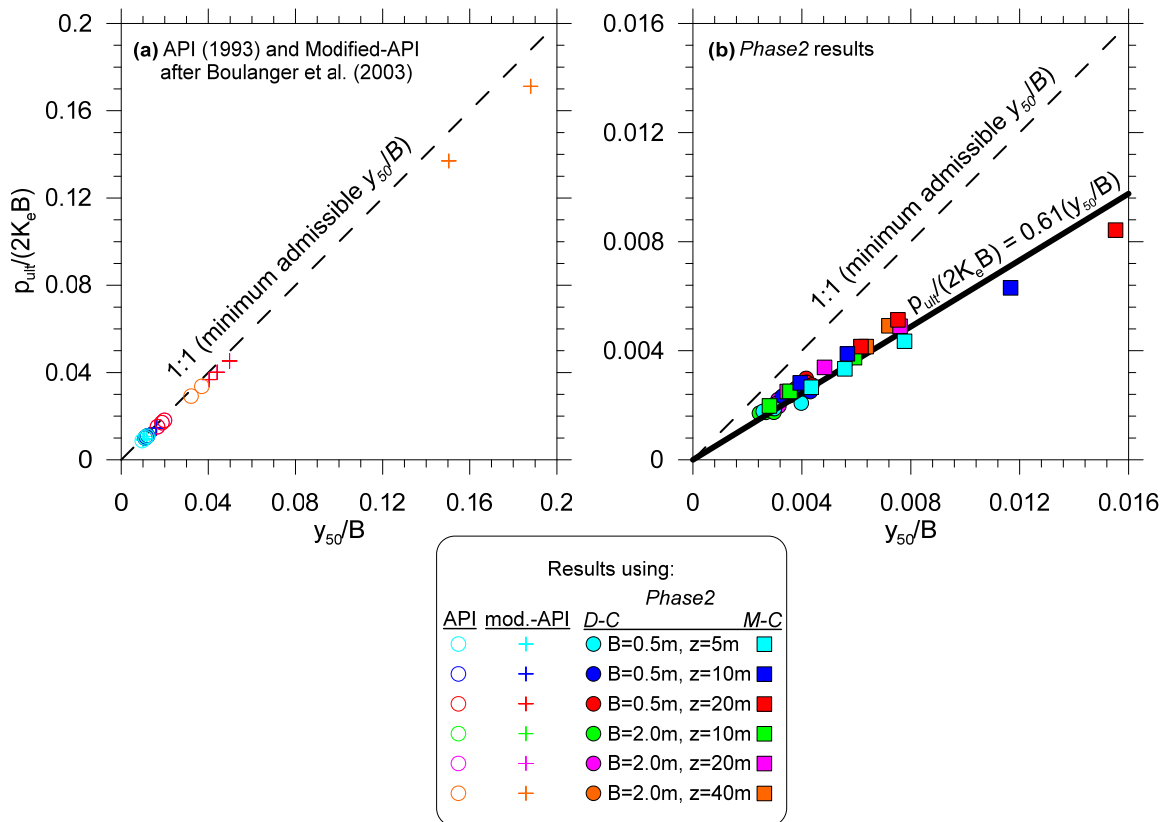


**Figure 3.10** Comparison of normalized  $y_{50}$  values using (a) existing  $p$ - $y$  relationships and (b) from results of plane-strain finite element simulations of laterally-loaded piles in *Phase2* using Duncan-Chang nonlinear-elastic (D-C) and Mohr-Coulomb (M-C) soil constitutive models.

### 3.4.4 Radiation Damping

As a pile vibrates, stress waves propagate or “radiate” away into the surrounding soil. This form of energy dissipation is known as radiation damping or alternatively as geometric damping because the radiated energy tends to attenuate with increasing propagation distance. For dynamic pile analyses using continuum elements, radiation damping is usually accounted for by using an energy-absorbing boundary that prevents incident stress waves from reflecting back into the domain (e.g., Lysmer and Kuhlemeyer [1969]). For Winkler-type analyses, if radiation damping is to be considered, it must be incorporated into the pile–soil interaction elements. Equivalent viscous damping, modeled through a rate-dependent viscous dashpot, is typically utilized for this purpose. The viscous dashpot component is characterized by a dashpot coefficient,  $c$ , which is defined as the ratio of the force in the dashpot  $p_{dashpot}$  to velocity  $dy/dt$ , i.e.:

$$p_{dashpot} = c \frac{dy}{dt} = c\dot{y} \quad (3.15)$$

The dashpot coefficient has units of  $[F][T][L]^{-1}$  or equivalent, such that when multiplied by a velocity a force results.

For Winkler-type analyses, the energy dissipation due to radiation damping can be thought of as additional soil resistance for a given amount of relative pile–soil displacement ( $y$ ) compared to the equivalent static or slow-monotonic loading case. Hence, a dynamic  $p$ - $y$  curve including radiation damping would be stiffer than the  $p$ - $y$  curve for the same pile and soil conditions undergoing static loading. This is depicted in Figure 3.11.

Supporting this concept, cyclic lateral load tests of a full-scale four-pile group in granular soil by McManus and Alabaster [2004] found an increase in dynamic stiffness of about 50% over the static stiffness, which they concluded was at least partially due to radiation damping effects. Ignoring radiation damping for dynamic loading conditions would therefore result in an underestimate of foundation stiffness and a corresponding overestimate of superstructure displacement and rotation. This may be a conservative design assumption for certain scenarios, but for the purpose of quantifying foundation input motions it could result in an unconservative overestimate of the kinematic pile–soil interaction effect since the stiffness contrast between the pile and soil is a dominant factor controlling the interaction. Indeed, even the pioneering work on pile dynamics (e.g., Novak [1974]) recognized the importance of radiation damping in forming an accurate solution.

Much of the previous research utilizing Winkler-type and continuum models for dynamic analysis of piles used equivalent-linear viscoelastic elements without a plastic component (e.g., Novak [1974], Kaynia and Kausel [1982], Gazetas and Dobry [1984a], Banerjee et al. [1987], and Fan et al. [1991]). Recognizing the importance of soil nonlinearity, especially for dynamic time domain analyses, other researchers have attempted to modify nonlinear  $p$ - $y$  relationships to include dynamic effects, including radiation damping. Matlock et al. [1978] proposed adding a viscous dashpot in parallel with existing static  $p$ - $y$  curves [Matlock 1970], perhaps the first attempt to explicitly capture dynamic effects with the nonlinear  $p$ - $y$  method. Nogami and Konogai [1988] formulated a dynamic  $p$ - $y$  element with separate near-field and far-field elements, where the nonlinear near-field element captured material hysteretic damping and the linear far-field element included a dashpot in parallel with a linear spring; a similar formulation has been adopted for the

*PySimple3* material as described above. Badoni and Makris [1996] and Bentley and El Naggar [2000] also performed analyses with viscous damping in parallel to the hysteretic  $p$ - $y$  response. However, Wang et al. [1998] demonstrated that this arrangement, which they term “parallel radiation damping”, can produce erroneous results because forces in the pile can effectively bypass the near-field hysteretic pile–soil interaction during high-velocity loading pulses by transmitting through the dashpot component directly to the far field. Wang et al. proposed that a more appropriate arrangement is “series radiation damping” in which a nonlinear near-field element accounts for elastic or elastoplastic interaction at the soil–pile interface and a separate far-field element, connected in series to the near-field element, captures radiation damping. This formulation satisfies the intuitive notion that lateral loads must mobilize a response in the zone immediately surrounding the pile before energy can be radiated away to the far field. The modified *PySimple3* element uses series radiation damping.

While the conceptual motivation for including radiation damping is clear, successful implementation is dependent on accurately quantifying the dashpot coefficients, which is nontrivial and unfamiliar in the realm of traditional foundation design. Engineers face two significant challenges when quantifying dashpots: (i) choosing an appropriate relationship from the many available in the literature, and (ii) addressing frequency-dependence.

Quantifying pile radiation damping based on experimental results is a difficult proposition, to say the least. While it is feasible to estimate the total damping of a pile–soil system during forced-vibration testing (e.g., Ashford and Juirnarongrit [2003]), this will include the combined effects of hysteretic damping in the pile and soil materials as well as radiation damping. While the former can be approximately inferred from material stress–strain curves if extensive instrumentation is used, there is no simple means for measuring radiation damping directly. Furthermore, even if the contribution of radiation damping to the total damping could be determined, there is an additional challenge in formulating the corresponding dashpot coefficients to be used with distributed springs and dashpots for Winkler-type analysis. Even if these results could be generated from a single test, there remains the issue of formulating generalized expressions for practical use. In light of these challenges, the available models for  $c$  are derived from a theoretical approach. Future experimental campaigns that are able to measure pile radiation damping more directly would be a valuable contribution to the field of pile dynamics.

Many researchers have used the theory of wave propagation in a linear viscoelastic medium to derive expressions for  $c$ . Berger et al. [1977] derived theoretical frequency-independent dashpot coefficients for a wave propagating in a one-dimensional elastic rod. Novak et al. [1978], expanding on the work of Novak [1974], developed a plane-strain solution based on a cylindrical elastic rod embedded in a viscoelastic half-space (Baranov’s solution). Gazetas and Dobry [1984a; 1984b] took a similar approach but assumed the rod was rigid and infinitely long, hence their expression does not include a pile modulus or length term. Makris and Gazetas [1992] proposed a simplified expression for  $c$  based on the results of the aforementioned studies and their own further analyses, and Kavvadas and Gazetas [1993] provided yet another expression with the same form as Gazetas and Dobry [1984a] but with slightly simplified coefficients. Nogami and Konagai [1988] approximated frequency-independent dashpot coefficients by calibrating the results of equivalent-linear viscoelastic time-domain BDWF analyses of a pile undergoing inertial head loading to frequency domain solutions. The relationship between normalized  $c$  and dimensionless frequency  $a_0$  [defined in this case using the Equation (1.5) definition] from these references are shown in Figure 3.12. Note that the Nogami and Konagai [1988] far-field element formulation is

actually a series of three elements; the value plotted in Figure 3.12 is the third and softest of the three dashpots. Note also that NIST [2012] Table 2-4b provides an impedance function for the equivalent pile head radiation damping to be used with the substructure method, but not dashpot coefficients for distributed Winkler-type springs for BDWF analyses.

The frequency-dependent models indicate a sharp increase in  $c$  at low frequencies, but an approximately constant value for  $a_0$  greater than about 0.5. While  $c$  may indeed be frequency-dependent, only frequency-domain solution approaches (e.g., Banerjee et al. [1987] and Wu and Finn [1997a]) can explicitly implement such behavior. For time-domain solutions, which are used for this study and are the predominant method used for structural and geotechnical nonlinear analyses, it is necessary to specify a single value of  $c$  for the entire duration of the analysis. To do so, the foundation designer can either: (1) choose a representative frequency, such as the fundamental frequency of the pile–soil system to be used with a frequency-dependent expression for  $c$ ; or (2) use a frequency-independent expression for  $c$ . Researchers that have made an effort to develop and evaluate nonlinear time-domain solution approaches for laterally-loaded piles tend to favor the latter, while those that have focused on developing analytical solutions can accommodate frequency dependence.

Using a computer implementation of the plane-strain solutions of Novak et al. [1978], Novak et al. [1983] found an approximately linear relationship between pile damping and increasing frequency above the fundamental frequency of the soil profile. They concluded that a constant value of  $c$  can be used to represent equivalent viscous radiation damping at frequencies above the profile fundamental frequency, and that below this frequency only the soil hysteretic damping (also referred to as “material” damping) was significant. Gazetas [1991] and Syngros [2004] also proposed that radiation damping only be considered above a dimensionless “cutoff frequency” defined as:

$$a_{0,CUTOFF} = \frac{\omega_s B}{V_s} = \frac{2\pi \left( \frac{V_s}{4H} \right) B}{V_s} = \frac{\pi B}{2H} \quad (3.16)$$

where  $B$  is pile diameter, and  $\omega_s$  is the natural angular frequency of the site, based on the natural site period  $T$  computed from the well-known formula relating one-quarter wavelength of a harmonic oscillation to the thickness of the soil profile  $H$ :

$$K_0 = 1 - \sin \phi' \quad (3.17)$$

where  $V_s$  is the soil shear-wave velocity. The fundamental frequency of the site is the inverse of Equation (3.17).

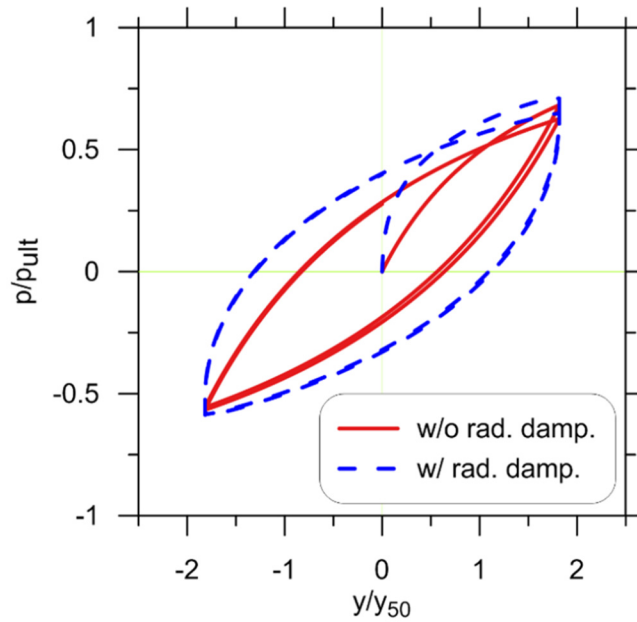


**Figure 3.11** Effect of radiation damping in *PySimple3* material.

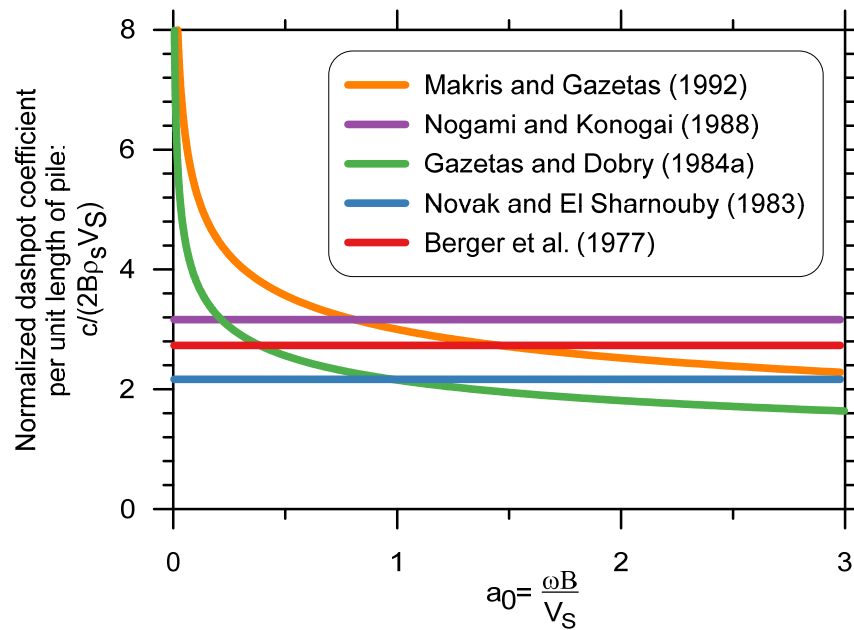


**Figure 3.12** Normalized dashpot coefficient for  $\nu = 0.25$  m,  $\rho_s = 1.7$  Mg/m<sup>3</sup> and  $E_p/E_s \approx 690$ .

The concept that pile radiation damping cannot occur at frequencies below the site fundamental frequency only applies for an elastic pile embedded in an elastic soil layer underlain by rigid bedrock, which is hardly representative of realistic soil conditions. In this author's opinion, this limitation can safely be ignored for realistic conditions.

The approach taken for this study is to define the dashpot coefficient using the Gazetas and Dobry [1984a] relationship at the frequency corresponding to the dimensionless frequency  $\omega/\lambda V_s$

= 1.25. This value approximately corresponds to  $H_u = 0.5$  for the elastic analytical solutions (e.g., see Figure 2.3), and as will be shown in the next chapter, for the nonlinear analyses as well. The frequency corresponding to a 50% reduction in free-field motions was chosen because the purpose of this study is to define the conditions for which kinematic pile–soil interaction is significant and especially to identify the frequency range over which significant de-amplification of free-field motions could occur.

In addition to radiation and hysteretic damping, Rayleigh damping was used in the *OpenSees* analyses to achieve damping at low strains. Unlike hysteretic damping or the type of radiation damping discussed above that are incorporated into the material model, Rayleigh damping operates directly on the mass and stiffness matrices in the formulation of the equation of motion that is solved in the finite-element method. Since soil is known to exhibit damping even at the smallest levels of measurable strain (e.g., Vucetic and Dobry [1991]), incorporating small-strain damping is realistic, and is also computationally beneficial for achieving convergence.

### 3.5 PILE MODELING

For the present study, piles are modeled using 0.5-m-long displacement-based beam–column elements. Pile nonlinearity is considered by using an equivalent  $EI$  representative of a reduced moment of inertia due to concrete cracking. The following subsections describe specific aspects of the structural modeling approach.

#### 3.5.1 Pile Moment-Curvature Behavior

Reinforced-concrete elements exhibit nonlinear moment-curvature ( $M-\phi$ ) behavior when flexural demands exceed the yield strength of either the concrete or reinforcing steel in tension or compression. Of greatest interest in the context of a laterally-loaded pile is the reduction in stiffness that occurs when concrete cracks in tension since flexural demands during extreme event loading would typically be expected to exceed the cracking moment. As illustrated in Figure 3.13, the initial portion of the  $M-\phi$  curve corresponds to linear-elastic material behavior across the entire section. Because the slope of a  $M-\phi$  curve is the flexural rigidity of the section, the slope of the elastic region corresponds to the elastic  $E_p I_p$  computed using the gross moment of inertia of the section. The upper bound of the elastic region is defined by cracking of the concrete in tension, which is typically the first nonlinear material behavior. In accordance with §5.6.1.1 of the Caltrans [2013] *Seismic Design Criteria*, this study defined the cracked section stiffness by the secant slope of the  $M-\phi$  plot between the origin and the moment corresponding to the first yielding of the longitudinal reinforcing steel in tension,  $M_y$ .

For the generalized transfer function and spectral ratio prediction models generated from the results of this study, flexural rigidity of the pile is an input variable. Whether or not the value used should correspond to the elastic or cracked section stiffness depends on the anticipated behavior under design loading, and the foundation engineer is responsible for making this decision.

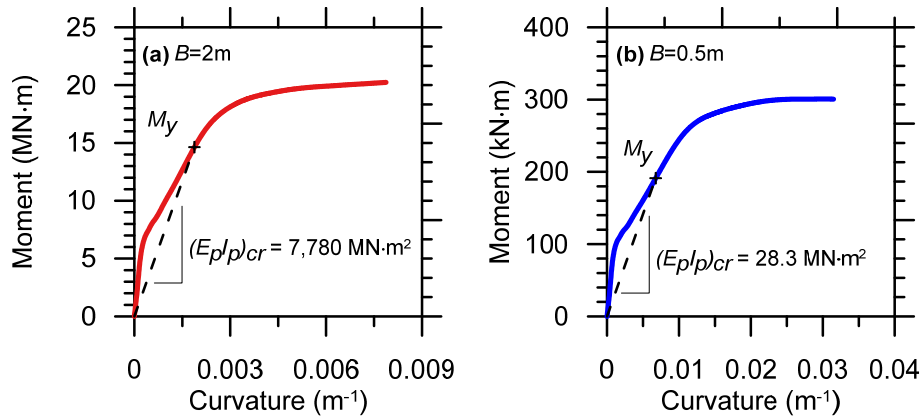


**Figure 3.13** Moment curvature analyses conducted at axial load  $P = 0.05 \cdot A_g \cdot f'_c$  for (a) 2-m- and (b) 0.5-m-diameter pile sections.

The  $M-\phi$  plots shown in Figure 3.13 were computed using fiber models of the 2-m- and 0.5-m-diameter pile sections in *OpenSees*. In the fiber-modeling approach, the section is discretized into separate zones (fibers) characterized by unique uniaxial stress–strain behavior representative of, e.g., reinforcing steel, confined concrete, and unconfined concrete. Radial discretization is used to define the circular cross sections. The following assumptions and analysis parameters were used for the  $M-\phi$  analyses:

- The longitudinal reinforcing steel layout was based on a target steel ratio ( $\rho_{steel}$ ) of 1.5%, with the following layouts used for the analyses:
  - For the 2-m-diameter shaft, 32 No. 14 bars bundled in groups of two (to achieve adequate spacing between adjacent bars) with 6 in. (15.2 cm) of clear cover— $\rho_{steel} = 1.48\%$ .
  - For the 0.5-m-diameter shaft, 8 No. 7 bars with 3 in. (7.6 cm) of clear cover— $\rho_{steel} = 1.58\%$ .
- Clear-cover from the edge of the pile to the edge of the longitudinal bars is based on the recommendations in the FHWA drilled shaft design manual [Brown et al. 2010] based on the diameter of the pile.
- Assumed concrete compressive strength of 5 ksi (34.5 MPa) modelled with the *ConcreteCM* uniaxial material model in *OpenSees*.
- Grade 60 steel for the longitudinal bars modelled using the *ReinforcingSteel* uniaxial material model with expected material properties (i.e., accounting or overstrength in accordance with the Caltrans [2013] Seismic Design Criteria).
- Confinement of the core concrete was not considered, where the core is the portion of the section inside the perimeter formed by the longitudinal bars. Because confined and unconfined concrete exhibit similar stress–strain behavior up to point of crushing of the unconfined concrete in compression, the effect on the  $M-\phi$  behavior is only significant in the post-yield range.
- The number of discrete fibers was increased until the results were stable, which was achieved with 24 radial and 24 angular divisions within the core of the

section and four radial and 24 angular divisions outside the core for the cover concrete.

- Analysis were performed for an axial load  $P$  equal to 5% of the gross compressive capacity of the concrete section, i.e.,  $P = 0.05 * A_g * f'_c$ .

The axial load imposed on a pile is a function of the tributary load supported by each bridge bent, the number and layout of piles relative to the number of columns or pier walls per bent, geotechnical conditions over the length of the pile, whether axial or lateral loads govern the pile diameter, and many other factors. In addition, the pile axial load is likely to fluctuate during an earthquake as bents undergo frame action, and the axial load changes over the depth of the pile as load is shed into or added from the ground. Clearly there is no unique definition for a “typical” axial load for a pile foundation based solely on the section diameter. As discussed above, the axial load used to define the effective flexural rigidity for design cases should be based on the actual anticipated axial load during extreme event loading. In the absence of such information for the parametric analyses performed for this study, the arbitrary definition of  $P = 0.05 * A_g * f'_c$  was adopted for simplicity, which is consistent with the typical axial load for RC columns and is therefore a good approximation for extended-shaft column type foundations.

### 3.5.2 Pile Head Fixity Condition

The pile head-fixity conditions used in this study are either “fixed-head”—perfectly fixed against rotation, or “free-head”—completely free to rotate without encountering any rotational resistance. While these idealized assumptions are conceptually attractive and convenient for analytical purposes, the pile-head boundary condition in a real structure falls somewhere between the two extremes.

Piles embedded in a reinforced pile cap or interconnected with stiff grade beams are often characterized as fixed head, which implies that an imposed moment will result in zero rotation at the connection. However, the true rotational stiffness of these connections is less than rigid. Rotation at the connection could be accommodated either on a global or local scale, for example by rocking of the entire pile cap or by strain concentrated in the zone around the connection, respectively. Short of experimental measurements or continuum numerical modeling, the author is not aware of any geotechnical or structural references that provide general guidance on quantifying this rotational stiffness. However, previous experience by the author has shown that while allowing a small amount of rotation at the pile head in BNWF analyses can significantly decrease moment demands, it does not have a significant influence on the pile head horizontal translation. Hence, use of a less-than-rigid boundary condition would not be expected to significantly change transfer functions computed for free-field versus pile-head horizontal displacement.

For conventional foundation design applications in which superstructure loads are carried through the foundation into the ground, a free-head assumption is reasonable for extended-shaft columns (i.e., the “flagpole” condition) or for piles that lack significant embedment or structural anchorage into a pile cap. However, for the kinematic pile–soil interaction case, it is important to remember that the load path acts in the opposite direction—ground movement results in foundation displacements and force effects that are subsequently imposed on the base of the superstructure. Hence, the pile-head fixity condition should be assessed in terms of the following question: *What*

*resisting force/moment would be mobilized in above-ground structural elements due to a unit displacement/rotation at the pile head?* For extended-shaft columns, pile head rotation due to kinematic interaction would encounter resistance as the resulting rotation and corresponding moment and translations are carried up the column, through the column-to-superstructure connection (e.g., bearings and/or other anchorage between the bent cap and girders), and into the superstructure. Clearly these elements would provide some resistance to rotation such that the pile head is not truly “free” to rotate.

Despite these inconsistencies between real behavior and the idealized extremes, fixed- and free-head boundary conditions will be used for this study for several reasons. First, these extremes provide bounds on the problem. The true behavior is somewhere in between, and the foundation designer can use judgment to interpret where in between these bounds their problem lies or simply use whichever assumption results in greater demands. The latter approach is advocated in the realm of conventional deep foundation design for lateral loading by Reese et al. [2005]. Second, the rotational resistance provided by pile-to-pile-cap connections and other above-ground structural elements depends on the specific geometry and material properties of each project; thus, it is hard to generalize in a simplified design tool such as the transfer function models being developed for the present study. Finally, because free-head or fixed-head boundary conditions are the standard of practice for routine design, and because there are no established guidelines for quantifying rotational resistance, including rotational stiffness as a parameter in the transfer function model would make the model more difficult to implement in practice. Given that the intent of this study is to provide a transfer function model that is compatible with the current state of practice for seismic design, such a limitation would be counterproductive. Future studies could investigate the influence of head-fixity through parametric analysis of varying rotational spring stiffness applied at the pile head.

### **3.5.3 Pile Shear Deformations**

Conventional beam-on-Winkler-foundation analyses treat the pile as an Euler-Bernoulli beam, for which flexural demands are resisted structurally by the flexural rigidity ( $EI$ ) of the pile (see derivation in §2.1). Shear deformations are neglected in this approach, which is a reasonable assumption when it is kinematically possible for the pile to respond to imposed demands primarily in flexure, such as for the “flagpole” configuration. However, significant rotational resistance provided by embedment into a pile cap or toe embedment into rock may result in shear deformations that are significant within a few pile diameters of the point of rotational restraint. For example, Massone and Lemnitzer [2012] found that shear deformations accounted for up to 40% of total horizontal displacement near the pile head connection during full-scale lateral load tests of 24-in.- (0.61-m-) diameter piles. Moreover, when flexural demands approach the pile plastic moment capacity, these shear deformations can be nonlinear in terms of the shear–stress versus shear–strain behavior even when shear stresses are well below the shear strength of the concrete (e.g., Massone and Wallace [2004]), which further complicates interpretation of load test results. The Massone and Lemnitzer study along with follow-up work by Khalili-Tehrani et al. [2014] suggests that commonly used semi-empirical  $p$ - $y$  curve models derived from free-head lateral load test results (e.g., API [1993]) are inaccurate for fixed-head conditions because shear deformations were not considered explicitly in their derivation.

For the case of kinematic pile–soil interaction for fixed-head piles, using a numerical model that allows shear deformations would be expected to result in slightly larger total displacement near the pile head and thus would increase transfer function ordinates ( $H_u$ ) relative to the same case analyzed without consideration of shear deformations, such as done herein. However, simply using a structural model that accounts for shear deformations, such as the Timoshenko beam column element in *OpenSees*, or the recently added cyclic shear-flexure interaction model by Kolozvari et al. [2015a, b], could provide misleading results. This is because, as determined from the experimental work described above, alternative  $p$ - $y$  curves should be used in combination with structural consideration of shear deformations, and a generalized  $p$ - $y$  model for this purpose is not currently available. A future study that integrates the Kolozvari et al. cyclic shear-flexure interaction elements and  $p$ - $y$  curves that explicitly consider shear deformations into the numerical modeling framework used for the present study could shed light on the influence of shear-flexure interaction for kinematic transfer functions.

### 3.5.4 Pile Groups

Pile groups were modeled as multiple individual piles connected at their heads through massless rigid links using the *equalDOF* command in *OpenSees*. Pile caps were not modelled explicitly because their mass and stiffness would result in inertial and kinematic interaction in addition to the pile–soil interaction. The rigid link between piles combined with a fixed-head pile boundary condition essentially captures the restraint offered by the pile cap without introducing additional SSI, such that pile–soil interaction can be studied independently. In real systems utilizing pile groups, the pile cap motion, which excites the superstructure, depends on kinematic pile–soil interaction as well as kinematic interaction between the pile cap and the ground. For example, an embedded pile cap is subjected to ground motions imposed through lateral earth pressure on its sides, horizontal motions imposed on its base, and the motions of the piles which it connects. Depending on the surficial soil stiffness and the pile cap dimensions, particularly the depth of embedment, the pile cap motion could be dominated by cap–soil interaction more than pile–soil interaction. Future studies could investigate this effect by explicitly modeling pile caps in addition to piles.

The pile group layout considered for the present study is for a  $2 \times 3$  group of 2-m-diameter piles on a 7.5-m center-to-center spacing (i.e.,  $3.75 \cdot B$ ) as shown in Figure 3.14. This configuration is typical for support of large bridge bents, and use of  $B = 2$ -m piles allows for direct comparison to the 2-m single pile results. The incoherent ground motions discussed below in §3.7.3 were imposed on the piles such that each pile in the group experienced a different input motion. The motion at each pile head is identical because of the rigid links and effectively is an average of the motions imposed on the individual piles, which is similar to the concept of base slab averaging. Additional group configurations were not considered because of the considerable effort required to generate incoherent ground motions at each pile location as well as the significant computational demand for running dynamic group analyses.

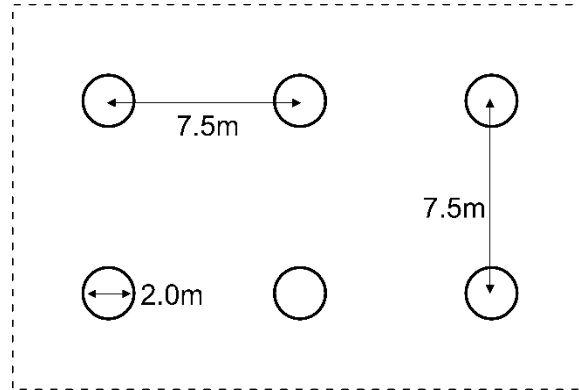


Figure 3.14 Pile-group layout considered for analyses.

### 3.6 SOIL PROFILES FOR ANALYSES

Six soil profiles were developed based on cone penetration test (CPT) soundings. The purpose of developing soil profiles from real sites rather than using simple fictitious homogeneous or layered models such as those used in past studies is to examine the effect that realistic subsurface variability has on the results. Soil stiffness, quantified by the time-averaged shear-wave velocity in the upper 30 m of the profile ( $V_{S30}$ ), ranges between about 100 and 400 m/sec for the six soil profiles. These bounds are intended to capture the range of soil stiffness over which kinematic pile–soil interaction is likely to be significant as suggested by the elastic solutions presented in the previous chapter. Likewise, for a given pile stiffness, the range is intended to extend to high enough soil stiffness such that the conditions for which kinematic interaction is no longer significant can be defined.

The CPT data used to develop the six soil profiles was obtained from the United States Geological Survey (USGS) research division’s repository of CPT data, available online (<http://earthquake.usgs.gov/research/cpt/>). As indicated by the shear-wave velocity profiles in Figure 3.15, sites were chosen that showed relatively uniform gradients of shear-wave velocity versus depth in order to avoid the large shear demands that are imposed on piles at such an impedance contrast. Sites 1, 2, and 4 contain a combination of granular and cohesive layers, Sites 3 and 6 are all granular, and Site 5 is all stiff clay. Layer thicknesses and relevant soil properties for each of the six sites are presented in Appendix A. A general description is also provided of the real sites that are represented, including their inferred geologic history and depositional environment. In general, the profiles were discretized into 0.5-m-thick layers to match the discretization of pile elements so that input displacement time series could be computed from ground response analysis without interpolation.

The arbitrary metric  $V_{S30}$  was used as a convenient measure of the site stiffness and because of its familiarity in practice (e.g., for building code site classifications); as will be shown in the results chapter, shear-wave velocity computed over the length of the pile is more relevant for describing pile–soil interaction. Table 3.2 gives values of time-averaged  $V_S$  computed over depth intervals corresponding to the four pile lengths from Table 3.1, denoted as  $V_{S,z}$ , where  $z$  is the depth increment over which the computation is made. When not referring to a specific pile length, this term will subsequently be denoted by the variable  $V_{S,L}$ .

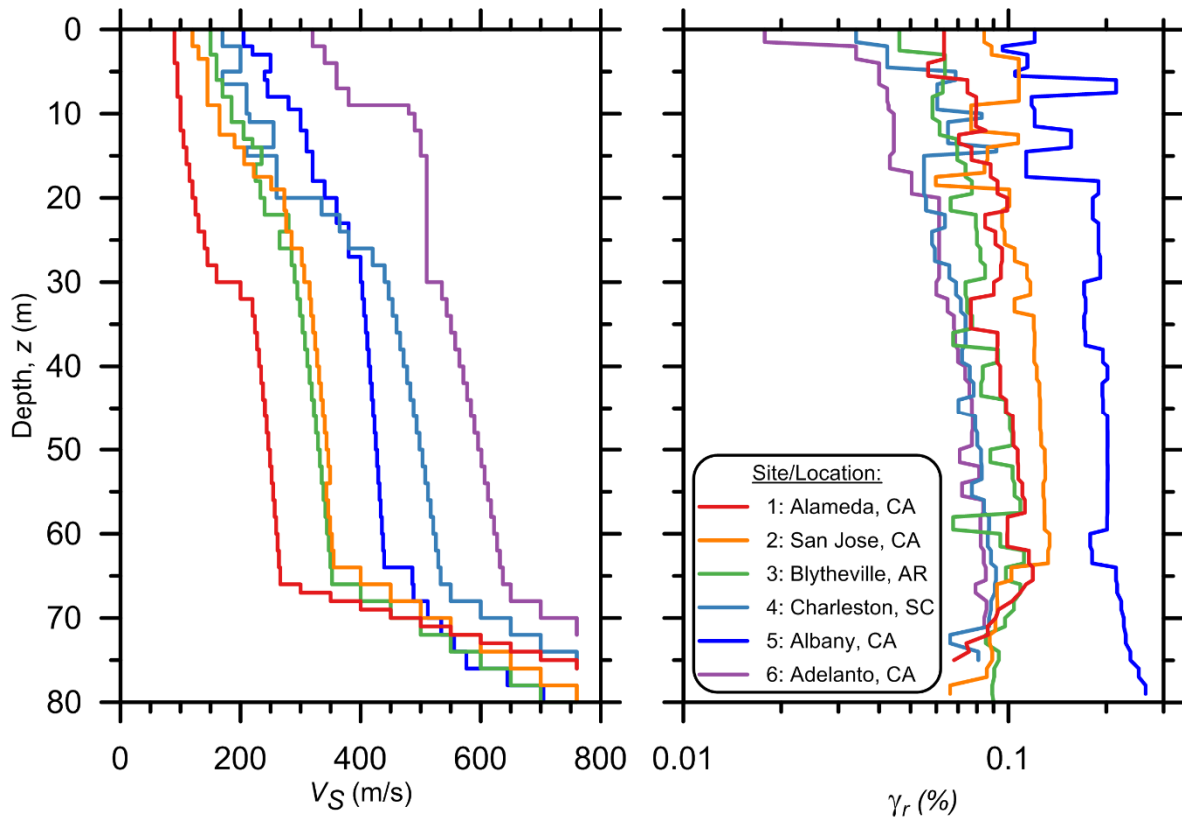


**Figure 3.15** Shear-wave velocity and reference strain ( $\gamma_r$ ) profiles for Sites 1–6.

**Table 3.2** Site time-averaged shear-wave velocity characteristics for Sites 1–6.

Site:	1	2	3	4	5	6
$V_{S7.5}$ (m/sec)	92	134	158	186	230	344
$V_{S15}$ (m/sec)	97	150	176	204	259	396
$V_{S30}$ (m/sec)	111	192	217	264	305	446
$V_{S60}$ (m/sec)	151	244	253	332	351	504
$V_{SH}$ (m/sec)	173	280	289	367	383	525
Thickness (H, m)	76.0	80.0	82.0	76.0	80.0	72.00

### 3.7 GROUND MOTIONS

#### 3.7.1 Baker et al. [2011] Ground Motion Suite

Input motions for the ground response analyses were sourced from the collection of motions developed by Baker et al. [2011] for PEER Transportation Research Program projects. Multiple

sets of motions are included in the Baker et al. set; for this study the “*Set #2, broad-band ground motions corresponding to M 7.0, R [source-to-site distance] = 10 km, and rock conditions*” were used. These motions are specifically intended to represent rock conditions with an average  $V_S$  of 760 m/sec for use in ground response analysis, and were selected by Baker et al. such that the median and  $\pm$  standard deviation response spectra computed from the 40 unscaled motions match the Boore and Atkinson [2008] ground-motion prediction equations. A basic description of the motions is provided in Table 3.3, and Table 3.4 lists their peak ground acceleration, velocity, and displacement (PGA, PGV, and PGD) values. Table 3.5 lists minimum, maximum, and mean PGA/PGV/PGD for the 40 motions, showing that the set covers a wide range in terms of these intensity measures. For each motion, a fault-normal (FN), fault-parallel (FP), and vertical record are available. The FN component of each ground motion was used for this study, which on average is slightly stronger than the FP component. Further details of the motions are available in the Baker et al. report.

**Table 3.3 Ground-motion records used for analyses (after Baker et al. [2011]).**

<b>Record No.</b>	<b>NGA Record Sequence No.</b>	<b>Earthquake Name</b>	<b>Year</b>	<b>Station</b>	<b>Magnitude</b>	<b>Closest Distance</b>
1	72	San Fernando	1971	Lake Hughes #4	6.6	25.1
2	769	Loma Prieta	1989	Gilroy Array #6	6.9	18.3
3	1165	Kocaeli, Turkey	1999	Izmit	7.5	7.2
4	1011	Northridge-01	1994	LA - Wonderland Ave	6.7	20.3
5	164	Imperial Valley-06	1979	Cerro Prieto	6.5	15.2
6	1787	Hector Mine	1999	Hector	7.1	11.7
7	80	San Fernando	1971	Pasadena - Old Seismo Lab	6.6	21.5
8	1618	Duzce, Turkey	1999	Lamont 531	7.1	8.0
9	1786	Hector Mine	1999	Heart Bar State Park	7.1	61.2
10	1551	Chi-Chi, Taiwan	1999	TCU138	7.6	9.8
11	3507	Chi-Chi, Taiwan-06	1999	TCU129	6.3	24.8
12	150	Coyote Lake	1979	Gilroy Array #6	5.7	3.1
13	572	Taiwan SMART1(45)	1986	SMART1 E02	7.3	-
14	285	Irpinia, Italy-01	1980	Bagnoli Irpinio	6.9	8.2
15	801	Loma Prieta	1989	San Jose - Santa Teresa Hills	6.9	14.7
16	286	Irpinia, Italy-01	1980	Bisaccia	6.9	21.3
17	1485	Chi-Chi, Taiwan	1999	TCU045	7.6	26.0
18	1161	Kocaeli, Turkey	1999	Gebze	7.5	10.9
19	1050	Northridge-01	1994	Pacoima Dam (downstr)	6.7	7.0
20	2107	Denali, Alaska	2002	Carlo (temp)	7.9	50.9
21	1	Helena, Montana-01	1935	Carroll College	6.0	-
22	1091	Northridge-01	1994	Vasquez Rocks Park	6.7	23.6
23	1596	Chi-Chi, Taiwan	1999	WNT	7.6	1.8
24	771	Loma Prieta	1989	Golden Gate Bridge	6.9	79.8
25	809	Loma Prieta	1989	UCSC	6.9	18.5
26	265	Victoria, Mexico	1980	Cerro Prieto	6.3	14.4
27	1078	Northridge-01	1994	Santa Susana Ground	6.7	16.7
28	763	Loma Prieta	1989	Gilroy - Gavilan Coll.	6.9	10.0
29	1619	Duzce, Turkey	1999	Mudurnu	7.1	34.3
30	957	Northridge-01	1994	Burbank - Howard Rd.	6.7	16.9
31	2661	Chi-Chi, Taiwan-03	1999	TCU138	6.2	22.2
32	3509	Chi-Chi, Taiwan-06	1999	TCU138	6.3	33.6
33	810	Loma Prieta	1989	UCSC Lick Observatory	6.9	18.4
34	765	Loma Prieta	1989	Gilroy Array #1	6.9	9.6
35	1013	Northridge-01	1994	LA Dam	6.7	5.9
36	1012	Northridge-01	1994	LA 00	6.7	19.1
37	1626	Sitka, Alaska	1972	Sitka Observatory	7.7	34.6
38	989	Northridge-01	1994	LA - Chalton Rd	6.7	20.5
39	748	Loma Prieta	1989	Belmont - Envirotech	6.9	44.1
40	1549	Chi-Chi, Taiwan	1999	TCU129	7.6	1.8

**Table 3.4 Intensity measures for ground-motion set.**

<b>Record number</b>	<b>Earthquake name</b>	<b>Year</b>	<b>Magnitude</b>	<b>PGA (g)</b>	<b>PGV (m/sec)</b>	<b>PGD (m)</b>
1	San Fernando	1971	6.6	0.15	0.08	0.02
2	Loma Prieta	1989	6.9	0.16	0.17	0.06
3	Kocaeli, Turkey	1999	7.5	0.15	0.23	0.10
4	Northridge-01	1994	6.7	0.16	0.11	0.03
5	Imperial Valley-06	1979	6.5	0.15	0.18	0.08
6	Hector Mine	1999	7.1	0.34	0.37	0.14
7	San Fernando	1971	6.6	0.09	0.07	0.01
8	Duzce, Turkey	1999	7.1	0.16	0.13	0.08
9	Hector Mine	1999	7.1	0.07	0.07	0.03
10	Chi-Chi, Taiwan	1999	7.6	0.20	0.41	0.36
11	Chi-Chi, Taiwan-06	1999	6.3	0.34	0.17	0.06
12	Coyote Lake	1979	5.7	0.45	0.52	0.07
13	Taiwan SMART1(45)	1986	7.3	0.13	0.13	0.05
14	Irpinia, Italy-01	1980	6.9	0.19	0.29	0.10
15	Loma Prieta	1989	6.9	0.27	0.26	0.13
16	Irpinia, Italy-01	1980	6.9	0.12	0.18	0.11
17	Chi-Chi, Taiwan	1999	7.6	0.60	0.44	0.38
18	Kocaeli, Turkey	1999	7.5	0.24	0.52	0.44
19	Northridge-01	1994	6.7	0.50	0.49	0.06
20	Denali, Alaska	2002	7.9	0.09	0.10	0.05
21	Helena, Montana-01	1935	6.0	0.15	0.06	0.01
22	Northridge-01	1994	6.7	0.16	0.18	0.02
23	Chi-Chi, Taiwan	1999	7.6	0.96	0.69	0.31
24	Loma Prieta	1989	6.9	0.14	0.29	0.07
25	Loma Prieta	1989	6.9	0.37	0.12	0.06
26	Victoria, Mexico	1980	6.3	0.63	0.31	0.13
27	Northridge-01	1994	6.7	0.23	0.14	0.03
28	Loma Prieta	1989	6.9	0.29	0.31	0.07
29	Duzce, Turkey	1999	7.1	0.11	0.10	0.09
30	Northridge-01	1994	6.7	0.11	0.08	0.02
31	Chi-Chi, Taiwan-03	1999	6.2	0.13	0.20	0.04
32	Chi-Chi, Taiwan-06	1999	6.3	0.06	0.09	0.04
33	Loma Prieta	1989	6.9	0.41	0.18	0.05
34	Loma Prieta	1989	6.9	0.43	0.39	0.07
35	Northridge-01	1994	6.7	0.58	0.77	0.20
36	Northridge-01	1994	6.7	0.38	0.22	0.05
37	Sitka, Alaska	1972	7.7	0.10	0.07	0.05
38	Northridge-01	1994	6.7	0.19	0.19	0.02
39	Loma Prieta	1989	6.9	0.14	0.20	0.06
40	Chi-Chi, Taiwan	1999	7.6	1.01	0.60	0.51

**Table 3.5 Summary of ground-motion intensity measures.**

Value	PGA (g)	PGV (m/sec)	PGD (m)
Minimum	0.06	0.06	0.01
Maximum	1.01	0.77	0.51
Mean	0.28	0.25	0.11

### 3.7.2 Ground Response Analyses

To define the free-field ground motion at the  $p$ - $y$  spring depths for the BDNWF models, each of the 40 motions was propagated through a one-dimensional ground response analysis model in the program *DEEPSOIL* [Hashash et al. 2015]. *DEEPSOIL* analyses were conducted using the nonlinear time-domain total stress method. Using the idealized profiles for each of the six sites presented in Appendix A, modulus reduction and damping curves were developed using the procedures of Menq [2003] and Darendeli [2001] for granular and cohesive materials, respectively. The “hybrid” procedure recommended by Yee et al. [2013] was used to ensure that the modulus reduction curves matched the inferred shear strength of the material at large strains, although strains approaching these levels were generally not mobilized during the analyses. Profiles of reference strain  $\gamma_r$  for the modulus reduction curves are shown alongside the  $V_S$  profiles in Figure 3.15. The reference strain corresponds to 50% modulus reduction (i.e.,  $G/G_{max} = 0.5$ ) and thus is a good proxy for the amount of nonlinearity exhibited by the material; smaller values indicate that the soil will exhibit greater nonlinearity at small strains.

As described above, the idealized site stratigraphy is based on real CPT data to the approximate maximum depth of the CPT sounding, typically between 30 and 40 m. Below this depth, additional layers were added to the profile to create a gradual transition to the elastic bedrock. This was done so that the input motions, which are representative of outcrop motions on rock with an average  $V_S = 760$  m/sec, would not encounter a strong impedance contrast at the base of the profiles.

The following options were used for the *DEEPSOIL* analyses:

- Pressure-dependent modified Kodner-Zelesko nonlinear backbone formulation [Matasovic 1993] with non-Masing unloading/reloading formulation.
- Input motions specified as outcrop motions.
- Elastic half-space (bedrock) with  $V_S = 760$  m/sec and unit weight  $22 \text{ kN/m}^3$  underlying the soil profiles.
- Frequency-independent damping formulation.
- When needed to achieve convergence, sub-stepping of time increments using linear interpolation of input motion with maximum strain increment of 0.005.

Acceleration time series computed from *DEEPSOIL* for each layer were manually post-processed to generate displacement records, which are needed as the input to the soil nodes of the  $p$ - $y$  springs for the *OpenSees* analyses. Performing the integration necessary to compute

displacement from acceleration time series, whether executed in the time or frequency domain, is a nontrivial exercise that can result in spurious amplification of low-frequency noise if proper filtering procedures are not implemented. Recent versions of *DEEPSOIL* offer the option to export displacement records computed during direct integration of the equation of motion, but no filtering was applied to these records.

For this study, high-pass filtering was applied to remove low-frequency noise using a third-order Butterworth filter at frequencies above about 0.1–0.2 Hz. To remove spurious high-frequency noise, the motions were also filtered using a low-pass Butterworth filter at the higher of (i) the low-pass frequency used for the original PEER ground motion processing or (ii) the maximum frequency that could be propagated through the *DEEPSOIL* model, which depends on thickness and shear-wave velocity of the layers. In most cases the low-pass frequency used for the original PEER ground motion processing was higher, so this was used for the low-pass filtering. In addition, the acceleration time series were baseline corrected and zero-padded at the beginning and end of each record. The transition between a displacement of zero and the computed displacement was achieved with a cosine filter over 20 time increments; failure to do so can result in significant low-frequency noise even if the beginning and end displacements have relatively small amplitudes. The fundamental frequency of each site as computed by *DEEPSOIL* is given in Table 3.6.

**Table 3.6 Site fundamental frequencies.**

Site:	1	2	3	4	5	6
Site fundamental frequency $f_s$ (Hz)	0.57	0.87	0.88	1.21	1.20	1.82

### 3.7.3 Ground Motion Incoherence

Real ground motions exhibit incoherence, or variation between two physical locations because of two effects: (i) the wave-passage effect, which for inclined waves simply characterizes the delay in arrival time of a uniform planar wave front between two locations; and (ii) “stochastic” incoherence, which is due to the inherent spatial variability of the ground motion itself since earthquake ground motions are generated not at a single point but along a heterogeneous fault, and from the scattering of waves due to material heterogeneity at the site. Abrahamson and Youngs [1992a] and others have demonstrated that this can have important consequences for SSI.

Because *DEEPSOIL* performs one-dimensional ground response analysis assuming vertically-propagating shear waves, the only component of incoherence that is captured is the influence of changing soil properties with depth; the wave passage effect and stochastic incoherence are not captured. For a single pile foundation, this is acceptable. For pile groups, however, ground-motion incoherence results in different motion being imposed on each pile within the group. Much like the concept of base-slab averaging for shallow and mat foundations, the response of a stiff pile cap represents an average of the motions imposed on each pile within the group.

To capture ground motion incoherence in the horizontal direction for the pile group simulations in this study, spatially-variable ground motions (SVGM) were generated using the program *FDW2D.r*, which is based on a simulation routine described by Ancheta and Stewart [2015]. Starting with one of the 40 input motions as a “seed” motion corresponding to a corner pile location within the pile group shown in Figure 3.14, a motion was generated at each of the five remaining pile locations that matches a set of target spatially variable ground-motion (SVGM) functions. Dr. Timothy Ancheta was hired as a sub-consultant for this project to generate the incoherent motions, and the following is a summary of his work.

The basic process of simulating an incoherent motion is to modify a seed ground motion by adding a random phase and amplitude at each frequency to match target coherency and amplitude models that are consistent with empirical observations. Additionally, for the method used here, the coherency between the seed-to-simulation and simulation-to-simulation matches the target coherency function for all locations simultaneously. The *FDW2D.r* simulation method uses an energy randomization process called Frequency Dependent Windowing (FDW). The FDW method is used to conserve the low-frequency (coherent) energy and resample the high-frequency (random) energy to be consistent with a set of SVGM functions without introducing unwanted spectral leakage.

The FDW method is a non-stationary simulation routine that utilizes a modified short-time Fourier transform (MSFT) routine. The MSFT routine allows preservation of the non-stationary properties of the motion and incorporation of time-varying nonlinear spectral modifications. The routine is summarized in the following steps:

- The seed time series is split into short time segments.
- A discrete Fourier transform (DFT) is performed on the segment.
- Phase angles at each frequency within a desired frequency range (dependent on segment length) are modified consistent to a coherency function for each segment (this procedure is fully described in Ancheta [2010]).
- The new set of Fourier phase angles is combined with the seed Fourier amplitudes and transformed into the time domain with an inverse Fourier transform (IFT).
- The modified short time segments are recombined to form a modified time series.
- The preceding steps are performed multiple times for multiple segment lengths, with each segment length having a specified frequency range over which phase angles are modified. Hence, multiple modified time series are created. Segment lengths and corresponding frequency limits used are shown in Table 3.7.
- The multiple modified time series are band-pass filtered within the limits of the pass-band matching the band of the modification to combine the modified frequency bands in the frequency domain.
- The non-overlapping frequency bands are transformed back to the time domain to create the final broadband modified time series.

The SVGM generated using this procedure all occur within a single horizontal plane. In other words, the seed and simulated motions exist at different  $x$  and  $y$  horizontal locations, but at the same depth  $z$ . For the purpose of this study, this depth corresponds to the base of the soil profiles. To generate motions at each depth increment for input to the BDNWF group analyses, transfer functions were computed from the *DEEPSOIL* results relating the seed input motions to the motion computed at the depth of each layer. These transfer functions were then used to compute a ground motion at the depth of each layer from the SVGM, thus effectively propagating the same amount of spatial variability generated at the base of each profile from *FDW2D.r* uniformly over the full depth of the profile. In other words, horizontal and vertical incoherence are uncoupled in the approach used here, but both are ultimately reflected in the ground motions imposed on the pile group.

An example of the seed and SVGM is shown in Figure 3.16 in terms of acceleration and displacement. Note that only a short time window of two seconds is shown. It is apparent from this figure that while a modest amount of variability exists between pile locations in terms of acceleration, the displacement time series are nearly identical. This is because incoherence increases with increasing frequency, and displacement tends to amplify low-frequency energy and de-amplify high-frequency energy relative to acceleration.

**Table 3.7** Segment duration ( $L$ ) and frequency bands ( $b$ ) used in the FDW routine.

Segment duration (sec)	Frequency limits (Hz)
1.28	2-Nyquist
2.56	1–2
5.12	0.5–1
10.24	0.25–0.5
20.48	0.12–0.25
Full duration of time series	0–0.12

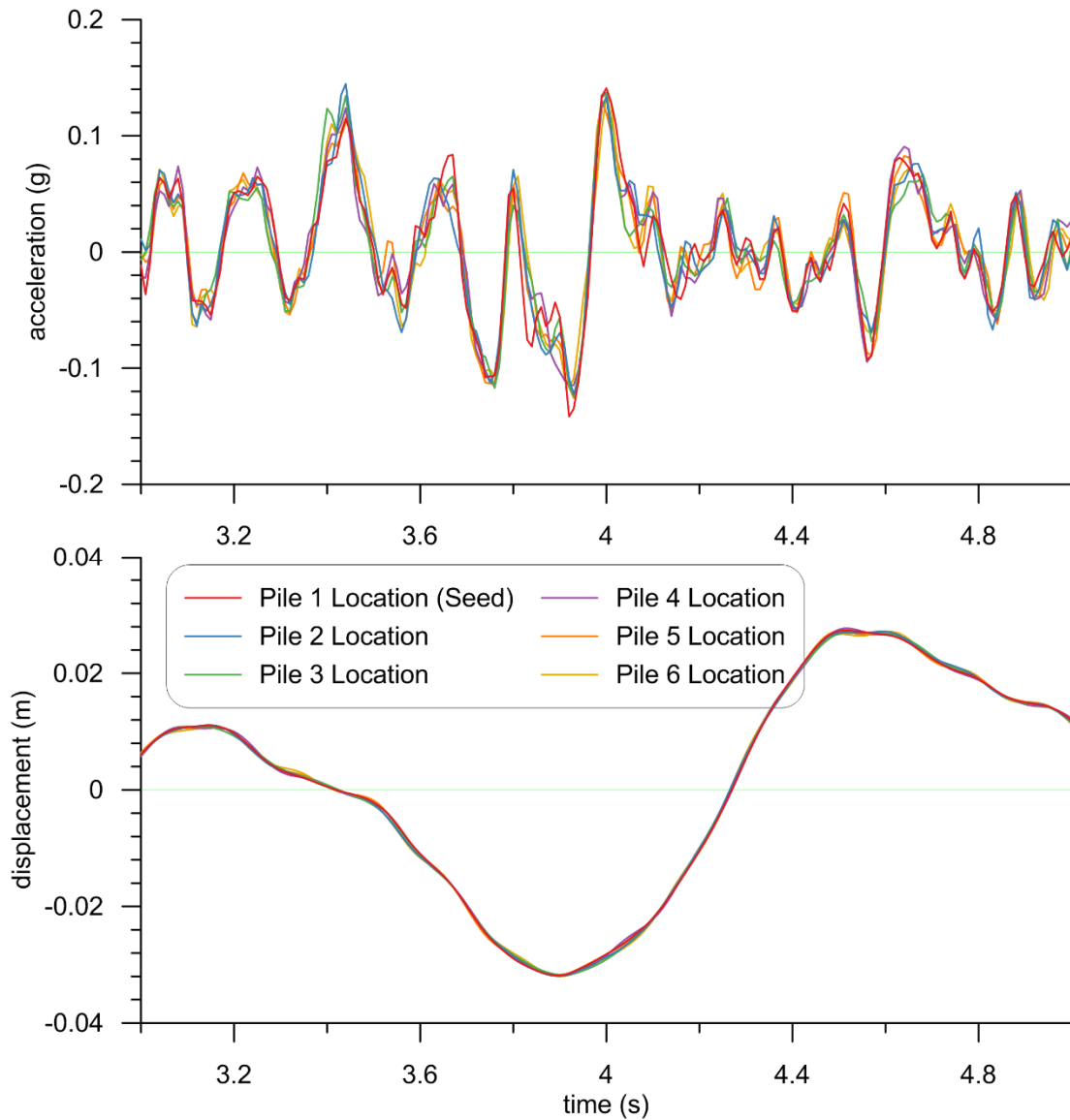


**Figure 3.16** Acceleration (top) and displacement (bottom) time series for seed motion (1971 San Fernando, California, earthquake, Lake Hughes #4 recording station) and simulated spatially-variable ground motions at locations corresponding to other piles in group layout shown in Figure 3.14.

### 3.8 OPENSEES ANALYSIS

The following parameters were used to define the *OpenSees* finite-element analyses:

- Penalty constraints to enforce boundary conditions.
- Norm of the displacement increment (*NormDispIncr* command) to test for convergence with a starting tolerance of  $10^{-6}$  m/
- Krylov-Newton solution algorithm [Scott and Fenves 2010] used to solve nonlinear system of equations.

- If convergence was not achieved at a particular step, the modified-Newton algorithm with initial stiffness was used; if this failed to converge, the tolerance was decreased by an order of magnitude and the Krylov-Newton algorithm was used again.
- Newmark integrator with  $\gamma = 0.5$  and  $\beta = 0.25$ .
- A  $P-\Delta$  transformation was utilized to capture secondary moments induced by offset axial loads

## 4 Results

### 4.1 SINGLE PILES

Horizontal displacement transfer function results for each pile/site/motion combination are presented in Figures 4.1–4.12. Each figure is for one site and contains four plots, one for each of the four piles, where each plot contains the computed transfer function ordinates with high coherence for the 40 ground motions along with the mean and  $\pm$  one standard deviation of the results shown in that plot. Separate figures are presented for the fixed- and free-head conditions. Collectively, the plots represent the results of 1920 single-pile simulations.

Because the time step, duration, and high- and low-pass filtering for the input ground motions vary, the frequency vector computed during the Fast Fourier Transform (FFT) operation varies between ground motions. To accommodate computing the mean and standard deviation at each frequency, the data were binned into 200 log-evenly spaced frequency bins spanning between the minimum high-pass and maximum low-pass frequencies used during processing of the 40 motions (0.0375 and 62.5 Hz, respectively). Furthermore, within each frequency bin it is typically the case that not all 40 transfer functions exceeded the minimum coherence threshold of 0.8. In general, the number of transfer functions meeting the minimum coherence threshold decreases with increasing frequency above the corner frequency. To avoid spurious fluctuations at these higher frequencies, the mean and  $\pm$  one standard deviation were only computed if at least 25% (10) of the 40 transfer functions exist in a given frequency bin. For this reason, the plots show individual transfer functions at higher frequencies than the mean, and  $\pm$  one standard deviation were generally plotted.

Following presentation of the single pile results versus plain frequency, normalized plots versus dimensionless frequency are presented in §4.2. This is followed by identification of the controlling parameters for kinematic pile–soil interaction and a comparison to previous elastic solutions in §4.3. Models for predicting transfer functions and spectral ratios for design applications are developed in §4.4 and §4.5. The chapter concludes with a summary of pile group simulation results.

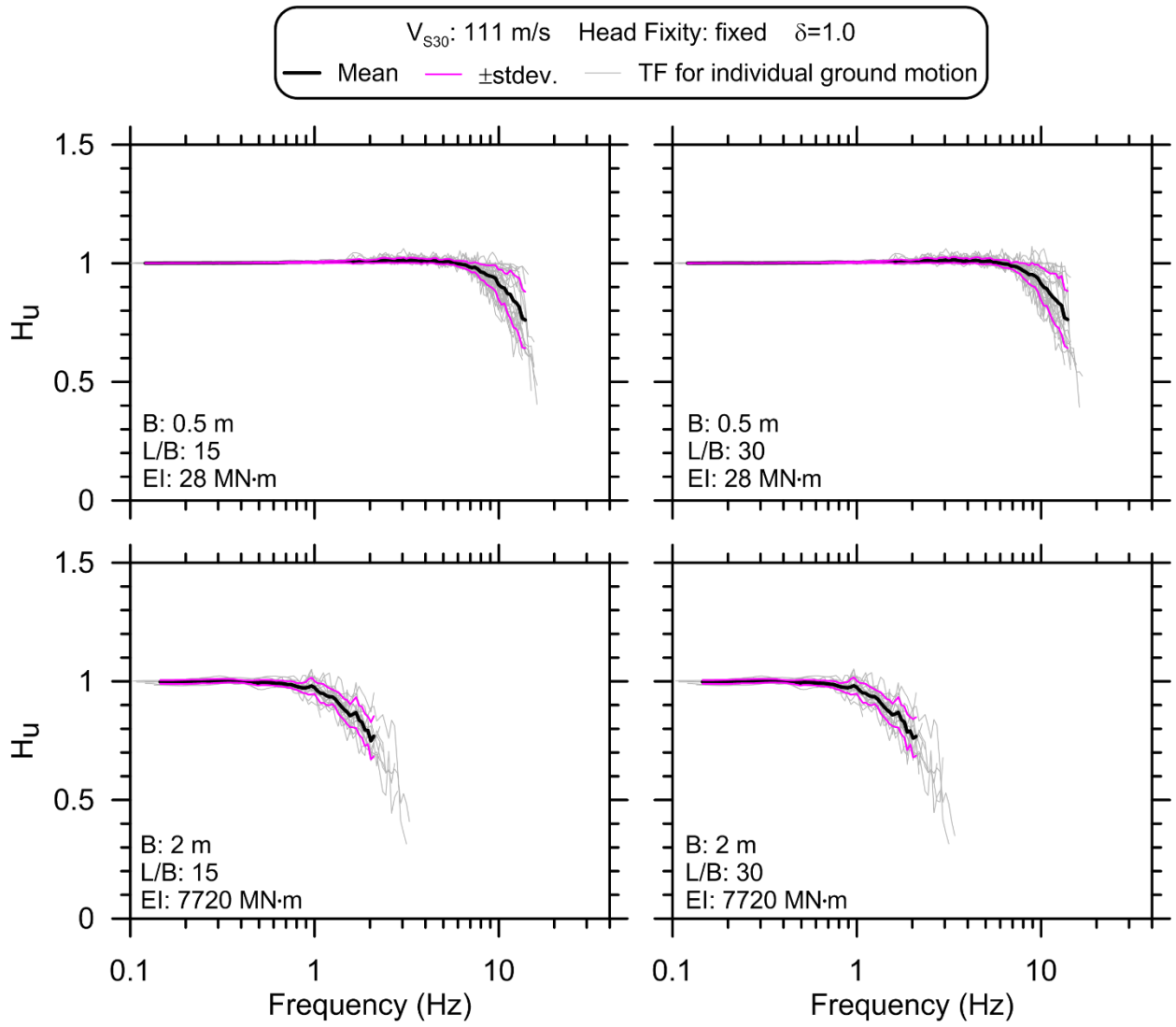


**Figure 4.1**    Transfer functions for Site 1 fixed-head piles.

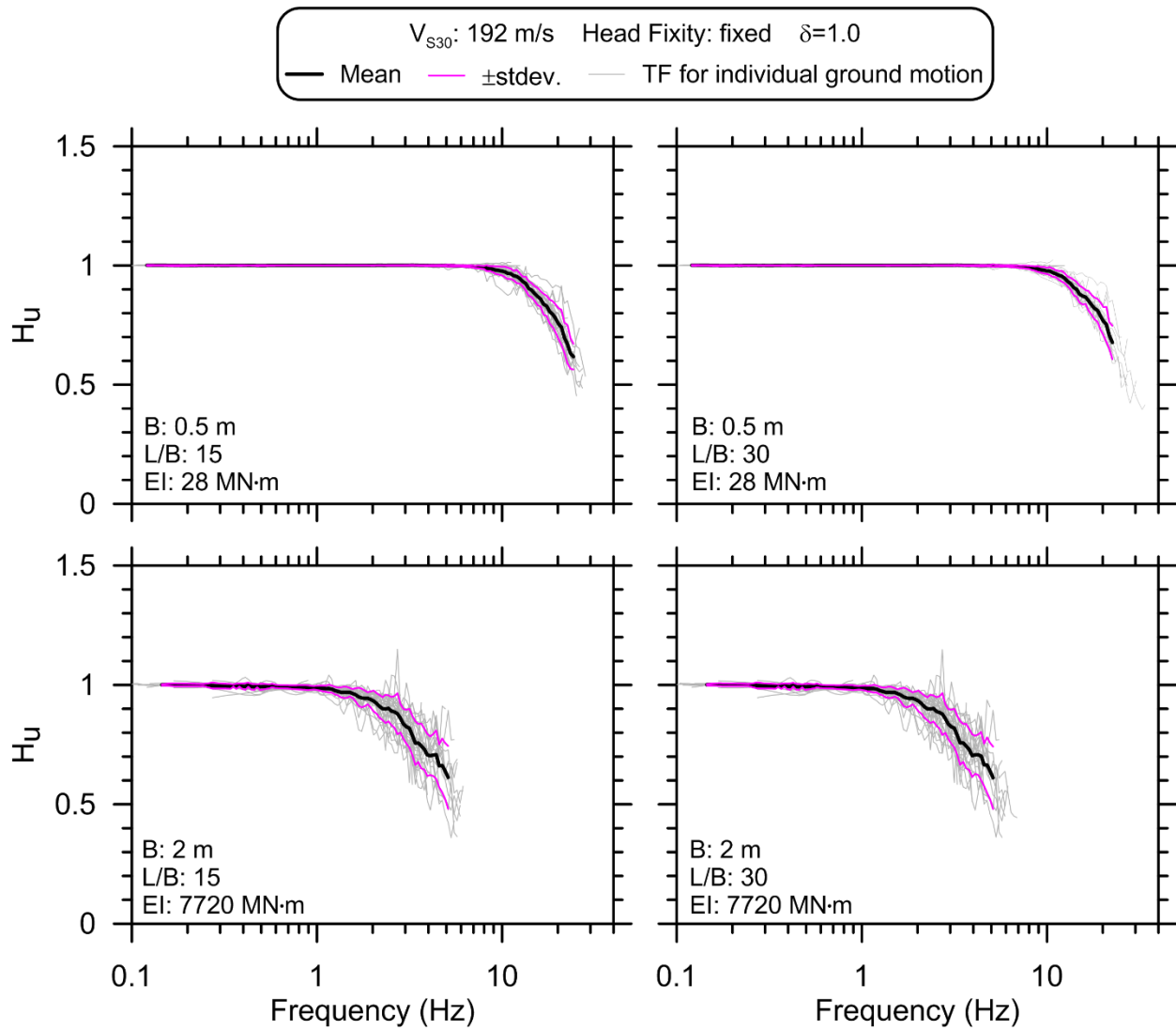


**Figure 4.2**    Transfer functions for Site 2 fixed-head piles.

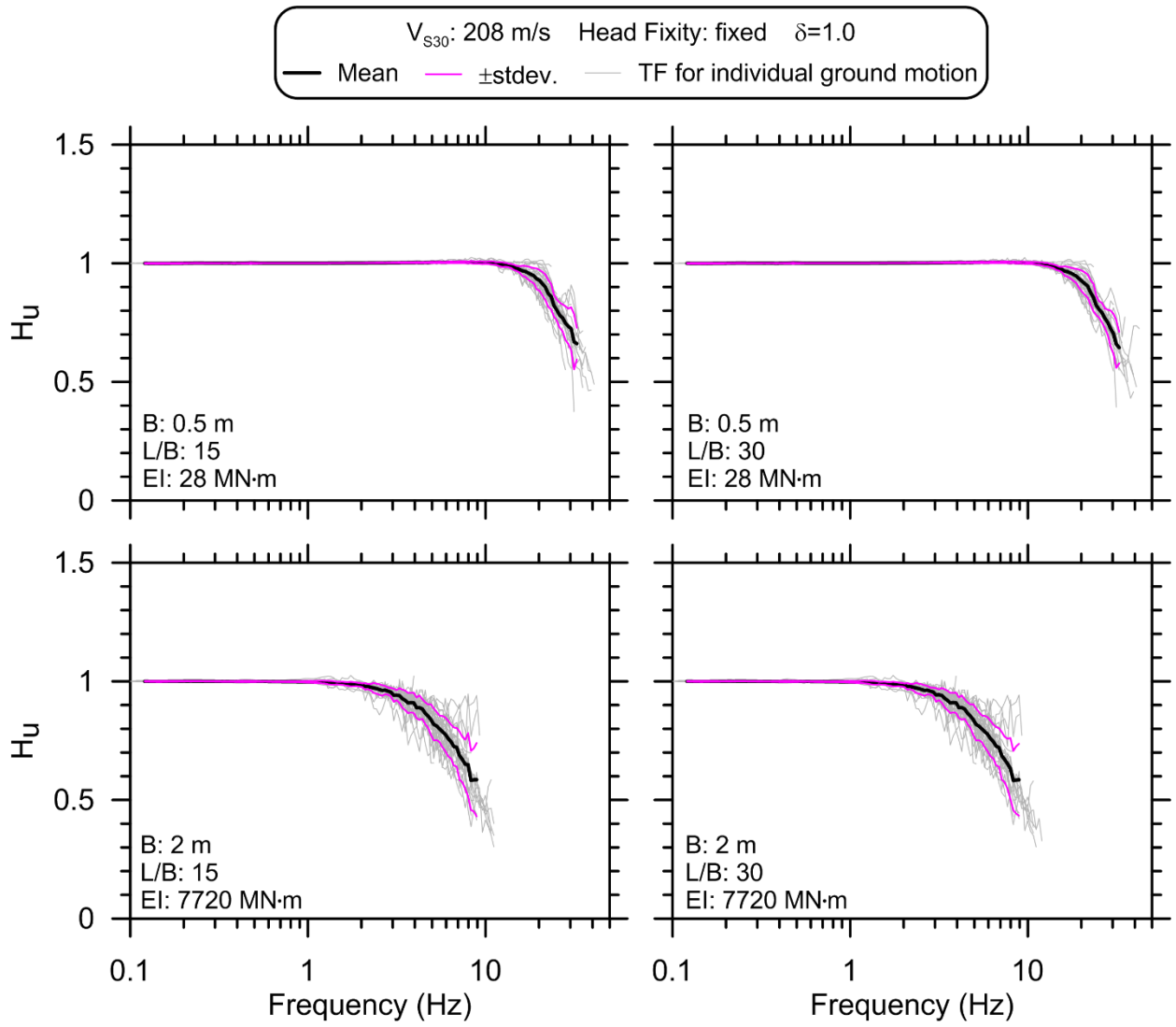


**Figure 4.3** Transfer functions for Site 3 fixed-head piles.

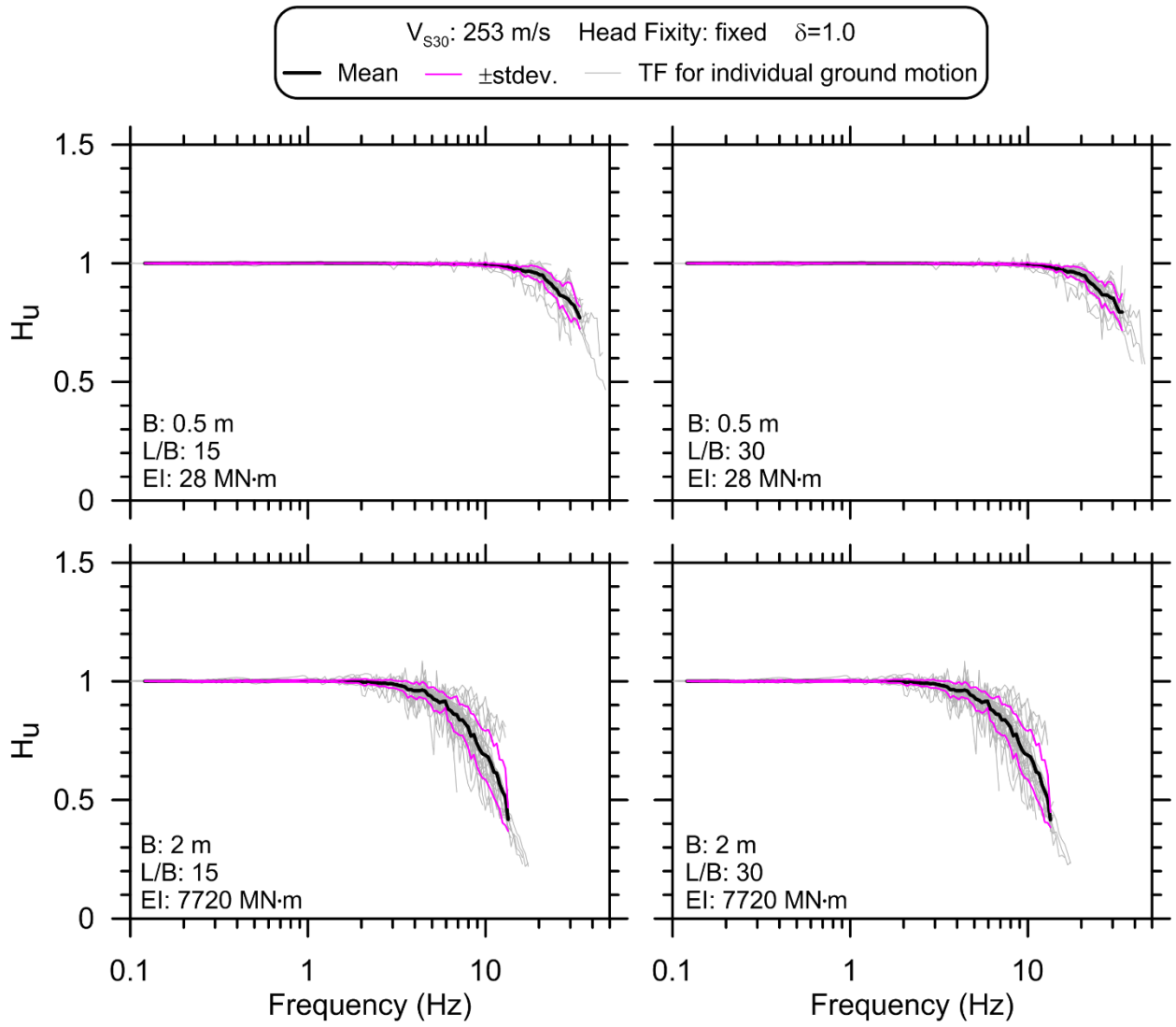


**Figure 4.4**    Transfer functions for Site 4 fixed-head piles.

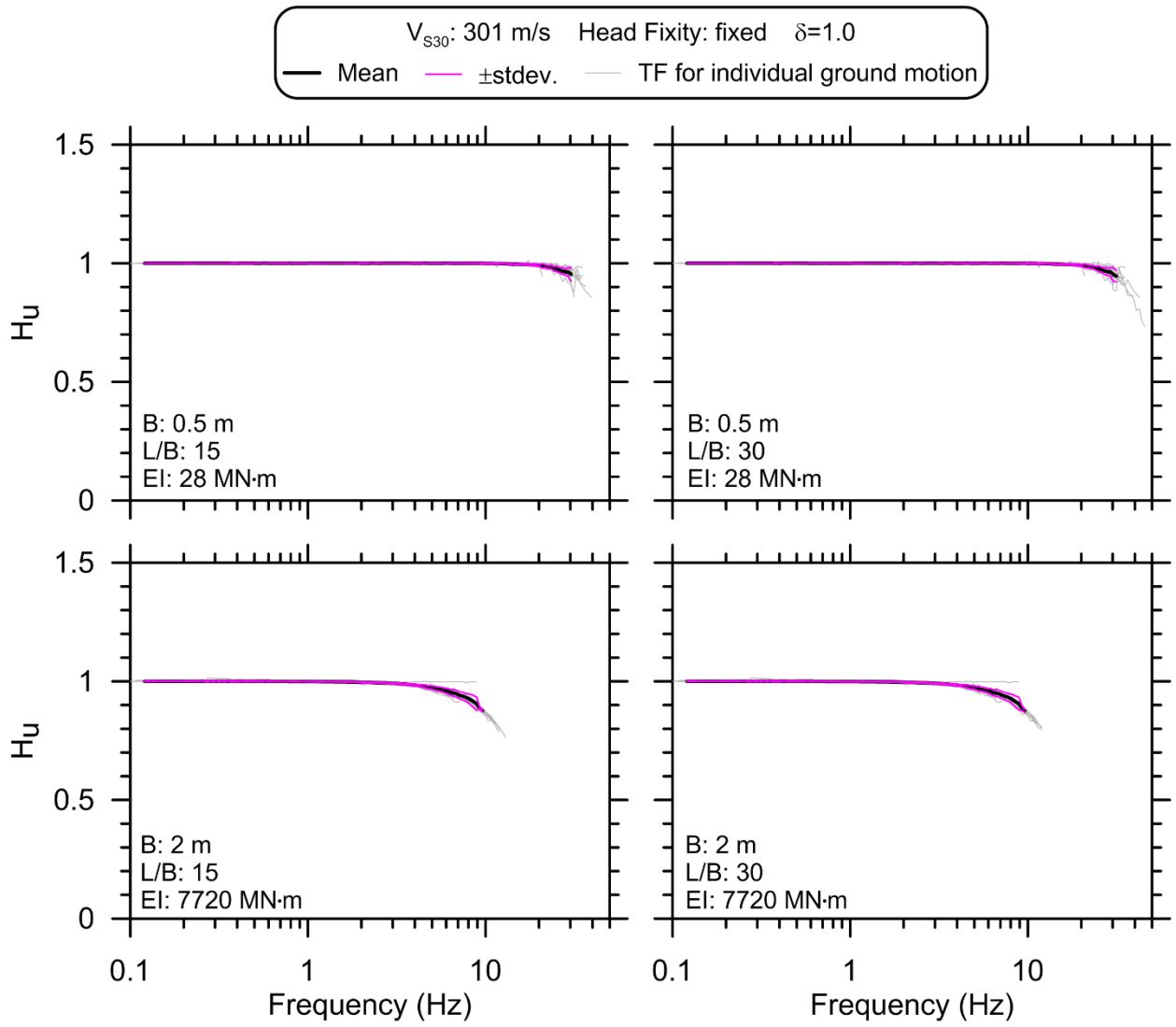


**Figure 4.5**    Transfer functions for Site 5 fixed-head piles.

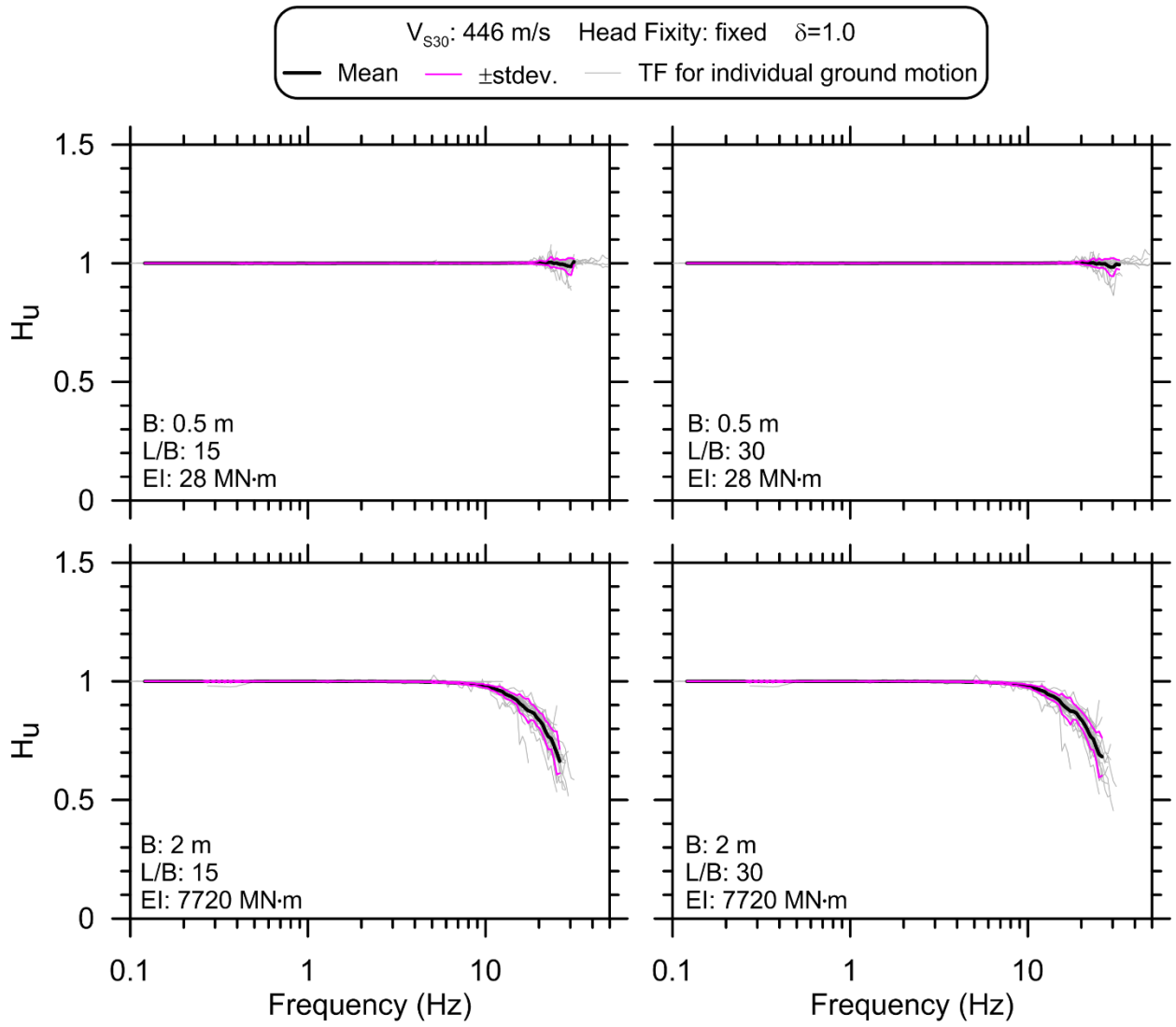


**Figure 4.6**    Transfer functions for Site 6 fixed-head piles.

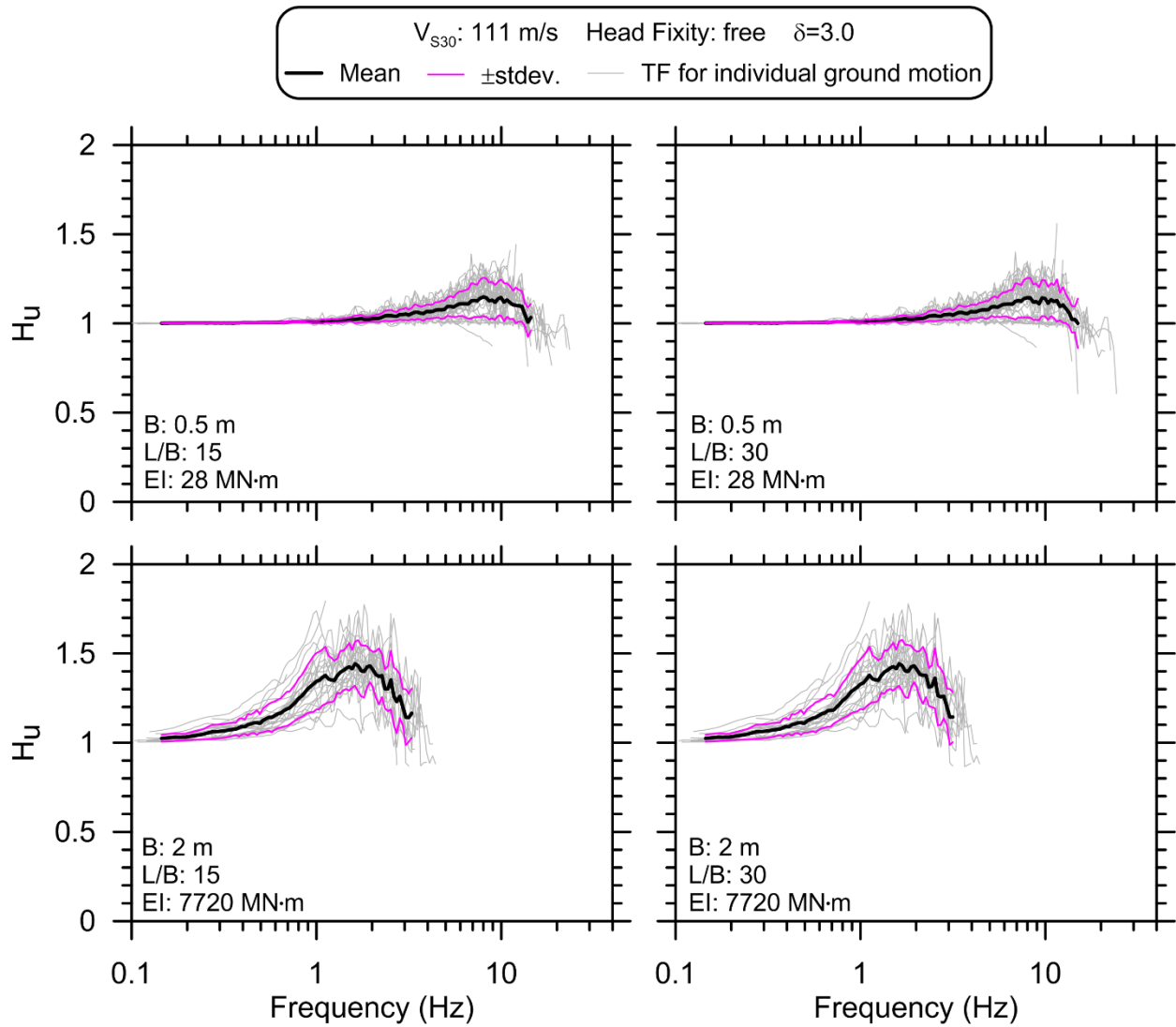


**Figure 4.7** Transfer functions for Site 1 free-head piles.

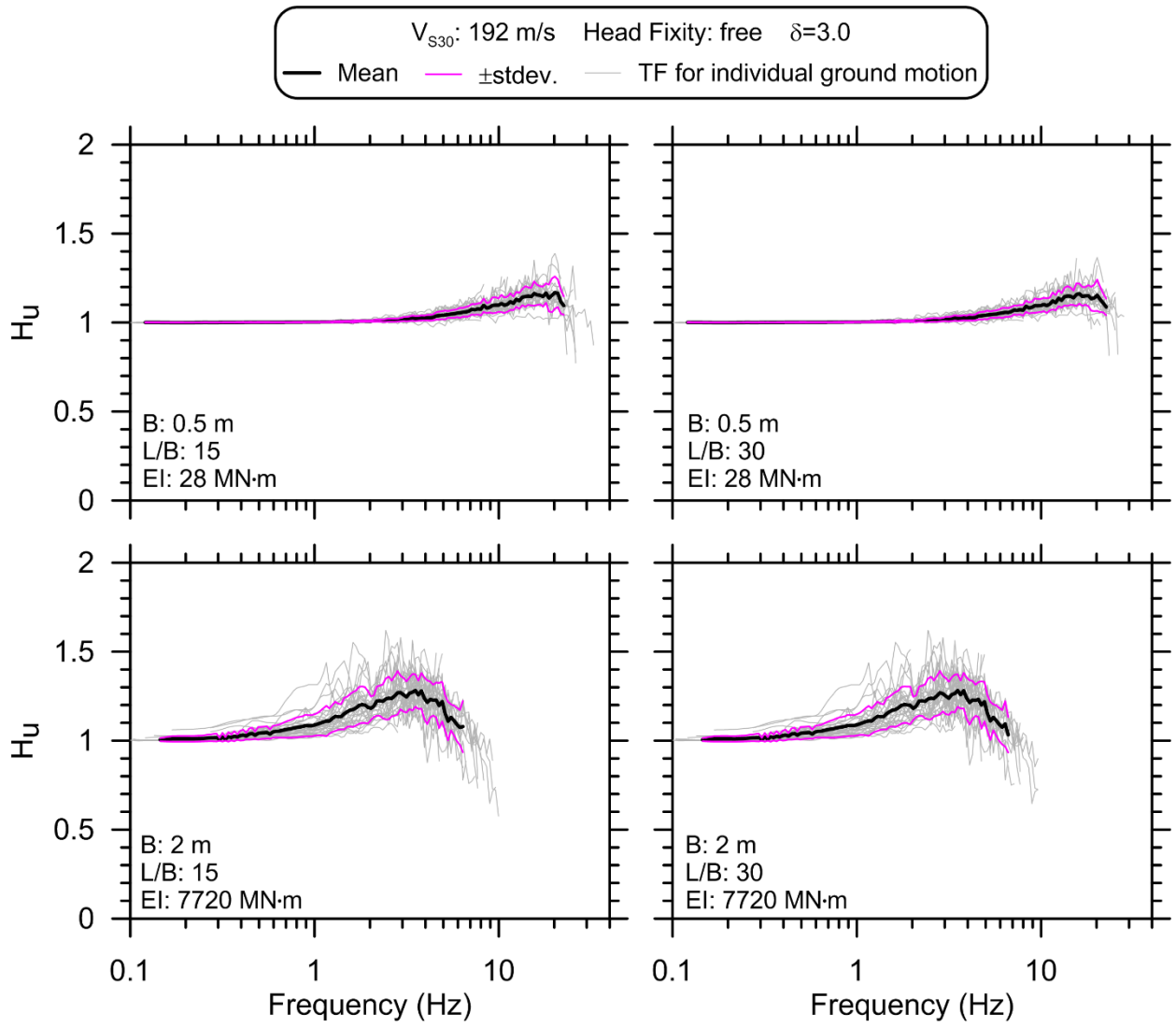


**Figure 4.8**    Transfer functions for Site 2 free-head piles.

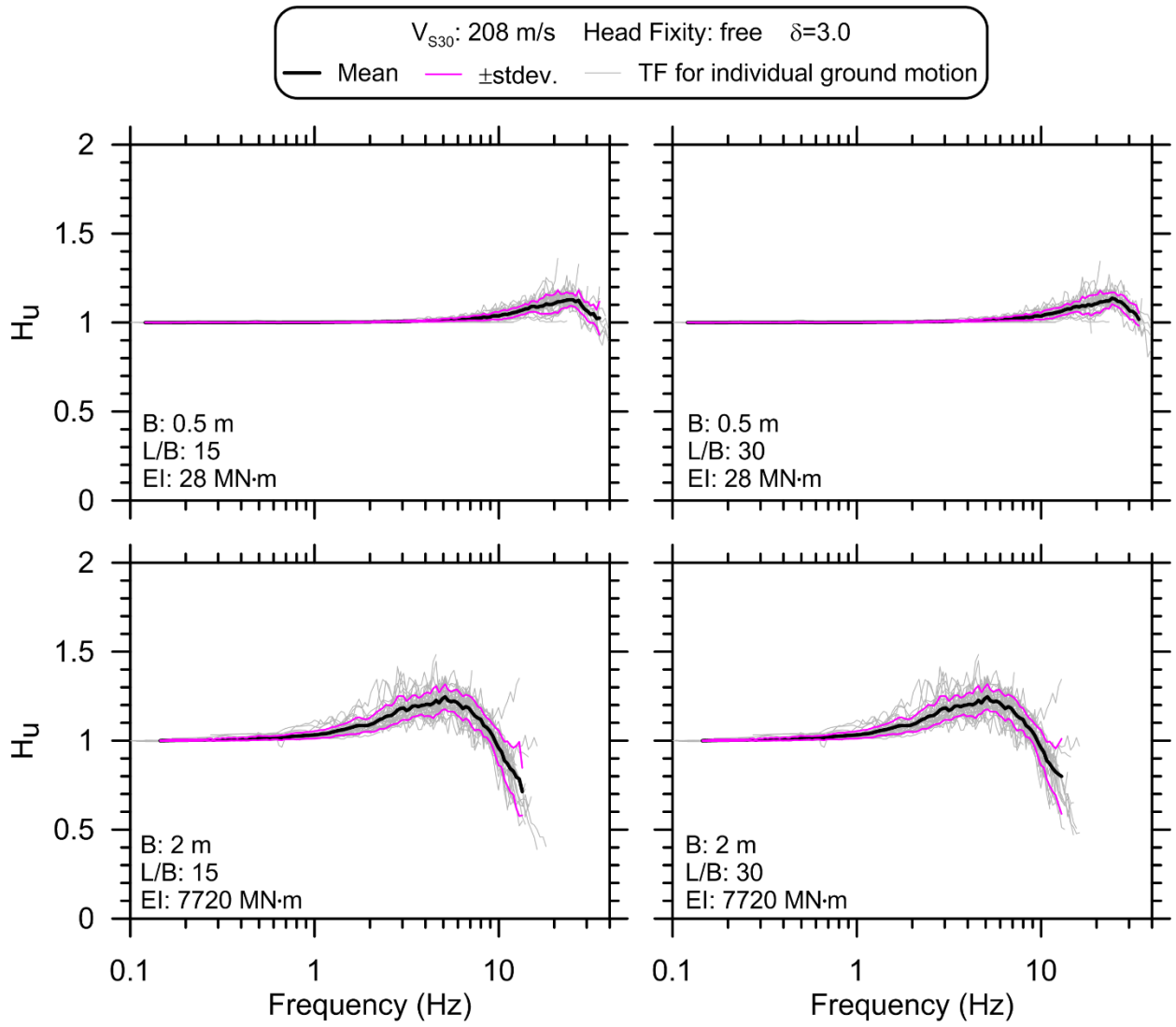


**Figure 4.9**    Transfer functions for Site 3 free-head piles.

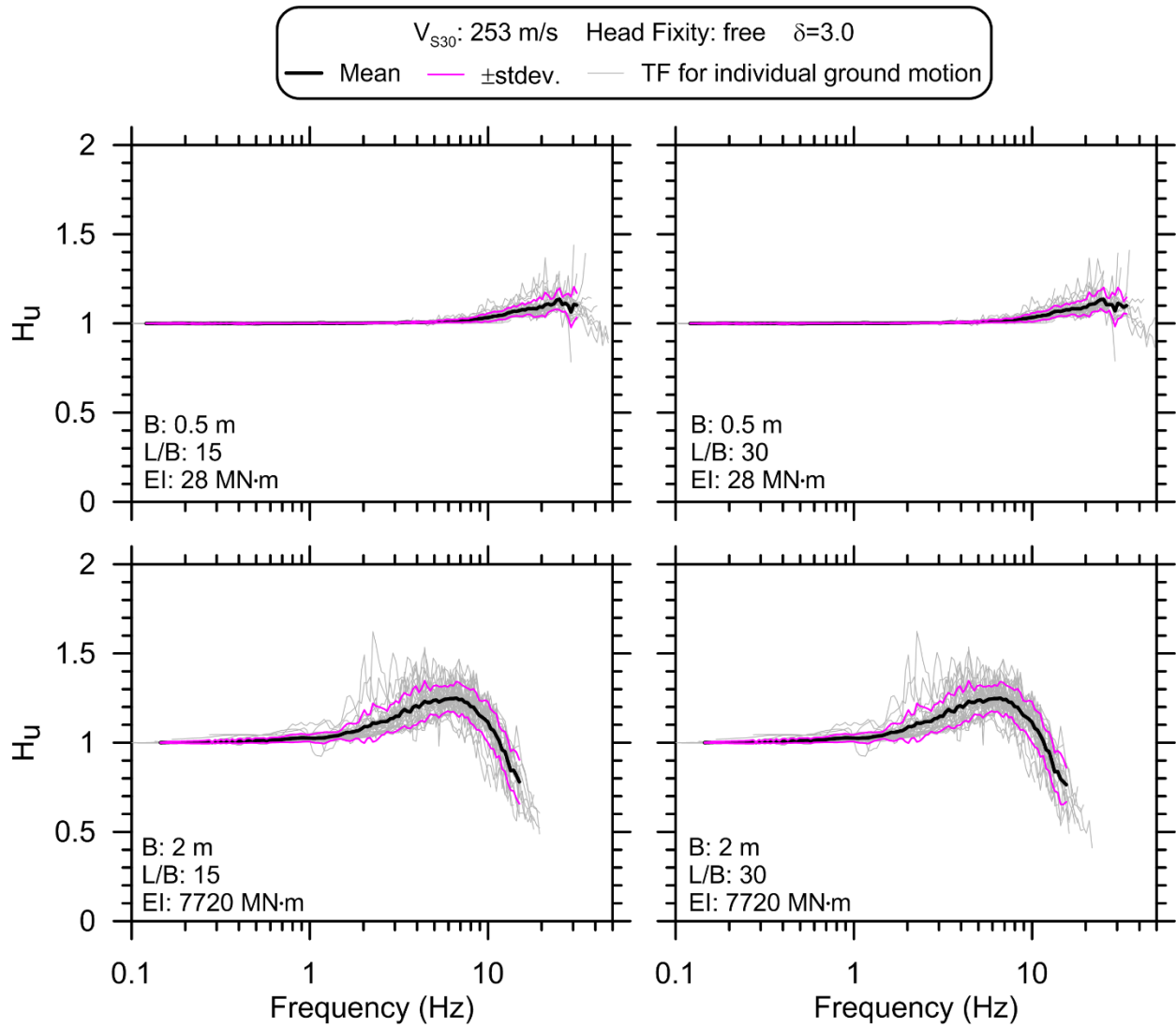


**Figure 4.10** Transfer functions for Site 4 free-head piles.

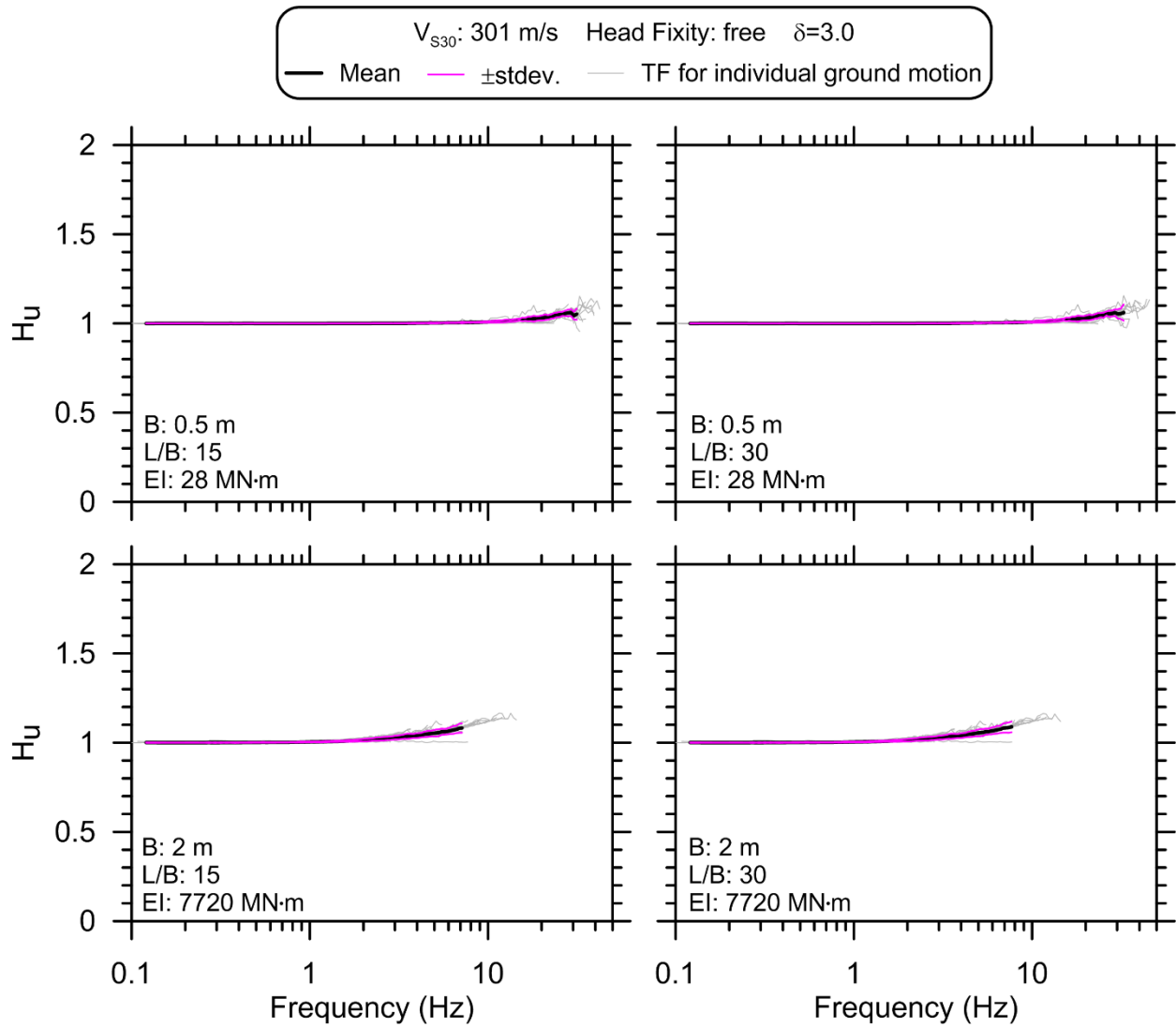


**Figure 4.11** Transfer functions for Site 5 free-head piles.

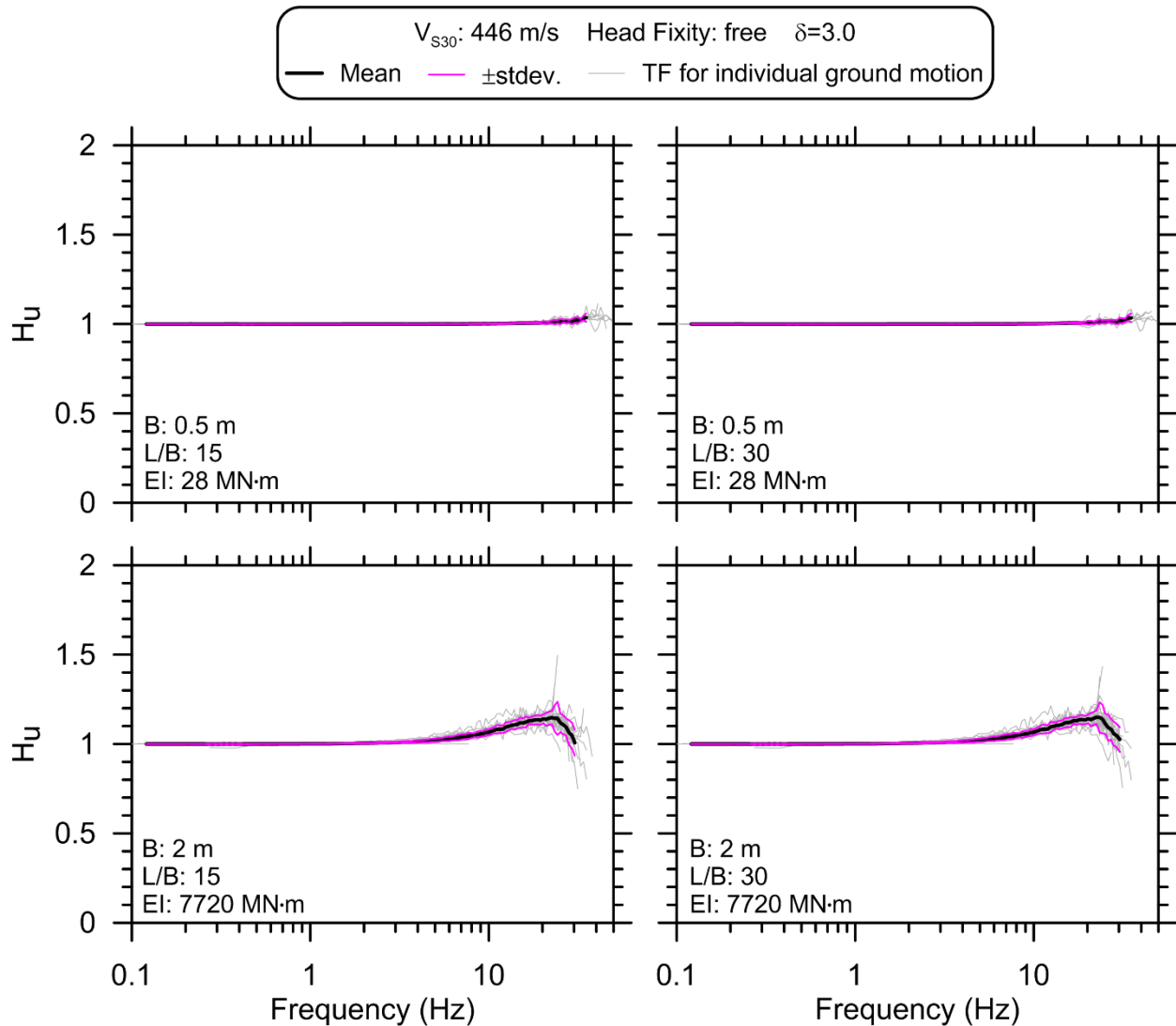


Figure 4.12 Transfer functions for Site 6 free-head piles.

## 4.2 NORMALIZED RESULTS USING DIMENSIONLESS FREQUENCY

To be of practical use in foundation design, the results of soil–structure interaction studies are usually presented in a normalized fashion in which the independent variable is a dimensionless function of frequency rather than plain frequency. The intention of normalization is to collapse the range of results into a narrow band which can then be represented by a single mathematical model (equation) for use in a forward-design scenario.

The normalization scheme developed by Di Laora and Sanctis [2013] and Anoyatis et al. [2013] is adopted here because of its strong fundamental basis and demonstrated ability to achieve near-perfect normalization for flexible piles considering elastic behavior. Furthermore, this allows for comparison between the elastic analytical solutions and the nonlinear results computed for this study. The dimensionless frequency for this approach is computed as  $\omega/(\lambda V_s)$ . Recall that the improvements realized with this normalization scheme over the previous  $(\omega B)/V_s$  scheme are due

to: (i) the use of flexural rigidity  $E_p I_p$  in the  $\lambda$  term instead of diameter; and (ii) inclusion of the characteristic length relative to the free-field wavelength, which drives the frequency-dependence of the problem.

Following the approach of Di Laora and Rovithis [2014],  $\lambda$  and  $V_S$  are computed over the depth increment corresponding to the uppermost pile active length, denoted by  $\lambda_{La}$  and  $V_{S,La}$ . Consistent with Equation (1.9),  $\lambda_{La}$  is computed using the initial stiffness of pile–soil interaction  $K_e$ . Nonlinearity due to degradation of the  $p$ - $y$  springs is reflected in the results and will be considered in development of the prediction models.

Figure 4.13 presents the normalized transfer functions for fixed-head piles. Free-head pile transfer functions for horizontal displacement and head rotation are presented in Figure 4.14 and Figure 4.15. Unlike the plots in the previous section, computed transfer functions for the normalized versions are plotted as points rather than lines. This is simply because plotting 960 lines within a narrow band would make it nearly impossible to discern one from another. In contrast, plotting only points that represent transfer function ordinates with high coherence not only makes the overall trend clear, but it also provides a visual guide to where the greatest concentration of points lie. Prior to plotting, the results were binned into 200 equally spaced dimensionless frequency bins. The results were further grouped into nine equally spaced dimensionless frequency bins for computing mean and standard deviation trends as shown in the figures. Note that the “best-fit to functional form” curves in these figures are for the functional forms discussed subsequently in §4.4.

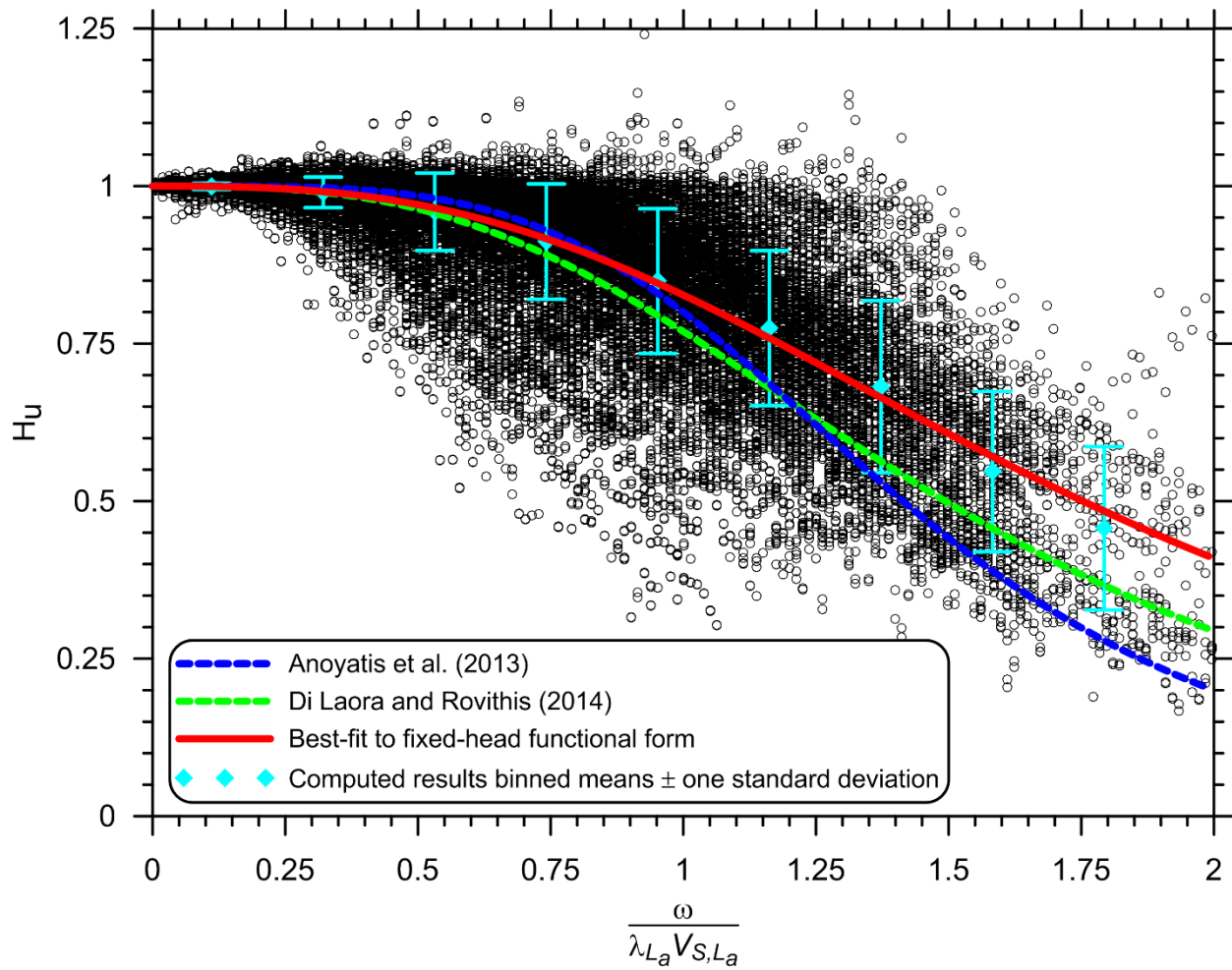


Figure 4.13 Normalized horizontal displacement transfer function results for fixed-head piles.

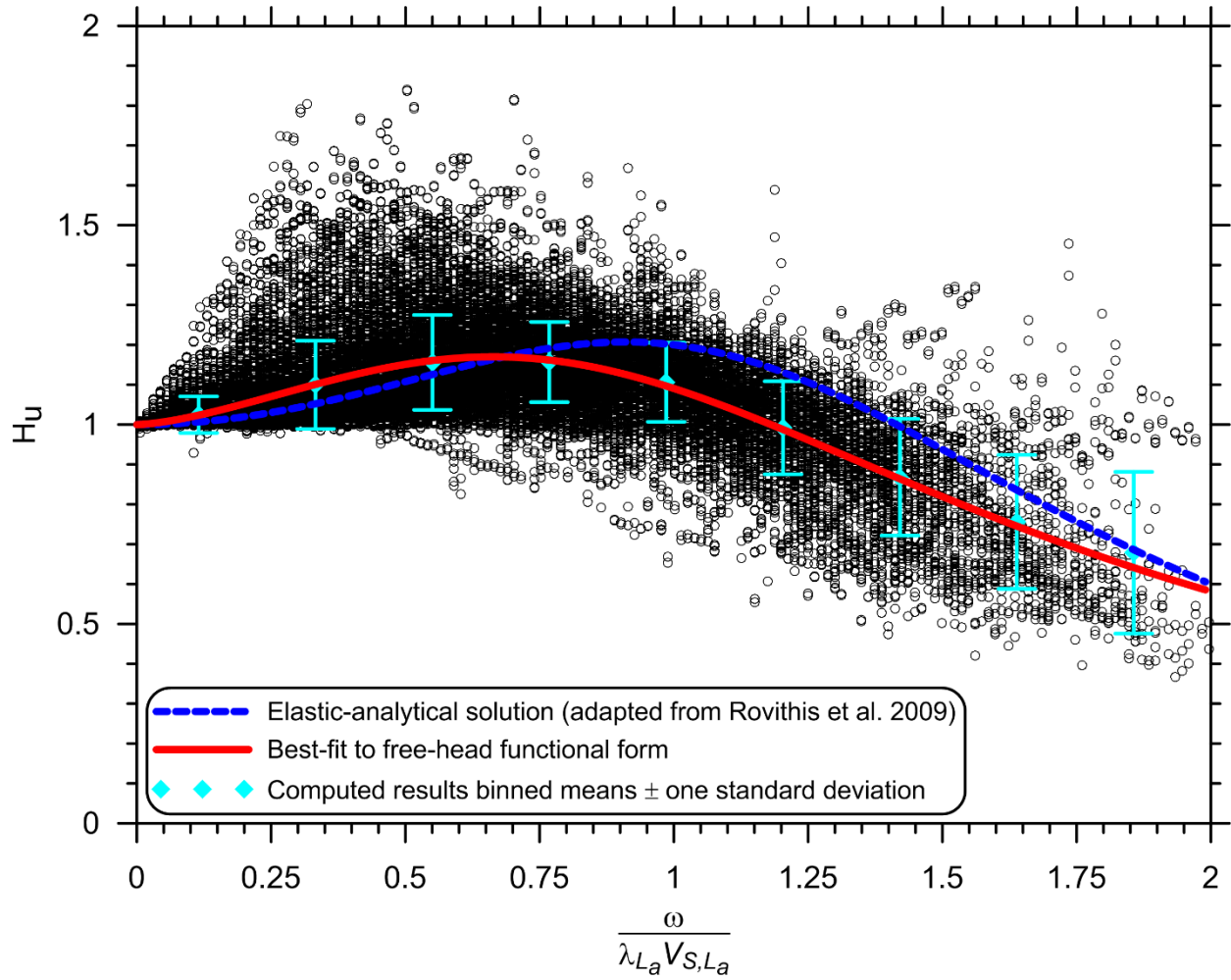


Figure 4.14 Normalized horizontal displacement transfer function results for free-head piles.

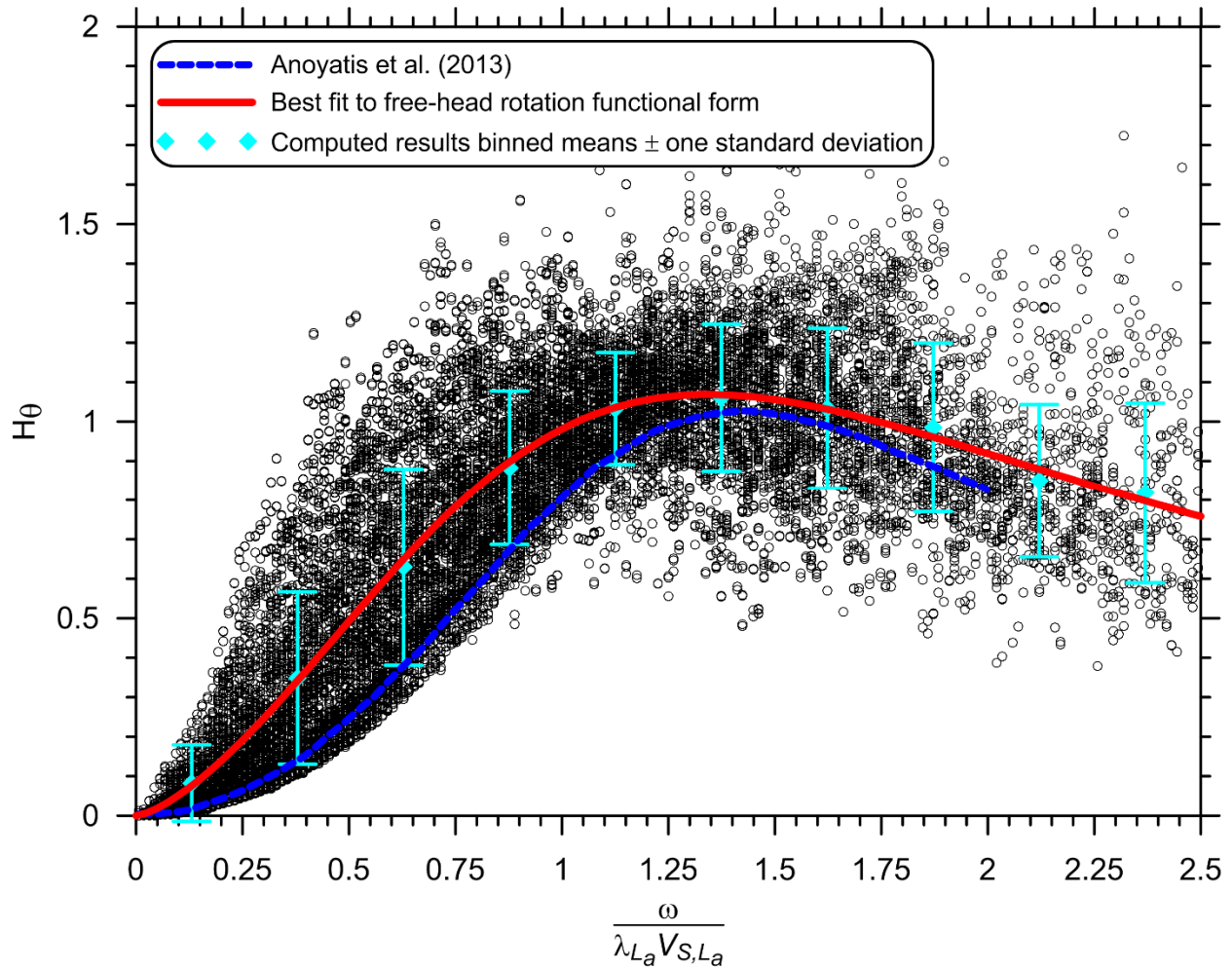


Figure 4.15 Normalized rotation transfer function results for free-head piles.

#### 4.3 CONTROLLING PARAMETERS AND COMPARISON TO ELASTIC SOLUTIONS

The normalized and plain-frequency transfer function results presented above allow for identification of the key parameters that control kinematic pile–soil interaction. These findings will be used subsequently to guide development of models for predicting transfer functions and spectral ratios for design applications. While identifying the key parameters, a comparison is also made to elastic analytical solutions to highlight the important effects of realistic modeling assumptions and material nonlinearity.

Previous work using simplified elastic models (e.g., Fan et al. [1991]) identified the key parameters for kinematic pile–soil interaction as (i) pile-to-soil stiffness contrast, (ii) variations (or lack thereof) in soil stiffness over the length of the pile, and (iii) pile head-fixity condition. The effect of head-fixity is so significant that the results of fixed- and free-head piles must be considered separately. This is because free-head piles show “kinematic amplification” over a frequency range where the free-field wavelength is similar to the pile length. Because of this fundamental difference, head-fixity is considered less of a controlling parameter than simply a

different category of results from this point forward, and separate predictive models will be developed for each case.

Consistent with elastic solutions, pile-to-soil stiffness ratio remains the dominant factor that determines over what frequency range kinematic pile-soil interaction will be significant. Comparison of the mean results for each pile/site combination (Figure 4.16) reveals that the corner frequency<sup>6</sup> shifts higher with decreasing pile-to-soil stiffness contrast (i.e., as the sites get stiffer), while the shape of the transfer function remains relatively consistent.

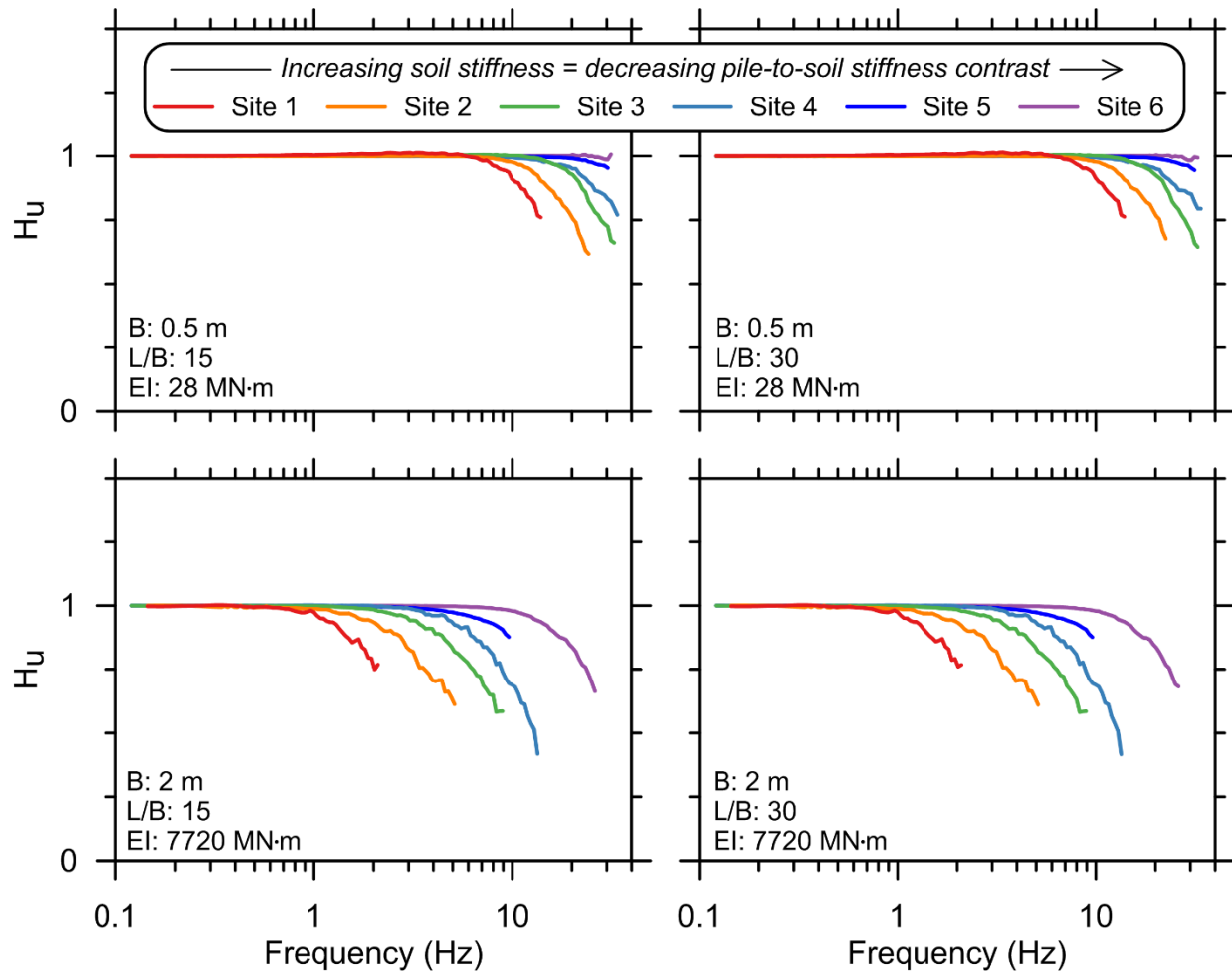


**Figure 4.16** Mean fixed-head transfer function results for each pile/site combination.

<sup>6</sup> See Chapter 7: “corner frequency” is the term used herein to refer to the frequency beyond which significant pile-soil interaction occurs such that the transfer function ordinates fall below about 0.95.

Variations in soil stiffness over the length of pile also play an important role as suggested by Fan et al. [1991] and others. For example, the difference between the Anoyatis et al. [2013] and Di Laora and Rovithis [2014] curves in Figure 4.13 is due to the fact that Di Laora and Rovithis used a soil profile with increasing stiffness versus depth, while Anoyatis et al. considered a homogeneous profile. Figure 4.17 compares transfer functions computed for the  $B = 2.0$  m,  $L = 30$  m pile for three ground motions at Sites 3 and 4. Recall that Sites 3 and 4 have similar shear-wave velocity profiles over the upper 20 m (see Figure 3.15) and both consist of predominantly granular soil; the only significant difference between the two sites is that the stiffness of Site 4 shows a marked increase below 20 m. The portion of the pile embedded in this stiffer layer influences the response of the upper portion of the pile at Site 4, whereas Site 3 lacks this behavior.

The two most significant effects that are not reflected in the elastic analytical solutions are (i) nonlinearity due to pile–soil interaction and (ii) radiation damping. An increase in ground-motion intensity generally results in greater pile–soil relative displacement and corresponding  $p$ - $y$  softening, effectively increasing the pile-to-soil stiffness contrast and shifting transfer function ordinates to lower values. On the other hand, because radiation damping manifests as an increase in stiffness for dynamic  $p$ - $y$  curves, its effect is to decrease the pile-to-soil stiffness contrast and shift transfer function ordinates higher. Hence, nonlinearity due to pile–soil interaction and radiation damping are competing effects in terms of their influence on the transfer functions.

This is illustrated in Figure 4.18, which shows transfer functions computed for the  $B = 0.5$  m,  $L = 7.5$  m pile in the Site 1 profile subjected to the 1971 San Fernando, California, earthquake (NGA record sequence number 72). A comparison of the transfer functions computed with (i) a constant value of elastic  $p$ - $y$  stiffness set equal to the initial stiffness  $K_e$ , versus (ii) an equivalent-linear degraded stiffness, verifies that a decrease in soil stiffness shifts the transfer function ordinates down. However, when a dashpot representing radiation damping is added to the degraded stiffness model, the transfer function ordinates are shifted back up, in this case above the transfer function representing initial stiffness but without the dashpot. Finally, the transfer function for the fully-nonlinear model is shown, which on average plots above the elastic transfer functions computed without radiation damping. Thus, the effect of nonlinearity due to pile–soil interaction is effectively outweighed by the increase in stiffness due to radiation damping for this case. (Note that all four models were subjected to the same input ground motions, so the effect of nonlinearity due to site response is equal for all cases).

Comparison of the trends indicated by the binned means in Figures 4.13– 4.15 shows that the nonlinear results computed for this study plot near or slightly above the elastic analytical solution. This is somewhat counterintuitive, as it would seem that including pile–soil interaction nonlinearity would shift the results below the elastic analytical solution due to soil softening. However, because the elastic solutions in these plots do not include radiation damping, this is a somewhat misleading comparison. Although radiation damping is included in the full derivation by Anoyatis et al. [2013], the best-fit curves from their study that are shown on the normalized transfer function plots in the previous section are for a static simplification in which pile inertia and radiation damping are ignored (the influence of hysteretic damping on the free-field ground response can be included by using a complex shear-wave velocity  $V_s^*$ ). Furthermore, ground-motion intensity does not influence elastic solutions except to the extent that the soil modulus values specified by the designer should be consistent with the anticipated level of strain. Unfortunately, little guidance is available on predicting this strain due to pile–soil interaction, and

methods for predicting free-field nonlinearity due to site response (e.g., NIST [2012]) are only approximate. Additionally, the elastic solutions will produce essentially the same transfer function regardless of the pile-to-soil stiffness contrast for any flexible pile as demonstrated in Chapter 2.

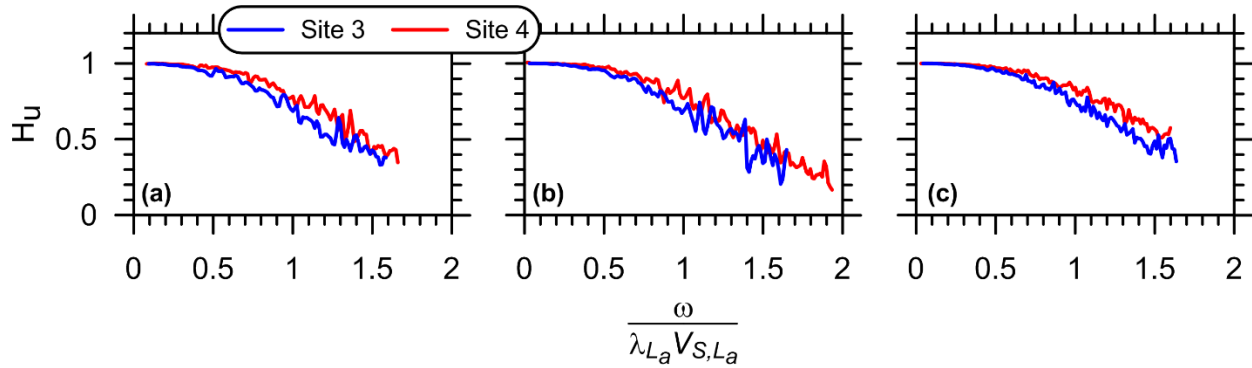


**Figure 4.17** Influence of changes in stiffness over pile length for  $B = 2.0$  m,  $L = 30$  m pile subjected to (a) 1971 San Fernando, California, earthquake (NGA record sequence number 72); (b) 1994 Northridge, California, earthquake (NGA record 1011); and (c) 1999 Chi-Chi, Taiwan, earthquake (NGA record 2661).

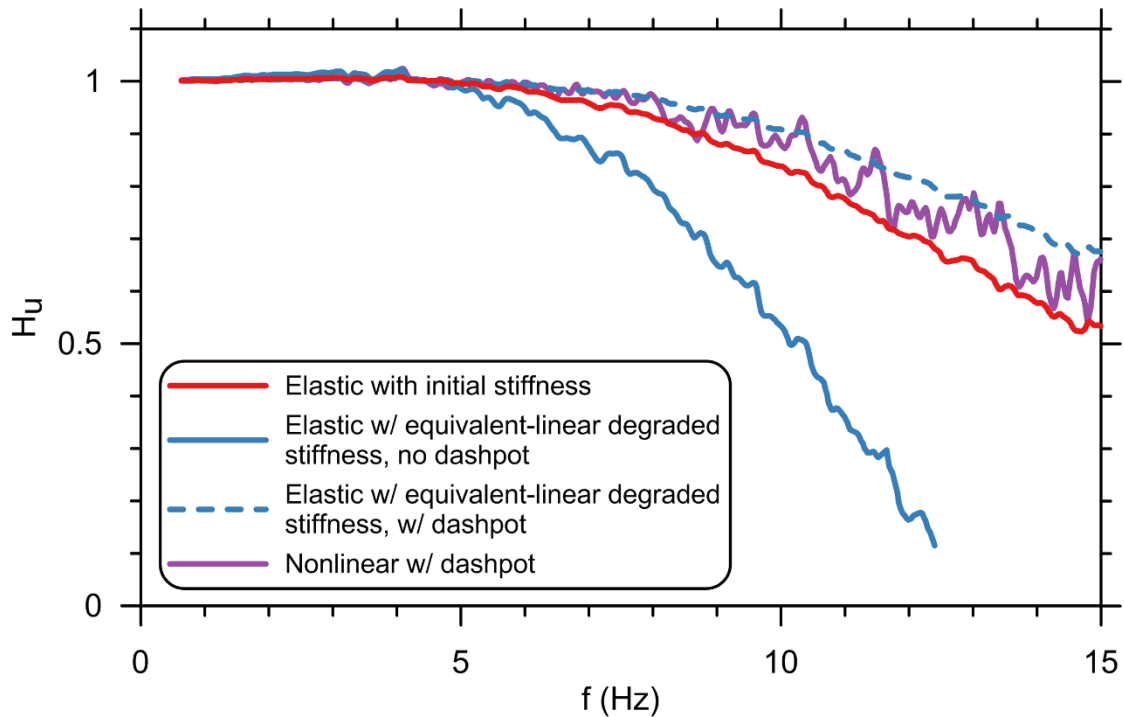


**Figure 4.18** Competing effects of radiation damping and stiffness degradation due to pile-soil interaction.

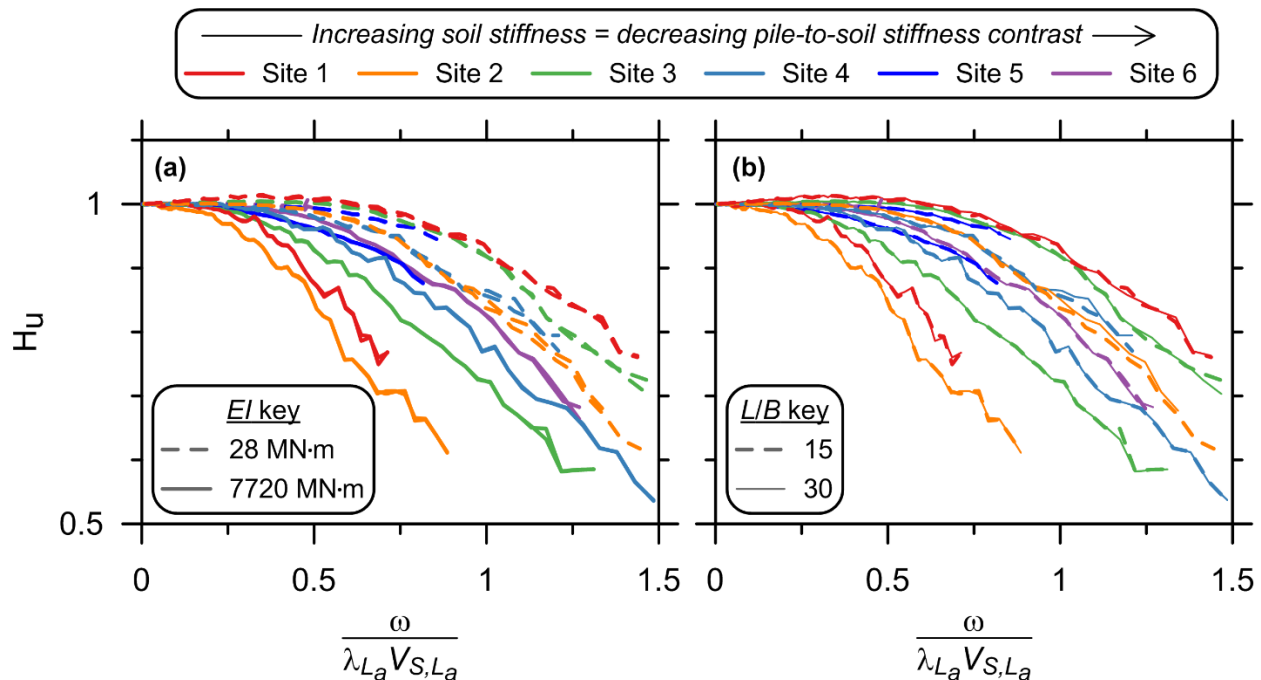


**Figure 4.19** Mean fixed-head transfer function results for each pile/site combination plotted versus dimensionless frequency: (a) shows variability in results due to pile stiffness, and (b) shows lack of variability in results due to pile slenderness ratio  $L/B$ .

It is immediately clear when examining the normalized transfer function plots that significant dispersion exists in the computed results relative to the perfect normalization suggested by elastic solutions. Figure 4.19 provides insight into this variability by showing only the mean transfer functions for each pile/site combination (rather than all 40), with all 24 pile/site combinations plotted versus dimensionless frequency on a single graph. Three key trends are apparent from this figure:

- Increasing soil stiffness (and thus decreasing pile-to-soil stiffness contrast) still shifts the corner frequency higher, as was seen in Figure 4.17 when the results were plotted versus plain frequency.
- Likewise, increasing pile stiffness (which is best characterized by flexural rigidity  $E_p I_p$ ) shifts the corner frequency down—it is apparent in Figure 4.19(a) that the larger-diameter piles result in more significant pile–soil interaction and thus produce lower transfer function ordinates.
- Figure 4.19(b) confirms a lack of dependence on pile slenderness ratio  $L/B$ , consistent with Anoyatis et al. [2013].

Again, it should be reiterated that the first two trends in the above list are not captured by elastic analytical solutions. The primary driver of these trends is that decreasing soil stiffness and increasing pile stiffness result in greater pile–soil interaction nonlinearity.

In addition to the variability exhibited by the means of each pile/site combination relative to one another, it is apparent that individual transfer functions show significant fluctuations relative to the smooth curves produced by elastic solutions (e.g., examine the individual transfer functions

in Figures 4.1 through 4.12). One of the causes of this variability is that pile/site combinations which are initially the same but then subjected to different ground motions exhibit different levels of nonlinearity due to free-field site response and pile–soil interaction. While the former effect is only approximately reflected in the results by means of the variable displacement time series imposed on each  $p$ - $y$  spring, nonlinearity due to pile–soil interaction directly alters the pile-to-soil stiffness contrast. The effect of this interaction nonlinearity is difficult to isolate in the resulting transfer function, because the level of nonlinearity varies over the duration of the earthquake.

A related effect is due to the variable frequency content between the different input motions. By using a nonlinear time-domain solution, the pile–soil system is subjected and responds to energy at multiple frequencies and amplitudes simultaneously, just like in a real earthquake. The resulting interaction of nonlinear responses to different frequencies can have a significant influence on the results that is not captured by elastic solutions, which assume the system response to all frequencies can be superimposed. As a simple example, consider excitation of a pile–soil system by a signal containing a low-frequency, large-amplitude pulse, and a second high-frequency component with a smaller amplitude. For an elastic system, the transfer function will be the same regardless of when the low-frequency energy arrives relative to the high-frequency waves. For a nonlinear system, if the high-frequency energy arrives during the low-frequency pulse such that the pulse has resulted in significant  $p$ - $y$  softening, the high-frequency excitation effectively occurs during a period of softened pile-to-soil stiffness contrast. Hence, the transfer function ordinate at the high frequency will be lower compared to a case where the high-frequency energy excitation occurs prior to the low-frequency pulse arrival.

Again, the effect of variable frequency content demonstrated by the preceding example is hard to pinpoint in the computed transfer functions, because many more than two frequencies of excitation are present in the input motions, and the effect of variable frequency content is conflated with the other effects discussed in this section. Rather, it can generally be stated that the effect of variable frequency content along with time-variable pile–soil interaction nonlinearity is to increase fluctuations in the computed transfer functions relative to the idealized elastic case. Moreover, the interplay of these effects with highly variable stratigraphy, as opposed to uniform or smoothly varying soil stiffness, further increases the irregularity of the transfer functions computed herein relative to elastic solutions.

In summary, the key parameters controlling kinematic pile–soil interaction are:

- Pile head-fixity condition
- Pile-to-soil stiffness contrast
- Variations in soil stiffness over the pile length
- Nonlinear soil behavior due to pile-soil-interaction, which depends on relative pile-to-soil stiffness contrast, and due to free-field ground response
- Radiation damping
- Variable frequency content of the free-field excitation

The key differences between simplified elastic solutions and the nonlinear results computed for the more realistic conditions considered in this study are caused by the latter three factors in the above list.

The results presented above make it clear that although using an elastic solution may provide a reasonable approximation of average behavior, it cannot capture the variability that is possible when more realistic subsurface conditions and ground motions are used along with explicit consideration of nonlinearity. It is noteworthy, and rather convenient, that the elastic solutions are approximately coincident with the average results of this study. While this suggests that elastic solutions provide a reasonable first-order approximation of behavior, it also means that they over-predict reductions in free-field motions roughly half the time. A need to capture the impact of realistic conditions, which is reflected by the variability in the results computed for this study, is the motivation for development of predictive models in the following sections.

#### 4.4 GENERALIZED MODELS FOR PREDICTING TRANSFER FUNCTIONS

The results presented above demonstrate that when the nonlinear transfer functions computed for this study are normalized using dimensionless frequency  $\omega/(\lambda V_s)$ , consistent trends are exhibited between the individual results, but significant dispersion still exists about the mean trend. In this section, predictive models (i.e., equations with a specified functional form) are developed to predict this variability so that it can be represented in transfer functions used for design applications. Coefficients used in these models depend on the controlling parameters identified in the previous section. Similar models are developed for predicting spectral ratios in the following section.

Two potential approaches for developing the models were considered. Each begins with specifying a functional form, which is described in more detail in the following subsection. For now, consider the functional form suggested by Anoyatis et al. [2013] for fixed-head piles:

$$H_u = \frac{u_{FIM}}{u_{FFM}} = \frac{1}{1 + C_0 \left( \frac{\omega}{\lambda V_s} \right)^{C_1}} \quad (4.1)$$

in which Anoyatis et al. recommended values of  $C_0 = 0.25$  and  $C_1 = 4$  for the coefficients. Equation (4.1) with these values for the coefficients is plotted in Figure 4.13 through Figure 4.15. The first option for a fixed-head pile transfer function predictive model would be to add terms to Equation (4.1) that are functions of dimensionless frequency and other parameters in an attempt to achieve better normalization, for example:

$$H_u = \frac{1}{1 + C_0 \left( \frac{\omega}{\lambda V_s} \right)^{C_1}} + f_0 \left( \frac{\omega}{\lambda V_s}, parameter_0 \right) + f_1 \left( \frac{\omega}{\lambda V_s}, parameter_1 \right) + \dots etc. \quad (4.2)$$

Mathematically speaking, many potential variations of this approach are possible, e.g., including terms in the denominator of the fraction rather than as additive terms. The alternative approach is to leave the functional form of the model unchanged—e.g., the use of Equation (4.1)—and develop regression models to predict the coefficients:

$$C_j = \beta_0 f(\text{predictor}_0) + \beta_1 f(\text{predictor}_1) + \dots \beta_n f(\text{predictor}_n) + \text{intercept} \quad (4.3)$$

Equation (4.3) is an example of a multiple linear regression model for predicting a coefficient  $C_j$  as a linear combination of functions of predictor variables, each with an independent coefficient (slope)  $\beta$ . In a multiple linear model, functions of predictor variables do not necessarily have to be linear, but they must be combined in a linear fashion. For example, the following is a permissible multilinear model:

$$C_j = \beta_0(\text{predictor}_0) + \beta_1(\text{predictor}_0^2) + \text{intercept} \quad (4.4)$$

while this is not:

$$C_j = \beta_0(\text{predictor}_0) + [\beta_1(\text{predictor}_0)]^2 + \text{intercept} \quad (4.5)$$

The approach of using multiple linear regression to predict individual coefficients rather than attempting to modify the functional form has several benefits. First, performing multiple linear regressions for one coefficient model at a time is much simpler and faster than performing a nonlinear mixed-effects regression on the entire 60,000+ data points reflected in each of the Figure 4.13 through Figure 4.15. Second, it maintains the ability to compare to elastic solutions. If the functional form were modified to improve normalization of the nonlinear results, the  $x$ -axis value of the normalized plots would no longer have a clear physical meaning like  $\omega/(\lambda V_S)$  does. A modified  $x$ -axis variable would also complicate the process of converting the normalized transfer function back to  $H_u$  as a function of plain frequency, a necessary step to actually implement the transfer function for practical applications. Furthermore, there would be no clear way to express the elastic solutions in the new normalized space if the  $x$ -axis values were functions of parameters describing nonlinearity. It is useful to retain the ability to make the elastic versus nonlinear comparison, because it highlights the shortcoming of elastic solutions in terms of their inability to predict the variability that occurs when realistic conditions are modelled. Hence, the multiple linear regression approach is used here.

Predictor variables used in the multiple linear regression models must capture the physical mechanisms that control kinematic pile–soil interaction in order for the models to be meaningful and reliable. The recent work by Anoyatis et al. [2013] and Di Laora and Rovithis [2014] shows that the  $\omega/(\lambda V_S)$  normalization scheme captures two of the controlling parameters well for elastic conditions: (i) pile-to-soil stiffness contrast and (ii) the ratio of pile characteristic length to the wavelength of free-field excitation, which controls the frequency-dependence of the problem. Hence, the primary goal of the of the coefficient prediction models is to capture the effects that are not present in the elastic solutions, namely:

- Nonlinearity due to pile–soil interaction.
- The influence of ground response on the free-field motions that excite the pile, and nonlinearity associated with the free-field response.
- Ground motion intensity and frequency content characteristics.
- Furthermore, parameters used in the models should be dimensionless if possible
- Easy to define with routine project information, i.e., without the need for *in situ* or laboratory testing that is outside the bounds of conventional practice, and using readily-quantifiable structural properties.

- Based on parameters consistent with the level of seismic hazard analysis appropriate for the project. For example, if spectral ratios are desired for a response-spectrum based design, the parameters in the spectral ratio prediction model should be based on the free-field response spectrum rather than requiring parameters that describe an appropriate acceleration time series.

#### 4.4.1 Functional Form

The functional forms used here for fixed- and free-head horizontal displacement transfer functions are adopted from the Anoyatis et al. [2013] and Rovithis et al. [2009] studies, respectively. Note that Anoyatis et al. provide results for free-head piles in terms of plots of normalized transfer functions, but they only present a best-fit function for the fixed-head case. Although Rovithis et al. do not present the free-head function in the same form that it is presented below, the form below can be derived from other equations presented in their paper.

Prior to adopting these previously-established functional forms, an independent study was conducted to derive expressions for the fixed- and free-head cases in order to evaluate if alternative forms existed that could capture the underlying trends with fewer coefficients or simply provide a better fit. To do this, the derivation presented in Chapter 2 was distilled down to the simplest possible mathematical form, and then terms were dropped one at a time to evaluate whether or not each term was necessary to capture the underlying trends. This exercise produced results that were essentially the same as Anoyatis et al. [2013] and Rovithis et al. [2009], presumably because they used a similar process, so their functional forms will be used herein.

The functional form for normalized (i.e., versus dimensionless frequency) fixed-head transfer functions is:

$$H_u = \frac{u_{FIM}}{u_{FFM}} = \frac{1}{1 + C_0 \left( \frac{\omega}{\lambda_{L_a} V_{S,L_a}} \right)^{C_1}} \quad (4.6)$$

The only difference between this functional form and Equation (4.1) used by Anoyatis et al. [2013] is that Equation (4.6) uses  $\lambda_{L_a}$  and  $V_{S,L_a}$ , that is, values of  $\lambda$  and  $V_S$  computed over the depth increment corresponding to the uppermost active length of the pile. This makes Equation (4.6) consistent with the form recommended by Di Laora and Rovithis [2014], who proposed  $C_0 = 0.3$  and  $C_1 = 3$  as an approximate best-fit to their elastic results.

The functional form for normalized free-head horizontal displacement transfer functions is:

$$H_u = \frac{u_{FIM}}{u_{FFM}} = \frac{1}{1 + C_2 \left( \frac{\omega}{\lambda_{L_a} V_{S,L_a}} \right)^{C_3}} \left[ 1 + C_4 \left( \frac{\omega}{\lambda_{L_a} V_{S,L_a}} \right)^{C_5} \right] \quad (4.7)$$

The second term in Equation (4.7) containing coefficients  $C_4$  and  $C_5$  captures the kinematic amplification exhibited by free-head piles. Note that although Equation (4.6) appears as the first

term in Equation (4.7), coefficients  $C_0$  and  $C_1$  generally do not take on the same values as  $C_2$  and  $C_3$  for a given pile/site/ground-motion combination in which all factors are equal other than the head-fixity condition. Although Rovithis et al. [2009] used the same coefficients for this portion of their free- and fixed-head equations, the models developed herein were found to have more predictive power if the coefficients were defined independently for each head-fixity case.

To the best of the authors' knowledge, no functional form for the underlying trend of free-head pile rotation transfer functions has previously been established. The curve shown in Figure 4.15 for Anoyatis et al. is simply a replication of results they presented graphically. Based on the similarity between these transfer functions (see Figure 4.15) and the kinematic amplification region of free-head horizontal displacement transfer functions (see Figure 4.14), the following functional form for normalized free-head rotation transfer functions has been established for this study:

$$H_{\theta} = \frac{\theta_{FIM}}{u_{FFM} \cdot \lambda_{L_a}} = \frac{C_6 \left( \frac{\omega}{\lambda_{L_a} V_{S,L_a}} \right)^{C_7}}{1 + C_8 \left( \frac{\omega}{\lambda_{L_a} V_{S,L_a}} \right)^{C_9}} \quad (4.8)$$

#### 4.4.2 Approach

The statistical software package *R* [R Core Team 2015] was used to aid in development of the multiple linear regression for each coefficient prediction model. The steps taken to develop the models can be summarized as follows:

- Use *R* software to perform nonlinear least-squares regression (NLSR) to determine best-fit coefficients for each transfer function result for fixed- and free-head piles. For example, see Figure 4.20. These values of coefficients become the “targets” that the coefficient models will be used to predict. Computed transfer functions that lacked a significant number of high coherence points or did not extend to a high enough dimensionless frequency such that the underlying trend was well-constrained by the data were excluded from the regression model at this step.
- Evaluate a number of statistically independent predictive parameters for possible inclusion in the models by looking for strong correlation, low standard error, and an approximately linear trend between a given parameter and coefficient. In most cases, a log transformation of both the predictive parameters and pool of target coefficients [e.g.,  $\log(\text{parameter}_i)$  and  $\log(C_i)$ ] was found to improve linearity, correlation, and normality/variance structure of residuals, while in other cases either no transformation or a power transformation was found to be optimum. The Box-Cox test [Box and Cox 1964] was used to determine the optimum transform power.
- Once best candidates for predictive parameters have been identified, use *R* to assess the performance of the models. Begin with a null model (predicted

coefficient = mean of best-fit results from NLSR), then add the single-best standalone predictor and test for statistical significance; look for next-best predictor that can be added that will have most predictive power and statistical significance, etc., until adding additional predictors does not significantly increase the predictive power of the model. This saturation usually occurred once three strong predictors were identified.

- After a model has been developed for each coefficient needed for a given functional form, identify the predictors that (i) have the clearest physical meaning; (ii) have the most predictive power; and (iii) appear in multiple coefficient prediction models. Reformulate all coefficient prediction models to use the same set of predictors. While this may decrease the predictive capability of an individual coefficient prediction model, using the same predictors in each model makes them easier to implement.
- Throughout the process outlined by the above steps, but especially when a potential set of final models has been produced, check that the underlying assumptions of multiple linear regression are satisfied (after Kutner et al. [2004]):
  - Linear relationship between predictor and target parameter
  - Normally-distributed predictor variables, e.g. as tested by a Q-Q plot
  - Little or no multicollinearity between predictor variables
  - Homoscedasticity and lack of autocorrelation of residuals

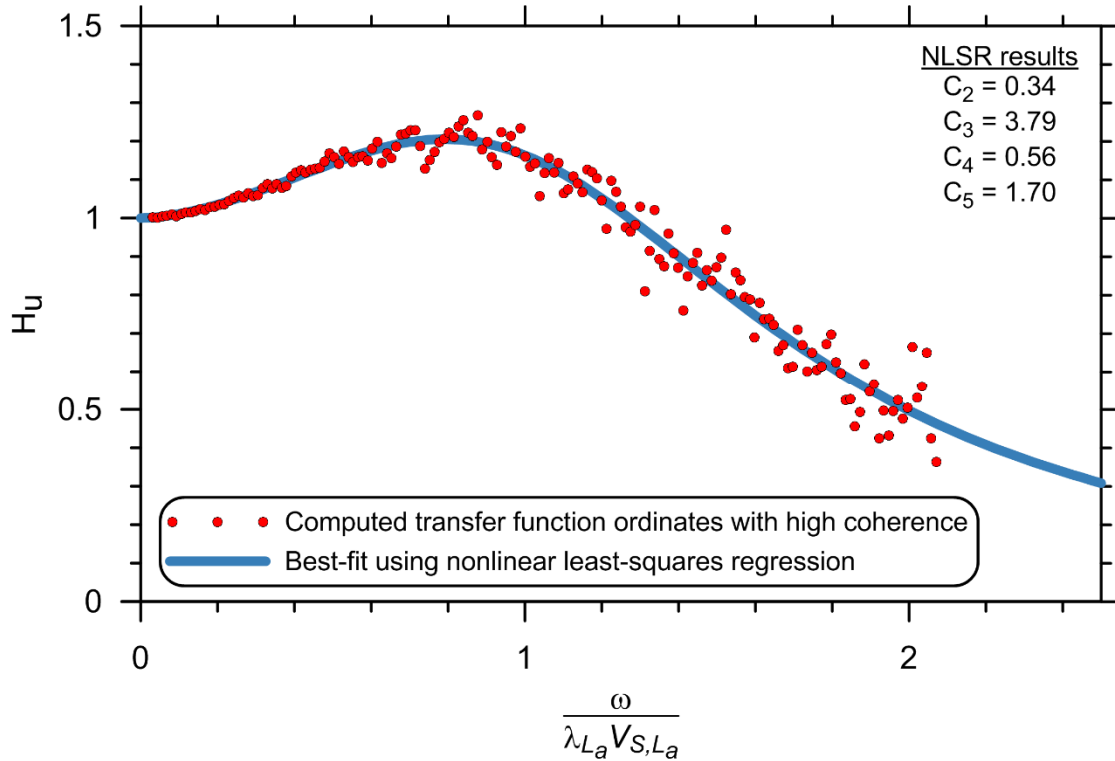


**Figure 4.20** Example of nonlinear least-squares regression to determine coefficients for free-head pile functional form [Equation (4.7)] using computed data for  $B = 2$  m,  $L = 60$  m pile embedded in Site 4 and subjected to 1999 Hector Mine earthquake (NGA record sequence number 1786).

#### 4.4.3 Models for Predicting Fixed-Head Transfer Function Coefficients

Models for predicting the coefficients to be used in Equation (4.6) are given in Equations (4.9) and (4.10). Metrics for assessing the statistical significance of the models are presented in Table 4.1 and Figure 4.21.

$$\log(C_0) = 0.47 \log \left[ \left( \frac{f_m}{\lambda_{L_a} V_{S,L_a}} \right) \left( \frac{PGV}{V_{S,L_a}} \right) \right] - 1.37 \left( \frac{V_{S,L_a}}{V_{S,L}} \right) + 0.046 \left( \frac{PSA_{T=0.5s}}{PSA_{T=0.05s}} \right) + 2.60 \quad (4.9)$$

$$\log(C_1) = -0.065 \log \left[ \left( \frac{f_m}{\lambda_{L_a} V_{S,L_a}} \right) \left( \frac{PGV}{V_{S,L_a}} \right) \right] + 0.38 \left( \frac{V_{S,L_a}}{V_{S,L}} \right) + 0.022 \left( \frac{PSA_{T=0.5s}}{PSA_{T=0.05s}} \right) - 0.14 \quad (4.10)$$

The physical interpretation and motivation for using each of the predictor variables that appear in Equations (4.9) and (4.10) are summarized as follows:

- $\left( \frac{f_m}{\lambda_{L_a} V_{S,L_a}} \right)$  is essentially a dimensionless frequency term, inspired by the dependence of kinematic interaction on  $\omega/(\lambda V_s)$ . The difference is that the term used here corresponds to a single value of frequency  $f_m$ , which is the inverse of the mean period  $T_m$  defined by Rathje et al. [2004]:

$$T_m = \frac{\sum_i FAS_i^2 (1/f_i)}{\sum_i FAS_i^2} \quad \text{for } 0.25 \text{ Hz} \leq f_i \leq 20 \text{ Hz, with } \Delta f \leq 0.05 \text{ Hz} \quad (4.11)$$

where  $FAS_i$  are the Fourier amplitude coefficients from the Fourier Amplitude Spectrum (FAS) of the free-field ground surface motion,  $f_i$  are the frequencies corresponding to each  $FAS_i$ , and  $\Delta f$  is the frequency interval used in the FFT computation. This term will be referred to as “mean frequency” of the surface motion, although Rathje et al. do not use this terminology because they refer to it only in terms of period. Use of mean frequency as a predictor term is a convenient way to represent the frequency content of the ground surface motion with a single value. (Note: in order to be consistent with this model,  $f_m$  must be computed from the ground surface motion and not the input motion used for one-dimensional ground response analysis). Using mean frequency in a dimensionless frequency term effectively compares the pile characteristic length to the wavelength of free-field excitation corresponding to the predominant energy in the ground motion. Finally, the  $\lambda_{L_a}$  term allows the coefficient to have a dependence on pile-to-soil stiffness contrast, which has been demonstrated in this study to influence the results due to its effect on nonlinearity beyond what is captured by the dimensionless frequency term in the basic fixed-head functional form.

- $\left( \frac{PGV}{V_{S,L_a}} \right)$  is a proxy for shear strain in the free field due to ground response, and also serves as a general proxy for ground-motion intensity. The former is based on the fundamental relationship of ground velocity normalized by shear-wave velocity in the transverse direction being equal to shear strain (e.g., see Newmark [1967]). Again, PGV is the peak ground velocity (PGV) of the free-field ground surface motion and is not the base input motion used for ground response analysis. In addition to producing a dimensionless ratio when normalized by shear-wave velocity, PGV was found to be a strong predictor because it is mostly dependent on mid-range frequency content of the ground motion, which is where kinematic pile–soil interaction becomes significant.
- The preceding two terms are multiplied in order to allow the ground motion intensity to interact with the pile-to-soil stiffness term, which is an attempt to capture the increase in pile–soil interaction nonlinearity that is caused by increasing ground-motion intensity.

- $\left(\frac{V_{S,L_a}}{V_{S,L}}\right)$  is the ratio of shear-wave velocity over the uppermost pile active length (hence, near the ground surface) to the shear-wave velocity over the full length of the pile. This quantifies the increase, or lack thereof, in soil stiffness over the length of the pile.
- $\left(\frac{PSA_{T=0.5s}}{PSA_{T=0.05s}}\right)$  is the ratio of free-field ground surface acceleration response spectrum ordinates at 0.5 and 0.05 sec, which serves as another descriptor of free-field ground motion frequency content. The periods 0.5 and 0.05 sec ( $f = 2$  to 20 Hz) were chosen because the transfer function corner frequencies and bandwidth over which significant de-amplification occurs usually falls within this range (e.g., see Figure 4.16). The term may also capture, at least in part, the influence of free-field motion variable frequency-content on nonlinearity as discussed in §4.3.

As shown in Figure 4.19(a), there is variability between the normalized transfer functions computed for the two diameters of piles considered in this study. This is shown again in terms of all computed transfer function ordinates with high coherence in Figure 4.22. This variability provides an opportunity to test the predictive capabilities of the coefficient models (4.9) and (4.10) by comparing the mean model predictions to the study results for each diameter independently. Figure 4.23 and Figure 4.24 show that the models match the overall trends exhibited by the two sizes of piles well. Note that although this variability is discussed here in terms of diameter, the actual behavior is better characterized by its dependence on  $E_p I_p$ , and diameter only appears in the functional form and coefficient prediction models through its inclusion in the  $E_p I_p$  term.

**Table 4.1 Fixed-head transfer function coefficient prediction model metrics.**

<b>Coefficient:</b>	<b>Adjusted R<sup>2</sup></b>	<b>F-Statistic</b>	<b>P-Value</b>
C <sub>0</sub>	0.44	139	2.2E-16
C <sub>1</sub>	0.19	43	2.2E-16

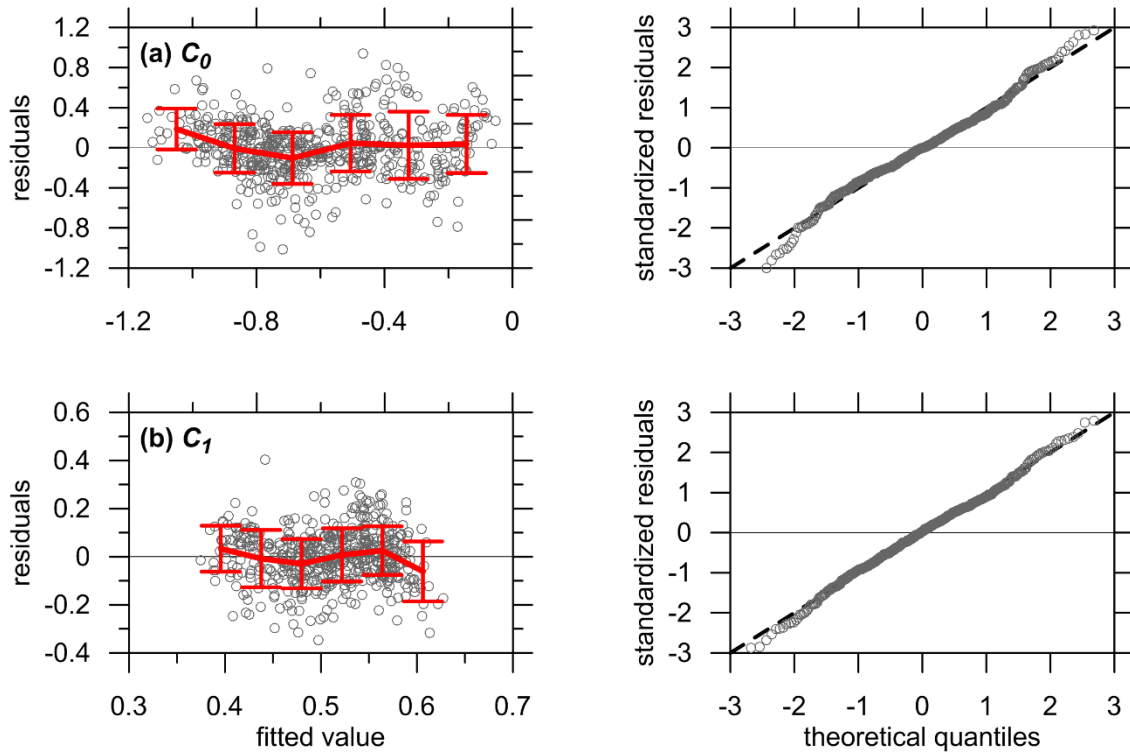


**Figure 4.21** Residuals versus predicted values plots (left) and normal Q-Q plots (right) for fixed-head transfer function coefficient prediction models. Lines on residuals plots show trend and  $\pm$  one standard deviation.

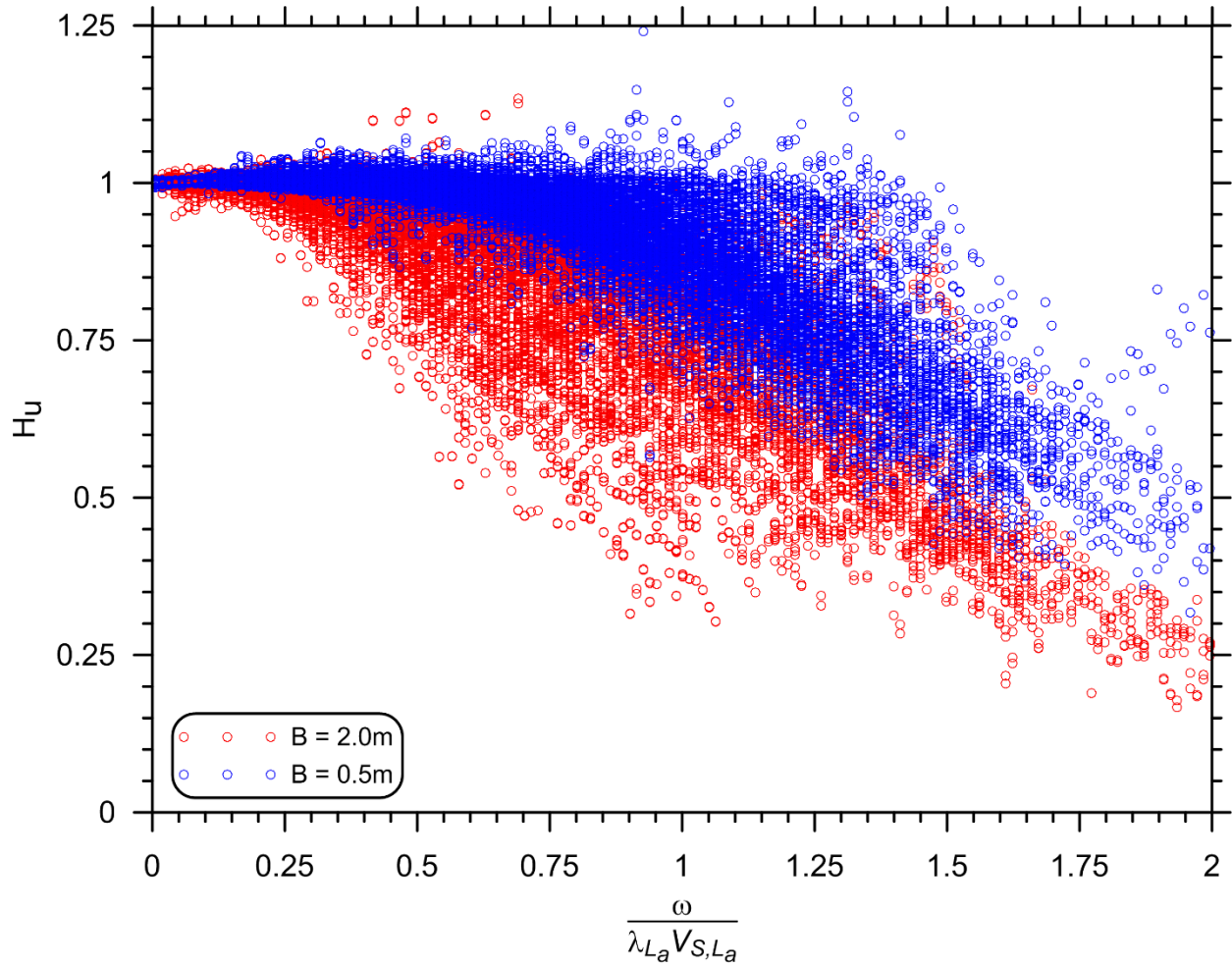


**Figure 4.22** Variability in fixed-head transfer function results for the two pile diameters considered in this study.

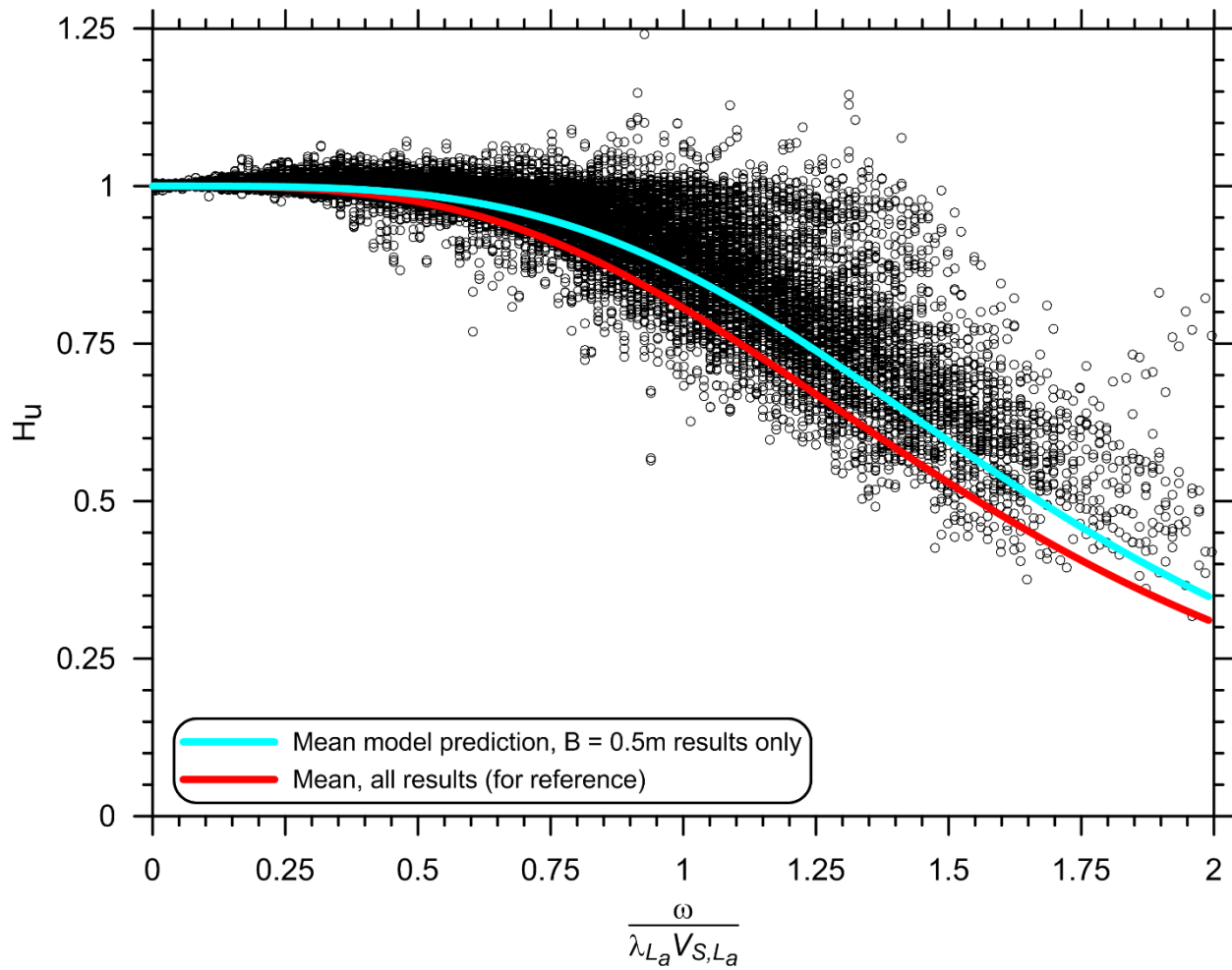


**Figure 4.23** Mean fixed-head transfer function model prediction for  $B = 0.5$  m compared to computed results.

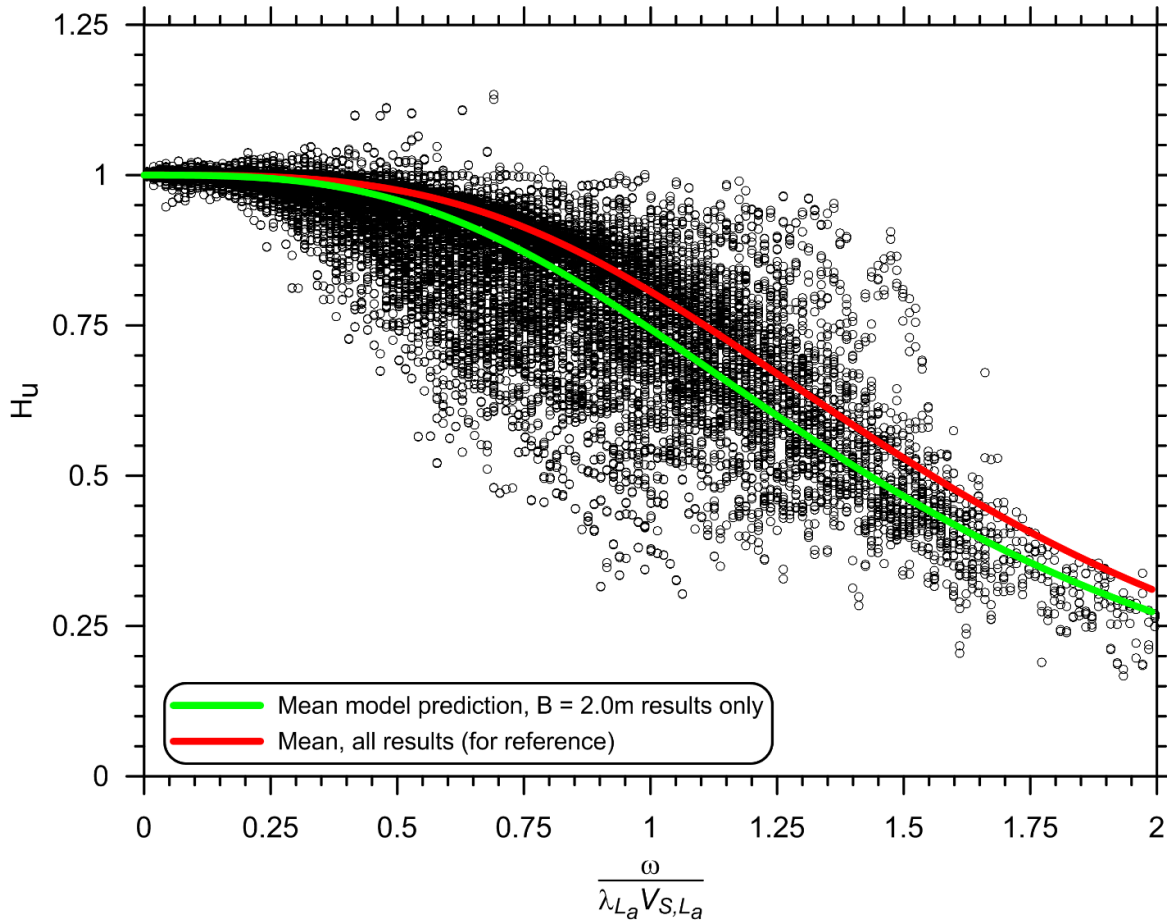


**Figure 4.24 Mean fixed-head transfer function model prediction for  $B = 2.0$  m compared to computed results.**

#### 4.4.4 Models for Predicting Free-Head Displacement Transfer Function Coefficients

Models for predicting the coefficients to be used in Equation (4.7) are given in Equations (4.12) through (4.15). Metrics for assessing the statistical significance of the models are presented in Table 4.2 and Figure 4.25. The same predictive parameters used for the fixed-head pile coefficient prediction models were used here for the free-head case, and the physical meaning and motivation for each parameter that was described above applies here as well.

$$\log(C_2) = 1.18 \log \left[ \left( \frac{f_m}{\lambda_{L_a} V_{S,L_a}} \right) \left( \frac{PGV}{V_{S,L_a}} \right) \right] - 0.26 \left( \frac{V_{S,L_a}}{V_{S,L}} \right) + 0.11 \left( \frac{PSA_{T=0.5s}}{PSA_{T=0.05s}} \right) + 5.01 \quad (4.12)$$

$$(C_3)^{-0.79} = 0.10 \log \left[ \left( \frac{f_m}{\lambda_{L_a} V_{S,L_a}} \right) \left( \frac{PGV}{V_{S,L_a}} \right) \right] - 0.074 \left( \frac{V_{S,L_a}}{V_{S,L}} \right) - 0.0015 \left( \frac{PSA_{T=0.5s}}{PSA_{T=0.05s}} \right) + 0.86 \quad (4.13)$$

$$(C_4)^{-0.31} = -0.63 \log \left[ \left( \frac{f_m}{\lambda_{L_a} V_{S,L_a}} \right) \left( \frac{PGV}{V_{S,L_a}} \right) \right] + 0.20 \left( \frac{V_{S,L_a}}{V_{S,L}} \right) - 0.056 \left( \frac{PSA_{T=0.5s}}{PSA_{T=0.05s}} \right) - 1.73 \quad (4.14)$$

$$\log(C_5) = -0.049 \log \left[ \left( \frac{f_m}{\lambda_{L_a} V_{S,L_a}} \right) \left( \frac{PGV}{V_{S,L_a}} \right) \right] + 0.18 \left( \frac{V_{S,L_a}}{V_{S,L}} \right) + 0.026 \left( \frac{PSA_{T=0.5s}}{PSA_{T=0.05s}} \right) - 0.20 \quad (4.15)$$

As for the fixed-head pile transfer functions, the free-head transfer functions exhibit variability between the two diameters considered in the study. Figure 4.26 and Figure 4.27 demonstrate that the coefficient prediction models are capable of capturing these trends well.

**Table 4.2 Metrics for free-head displacement transfer function coefficient prediction models.**

<b>Coefficient:</b>	<b>Adjusted R<sup>2</sup></b>	<b>F-Statistic</b>	<b>P-Value</b>
C <sub>2</sub>	0.51	72	2.2E-16
C <sub>3</sub>	0.22	21	8.0E-12
C <sub>4</sub>	0.47	62	2.2E-16
C <sub>5</sub>	0.06	5	1.5E-3

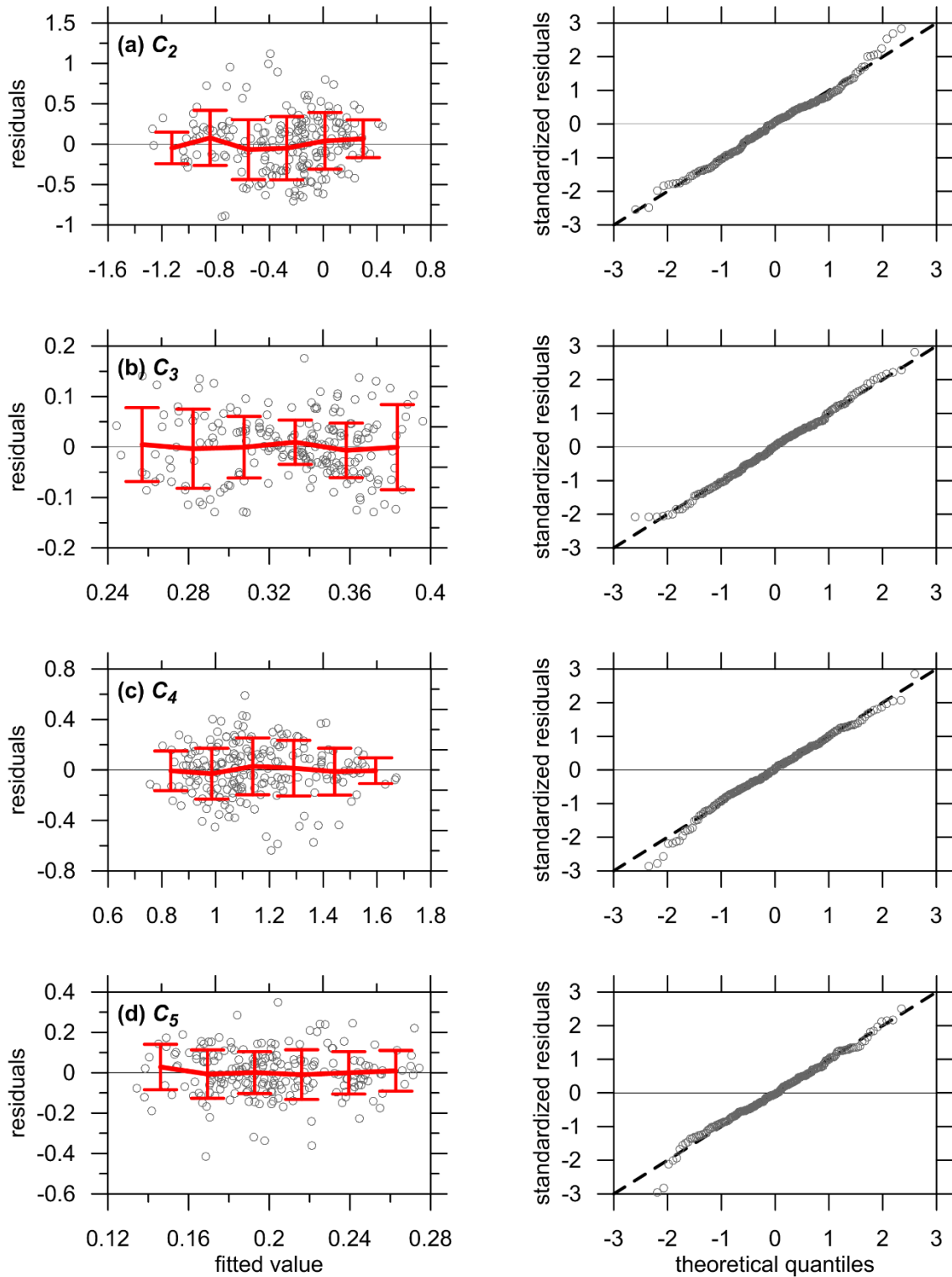


**Figure 4.25** Residuals versus predicted values plots (left) and normal Q-Q plots (right) for free-head displacement transfer function coefficient prediction models. Lines on residuals plots show trend and  $\pm$  one standard deviation.

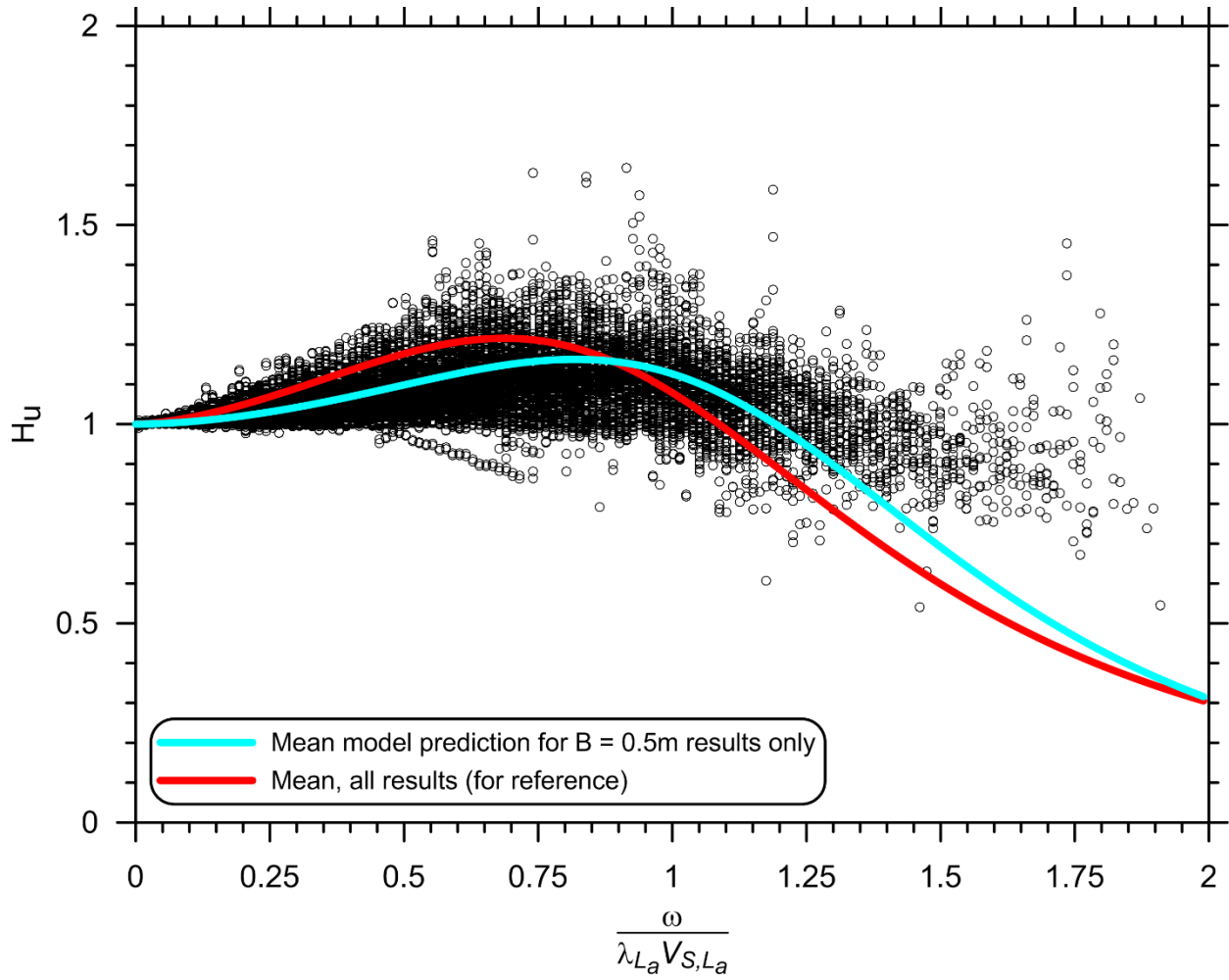


**Figure 4.26** Mean free-head displacement transfer function model prediction for  $B = 0.5$  m compared to computed results.

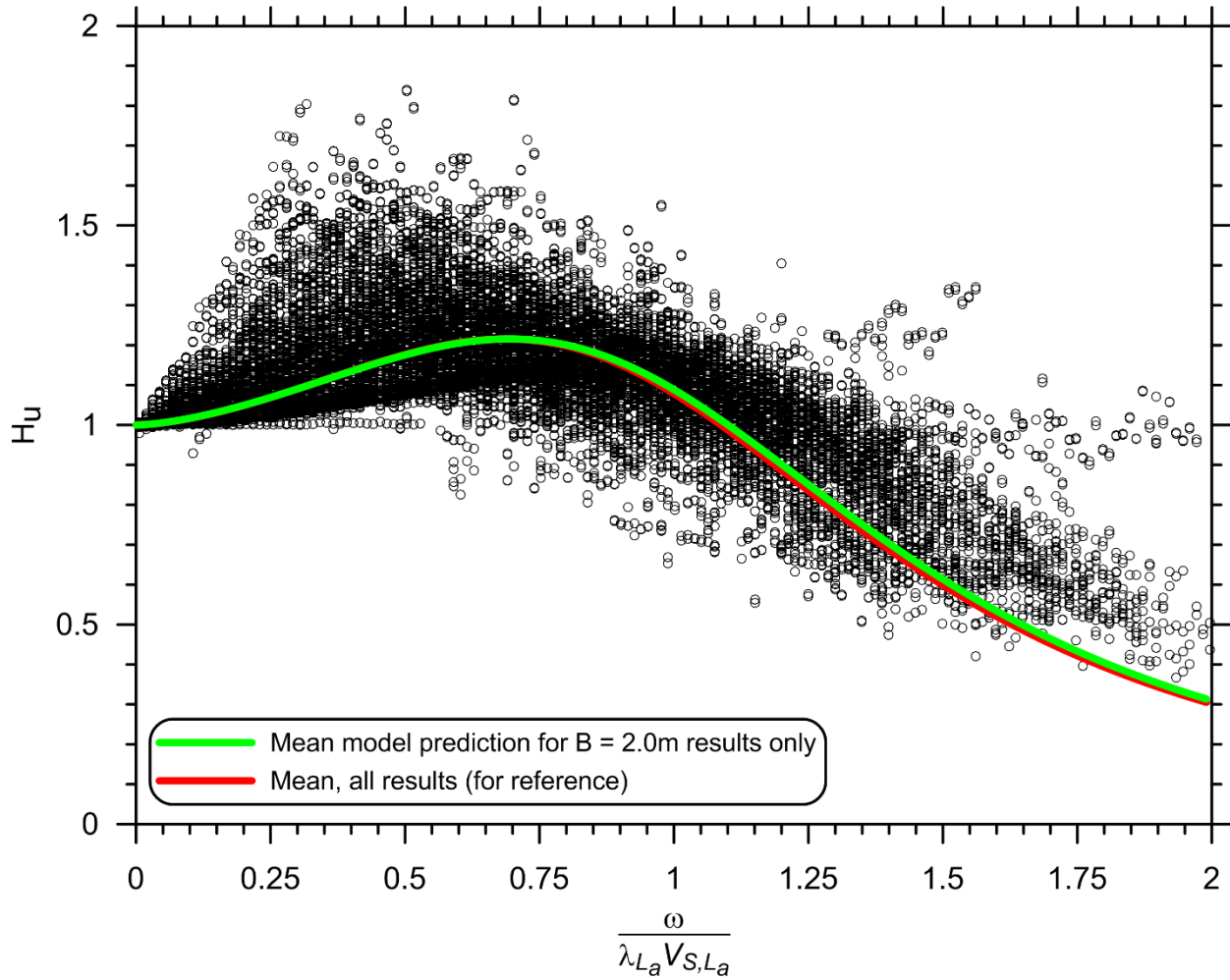


**Figure 4.27 Mean free-head displacement transfer function model prediction for  $B = 2.0$  m compared to computed results.**

#### 4.4.5 Models for Predicting Free-Head Rotation Transfer Function Coefficients

Models for predicting the coefficients to be used in Equation (4.8) are given in Equations (4.16) through (4.19). Metrics for assessing the statistical significance of the models are presented in Table 4.3 and Figure 4.28, and the ability to capture diameter-variability in the results (see Figure 4.29) is shown in Figure 4.30 and Figure 4.31.

$$(C_6)^{-0.69} = -0.44 \log \left[ \left( \frac{f_m}{\lambda_{L_a} V_{S,L_a}} \right) \left( \frac{PGV}{V_{S,L_a}} \right) \right] + 0.31 \left( \frac{V_{S,L_a}}{V_{S,L}} \right) - 0.0066 \left( \frac{PSA_{T=0.5s}}{PSA_{T=0.05s}} \right) - 1.48 \quad (4.16)$$

$$(C_7)^{1.45} = -1.13 \log \left[ \left( \frac{f_m}{\lambda_{L_a} V_{S,L_a}} \right) \left( \frac{PGV}{V_{S,L_a}} \right) \right] - 0.089 \left( \frac{V_{S,L_a}}{V_{S,L}} \right) - 0.16 \left( \frac{PSA_{T=0.5s}}{PSA_{T=0.05s}} \right) - 2.19 \quad (4.17)$$

$$\log(C_8) = 0.92 \log \left[ \left( \frac{f_m}{\lambda_{L_a} V_{S,L_a}} \right) \left( \frac{PGV}{V_{S,L_a}} \right) \right] - 0.44 \left( \frac{V_{S,L_a}}{V_{S,L}} \right) + 0.12 \left( \frac{PSA_{T=0.5s}}{PSA_{T=0.05s}} \right) + 4.07 \quad (4.18)$$

$$(C_9)^{-1.31} = 0.10 \log \left[ \left( \frac{f_m}{\lambda_{L_a} V_{S,L_a}} \right) \left( \frac{PGV}{V_{S,L_a}} \right) \right] + 0.057 \left( \frac{V_{S,L_a}}{V_{S,L}} \right) - 0.012 \left( \frac{PSA_{T=0.5s}}{PSA_{T=0.05s}} \right) + 0.63 \quad (4.19)$$

**Table 4.3 Metrics for free-head rotation transfer function coefficient prediction models.**

<b>Coefficient:</b>	<b>Adjusted R<sup>2</sup></b>	<b>F-Statistic</b>	<b>P-Value</b>
C <sub>6</sub>	0.52	40	2.2E-16
C <sub>7</sub>	0.31	17	4.1E-09
C <sub>8</sub>	0.44	29	1.3E-13
C <sub>9</sub>	0.18	9	2.3E-05

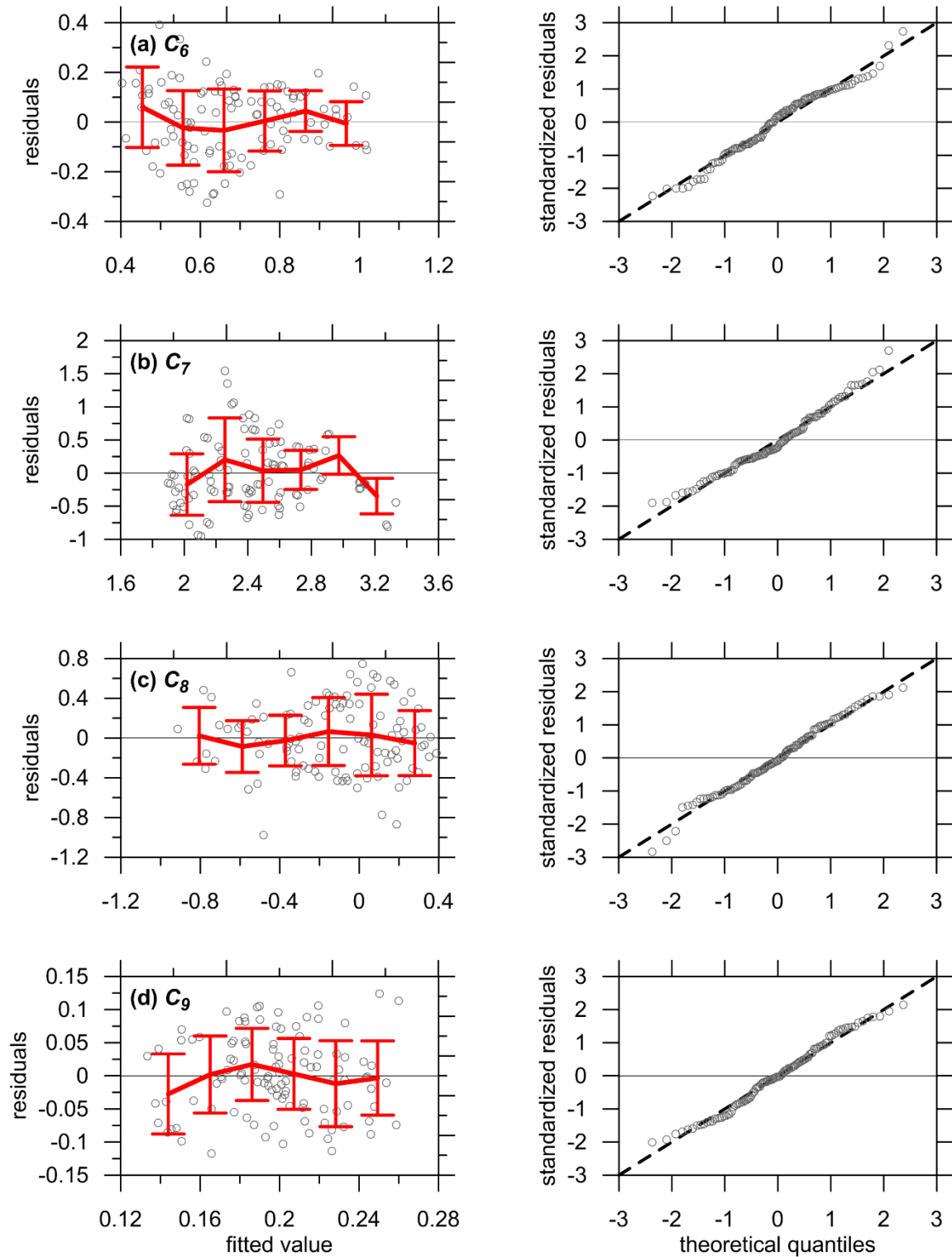


**Figure 4.28** Residuals versus predicted values plots (left) and normal Q-Q plots (right) for free-head rotation transfer function coefficient prediction models. Lines on residuals plots show trend and  $\pm$  one standard deviation.

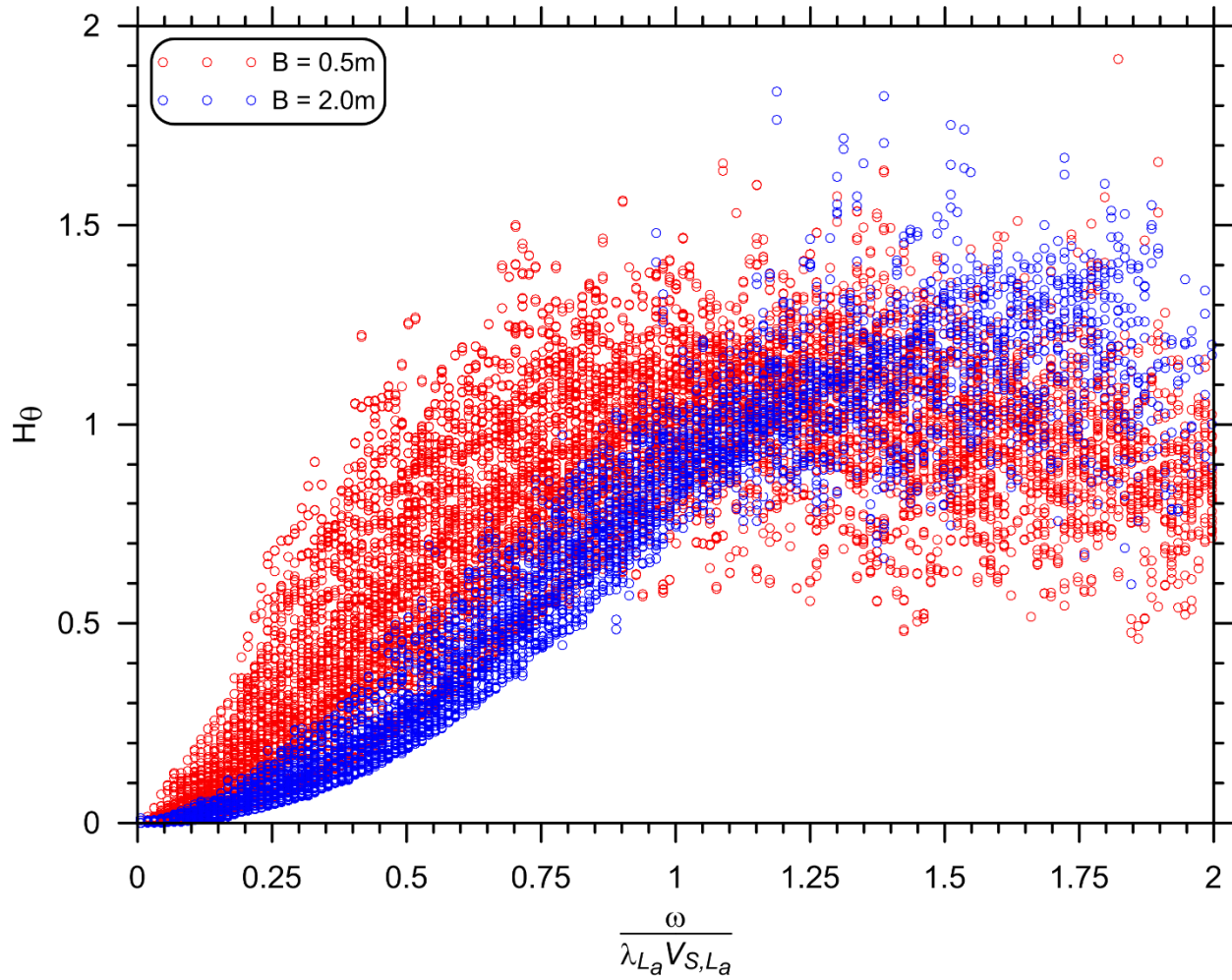


**Figure 4.29** Variability in free-head rotation transfer function results for the two pile diameters considered in this study.

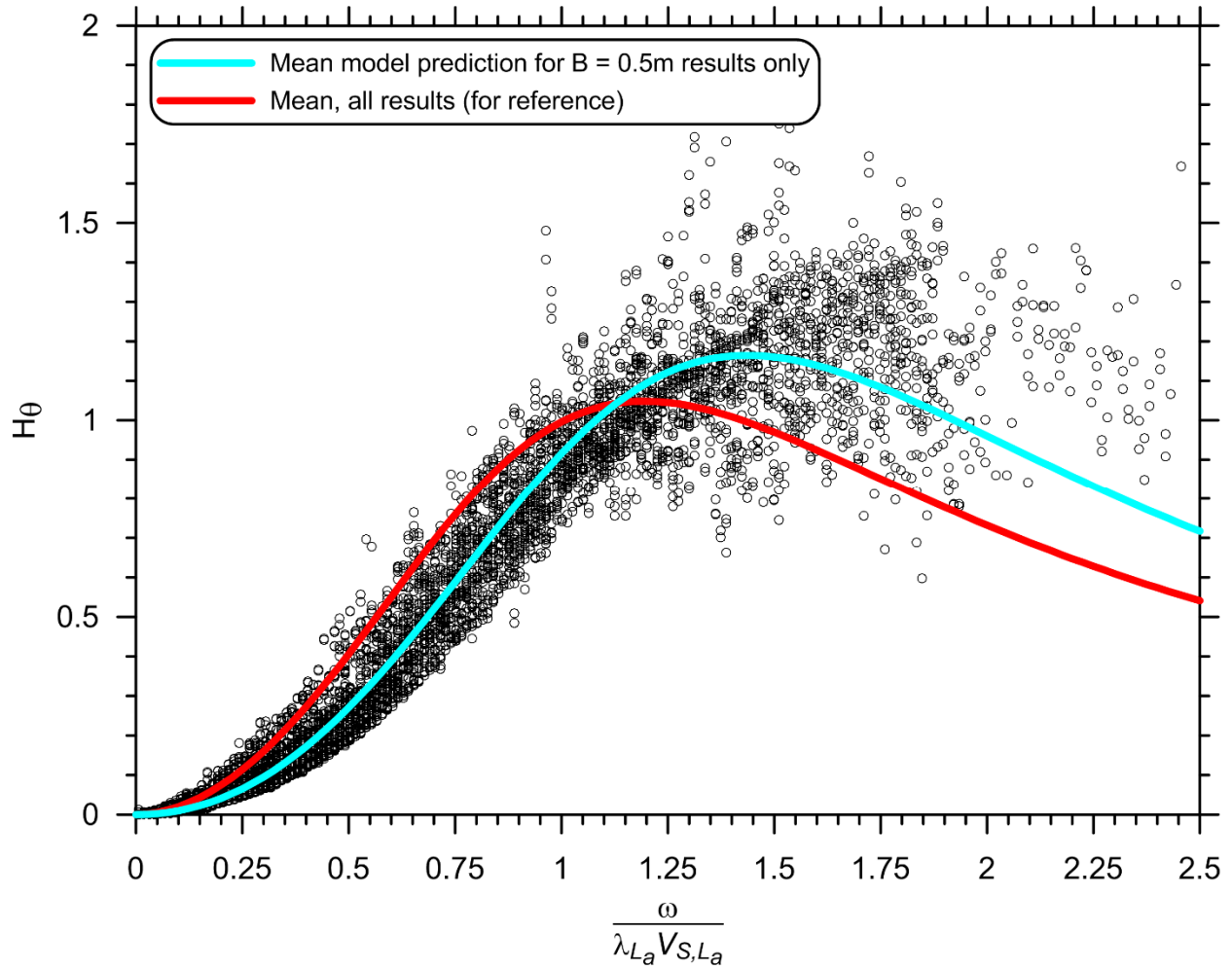


Figure 4.30 Mean free-head rotation transfer function model prediction for  $B = 0.5$  m results.

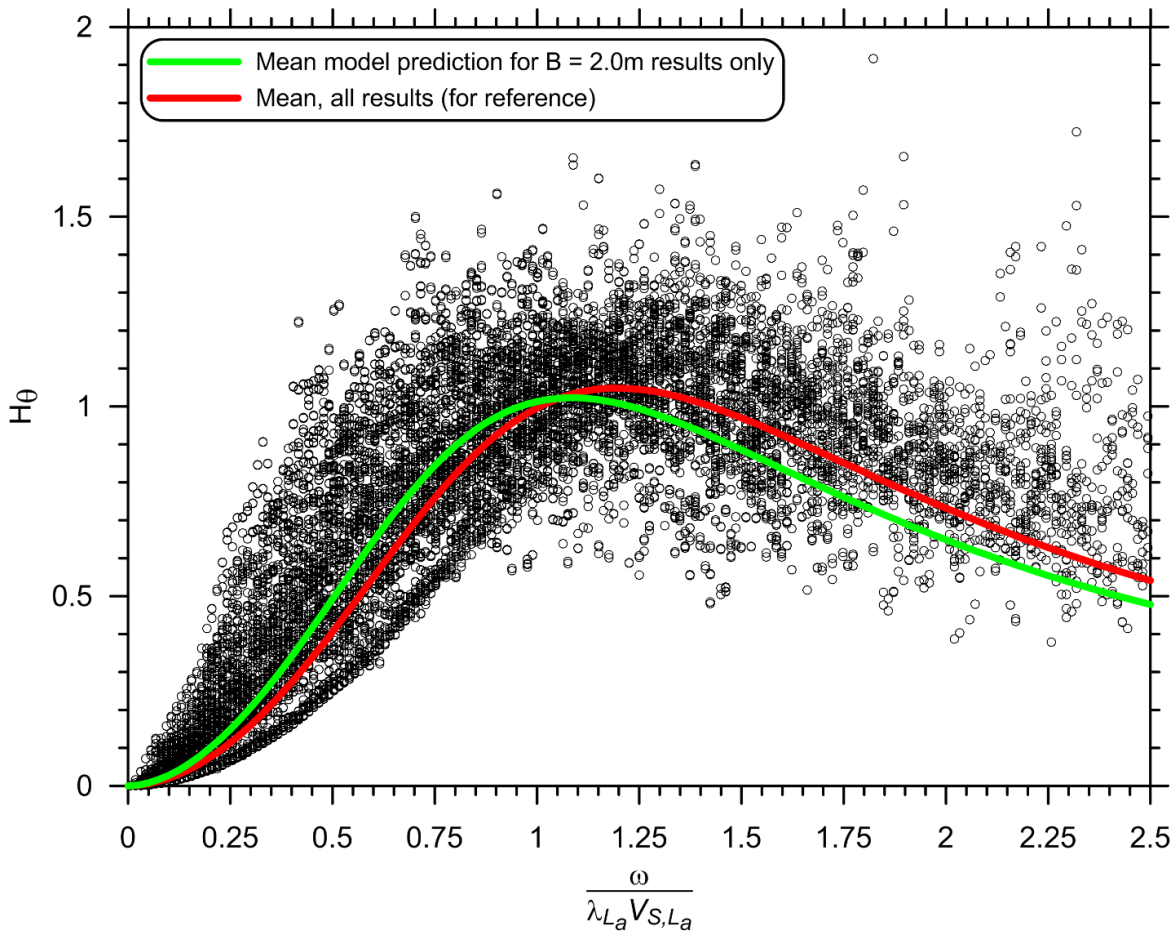


Figure 4.31 Mean free-head rotation transfer function model prediction for  $B = 2.0$  m results.

## 4.5 GENERALIZED MODELS FOR PREDICTING SPECTRAL RATIOS

The same approach described above for development of transfer function prediction models was used to develop models for predicting spectral ratios that include variability due to the controlling parameters identified in §4.3. Spectral ratios primarily depend on the same physical mechanisms that influence transfer functions, except that short-period (high-frequency) spectral ordinates are controlled by the largest amplitude peak in the signals rather than the high-frequency energy. Response spectra used to compute spectral ratios were computed from the free-field ground surface and pile-head motions for 5% damping.

### 4.5.1 Functional Form

Spectral ratios for kinematic pile–soil interaction exhibit a characteristic form in which the ordinates generally decrease with decreasing period, down to some limiting value corresponding to the period  $T_{min}$  (see Figure 4.32). The minimum value defines a transition point in the pile–soil system behavior. At periods below  $T_{min}$  (i.e., frequencies above  $1/T_{min}$ ), spectral acceleration of both the pile head and free-field ground surface motion are controlled by the largest amplitude peak in the respective motions. This behavior is maximized at  $T = 0$  sec (i.e., PGA), when the

spectral acceleration is simply equal to the maximum of the acceleration time series. The largest amplitude peak of design-level earthquake motions usually occurs within mid-range frequencies of 2–5 Hz (e.g., periods around 0.2–0.5 sec), which corresponds to the range over which kinematic pile–soil interaction may be significant for stiff piles in soft soil but relatively insignificant for smaller piles in stiffer soil (see Figure 4.16). Hence the spectral ratio ordinate at zero period depends on the level of kinematic pile–soil interaction that occurs at frequencies corresponding to the peak amplitude of the free-field ground surface motion and for fixed-head piles will approach unity as the level of pile–soil interaction decreases.

The only published work that the authors are aware of in which kinematic pile–soil interaction spectral ratios are computed and discussed in terms of an underlying functional form is the elastic study by Di Laora and Sanctis [2013]. The functional form used here for fixed-head piles is adopted from their study:

$$\frac{PSA_{FIM}}{PSA_{FFM}} = \begin{cases} R_0 - (R_0 - R_{min}) \left( \frac{T}{T_{min}} \right)^2; & T \leq T_{min} \\ 1 - (1 - R_{min}) \left( \frac{T_{crit} - T}{T_{crit} - T_{min}} \right)^2; & T_{min} \leq T \leq T_{crit} \\ 1 & T \geq T_{crit} \end{cases} \quad (4.20)$$

Equation (4.20) is a piecewise combination of two parabolas and a straight line, where  $R_0$  and  $R_{min}$  are coefficients defining the spectral ratio at a period of zero and the minimum spectral ratio, and  $T_{min}$ , and  $T_{crit}$  are the period corresponding to the minimum spectral ratio and the period beyond which no significant reduction occurs, respectively. These parameters and the basic functional form are illustrated in Figure 4.32.

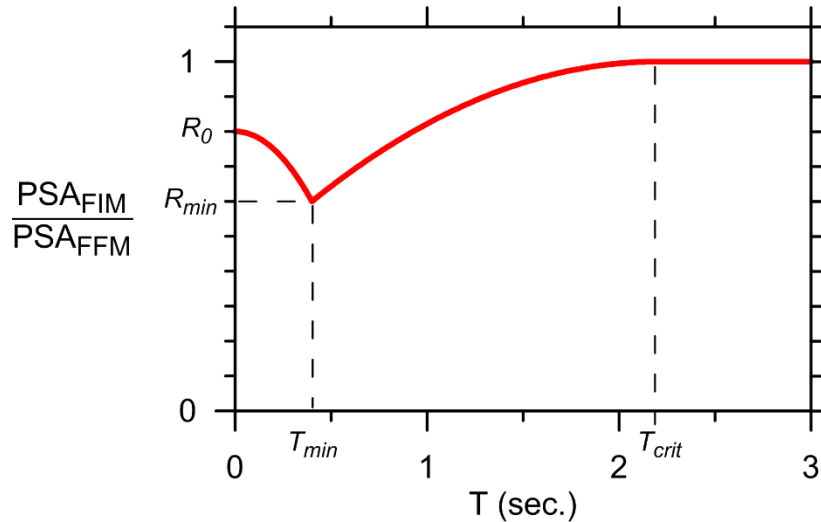
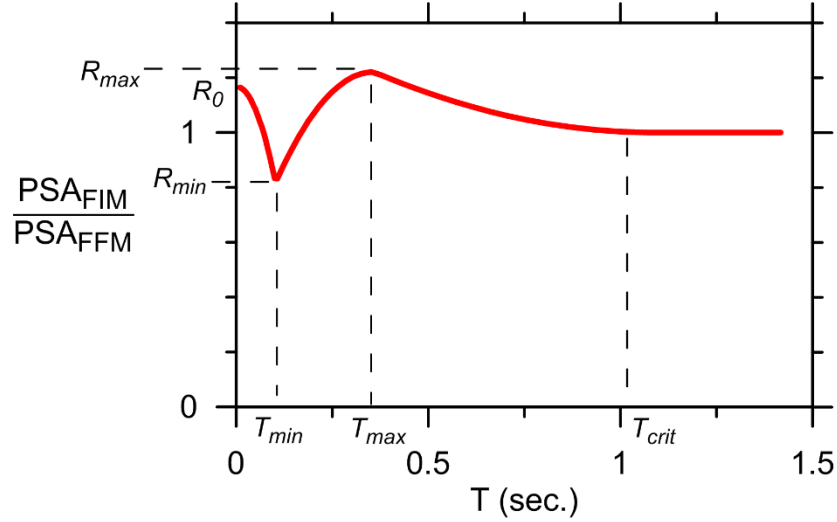


Figure 4.32 Fixed-head pile spectral ratio functional form after Di Laora and Sanctis [2013].



**Figure 4.33 Free-head pile spectral ratio functional form.**

Di Laora and Sanctis only considered fixed-head piles; for free-head pile spectral ratios, the authors are not aware of any published functional forms. The trend exhibited by free-head pile spectral ratios computed for this study is matched well by the following:

$$\frac{PSA_{FIM}}{PSA_{FFM}} = \begin{cases} R_0 - (R_0 - R_{min}) \left( \frac{T}{T_{min}} \right)^2; & T \leq T_{min} \\ R_{max} + \frac{(R_{min} - R_{max})(T - T_{max})^2}{(T_{max} - T_{min})^2}; & T_{min} \leq T \leq T_{max} \\ 1 + \frac{(R_{max} - 1)(T - T_{crit})^2}{(T_{max} - T_{crit})^2}; & T_{max} \leq T \leq T_{crit} \\ 1 & T \geq T_{crit} \end{cases} \quad (4.21)$$

Equation (4.21) is a modified version of the fixed-head form which captures the effect of kinematic amplification on the computed spectral ratios by adding a third parabolic leg to the piecewise formulation. The peak spectral ratio is defined by  $(R_{max}, T_{max})$  as shown in Figure 4.3.

#### 4.5.2 Models for Predicting Fixed-Head Spectral Ratio Coefficients

Models for predicting the coefficients to be used in Equation (4.20) are given in Equations (4.22)–(4.25). Metrics for assessing the statistical significance of the models are presented in Table 4.4 and Figure 4.34.

$$R_{0,FXH} = -0.086 \log \left( \frac{f_0}{\lambda_{L_a} V_{S,L_a}} \right) + 0.047 \left( \frac{V_{S,L_a}}{V_{S,L}} \right) - 0.046 \log \left( \frac{PSA_{max}}{g} \right) + 0.81 \quad (4.22)$$

$$R_{\min,FXH} = -0.38 \log\left(\frac{f_0}{\lambda_{L_a} V_{S,L_a}}\right) - 0.12 \left(\frac{V_{S,L_a}}{V_{S,L}}\right) - 0.026 \log\left(\frac{PSA_{\max}}{g}\right) + 0.16 \quad (4.23)$$

$$(T_{\min,FXH})^{-0.58} = -1.39 \log\left(\frac{f_0}{\lambda_{L_a} V_{S,L_a}}\right) + 4.53 \left(\frac{V_{S,L_a}}{V_{S,L}}\right) + 1.99 \log\left(\frac{PSA_{\max}}{g}\right) - 0.26 \quad (4.24)$$

$$\log(T_{crit,FXH}) = 0.79 \log\left(\frac{f_0}{\lambda_{L_a} V_{S,L_a}}\right) - 0.53 \left(\frac{V_{S,L_a}}{V_{S,L}}\right) - 0.27 \log\left(\frac{PSA_{\max}}{g}\right) + 1.01 \quad (4.25)$$

Note that  $T_{min}$  and  $T_{crit}$  in Equations (4.24) and (4.25) are in seconds.

The physical interpretation and motivation for using each of the predictor variables that appear in Equations (4.22) through (4.25) are summarized as follows:

- Similar to the transfer function models, the  $\left(\frac{f_0}{\lambda_{L_a} V_{S,L_a}}\right)$  term is a dimensionless frequency computed at a single frequency value. In this case  $f_0$  is used, which is the inverse of the “smoothed spectral predominant period” period  $T_0$  defined by Rathje et al. [2004]:

$$T_0 = \frac{\sum_i T_i \cdot \ln\left(\frac{PSA(T_i)}{PGA}\right)}{\sum_i \ln\left(\frac{PSA(T_i)}{PGA}\right)} \quad \text{for } T_i \text{ with } \frac{PSA}{PGA} \geq 1.2, \Delta \log T_i \leq 0.02 \quad (4.26)$$

where  $T_i$  are the discrete periods in the acceleration response spectrum equally spaced on a log axis and  $PSA(T_i)$  are the spectral accelerations at periods  $T_i$ . If the spacing criterion is not satisfied, the spectral values must be interpolated over a closer log interval. Equation (4.26) essentially extracts the spectral ordinates that are greater than 1.2 times PGA, thus exhibiting significant amplification and returns the period corresponding to the peak of a smoothed curve of these ordinates. The way in which  $T_0$  is defined makes it mostly dependent on the moderate- to high-frequency content of a ground motion, which is the important range for kinematic pile–soil interaction. As demonstrated by Rathje et al.,  $T_0$  is also a better overall descriptor of the mean frequency content of the motion than the peak of the unsmoothed spectrum because it represents a weighted average of the entire period bandwidth over which amplification occurs, and thus is not controlled by a single peak that may have narrow bandwidth. Furthermore,  $f_0$  was chosen because it is defined from the free-field ground surface motion response spectrum. For design applications in which spectral ratios for kinematic pile–soil interaction are desired, it would be impractical to have to compute a parameter like  $f_m$  which is defined by a ground motion

time series instead of a response spectrum. The empirical relationships developed by Rathje et al. could also be used to predict  $f_0$  for use in Equations (4.22)–(4.25) at the planning stages of a project or for cases when a site-specific seismic hazard analysis to define response spectra is not performed.

- $\left(\frac{V_{S,L_a}}{V_{S,L}}\right)$  quantifies changes in soil stiffness over the length of the pile.
- $\left(\frac{PSA_{\max}}{g}\right)$  is simply the maximum spectral acceleration normalized by gravity

such that the term is dimensionless. This measure of ground-motion intensity serves as a proxy for nonlinearity and was found to be a more effective predictor than spectral acceleration at any one specified period. As discussed above, the maximum spectral acceleration also plays an important role in defining the zero-period ordinate and thus is a powerful predictor of  $R_0$ .

**Table 4.4 Fixed-head spectral ratio coefficient prediction model metrics.**

<b>Coefficient:</b>	<b>Adjusted R<sup>2</sup></b>	<b>F-Statistic</b>	<b>P-Value</b>
$R_0$	0.19	74	2.2E-16
$R_{min}$	0.54	381	2.2E-16
$T_{min}$	0.33	157	2.2E-16
$T_{crit}$	0.70	734	2.2E-16

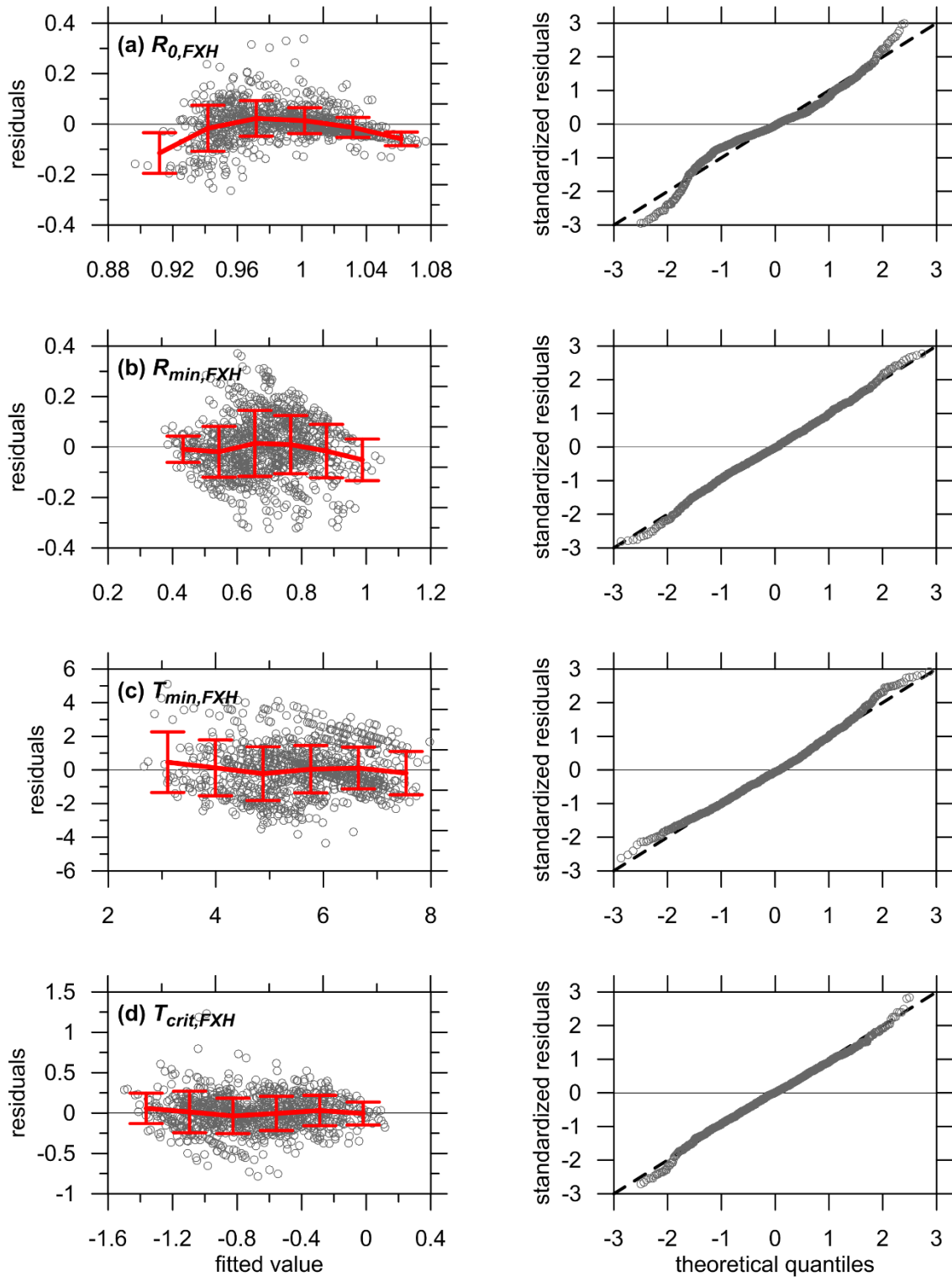


**Figure 4.34** Residuals versus predicted values plots (left) and normal Q-Q plots (right) for fixed-head spectral ratio coefficient prediction models. Lines on residuals plots show trend and  $\pm$  one standard deviation.

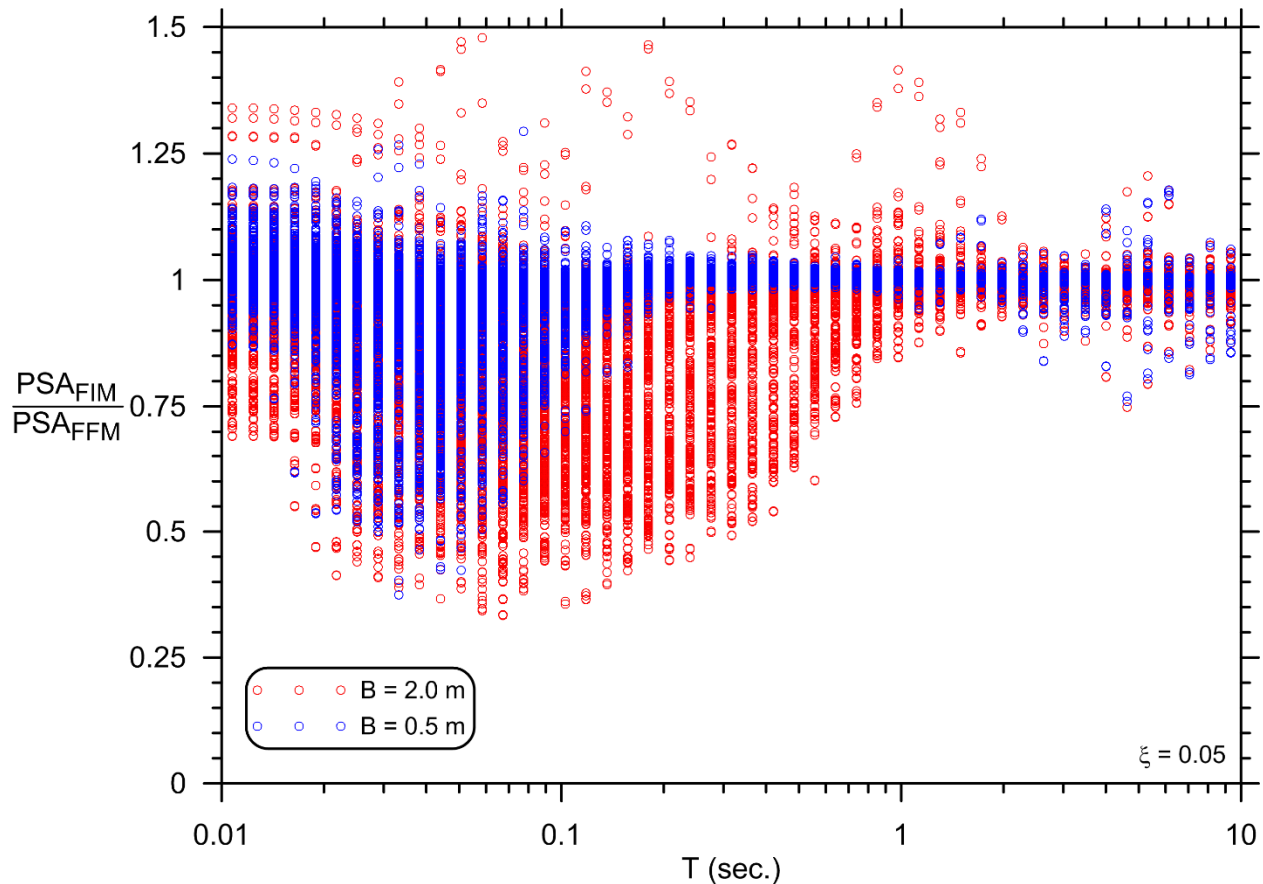


**Figure 4.35 Fixed-head spectral ratio results.**

As for the transfer functions, variability exists in the computed spectral ratios between the two diameters considered for this study (Figure 4.35). Since no normalization scheme is applied to the results—that is, the computed spectral ratios are presented versus period rather than a dimensionless combination of period and other variables—there is variability in the spectral ratio results that has effectively been removed (or at least reduced) from the corresponding normalized transfer function results by using a dimensionless frequency that captures the underlying physics (e.g., Figure 4.13 and Figure 4.14). While it would be possible to first normalize the spectral ratio results using a “dimensionless period” akin to the dimensionless frequency used for transfer functions, this would obscure the meaning of a spectral ratio at a given period. Moreover, promoting the false notion that spectral ratios are simply the mirror image of transfer functions since period is the inverse of frequency is undesirable, so “dimensionless period” is avoided herein.

Residuals between the predictive model and the computed spectral ratio results are shown in Figure 4.36. To compute these residuals, the coefficient prediction models [Equations (4.22)—(4.25)] were applied for a given combination of pile, site, and ground motion properties to predict spectral ratio values at each period. These predicted values were then subtracted from the spectral ratios computed in the parametric analyses for the same combination of pile, site, and ground-motion properties. The mean trend exhibited by the residuals is close to zero, indicating that the predictive model is generally unbiased. Furthermore, the  $\pm$  one standard deviation error bars shown that the majority of the residuals fall close to zero. The  $\pm$  one standard deviation error bars are the

best means of visually assessing these trends because the large number of points (over 60,000) shown on the plot make it visually difficult to assess where the greatest concentration of points lie.

The largest bias occurs around a period of 0.05 to 0.1 sec, which is where the minimum spectral ratio occurs. The mean bias at this period is approximately 0.1, meaning that, on average, predicted spectral ratios are about 10% below those computed for this study. This bias is attributable to the difficulty in predicting the period and corresponding ordinate at which the local minimum in the spectral ratio will occur ( $T_{min}$  and  $R_{min}$ , respectively). In future studies, it may be possible to reduce this bias and/or further reduce the total variability exhibited the residuals, thus improving the reliability of the model.

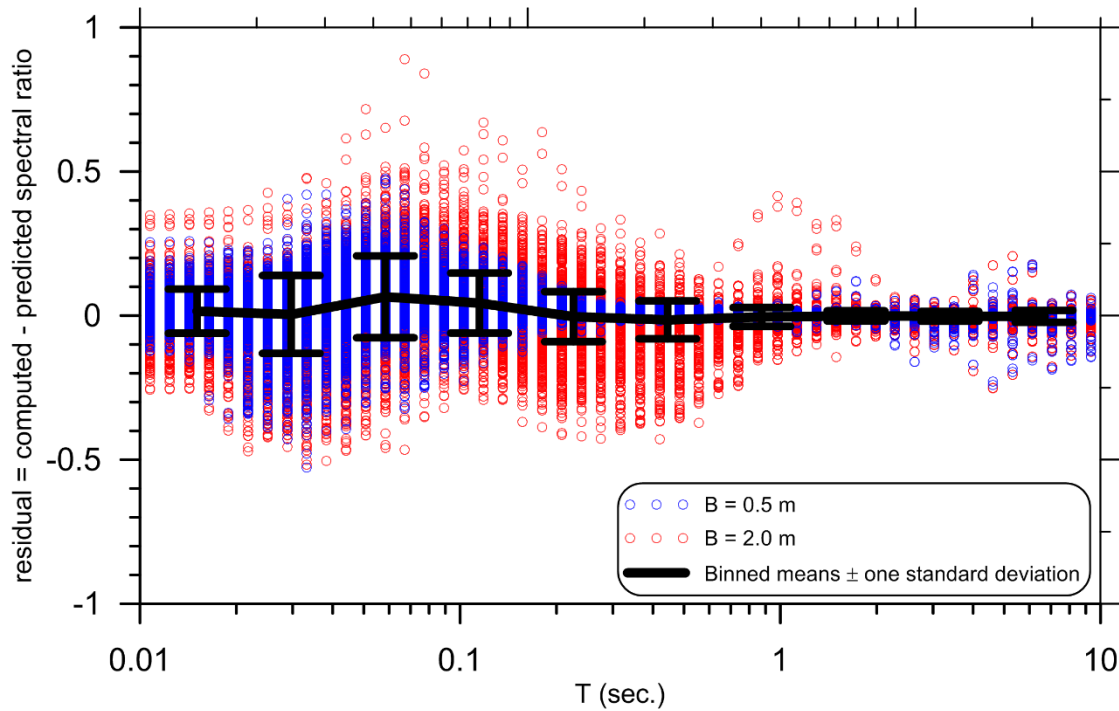


Figure 4.36 Fixed-head pile spectral ratio predictive model residuals.

### 4.5.3 Models for Predicting Free-Head Spectral Ratio Coefficients

Models for predicting the coefficients to be used in Equation (4.21) are given in Equations (4.27)–(4.32). Metrics for assessing the statistical significance of the models are presented in Table 4.5 and Figure 4.37. The same predictor variables used in the fixed-head models are used here.

$$\left(R_{0,FRH}\right)^{-4.49} = -0.60 \log\left(\frac{f_0}{\lambda_{L_a} V_{S,L_a}}\right) - 0.032 \left(\frac{V_{S,L_a}}{V_{S,L}}\right) + 0.15 \log\left(\frac{PSA_{max}}{g}\right) - 0.26 \quad (4.27)$$

$$\left(R_{min,FRH}\right)^{1.67} = -0.24 \log\left(\frac{f_0}{\lambda_{L_a} V_{S,L_a}}\right) - 0.36 \left(\frac{V_{S,L_a}}{V_{S,L}}\right) - 0.093 \log\left(\frac{PSA_{max}}{g}\right) + 0.60 \quad (4.28)$$

$$(T_{\min,FRH})^{-0.73} = -3.86 \log\left(\frac{f_0}{\lambda_{L_a} V_{S,L_a}}\right) + 6.97 \left(\frac{V_{S,L_a}}{V_{S,L}}\right) + 4.38 \log\left(\frac{PSA_{\max}}{g}\right) - 1.53 \quad (4.29)$$

$$(R_{\max,FRH})^{-3.38} = -0.39 \log\left(\frac{f_0}{\lambda_{L_a} V_{S,L_a}}\right) + 0.076 \left(\frac{V_{S,L_a}}{V_{S,L}}\right) + 0.10 \log\left(\frac{PSA_{\max}}{g}\right) - 0.11 \quad (4.30)$$

$$(T_{\max,FRH})^{-0.59} = -2.24 \log\left(\frac{f_0}{\lambda_{L_a} V_{S,L_a}}\right) + 2.34 \left(\frac{V_{S,L_a}}{V_{S,L}}\right) + 1.24 \log\left(\frac{PSA_{\max}}{g}\right) - 1.59 \quad (4.31)$$

$$\log(T_{crit,FRH}) = 0.73 \log\left(\frac{f_0}{\lambda_{L_a} V_{S,L_a}}\right) - 0.47 \left(\frac{V_{S,L_a}}{V_{S,L}}\right) - 0.24 \log\left(\frac{PSA_{\max}}{g}\right) + 1.09 \quad (4.32)$$

Note that  $T_{min}$ ,  $T_{max}$ , and  $T_{crit}$  in Equations (4.29), (4.31), and (4.32) are in seconds.

**Table 4.5 Metrics for free-head spectral ratio coefficient prediction models.**

<b>Coefficient:</b>	<b>Adjusted R<sup>2</sup></b>	<b>F-Statistic</b>	<b>P-Value</b>
$R_0$	0.47	203	2.2E-16
$R_{min}$	0.13	35	2.2E-16
$T_{min}$	0.41	163	2.2E-16
$R_{max}$	0.47	203	2.2E-16
$T_{max}$	0.58	313	2.2E-16
$T_{crit}$	0.60	350	2.2E-16

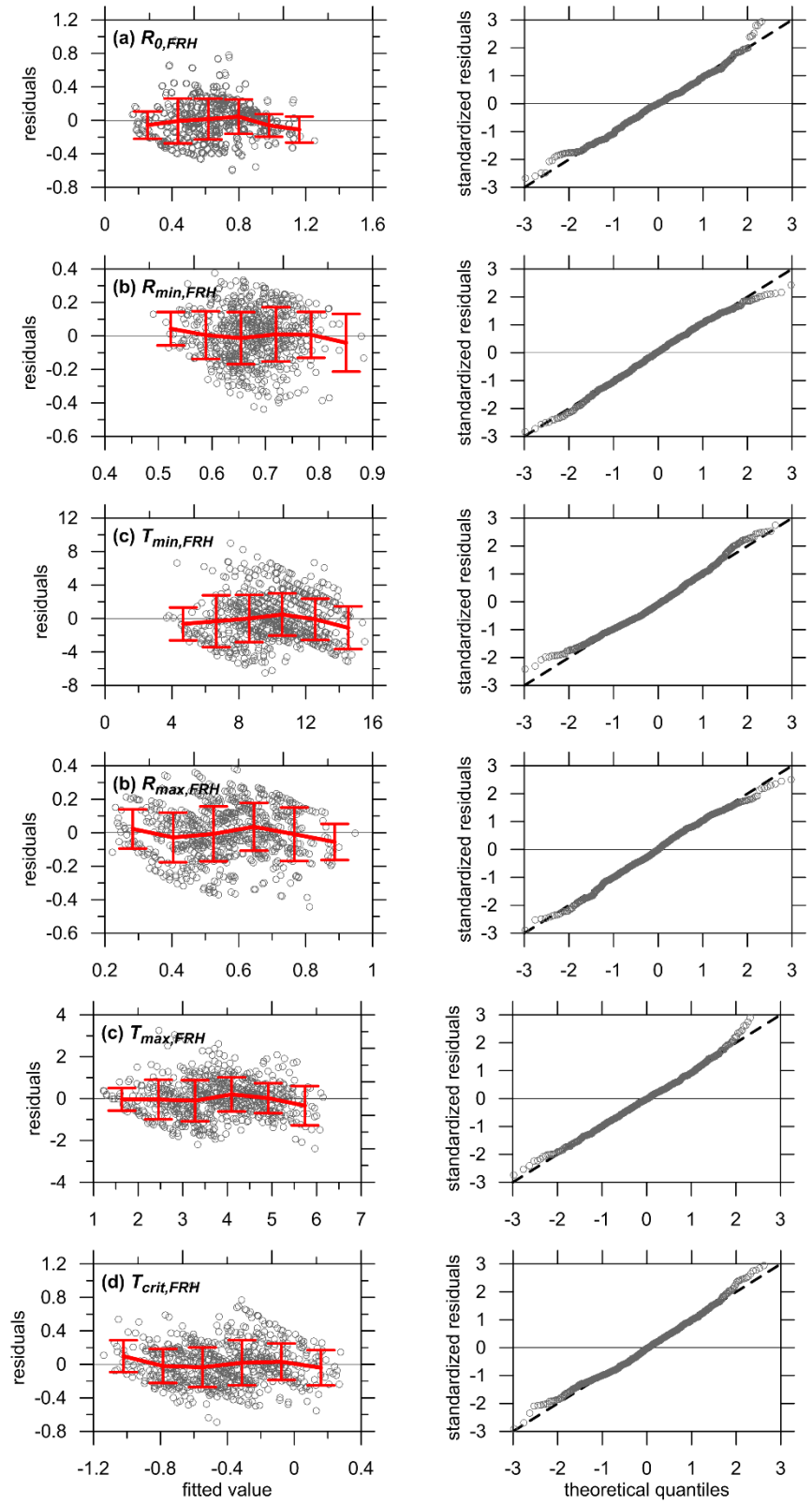


Figure 4.37 Residuals versus predicted values plots (left) and normal Q-Q plots (right) for free-head spectral ratio coefficient prediction models.

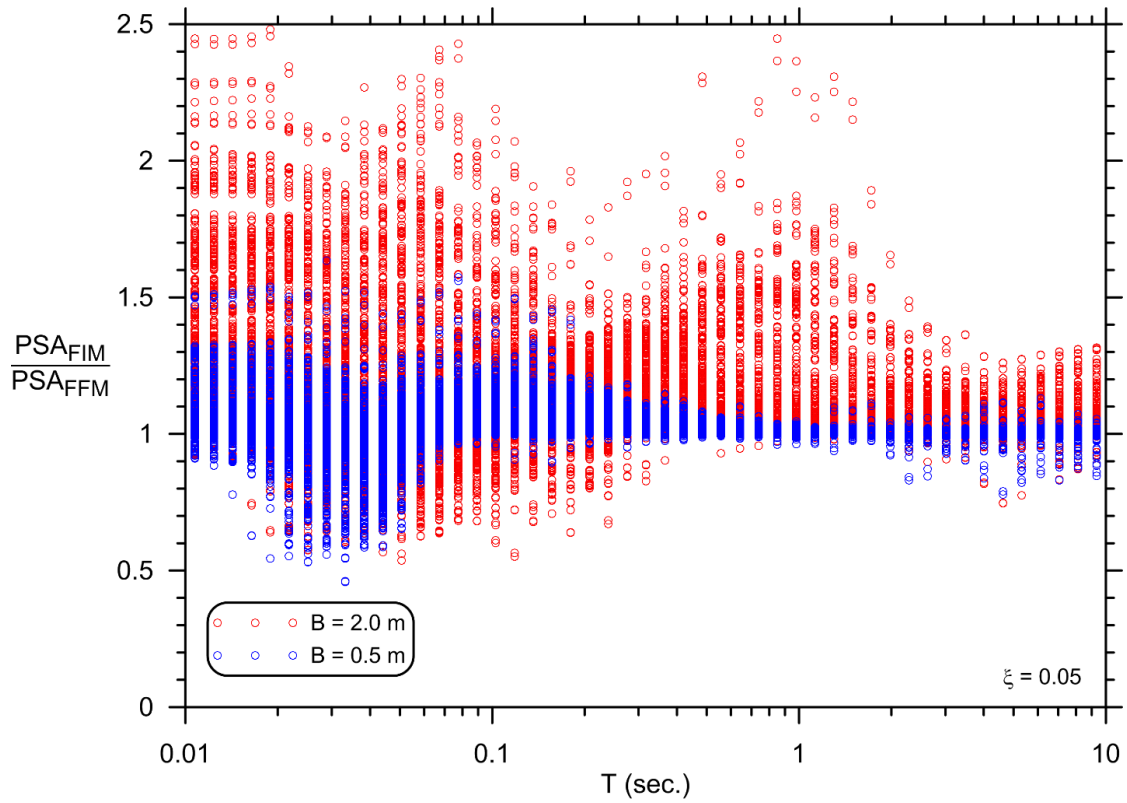


Figure 4.38 Free-head pile spectral ratio results.

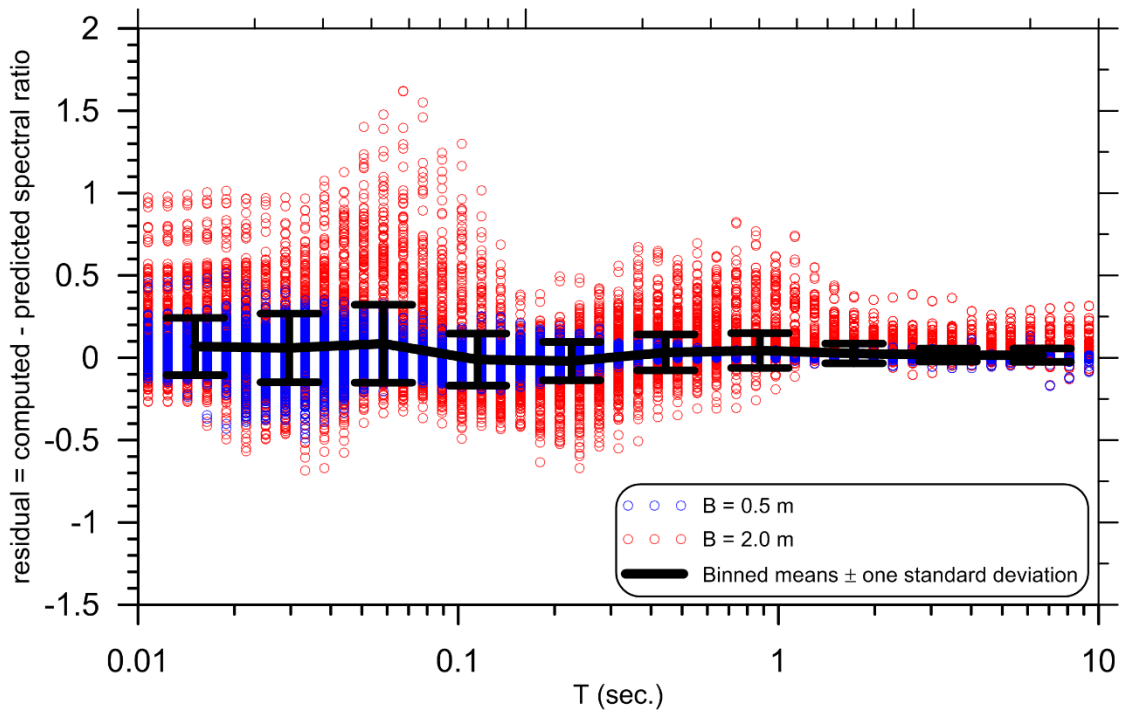


Figure 4.39 Free-head pile spectral ratio predictive model residuals.

Free-head pile spectral ratios show amplification (ordinates  $> 1.0$ ) at short periods because kinematic amplification usually occurs during the largest-amplitude pulse in the ground motion, which is the component of the motion that controls PGA and short-period spectral ordinates. What appears to be a large number of points showing significant amplification at short periods in Figure 4.38 is somewhat exaggerated as the points are approximately log-normally distributed, which is not visually apparent in Figure 4.38.

The ability of the predictive models to capture the effect of kinematic amplification at short periods is demonstrated in the plot of residuals shown in Figure 4.39. The average residual value is near zero at periods greater than about 0.1 sec and is around 0.05 to 0.1 at shorter periods. This indicates that the predictive model underestimates the computed spectral ratio by, on average, about 5 to 10%. Future studies may be able to reduce this bias by adjusting the coefficient prediction models.

## 4.6 PILE-GROUP RESULTS

Simulations of pile groups subjected to incoherent ground motions generally showed that group effects were minimal for the parametric bounds considered here, which is consistent with previous findings based on elastic solutions. For stiff-pile/soft-site combinations for which single piles exhibit significant reduction of the free-field motion at low frequencies, the average trends exhibited by pile-group transfer functions typically ranged between 0–10% below the corresponding single-pile transfer functions computed for the same ground motion. For pile/site combinations with less of a pile-to-soil stiffness contrast, pile groups amplified narrow-bandwidth frequency components of some ground motions up to about 10–20% relative to the single pile transfer functions, but the average trends of the group transfer functions still generally plotted slightly below the single pile results.

For design applications, a reasonable first-order approximation of pile group behavior could be estimated by reducing transfer functions predicted using the models presented in this chapter by an additional 5% at frequencies beyond the corner frequency. Because of the idiosyncratic nature of the group results, for critical projects, modeling of the type used for this study would be more appropriate than this rough approximation. Alternatively, group effects could be ignored due to their relatively insignificant contribution to kinematic pile–soil interaction. Pile-supported buildings that use a stiff mat foundation (i.e., piled-raft) or grade beams to connect piles over a large footprint could potentially experience a larger reduction due to the group averaging. This should be examined in future studies.

Examples results are shown in Figure 4.40–Figure 4.42. Comparison of Figure 4.40 to Figure 4.41 (same pile/site combination, different motion) shows that the group transfer function varies based on the ground-motion amplitude and frequency content in much the same manner as the single pile results. Comparison of Figure 4.41 to Figure 4.42 (same pile/motion, different site) shows that for stiffer sites, the pile groups may amplify or de-amplify certain frequency components, but the smoothed trend exhibits approximately the same difference between single pile and group pile results for both sites.

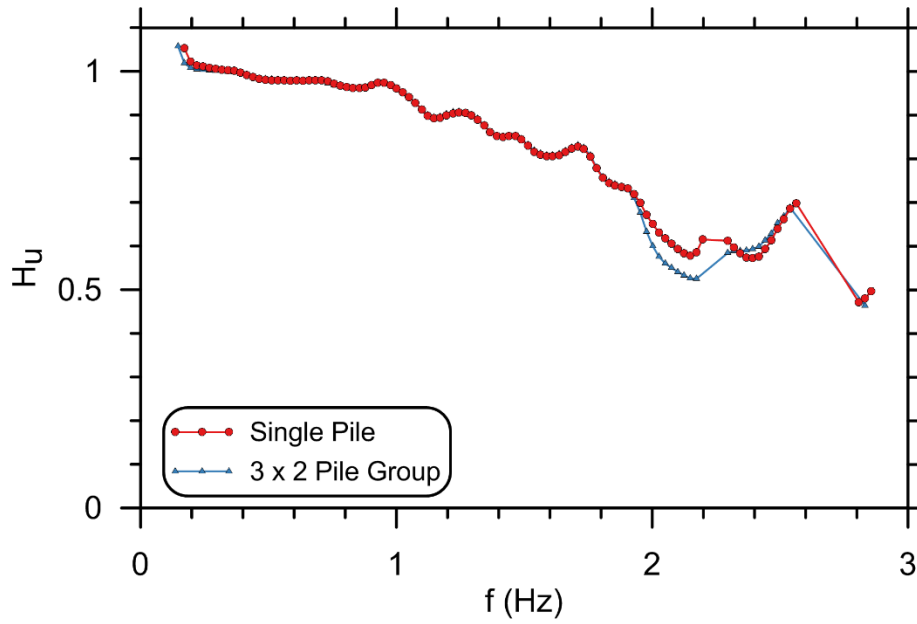


Figure 4.40 Group versus single-pile results for  $B = 2.0$  m.  $L = 30$  m pile, Site 1, subjected to 1994 Northridge, California, earthquake (NGA record sequence number 957).

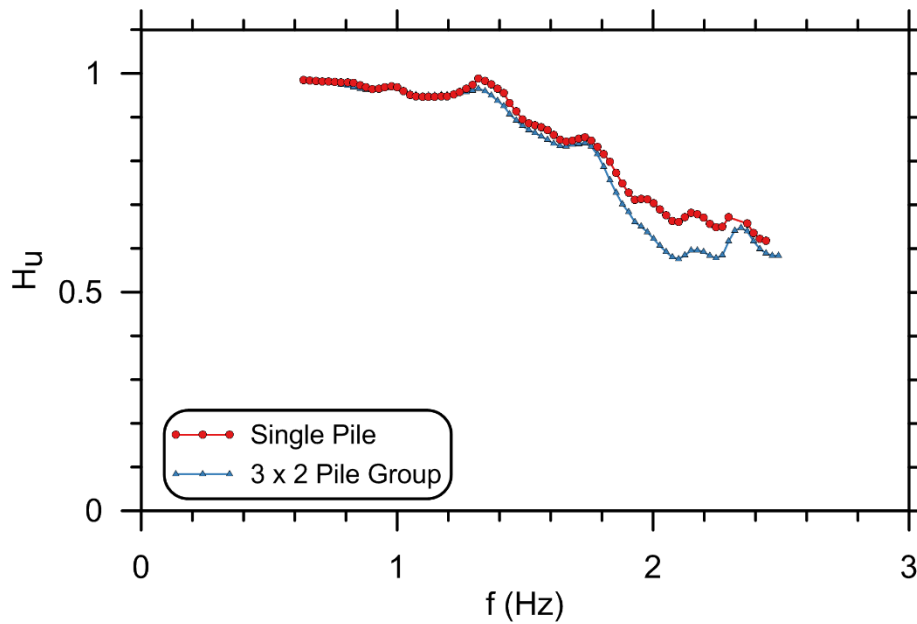


Figure 4.41 Group versus single-pile results for  $B = 2.0$  m.  $L = 30$  m pile, Site 1, subjected to 1971 San Fernando, California, earthquake (NGA record sequence number 72).

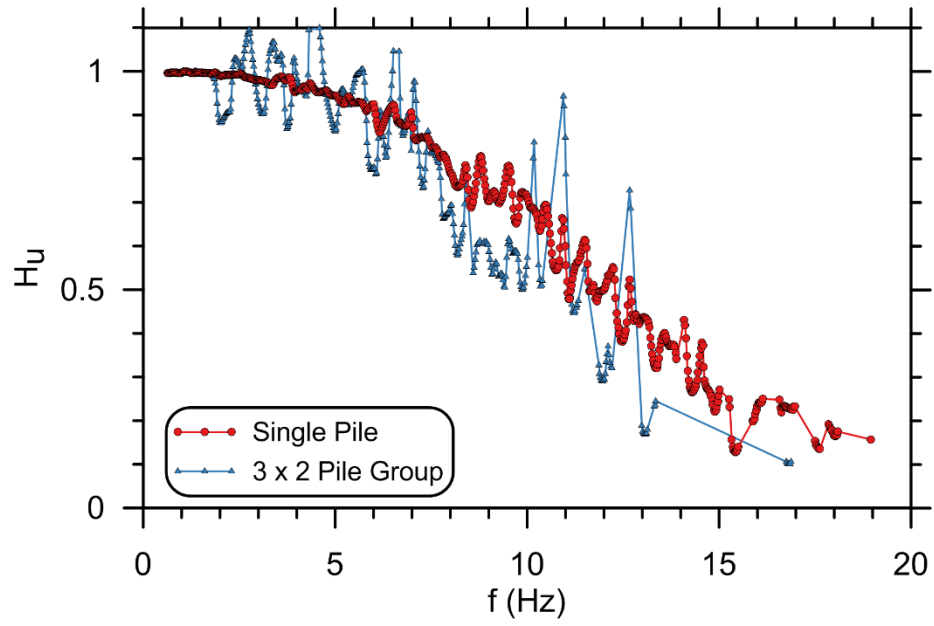


Figure 4.42: Group versus single-pile results for  $B = 2.0$  m.  $L = 30$  m pile, Site 4, subjected to 1971 San Fernando, California, earthquake (NGA record sequence number 72).

## 5 Combination of Inertial and Kinematic Pile–Soil Interaction

### 5.1 COMBINING INERTIAL AND KINEMATIC SSI

For comparison of predictive models to empirical transfer functions, and in a broader sense, for consideration of a structure’s earthquake response considering soil–structure interaction (SSI), it is necessary to consider the combination of kinematic and inertial effects. Analytically decoupling these effects for use with the substructure method of design is convenient but must be kept in check by considering important factors related to their combined effects. This chapter will discuss this topic prior to presentation of the example applications in the next chapter.

Three distinct motions will be considered in the context of combined inertial and kinematic SSI: the free-field motion (FFM), foundation-input motion (FIM), and foundation motion (FM). The FFM and FIM are consistent with the definitions given in previous chapters, and represent the modification of the free-field ground response due to kinematic pile–soil interaction. In the absence of inertia from the superstructure, the FM is the same as the FIM. When superstructure inertia is present, however, the FM will differ from the FIM because inertial force effects from the superstructure will induce additional foundation displacements and rotations, which is the concept of inertial SSI. In other words, the FM is influenced by both inertial and kinematic SSI.

When considering empirical transfer functions computed between recordings of instrumented structures and the adjacent free field, it is important to keep in mind that the empirical transfer function represents the ratio of FM/FFM—as opposed to FIM/FMM—since inertial effects are present in the structure foundation-level recording. To make a meaningful comparison between an empirical transfer function and a purely kinematic transfer function model such as the ones developed herein, it is necessary to simulate the response of the structure subjected to the FIM; the FM is an outcome of this analysis. An alternative method is to approximately remove inertial effects by ignoring the portion of an empirical transfer function that is near the first-mode frequency of the system, based on the assumption that this is where inertial effects are most pronounced (e.g., Mikami et al. [2008]). However, this is often where the greatest reductions between FM and FFM are observed, so ignoring this frequency range can leave important questions unanswered.

For many applications, the structure response can be idealized as a SDOFO, and the FM can be computed using the substructure analysis method. This process is illustrated in Figure 5.1 and can be summarized as follows:

1. Compute kinematic transfer function using site and pile parameters [Figure 5.1(a) and (b)]. This could be achieved using the generalized models presented in Equations (4.6)–(4.8) (depending on head-fixity) or by directly simulating the dynamic pile response to free-field motions at discrete depth intervals computed from a ground response analysis.
2. Convolve the transfer function from step 1 with the FFM to generate a FIM.
3. Impose this FIM on the free end of a spring representing foundation impedance for the appropriate degree-of-freedom. For example,  $K_{xx}$  represents the pile translational impedance in Figure 5.1(c). Additional impedance springs can be used to model pile rotation and/or vertical translation depending on the pile boundary conditions. The stiffness of impedance springs can be computed for specific site conditions or approximated using a simplified equivalent-linear approach (e.g., see NIST [2012]).
4. Compute dynamic response of system subjected to FIM through impedance spring(s), from which FM can be determined. The transfer function computed between the FM and FFM [Figure 5.1(d)] can be compared to empirical transfer functions for the system being modeled.

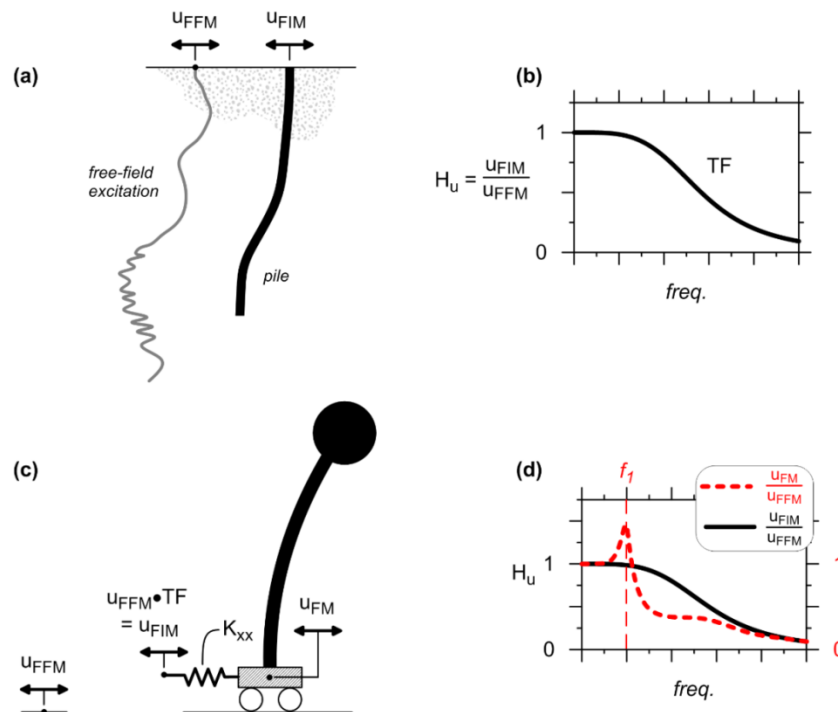


**Figure 5.1** (a) Schematic of pile-soil kinematic interaction, which produces foundation-input motion (FIM) to free-field motion (FFM) transfer function (b), and (c) application of kinematic transfer function using substructure approach to represent a structure supported by a fixed-head pile; (d) the foundation motion (FM) transfer function differs from the FIM transfer function because of additional foundation displacements resulting from superstructure inertial forces.

### 5.1.1 Linear-Elastic SDOFO-Pile–Soil System

A series of dynamic simulations of the idealized linear-elastic system depicted in Figure 5.2 were conducted to illustrate the effects of combining inertial and kinematic SSI.

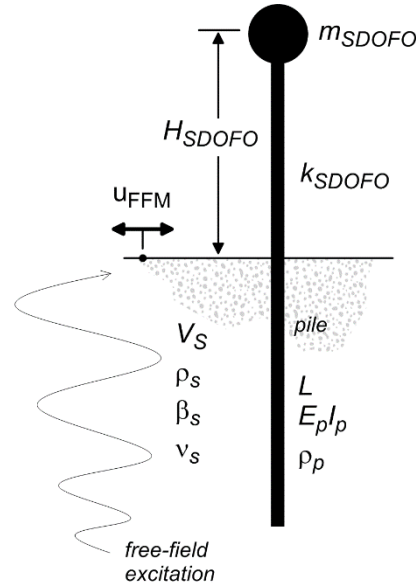


**Figure 5.2** Idealized system used for direct analysis method.

A structure represented by a SDOFO is supported on a single pile, embedded in a homogeneous soil medium excited by vertically-propagating shear waves. The SDOFO is defined by a lumped mass ( $m_{SDOFO}$ ) and a massless column of height  $H_{SDOFO}$  and swaying stiffness  $k_{SDOFO}$ . The swaying stiffness of a fixed-base SDOFO is related to the column flexural rigidity  $EI_{SDOFO}$  by:

$$k_{SDOFO} = \frac{3EI_{SDOFO}}{(H_{SDOFO})^3} \quad (5.1)$$

The first-mode fundamental frequency of the fixed-base SDOFO  $f_{1,SDOFO}$  can be computed from its mass and stiffness using the following basic relationship:

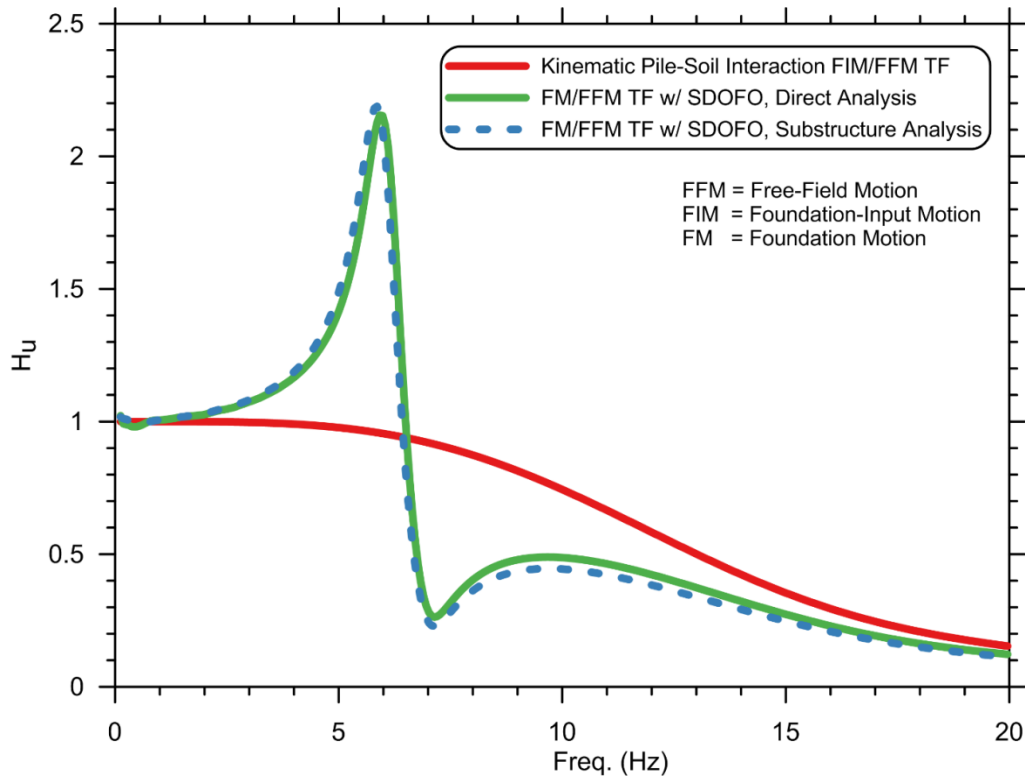
$$\omega_{SDOFO} = \sqrt{\frac{k_{SDOFO}}{m_{SDOFO}}} = 2\pi f_{1,SDOFO} \quad (5.2)$$

Figure 5.3 compares a kinematic pile–soil interaction transfer function (i.e., FIM/FFM) to FM/FFM transfer functions computed with superstructure inertia included. The following system properties were used for the analyses:

- Soil:  $V_s = 100$  m/sec,  $\rho_s = 17$  Mg/m<sup>3</sup>,  $\beta_s = 0.05$ ,  $\nu_s = 0.35$
- Pile:  $L = 10$  m, elastic stiffness  $E_p I_p = 84$  MN·m<sup>2</sup>,  $\rho_p = 24.5$  Mg/m<sup>3</sup>, and a fixed-head boundary condition
- Soil–pile Interaction: interaction modulus  $k = 37$  MPa, which represents a modulus reduction of about 20% from the initial elastic condition to

approximate nonlinearity due to site response and pile–soil interaction, and 5% damping modeled as equivalent viscous damping through distributed dashpots.

- SDOFO:  $H_{SDOFO} = 5$  m,  $m_{SDOFO} = 10$  Mg, and  $f_{1,SDOFO} = 7$  Hz, which corresponds to  $EI_{SDOFO} = 81$  MN·m<sup>2</sup>. Flexible-base (i.e., including foundation flexibility) first- and second-mode natural frequencies of  $\tilde{f}_{1,SDOFO} = 6.1$  and  $\tilde{f}_{2,SDOFO} = 33$  Hz, respectively, were computed using the *eigen* command in *OpenSees*.
- Rayleigh damping was imposed on the structural elements corresponding to 5% damping at  $\tilde{f}_{1,SDOFO}$  and  $\tilde{f}_{2,SDOFO}$ .
- Ground motion: sine-sweep motion of constant 0.1-m amplitude over a frequency range of 0.1–25 Hz, specified at the ground surface and computed at each depth increment of the pile using Equation (2.3).



**Figure 5.3 Comparison of transfer functions computed for pile–soil system and combined SDOF oscillator and pile–soil systems using direct and substructure analysis methods.**

The direct analysis transfer function in Figure 5.3 was computed from analyzing the complete system depicted in Figure 5.2, while the substructure analysis transfer function was computed from analyzing the system depicted in Figure 5.1(c). For the substructure analysis, the FIM was computed by convolving the free-field sine-sweep motion at the ground surface with the kinematic pile–soil interaction transfer function. The pile was replaced with an equivalent

macroelement representing the foundation translational impedance. To determine the foundation impedance, a “pushover” analysis of the pile was performed by imposing a lateral force on a model of the pile–soil domain (no SDOFO) and recording the lateral displacement. This produced a pile-head lateral force-versus-displacement stiffness  $K_{xx} = 54.7 \text{ MN/m}$ . To capture foundation damping, a dashpot with a coefficient of  $142 \text{ kN}\cdot\text{s/m}$  was modeled in parallel with the spring. This dashpot coefficient corresponds to 5% damping at  $\tilde{f}_{1,SDOFO}$  based on the following relationship relating damping ratio  $\beta$  to equivalent viscous damping [NIST 2012]:

$$c_j = \frac{2\beta_j k_j}{\omega_j} \quad (5.3)$$

In Equation (5.3),  $k$  is stiffness (in this case  $K_{xx}$ ),  $\omega$  is the frequency of interest, and the subscript  $j$  stands for the mode of interest, which in this case is the first mode.

The transfer functions computed from the direct and substructure analysis methods are in close agreement in this example. The slight misfit between them occurs because of the different modal properties of the two systems and the manner in which damping was implemented. While the substructure model with lumped mass and a SDOF has only one defined mode, the direct-analysis model has multiple higher modes associated with deflection of the pile’s distributed mass. Hence the modal-mass participation and mode-shapes of the two models are not identical. In addition,  $\tilde{f}_{1,SDOFO}$  of the substructure model is slightly less than for the direct-analysis model (6.01 versus 6.12 Hz) because of the different distribution of mass and stiffness that occurs when the pile is replaced by a single macroelement. Nonetheless, the good agreement between the two approaches verifies that the substructure method can provide a reasonably accurate response for linear-elastic systems. Note that at a single frequency of interest, the substructure method can provide an exact match to the direct analysis method, but a perfect match cannot be achieved over a wide frequency bandwidth for a time-domain solution when Rayleigh damping and equivalent viscous damping are combined in the manner of this example.

Two deviations between the complete SDOFO–pile–soil system transfer function and the purely kinematic pile–soil transfer function are of interest. First, significant amplification occurs in the complete-system transfer function near  $\tilde{f}_{1,SDOFO}$  as a result of resonance. At frequencies near  $\tilde{f}_{1,SDOFO}$ , the SDOFO mass undergoes displacements in excess of the ground displacement, which generates inertial base shear and moment acting on the foundation. In this example, note that in Figure 5.3 the purely-kinematic pile–soil transfer function predicts a negligible difference between the FIM and FFM near  $\tilde{f}_{1,SDOFO}$ ; therefore, it can be said that the FM is controlled by the structure response near  $\tilde{f}_{1,SDOFO}$ , and that kinematic pile–soil interaction has a negligible influence. This can be verified by repeating the substructure analysis with the FFM in place of the FIM—effectively bypassing kinematic pile–soil interaction. Figure 5.4 shows that this results in a nearly identical transfer function for frequencies up to the kinematic pile–soil interaction transfer function corner frequency (about 7 Hz). Only at frequencies above 7 Hz does the reduction of FIM due to kinematic pile–soil interaction result in a significant difference between the two transfer functions computed for the complete system.

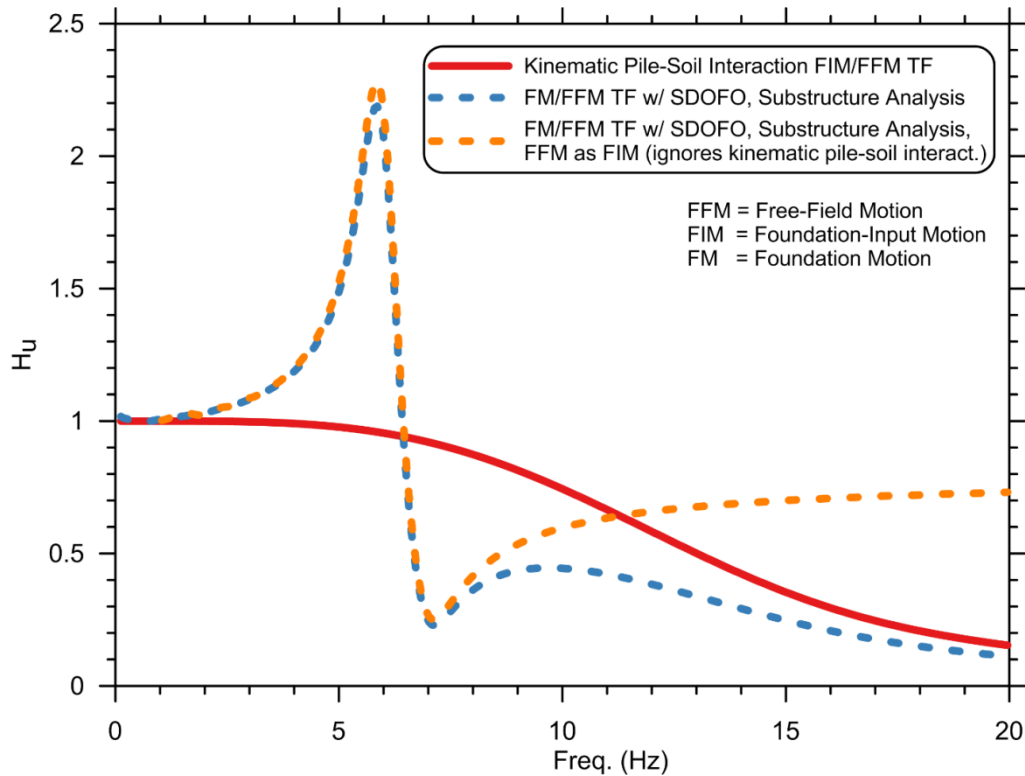


**Figure 5.4 Comparison of transfer functions computed with and without consideration of kinematic pile–soil interaction.**

The second difference of interest between the complete-system transfer function (i.e., including the SDOFO inertia) and pile-only kinematic transfer function is that the complete-system transfer function is significantly reduced relative to the pile-only kinematic transfer function at frequencies greater than the range where resonance occurs. For example, referring back to Figure 5.3, the complete-system transfer function is less than the pile-only kinematic transfer function at all frequencies shown in the plot above about 6.5 Hz. This is significant because it indicates that kinematic pile–soil interaction is not entirely responsible for reductions between FM and FIM that are observed in empirical transfer functions, even away from  $\tilde{f}_{1,SDOFO}$ . Even for the case where the FFM was used in place of the FIM with the substructure method, shown as the dashed-orange transfer function in Figure 5.4, the transfer function plots below 1.0 at all frequencies shown above about 6.5 Hz.

This reduction occurs as a result of phase lag between the oscillator response and the ground surface motion, which is depicted for the system in the above example by the phase angle frequency-response curve in Figure 5.5(a). In this context, phase lag is defined as the time difference between the peak ground response and the subsequent peak SDOFO response. As described by Chopra [2007], phase lag of a SDOF system varies over three distinct frequency ranges based on the ratio of excitation frequency to the system first-mode fundamental frequency. Chopra’s explanation is expanded here to include the SDOFO foundation-level response, including foundation flexibility and the influence of pile–soil kinematic interaction—two factors not present for a truly SDOF system. When these additional system components are considered, four distinct regions of phase-lag behavior are observed as depicted in Figure 5.5 and Figure 5.6:

1. At low frequencies ( $f \ll \tilde{f}_{l,SDOFO}$ ), the direction of base excitation changes slowly, hence inertial forces are low and damping is insignificant, so the stiffness of the system controls the response. Because insignificant inertial forces develop at the SDOFO mass-level, the SDOFO response is in-phase with the ground surface response at both the mass- and foundation-level. This is evident as near-zero phase-lag in the low-frequency range of Figure 5.5(a).
2. As the excitation frequency approaches the system fundamental frequency ( $f \approx \tilde{f}_{l,SDOFO}$ ), inertia increases, along with the corresponding displacement, velocity, and damping of the SDOFO. The magnitude of the peak SDOFO response at the mass level, which occurs at  $f / \tilde{f}_{l,SDOFO} = 1$ , is dependent primarily on the system damping. The large base shear and moment resulting from inertia dominates the SDOFO foundation-level response; hence, the response at mass level and foundation level are nearly in phase with each other. However, as illustrated in Figure 5.5(c) and Figure 5.6(e) and (f), the SDOFO response is approximately  $90^\circ$  out-of-phase with the ground surface response near  $f / \tilde{f}_{l,SDOFO} = 1$ , i.e., the peak SDOFO response occurs when the ground surface displacement passes through zero. This is a fundamental property of resonance of a SDOF system.
3. At high frequencies ( $f \gg \tilde{f}_{l,SDOFO}$ ), the direction of base excitation changes rapidly. The inertia of the SDOFO mass now opposes the rapidly-changing direction of ground displacement, hence the mass-level response approaches a phase lag of  $180^\circ$  (perfectly out-of-phase). As shown in Figure 5.6(j)-(l), this means that when the ground surface displaces to the right, the SDOFO mass displaces to the left and vice versa. As the SDOFO mass increases, the mass-level response approaches zero at high frequencies; hence, the SDOFO response is controlled by its mass in this frequency range. The pile displaced shape is controlled by the profile of ground displacement rather than the SDOFO response; hence, the pile-head motion (i.e., SDOFO foundation-level response) is in phase with the ground-surface response, so the phase lag returns to zero at high frequencies. The magnitude of the SDOFO foundation-level response is reduced from the ground-surface response by two mechanisms: (i) the tendency of the SDOFO mass to remain still due to its inertia; and (ii) kinematic pile–soil interaction, which reduces the foundation-level response relative to the ground-surface response even in the absence of inertial forces.
4. A transition between (2) and (3) occurs when the foundation-level response shifts from being dominated by inertia to being controlled primarily by the ground displacement. This transition is marked by the peak in the foundation-level response phase-lag plot [red line in Figure 5.5(a)] and the response history plot and graphics in Figure 5.5(d) and Figure 5.6(g)-(i). The local minimum of the complete-system transfer function occurring around 7 Hz in Figure 5.3 occurs approximately when the foundation-level response transitions from being out-of-phase with the ground surface response (phase lag  $> 90^\circ$ ) to in-phase (phase lag  $< 90^\circ$ ). The transfer function ordinate  $H_u$  may then increase slightly until kinematic pile–soil interaction becomes significant. This occurs between about 7 and 10 Hz in Figure 5.3.

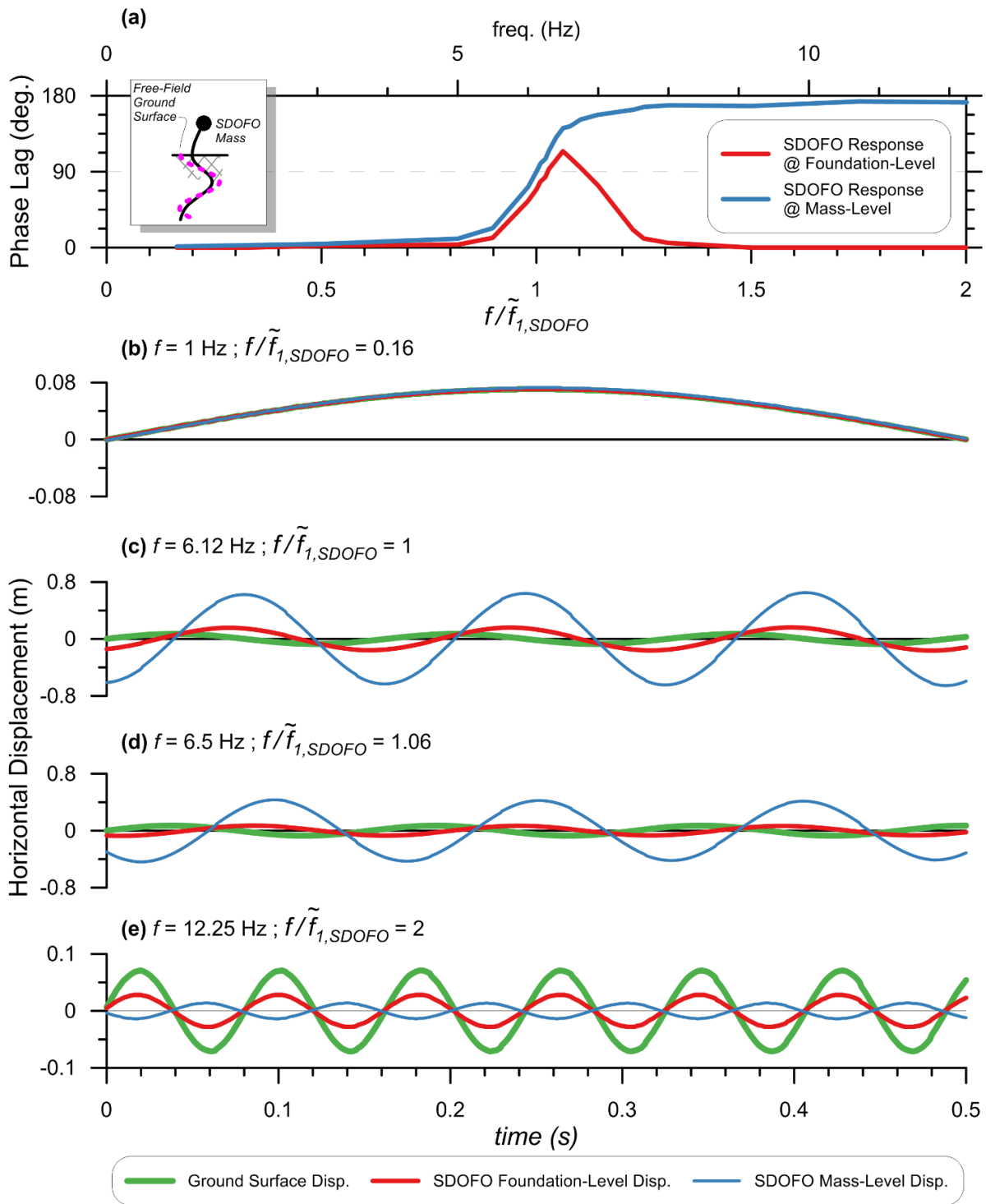


**Figure 5.5** (a) Phase angle frequency-response curves for SDOFO–pile–soil system (inset) and (b)-(e) response history of system components at different frequencies of harmonic free-field excitation.

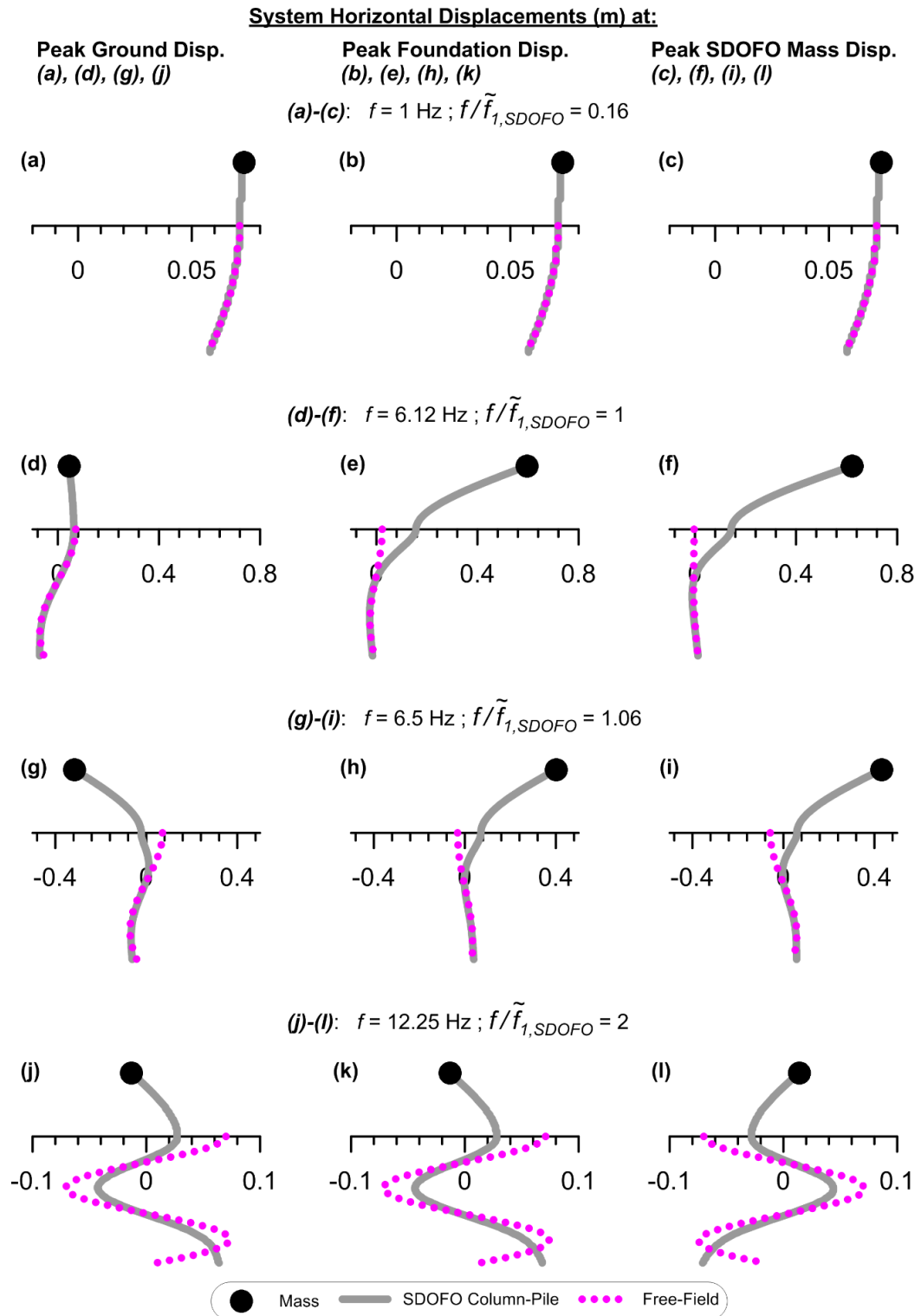


**Figure 5.6 Response of SDOFO-pile–soil system to harmonic free-field excitation.**

Several other issues can be investigated with the modeling framework presented above. A select few will be discussed in the following sections, although this is not meant to be an exhaustive treatment of the combination of kinematic and inertia SSI.

### 5.1.2 Effects of SDOFO Properties

In the familiar context of a response spectrum, a SDOFO is defined solely by its fundamental frequency (or period). When representing an actual structure as a SDOFO, however, the height, mass, and stiffness of the system—not just the fundamental frequency—also affect its seismic response. This is because a change to any of these properties will affect the inertial base shear and moment imposed on the foundation, in-turn altering the overall seismic response. To illustrate these effects, the complete system with the “baseline” properties given in §5.1.1 was re-analyzed with the following modifications:

- $m_{SDOFO}$  varied by a factor of three from the original 10 Mg to 3.33 and 30 Mg
- $H_{SDOFO}$  varied by a factor of three from the original 5 m to 1.67 and 15 m.
- Free-head pile boundary condition considered in addition to fixed head.

The fixed-base fundamental frequency of the SDOFO  $f_{l,SDOFO}$  was held constant at 7 Hz by changing  $EI_{SDOFO}$ . The transfer function computed from the results of these simulations are plotted in Figure 5.7, demonstrating that:

- The flexible-base fundamental frequency of the system  $\tilde{f}_{l,SDOFO}$  is decreased when the mass or height are increased, and is always less than the fixed-base  $f_{l,SDOFO}$ .
- The amount of amplification near  $\tilde{f}_{l,SDOFO}$  and de-amplification at  $f > \tilde{f}_{l,SDOFO}$  is also altered when the mass and height are changed,
- The trends of increasing versus decreasing the amount of amplification near  $\tilde{f}_{l,SDOFO}$  relative to the baseline properties as a result of changes in mass are opposite for the free- and fixed-head-pile systems, and
- The effect of changes in height is negligible for the fixed-head pile system over the range of properties considered for this example.

The different behavior of the free- versus fixed-head-pile systems occurs because the inertial base shear and moment result in greater rotations and displacements of the free-head pile than for the fixed-head pile.

The effect of SDOFO properties on the combined inertial-kinematic transfer function is highlighted here simply for the purpose of demonstrating that accurate mass, height, and stiffness must be specified for a meaningful comparison to be made between an empirical transfer function and a simplified model. Unfortunately, adequate information to model an instrumented structure as a SDOFO is not always available, even when recordings of the structure and ground motions are available. Likewise for forward-design scenarios, it is important to accurately specify more than just the fundamental frequency of the structure for consideration of combined kinematic-inertial SSI effects.

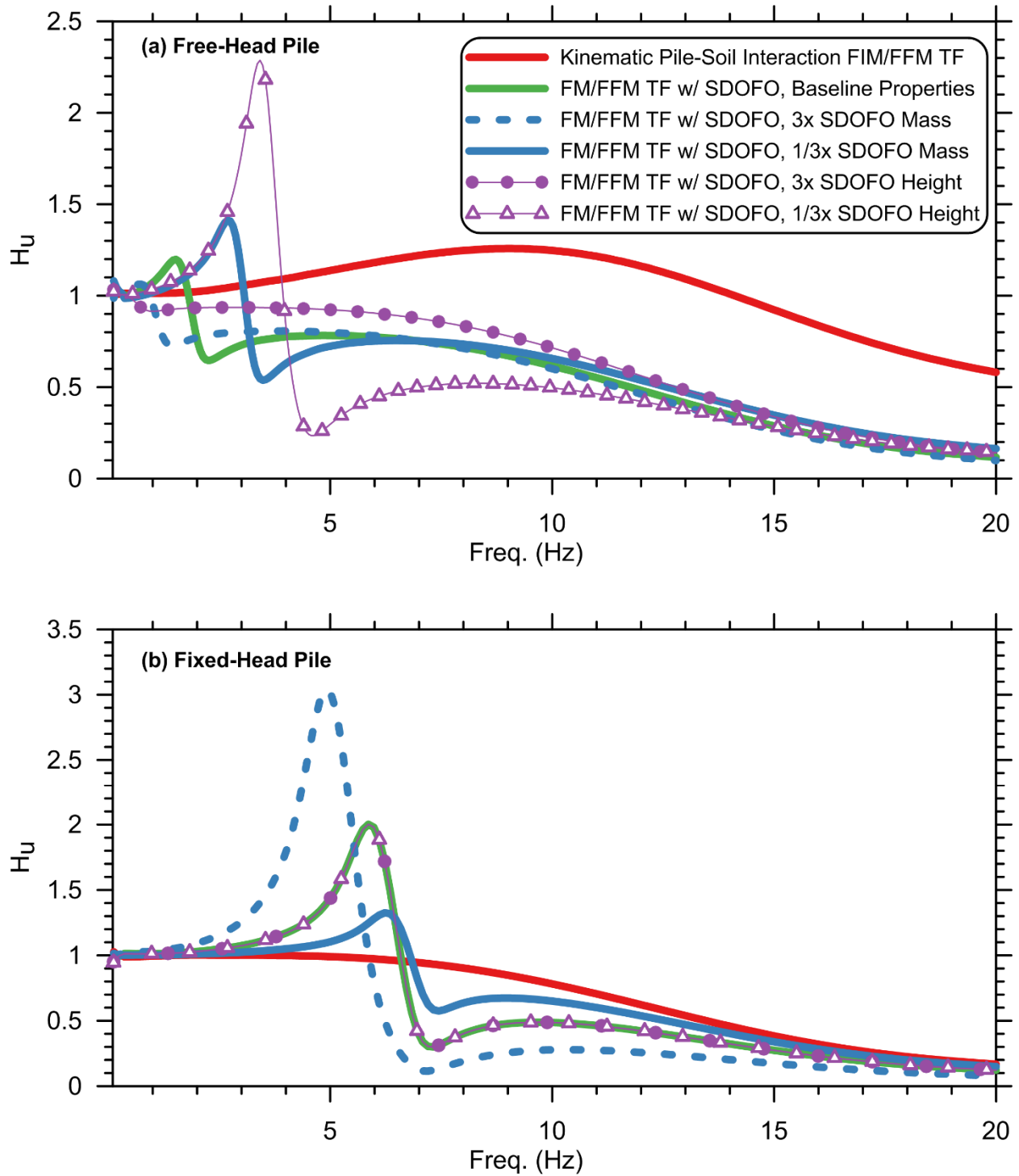


**Figure 5.7** Transfer functions computed for variable SDOFO properties. Note fixed-base fundamental frequency  $f_{1,SDOFO} = 7$  Hz for all cases.

### 5.1.3 Effect of Pile-Soil Kinematic Interaction Corner Frequency versus SDOFO Fundamental Frequency

In the preceding examples, the corner frequency  $f_c$  of the purely kinematic pile–soil interaction transfer functions have always been greater than  $\tilde{f}_{1,SDOFO}$  of the SDOFO–pile–soil system. (Recall that the corner frequency of the kinematic pile–soil interaction transfer function is the frequency beyond which significant de-amplification of the FFM occurs, e.g. approximately 7 Hz in Figure 5.3). This means that over the range where amplification occurs for the complete-system transfer function due to inertial resonance (e.g., approximately 4–7 Hz in Figure 5.3), kinematic SSI is negligible. This section investigates briefly the result of having  $f_c$  be approximately equal-to or less-than  $\tilde{f}_{1,SDOFO}$  since this is a possibility for flexible structures supported on stiff piles in soft soil.

A series of dynamic simulations similar to those described in §5.1.1 were performed, except that  $f_{1,SDOFO}$  was varied from 4 to 19 Hz while  $f_c$  remained constant at about 7 Hz.  $H_{SDOFO} = 5$  m and  $m_{SDOFO} = 10$  Mg were held constant, and  $EI_{SDOFO}$  was adjusted according to Equation (5.1) to yield the desired  $f_{1,SDOFO}$ . In other words, the only system component that was changed in order to vary  $f_{1,SDOFO}$  is the column stiffness. Rayleigh damping coefficients were adjusted to achieve 5% damping at  $\tilde{f}_{1,SDOFO}$  and  $\tilde{f}_{2,SDOFO}$ .

The results shown in Figure 5.8 demonstrate that the shape of the transfer function stays approximately the same as  $f_{1,SDOFO}$  is varied relative to  $f_c$ ; only the magnitude of the amplification near  $\tilde{f}_{1,SDOFO}$  and de-amplification at  $f > \tilde{f}_{1,SDOFO}$  change. For the example systems shown in the figure, the magnitude of these two mechanisms both increase as  $f_{1,SDOFO}$  increases, but this is not solely a function of  $f_{1,SDOFO}$  relative to  $f_c$ —inertial SSI increases as  $f_{1,SDOFO}$  increases because the higher acceleration of the excitation results in greater inertial force, in turn resulting in greater peak amplification at resonance. (Recall that for the constant-amplitude input displacement used for the analysis, as frequency is increased, velocity and acceleration increase.)

The influence of kinematic SSI on the results is primarily on the amount of de-amplification at  $f > \tilde{f}_{1,SDOFO}$ . For systems that have  $\tilde{f}_{1,SDOFO} < f_c$ , kinematic SSI is the primary mechanism controlling the transfer function at  $f > f_c$ . For example, the de-amplification at frequencies greater than about 7 Hz for the  $f_{1,SDOFO} = 4$  Hz transfer function is due almost entirely to kinematic SSI, whereas for the higher  $f_{1,SDOFO}$  transfer functions, inertial SSI still plays a significant role at  $f > f_c$ . Hence, the following statement can be made: if  $\tilde{f}_{1,SDOFO} < f_c$ , kinematic pile–soil interaction is the dominant mechanism causing reduction (or lack thereof) of the FM relative to the FFM at frequencies greater than  $\tilde{f}_{1,SDOFO}$ ; if  $\tilde{f}_{1,SDOFO} > f_c$ , both inertial and kinematic SSI influence the complete-system transfer function at frequencies greater than  $\tilde{f}_{1,SDOFO}$ .

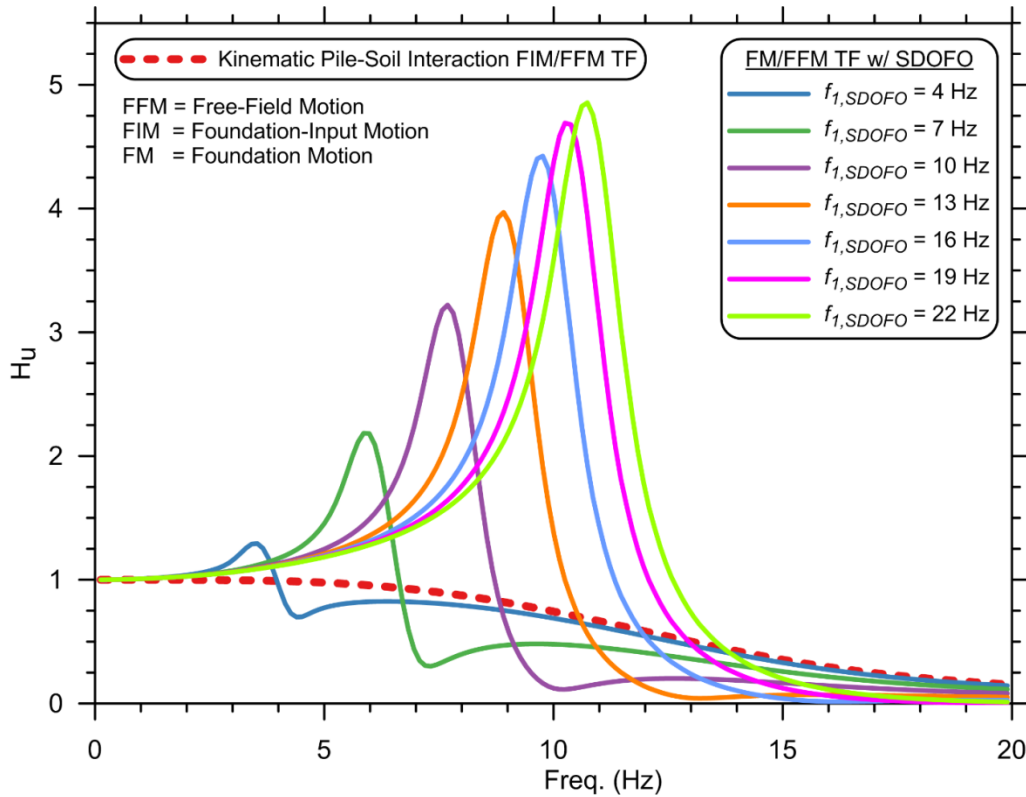


**Figure 5.8** Effect of varying fixed-base fundamental frequency of SDOFO–pile–soil system relative to kinematic pile–soil interaction transfer function corner frequency.

#### 5.1.4 Effect of Pile–Soil interaction Nonlinearity

The results presented in Chapter 4 show that kinematic pile–soil interaction is strongly dependent on soil nonlinearity. This issue is significant because the principal of superposition produces an exact result only for linear-elastic systems, and the substructure method relies on superposition to combine inertial and kinematic effects. In this section the error introduced to the substructure method as a result of neglecting nonlinear pile–soil interaction is examined. While not shown here, it should also be recognized that nonlinearity in other system components, such as free-field site response and nonlinear structural behavior, further violate the principal of superposition.

The SDOFO–pile–soil system with the properties given in §5.1.1 was again analyzed, except that the linear elastic soil springs and dashpots were replaced with nonlinear  $p$ - $y$  springs for the direct analysis. For the substructure analysis, the pile was replaced by a single macro-element representing foundation impedance with either a nonlinear or equivalent-linear impedance spring. For the analyses previously presented in §5.1.1 through §5.1.3, the  $p$ - $y$  modulus  $K_e$  was computed assuming a 20% modulus reduction to approximately account for nonlinearity. For the analyses in this section computed using nonlinear  $p$ - $y$  springs, the initial elastic behavior was defined based on the full elastic stiffness (i.e.,  $K_e = 46$  MPa corresponding to  $V_S = 100$  m/sec), not a reduced value, since the *PySimple3* material inherently captures the nonlinear behavior at larger displacement.

Figure 5.9 presents results generated using the same sine-sweep motion of constant 0.1-m amplitude over a frequency range of 0.1 to 25 Hz. For this case, the substructure analysis performed with a nonlinear foundation impedance spring closely matches the direct analysis results, with only a slight over-prediction of the peak response at resonance due to a minor mismatch in damping between the two systems.

Formulation of the nonlinear impedance spring is depicted in Figure 5.10. To begin, a pushover analysis of a model of the pile and soil was performed. Because nonlinear  $p$ - $y$  springs were used, the pile-head versus lateral deformation relationship is nonlinear. A single *PySimple3* element was then formulated to approximately match the pushover curve as shown in the figure. A close match can easily be achieved given the flexible user control over the *PySimple3* shape. Besides faithfully capturing the nonlinear pushover behavior of the pile–soil system, using a nonlinear impedance spring has an added benefit: the material and radiation damping that occur due to kinematic interaction are inherently captured by the pushover response (as long as the pushover analysis is performed at a velocity similar to the excitation velocity near the system  $\tilde{f}_{1,SDOFO}$ ). Hence by closely fitting the pushover curve with the nonlinear impedance spring, the effects of these damping mechanisms are included in the complete system response during the substructure analysis.

Also shown in Figure 5.10 is an equivalent-linear impedance spring with secant stiffness defined by passing through the origin and the peak displacement of approximately 0.1 m. The magnitude of the pushover displacement to which the impedance springs were matched was chosen based on the outcome of the direct analysis, which showed that the peak pile-head relative displacement was about 0.1 m. Since the nonlinear impedance spring matches the pushover curve over both small and large deformation regions, the largest displacement to which it is defined is not a critical factor as long as it lies within the range of the subsequent analyses. On the contrary, the modulus of the equivalent-linear impedance spring is directly dependent on the displacement at which it is defined, complicating the fitting process.

Furthermore, foundation damping must be modeled separately when using an equivalent-linear impedance spring. To some degree, foundation damping is inherently captured by fitting the equivalent-linear spring to the nonlinear pushover curve since the nonlinear soil response implies non-zero hysteretic damping under cyclic loading, but it is difficult to quantify the extent to which this is the case. For these analyses, it was found that use of a dashpot in parallel to the impedance spring resulted in spurious behavior at frequencies other than the frequency for which the dashpot coefficient was defined. Instead, foundation damping was imposed as Rayleigh damping corresponding to  $\beta = 0.05$  at 25 Hz and  $\beta = 0.22$  at  $3.9 \text{ Hz} \approx \tilde{f}_{1,SDOFO}$ . Foundation damping at  $\tilde{f}_{1,SDOFO}$  was computed using the following equations from NIST [2012]:

$$\beta = \frac{1}{4}\beta_p + \frac{3}{4}\beta_s + \frac{3}{4}\beta_r \quad (5.4)$$

$$\beta_r = \frac{3}{2\alpha(1+\nu_s)\delta} (a_0^p)^{\frac{3}{4}} \quad (5.5)$$

$$\alpha = 1 - \frac{3\pi}{32\delta} \left( \frac{\rho_p / \rho_s}{1 + \nu_s} \right) (a_0^p)^2 \quad (5.6)$$

In Equations (5.4) through (5.6) the damping subscripts  $p$ ,  $s$ , and  $r$  stand for pile and soil material damping and radiation damping, respectively;  $\alpha$  is the static stiffness modifier for pile lateral translation,  $\delta$  is the Winkler coefficient taken as 1.0 for fixed-head piles, and  $a_0^p$  is dimensionless frequency defined at  $\tilde{f}_{l,SDOFO}$  using the classical definition  $\omega B/V_s$ . Soil and pile material damping were approximated as 0.05.

When the equivalent-linear impedance spring is used with the substructure method, the computed system response is in reasonable agreement with the nonlinear impedance spring and direct analysis results for this example; see Figure 5.9. Given that the current state-of-practice for deep foundation lateral loading design is to use nonlinear  $p$ - $y$  curves, the tools necessary for creating a nonlinear force versus displacement head pushover curve to which an equivalent-linear stiffness can be matched are already available and should be used. The equivalent-linear impedance spring result appears to have over-estimated  $\tilde{f}_{l,SDOFO}$  by about 10% and under-estimated damping, causing an over-prediction of the peak FM/FFM ordinate by about 15%. Also shown for reference is the result computed using linear properties corresponding to the initial elastic soil properties, i.e., with no modulus reduction. This approach clearly produces an erroneous result, highlighting the importance—and difficulty—of selecting appropriate equivalent-linear properties. The equivalent-linear properties could be further refined to provide a closer match to the nonlinear system behavior in a design setting.

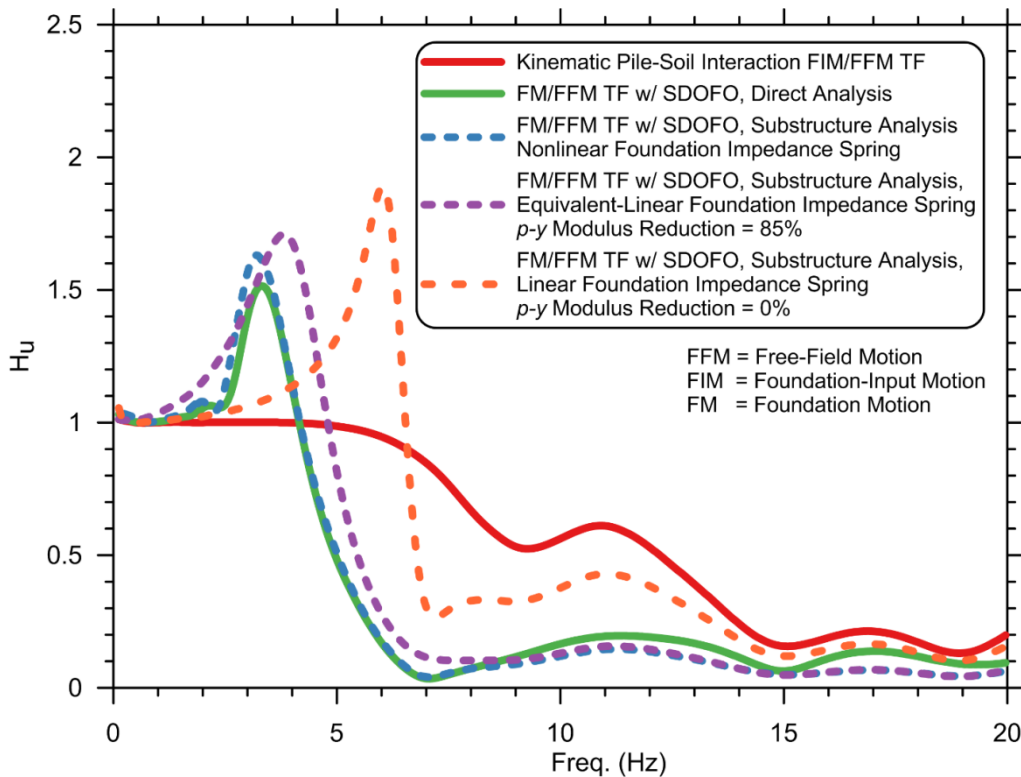


**Figure 5.9** Effect of nonlinear pile–soil interaction on SDOFO–pile–soil system transfer functions for homogeneous soil subjected to sine-sweep free-field excitation.

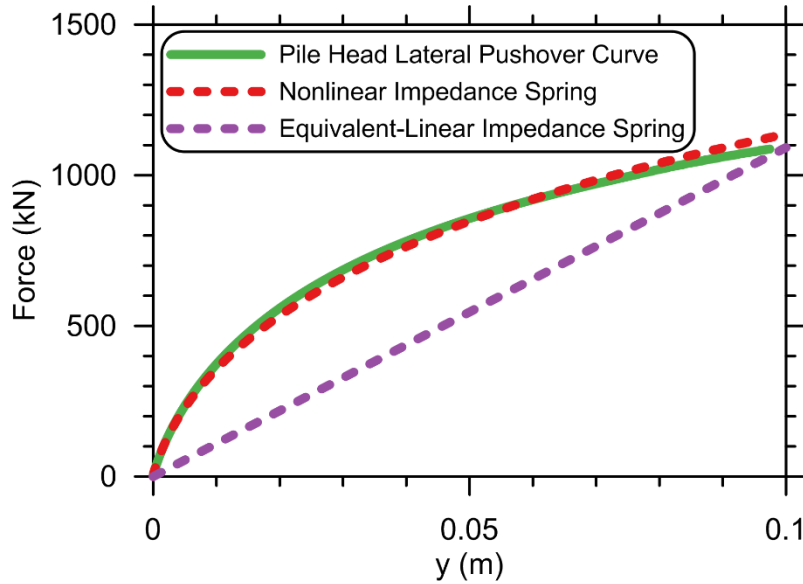


**Figure 5.10 Formulation of nonlinear and equivalent-linear impedance spring macro-elements to replace pile in substructure method of analysis.**

To assess the impact of pile–soil interaction nonlinearity for more realistic conditions, the analyses were repeated for the same SDOFO-pile system embedded in the soft soil Site 1 and subjected to the 1971 San Fernando, California, earthquake Lake Hughes #4 recording (known as ground motion 1 for this study; refer to §3.6 and §3.7 for site and motion descriptions). The mass of the SDOFO was varied from 10 Mg to 25 Mg to produce different amounts of period lengthening, while the remaining system properties were held constant. Foundation impedance springs were formulated in the same manner depicted in Figure 5.10. The results are shown in Figure 5.11.

For both the  $m_{SDOFO} = 10$  Mg and 25 Mg cases, the substructure analysis using a nonlinear foundation impedance spring gives a close match to the direct analysis result in terms of matching the correct  $\tilde{f}_{l,SDOFO}$  and peak transfer function ordinates. However, the accuracy of the results does appear to decrease slightly with increasing period lengthening. The results using the equivalent-linear impedance spring formulated from the nonlinear pushover curve also provide a reasonably close match to the direct analysis results. However, formulating these equivalent-linear springs and capturing the foundation damping required knowing the nonlinear behavior of the system in advance, which would not be known *a priori* if the equivalent-linear method was used as a standalone approach.

Also shown in Figure 5.11 are substructure analysis results computed with equivalent-linear impedance springs based on the modulus reduction values recommended in NIST [2012] Table 2-1 for SSI analysis. Based on a short-period spectral acceleration  $S_{DS} \approx 0.2g$  for the ground motions used, the modulus reduction factor ( $G/G_{max}$ ) for Site Class E ( $V_{S30} < 180$  m/sec) is given as 0.60. Since the  $p$ - $y$  modulus is linearly related to soil-shear modulus for the formulation used herein, these factors can be applied directly to  $K_e$  to approximately capture nonlinearity due to ground response for equivalent-linear pile–soil interaction modeling.

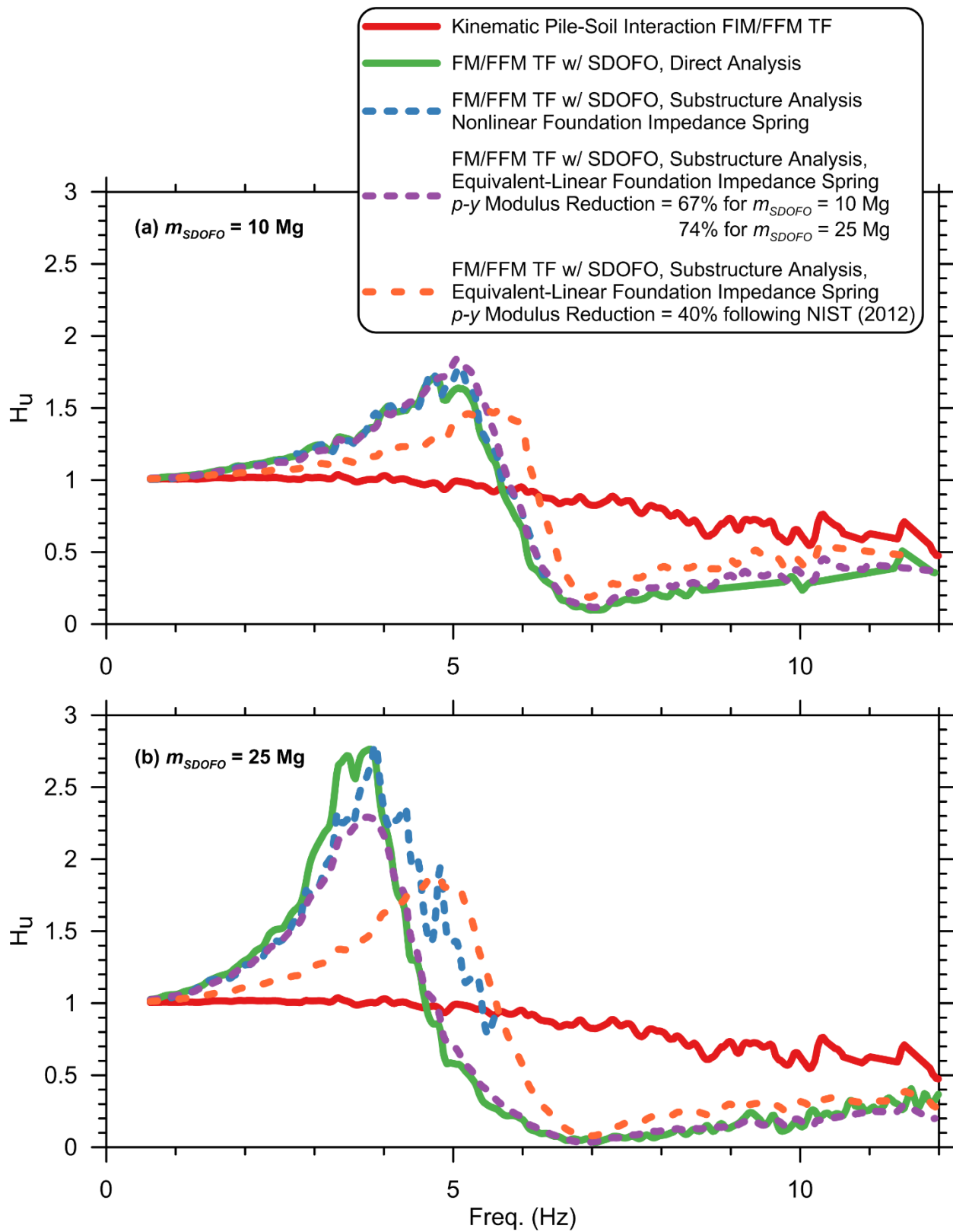


Figure 5.11 Effect of nonlinear pile–soil interaction on SDOFO–pile–soil system transfer functions for Site 1 subjected to 1971 San Fernando, California, earthquake Lake Hughes #4 recording.

The results show that as the amount of period lengthening increases, the accuracy of the transfer functions computed with the NIST reduction factors decreases. For the  $m_{SDOFO} = 10$  Mg system ( $\tilde{f}_{1,SDOFO}/f_{1,SDOFO} \approx 0.75$ ), the peak transfer function ordinate is under-predicted by about 10%; for the  $m_{SDOFO} = 25$  Mg system ( $\tilde{f}_{1,SDOFO}/f_{1,SDOFO} \approx 0.55$ ), the peak transfer function ordinate is under-predicted by about 20% and period lengthening is significantly underestimated. One of the reasons for this trend is that the NIST factors for estimating modulus reduction only depend on the magnitude of free-field excitation without consideration of the system properties such as mass, stiffness, and foundation flexibility because they are only intended to capture modulus reduction due to site response and not SSI. Since the amount of pile–soil interaction nonlinearity depends on all of these properties, a proxy for quantifying nonlinearity based only on ground-motion intensity is unlikely to provide a realistic estimate over a wide range of project conditions.

The period-lengthening ratio (or equivalently, the frequency-shortening ratio ( $\tilde{f}_{1,SDOFO}/f_{1,SDOFO}$ )) could therefore be a more useful metric for quantifying whether or not the error introduced to the substructure method of analysis by neglecting pile–soil interaction nonlinearity is significant. The results presented above indicate that  $\tilde{f}_{1,SDOFO}/f_{1,SDOFO}$  below about 0.75 could introduce significant errors to the substructure method, but a more comprehensive parametric study would be useful for refining this criterion. To make an accurate estimate of  $\tilde{f}_{1,SDOFO}/f_{1,SDOFO}$ , pile–soil interaction nonlinearity should be considered. Even for superstructure dynamic analysis using equivalent-linear foundation impedance springs, nonlinear pile–soil interaction analyses should be conducted to define the equivalent linear impedance properties.

## 6 Example Applications of Transfer Function and Spectral Ratio Prediction Models

In this chapter, the generalized kinematic pile–soil interaction transfer function and spectral ratio models developed in Chapter 4 will be compared to previously recorded empirical transfer functions and implemented for a bridge design scenario. This requires consideration of the effects of combined kinematic and inertia soil–structure interaction (SSI) discussed in Chapter 5.

### 6.1 EMPIRICAL CASE STUDIES

The empirical transfer functions for pile-supported buildings reported by Kim and Stewart [2003] and Givens et al. [2012] provide an opportunity to apply the predictive models developed for this study and investigate issues of combined kinematic and inertial SSI for real systems. The empirical transfer functions and attempts to replicate them in previous studies were originally discussed in §1.3.6.1. These case studies will be revisited in the following sections.

#### 6.1.1 Sendai, Japan, Site after Givens et al. [2012]

This site consists of an instrumented four-story reinforced-concrete building and adjacent free-field accelerographs located on the Tohoku Institute of Technology campus in Sendai, Japan. Multiple strong earthquakes have been recorded at the site. Transfer functions computed from these earthquakes show a significant reduction of the foundation motion (FM) relative to the free-field motion (FFM) over a frequency bandwidth of approximately 2.5 to 8 Hz. As reported by Givens et al. [2012], the reductions were observed to be approximately equal ( $H_u \approx 0.5$ ) for the **M** 7.1 2003 Off-Miyagi and **M** 9.0 2011 Tohoku earthquakes, despite significantly different recorded PGAs of 0.23g and 0.81g for the two earthquakes, respectively. This behavior is inconsistent with the notion that kinematic pile–soil interaction should result in lower values of  $H_u$  for stronger shaking due to greater modulus reduction of the soil. The original researchers hypothesized that the misfit between existing kinematic transfer function models and the empirical data could be due to ground-motion incoherence, and that perhaps nonlinear effects are not significant for kinematic interaction.

Further details regarding the site are presented in Figure 6.1 and Figure 6.2 based on information presented by Mikami et al. [2006], Givens et al. [2012], and from discussions with Professor Atsushi Mikami [*personal communication*, 2015]. The building’s lateral-force resisting system consists of shear walls in the transverse (narrow) direction and concrete moment frames in

the longitudinal direction. A total of 24 reinforced-concrete  $B = 0.75\text{-m}$ ,  $L = 8\text{-m}$  piles interconnected by stiff grade beams support the building. The piles pass through 6 m of soft to medium-stiff surficial soil ( $V_s \approx 130$  to  $200$  m/sec) and are socketed 2 m into soft mudstone ( $V_s \approx 320$  m/sec). Assuming good construction practices were followed, the piles likely exhibit significant base resistance given the diameter and stiffness of material at the base elevation.

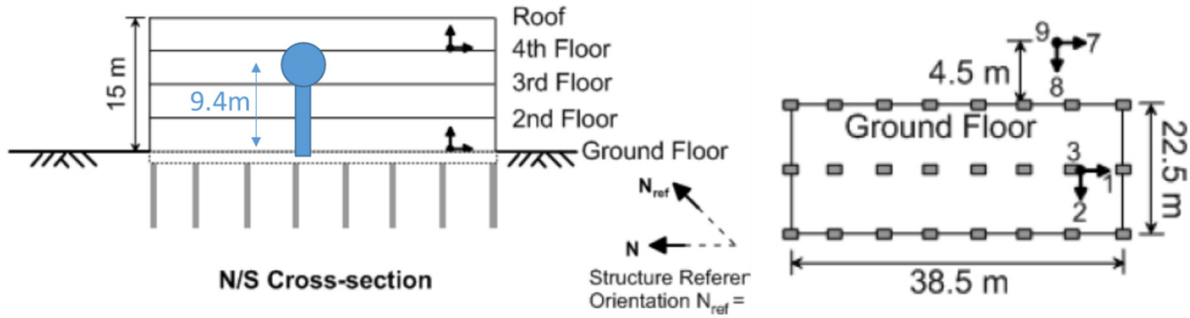


**Figure 6.1** Tohoku Institute of Technology building layout after Givens et al. [2012] and idealized single-degree-of-freedom oscillator representation.

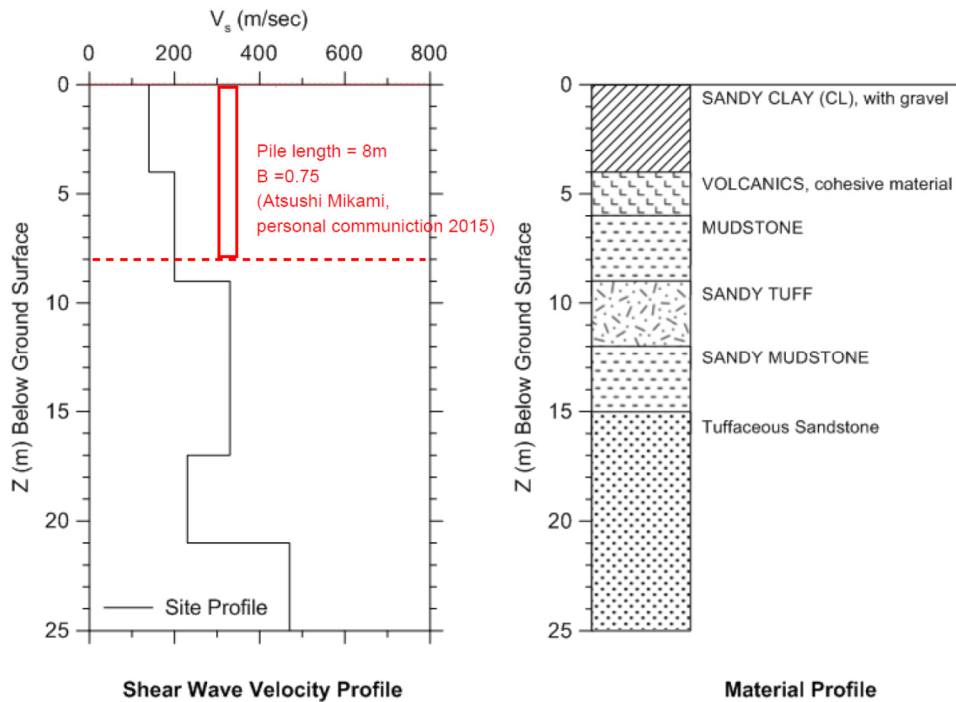


**Figure 6.2** Subsurface information for Sendai site after Givens et al. [2012]. Subsurface data originally reported by OYO Corporation [2007].

The substructure modeling approach presented in the previous chapter has been applied to this case study for the 2011 Tohoku earthquake recording originally reported by Givens et al. [2012]. The modeling steps are summarized as follows:

- The generalized transfer function model for fixed-head piles presented in §4.4.3 was used to predict a kinematic pile–soil interaction transfer function relating foundation-input motion (FIM) to FFM in the absence of superstructure inertia (i.e., FIM/FFM transfer function). This kinematic model considers only pile effects and not base slab averaging.
- The recorded FFM was convolved with the predicted kinematic FIM/FFM transfer function to produce a FIM for subsequent dynamic analysis.
- A beam-on-dynamic-nonlinear-Winkler-foundation (BDNWF) model of the pile embedded in the subsurface profile shown in Figure 6.2 was constructed in *OpenSees*. Nonlinear pile–soil interaction was modeled using  $p$ - $y$  curves defined by the *PySimple3* material. A “pushover test” of this pile was simulated to produce a nonlinear pushover curve (e.g., see Figure 5.10) relating lateral force imposed at the pile head to lateral displacement.
- The structure was idealized as a pile-supported SDOFO with height 9.4 m and mass 75 Mg. The mass is based on four 38.5 m × 28.5 m above-grade floors supporting an assumed uniform dead load of 5 kPa, evenly distributed to the 24 piles. The height corresponds to the centroid of the above-grade floors as shown in Figure 6.1. The SDOFO-pile model represents a single pile and its tributary mass, but the response of this system is assumed to approximately represent the entire structure.
- The flexible-based period of the building is reported by Mikami et al. [2006] as 0.43 s ( $\tilde{f}_{l,SDOFO} = 2.35$  Hz) based on system identification techniques. The SDOFO with mass = 75 Mg and height = 9.4 m described above was added to the *OpenSees* pile-soil model. After specifying an initial trial value for fixed-base period  $f_{l,SDOFO}$ , from which SDOFO column stiffness was computed using Equations (5.1) and (5.2), the *eigen* command was used to compute  $\tilde{f}_{l,SDOFO}$  of the combined SDOFO-pile–soil system. Using 2.35 Hz as the target  $\tilde{f}_{l,SDOFO}$ , the fixed-base frequency was adjusted until a good match was achieved using  $f_{l,SDOFO} = 2.45$  Hz (0.41 sec). This finding suggests that period lengthening was relatively insignificant, which is reasonable given the relatively flexible structure and stiff subsurface. Note that this calibration step would not have been possible if only the building period were known without information about its mass and stiffness.
- The pile and  $p$ - $y$  springs in the *OpenSees* model were replaced with a single macroelement impedance spring calibrated to fit the nonlinear pushover curve. This nonlinear spring was modelled using the *PySimple3* material. Rayleigh damping was specified as 10 and 5% at frequencies of 2.35 and 25 Hz, respectively.

- A dynamic analysis was performed by imposing the FIM on the free end of the impedance spring macroelement to excite the SDOFO-macroelement system [e.g., see Figure 5.1(c)].
- The foundation motion (FM) recorded at the base of the SDOFO column during this analysis was then used to compute a FM/FFM transfer function for comparison to the empirical transfer function as shown in Figure 6.3.

The kinematic pile–soil interaction FIM/FFM transfer function (purple line in Figure 6.3) predicts negligible reduction of the FFM over the frequency range where the empirical  $H_u \approx 0.5$ . On the other hand, the combined SDOFO-pile prediction computed using the substructure method (orange triangles) matches the empirical transfer function very well over this frequency range, including prediction of the sharp drop-off occurring just beyond  $\tilde{f}_{l,SDOFO}$ . It can be concluded from these results that the large reduction in the foundation-level motion relative to the free-field motion between 2.5 and 8 Hz is due primarily to the influence of inertial interaction and not the inability of the kinematic pile–soil interaction model to adequately capture the underlying mechanisms.

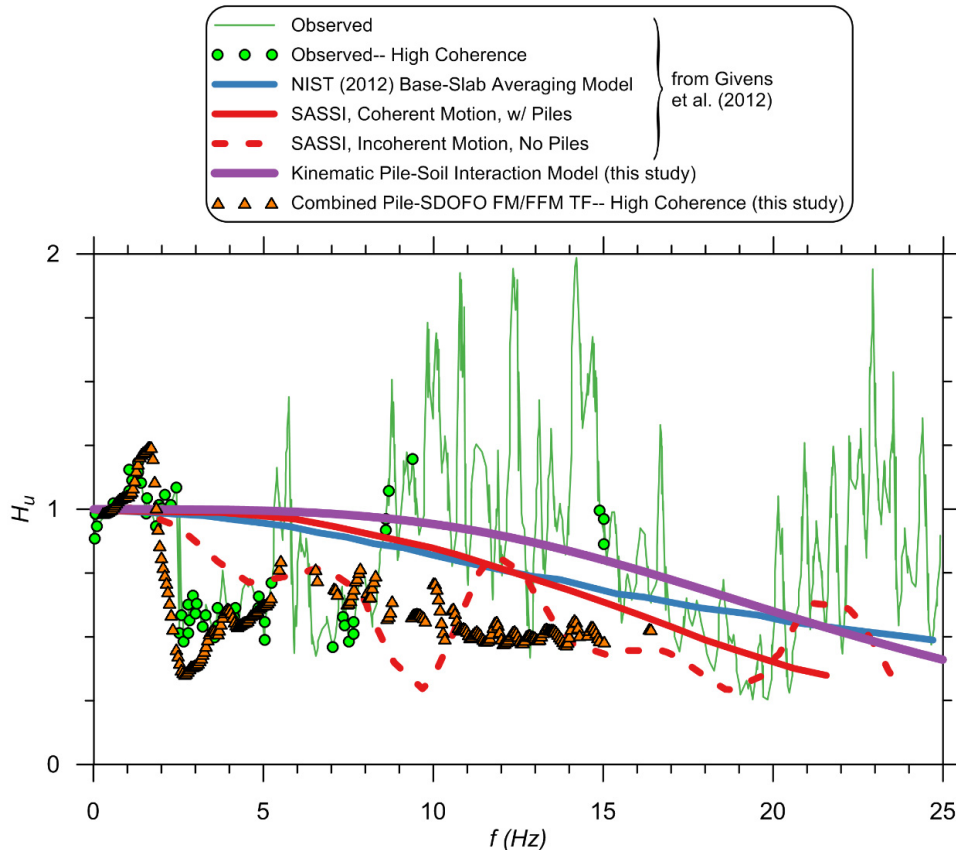


**Figure 6.3** Model predictions versus empirical data for Tohoku Institute of Technology building during 2011 Tohoku earthquake after Givens et al. [2012].

### 6.1.2 Lancaster, California, Site after Kim and Stewart [2003].

This site consists of a five-story pile-supported hospital building in Lancaster, California. During the 1994 **M** 6.7 Northridge earthquake, a free-field sensor located 360 ft (110 m) away from the building recorded a PGA of 0.071g. The Lancaster site is included in a database of 57 structure and adjacent free-field recordings compiled by Stewart and Stewart [1997] for empirical evaluation of SSI. Kim and Stewart [2003] reanalyzed 16 of the buildings that were pile-supported and found that the Fan et al. [1991] elastic model generally under-predicted reductions in foundation-level motions (FM) relative to FFM. In many of these cases, including the Lancaster site, a base-slab averaging model by Veletsos et al. [1997] modified with an empirically adjusted factor to approximate ground motion incoherence, foundation flexibility, and wave inclination effects was found to provide a better fit to the measured transfer functions. The authors concluded that interaction between shallowly embedded or surface foundation elements dominated the foundation motion, and that piles played an insignificant role. Given the relatively stiff soil (estimated  $V_S \approx 210$  to 370 m/sec) and flexible  $B = 20$ -in. (51 cm) piles at the Lancaster site, this hypothesis is consistent with the findings of the present study.

Re-evaluation of the Lancaster site therefore had two goals: (i) to compare the kinematic model from this study to the measured transfer function, for which a poor match was expected; and (ii) determine if including inertial SSI effects provides a better match to the measured transfer function as was the case for the Sendai site.

Further details of the building and site are presented in Figure 6.4 and Figure 6.5 based on original documentation presented in Stewart [1996] and Stewart and Stewart [1997], with additional information from Stewart et al. [1999], Kim [2001], and Kim and Stewart [2003]. The building was designed circa-1986 with steel moment frames serving as the lateral force resisting system in both building directions. Steel columns are supported by  $B = 20$ -in. (51 cm) drilled shafts ranging in length between 15 and 50 ft (4.6–15.2 m). Although not stated explicitly in the original documentation, based on the building layout shown in Figure 6.4 and typical design practices it assumed for the purpose of this analysis that each column is supported directly by an individual pile. The first floor of the building is not embedded below the ground surface. Fixed-base and flexible-base first-mode periods are reported by Stewart et al [1999] as 0.69 and 0.73 sec, respectively, corresponding to a relatively small period-lengthening value of 1.06. These values and the transfer functions computed below correspond to the building transverse direction, which is roughly east-west (see Figure 6.4). Subsurface conditions consist of interbedded medium-dense to dense silty sand and medium-stiff to very stiff silty clay. The unit weights and estimated shear-wave velocity profile shown in Figure 6.5 were used to define the subsurface profile for the transfer functions computed for the present study.

The procedures for computing the purely kinematic FIM/FFM transfer function and combined SDOFO-pile FM/FFM transfer function are the same as for the Sendai site and so will not be repeated here. The exception is that the system identification work done by Stewart [1996] provides some parameters for the Lancaster site that had to be estimated for evaluating the Sendai case. These are the equivalent-SDOFO height (40 ft) and fixed-base period (0.69 sec). As for the Sendai site, the building is modelled as a SDOFO supported by a single pile, where the mass of the SDOFO represents the estimated tributary mass supported by a single pile in the real structure. Using the same assumed uniform dead load of 5 kPa distributed over the floor plans shown in Figure 6.4, this resulted in an equivalent SDOFO mass of 145 Mg. The 50-ft pile length is used

for the model. The measured transfer function ordinates with high coherence do not indicate that strong kinematic amplification occurred, which would be indicative of a free-head pile condition, so the pile heads are assumed to be fixed. Although not shown on the building drawings or described in the original documentation, it is assumed that grade beams interconnect the piles and provide some resistance against rotation. The impedance spring macro-element used for the substructure analysis is defined to a stiffness of 0.01 m, which is in the range of the maximum differential displacement between the recorded FM and FFM.

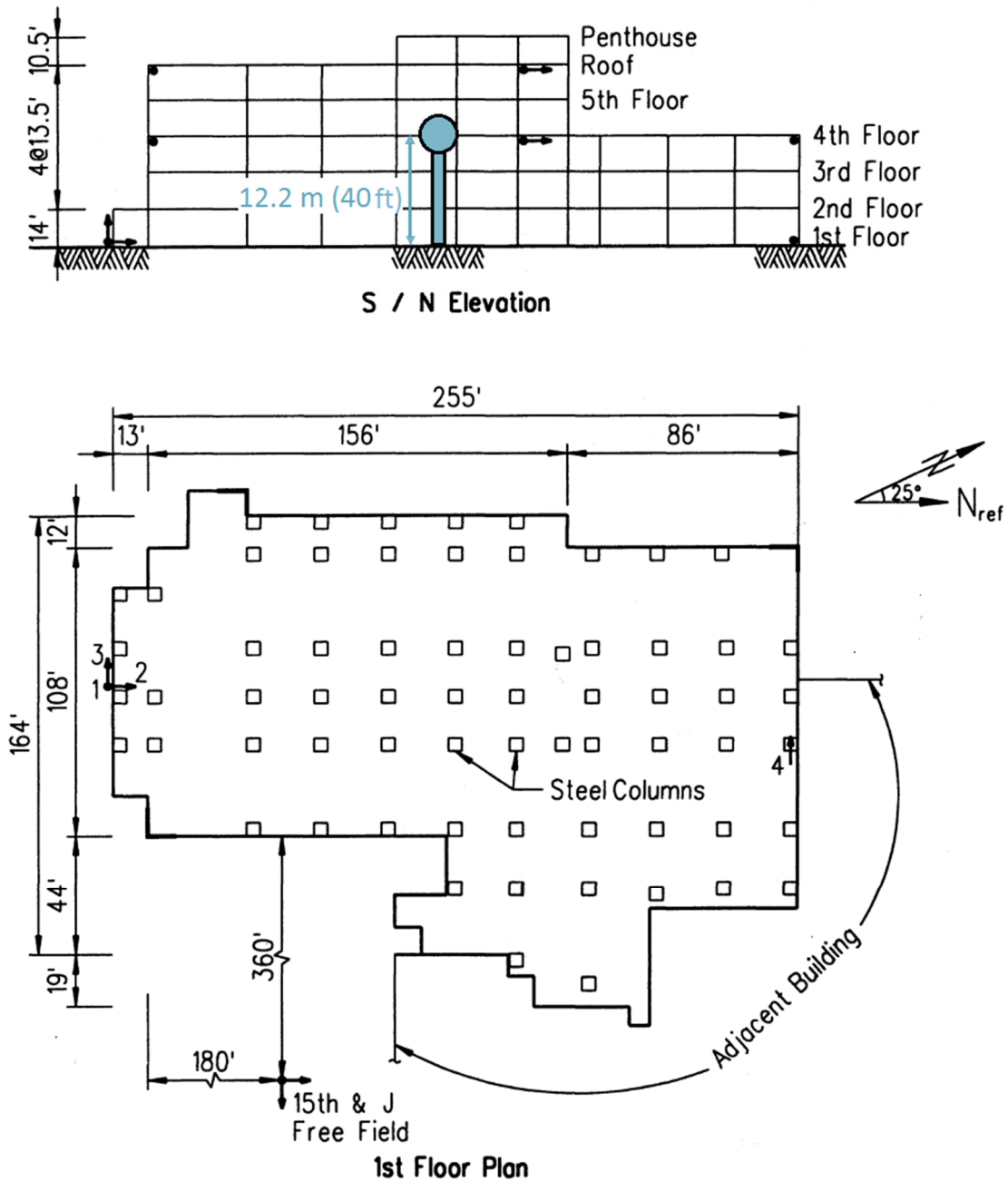


**Figure 6.4** Lancaster, California, hospital building layout and idealized single-degree-of-freedom oscillator representation after Stewart and Stewart [1997].

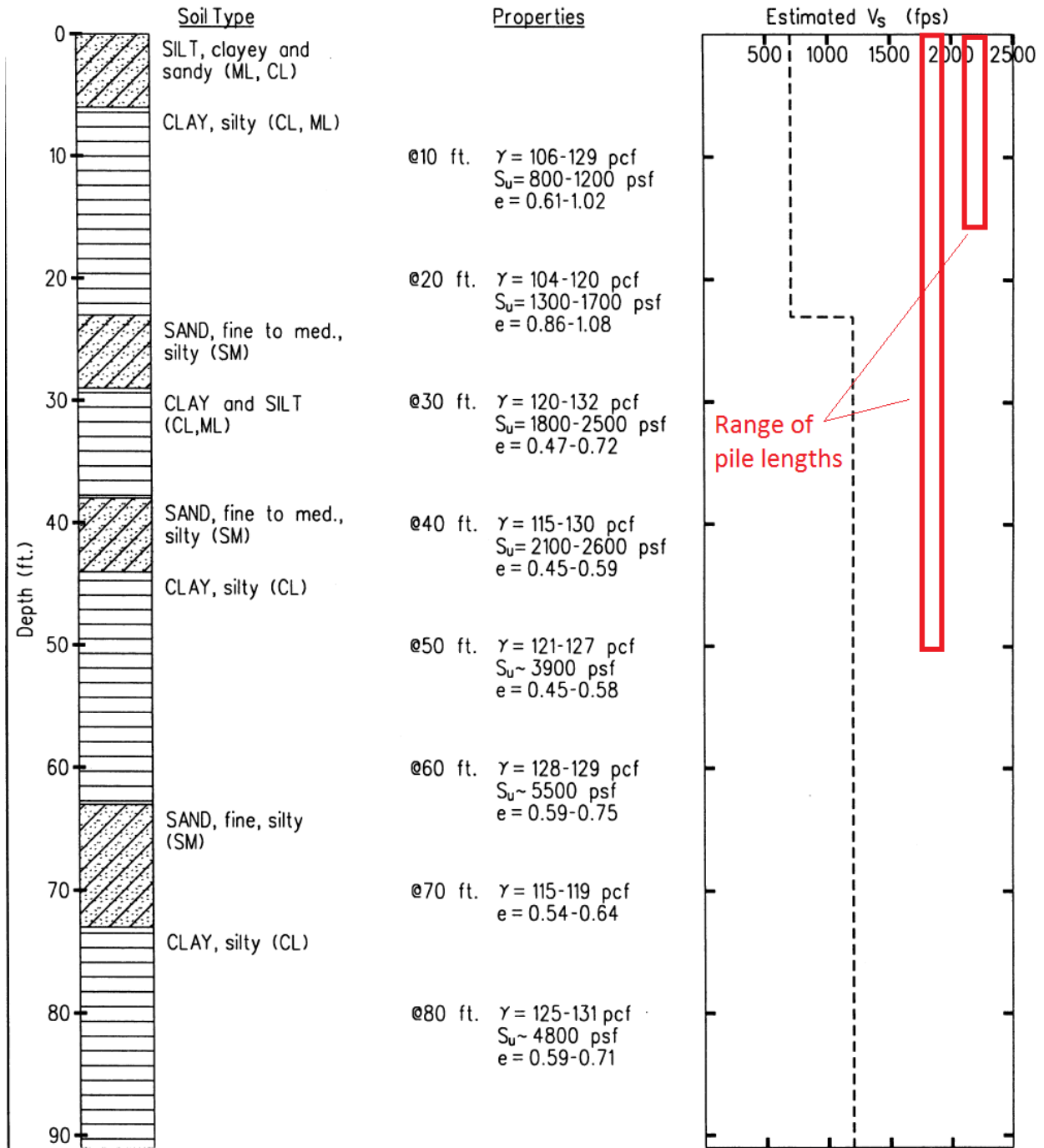


**Figure 6.5 Subsurface conditions at Lancaster site after Stewart and Stewart [1997].**

The kinematic FIM/FFM transfer function predicted using the models presented in §4.4.3 is shown in Figure 6.6. Note that significant reduction of the FIM relative to the FFM is predicted only at frequencies above about 30 Hz, which is well beyond the range of interest for this case and for most buildings in general. The FIM/FFM transfer function is also shown versus dimensionless frequency compared to the range of results computed for the parametric analysis done for this

study (e.g., see Figure 4.13). This comparison shows that the predicted transfer function falls within the range of the study results.

Comparison between the combined SDOFO-pile FM/FFM transfer function and recorded FM/FFM transfer function is shown in Figure 6.7. Note that a log-frequency scale is used to emphasize low frequencies near the building fundamental frequency. The computed transfer function (orange triangles) provides a good match to the recorded transfer function (green dots) up to the peak occurring around approximately 1.2–1.3 Hz, which occurs because of inertial resonance near the building’s flexible first-mode period. Immediately beyond this frequency, the computed transfer function predicts a significant drop-off down to  $H_u \approx 0.5$ , while the recorded transfer function only decreases to around  $H_u \approx 0.75$ .

Recalling Figure 5.5 and Figure 5.6, the local minimum in this region of the transfer function marks the transition between the foundation-level response being dominated by inertia to being controlled primarily by the ground displacement at higher frequencies. For the Lancaster case, over-prediction of the drop-off after  $\tilde{f}_{I,SDOFO}$  is likely a result of not including the surface–foundation elements in the SDOFO-pile substructure model. Interaction of surface foundation elements through base friction and rocking would decrease foundation-level motions in addition to the lateral resistance provided by piles, which in turn would decrease the effect of the foundation motion being dominated by inertia of the structure mass. Because the pile-to-soil stiffness contrast was relatively low at this site, and the piles are relatively small, base–slab averaging likely provides a better explanation for the observed behavior than the pile kinematic model, as concluded by the original researchers. Nonetheless, these results again highlight the fact that recorded FM/FFM transfer functions inherently contain inertial SSI effects, especially near the fundamental mode frequency, and comparison of empirical results to kinematic SSI models is more meaningful if the combined inertial-kinematic effects are explicitly considered.

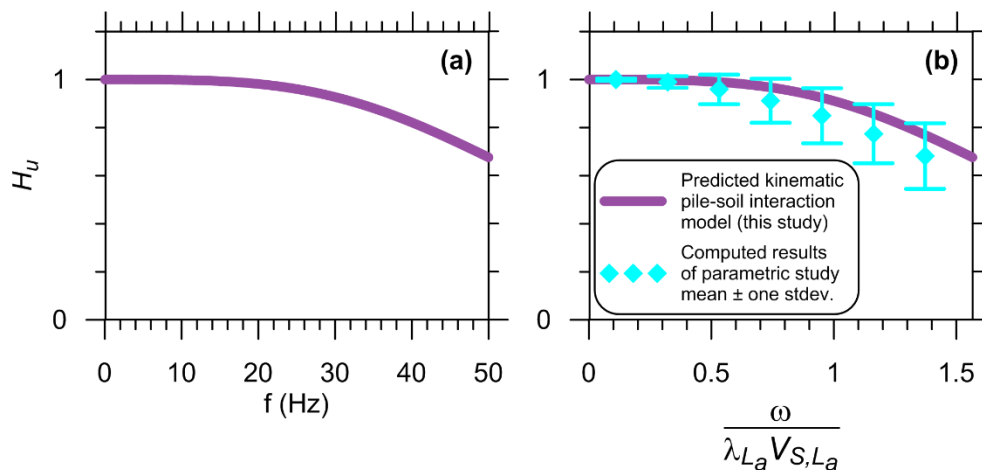


**Figure 6.6** Predicted kinematic pile–soil interaction transfer function for the Lancaster site plotted versus (a) plain frequency and (b) dimensionless frequency.

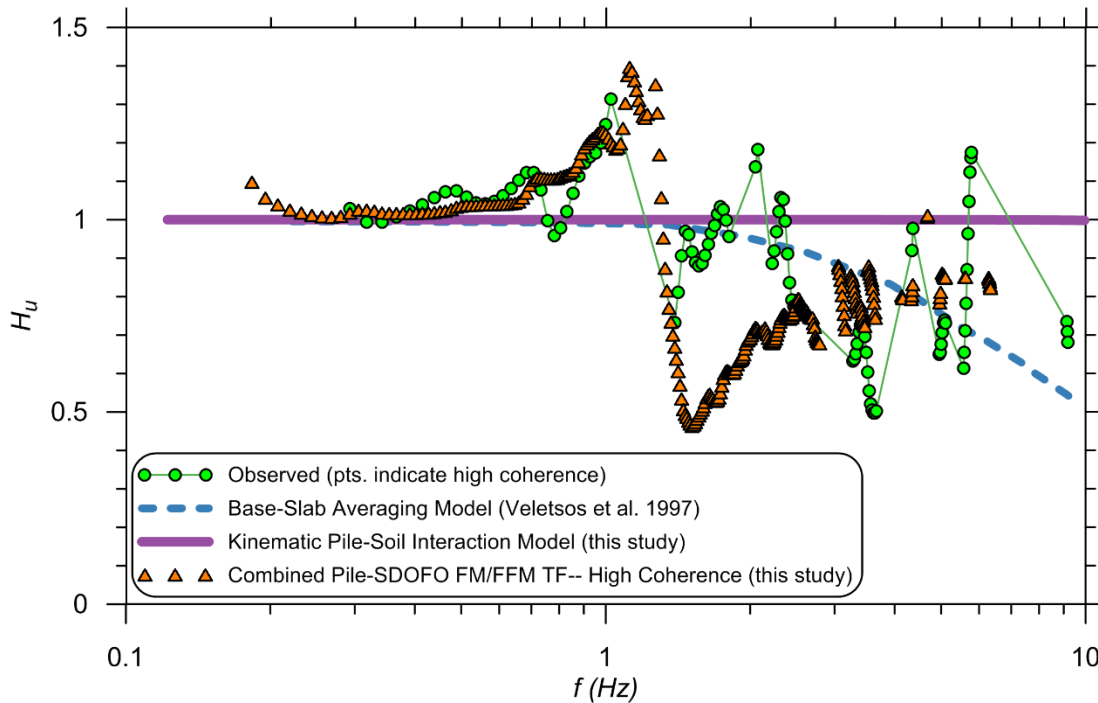


**Figure 6.7** Model predictions versus empirical data for the Lancaster building during 1994 Northridge, California, earthquake after Kim and Stewart [2003].

## 6.2 EXAMPLE APPLICATION OF SPECTRAL RATIO PREDICTION MODEL FOR PILE-SUPPORTED BRIDGE

The California Department of Transportation (Caltrans) is currently in the process of replacing a bridge at the Highway 101—Linden Avenue overcrossing in Carpinteria, California. Construction plans for the replacement bridge, which are available online [Caltrans 2016]<sup>7</sup>, show that 78-in.-diameter cast-in-steel-shell (CISS) piles will be used to support the single-bent structure; see Figure 6.8 and Figure 6.9. The CISS piles consist of a driven steel-pile shell that is subsequently filled with concrete and reinforcing steel, resulting in a stiff foundation element. The first-mode natural frequency of the bridge in the longitudinal direction is 0.45 sec [Caltrans, *personal communication*, 2015]. Based on the design response spectrum for free-field conditions shown in the plans (see Figure 6.10), the spectral acceleration at this period is approximately 1.34g.

Using the proposed bridge foundations as an example, the spectral ratio prediction model for free-head piles presented in §4.5.3 will be used to modify the free-field acceleration response spectrum to account for kinematic pile–soil interaction.

Subsurface conditions at the bent location generally consist of loose to medium-dense silty sand and sandy silt interbedded with soft to medium-stiff lean clay. The CISS piles will extend from elevation +18 ft to -58 ft for a total length of 75 ft. A shear-wave velocity profile measured using P-S suspension logging is shown in Figure 6.11. Considering the  $V_s$  profile and based on a

<sup>7</sup> [http://www.dot.ca.gov/hq/esc/oe/project\\_ads\\_addenda/05/05-4482U4/plans/](http://www.dot.ca.gov/hq/esc/oe/project_ads_addenda/05/05-4482U4/plans/)

review of the borings and CPT soundings done at the site, the stratigraphy is idealized as consisting of a surface layer extending from the ground surface to a depth of 15 m with unit weight 108 pcf (17 kN/m<sup>3</sup>) overlying a denser layer with unit weight 120 pcf (19 kN/m<sup>3</sup>). Both layers are assumed to behave as predominately granular soils.

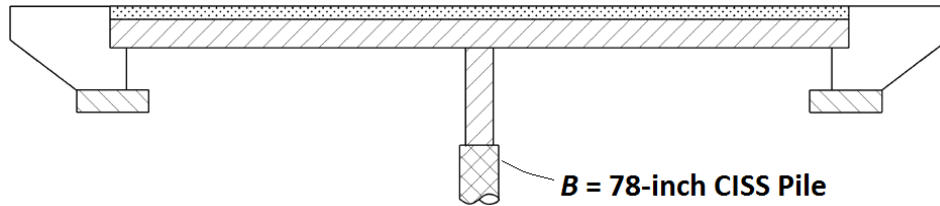


**Figure 6.8** Longitudinal elevation view of proposed Linden Street Overcrossing replacement (after Caltrans [2016]).

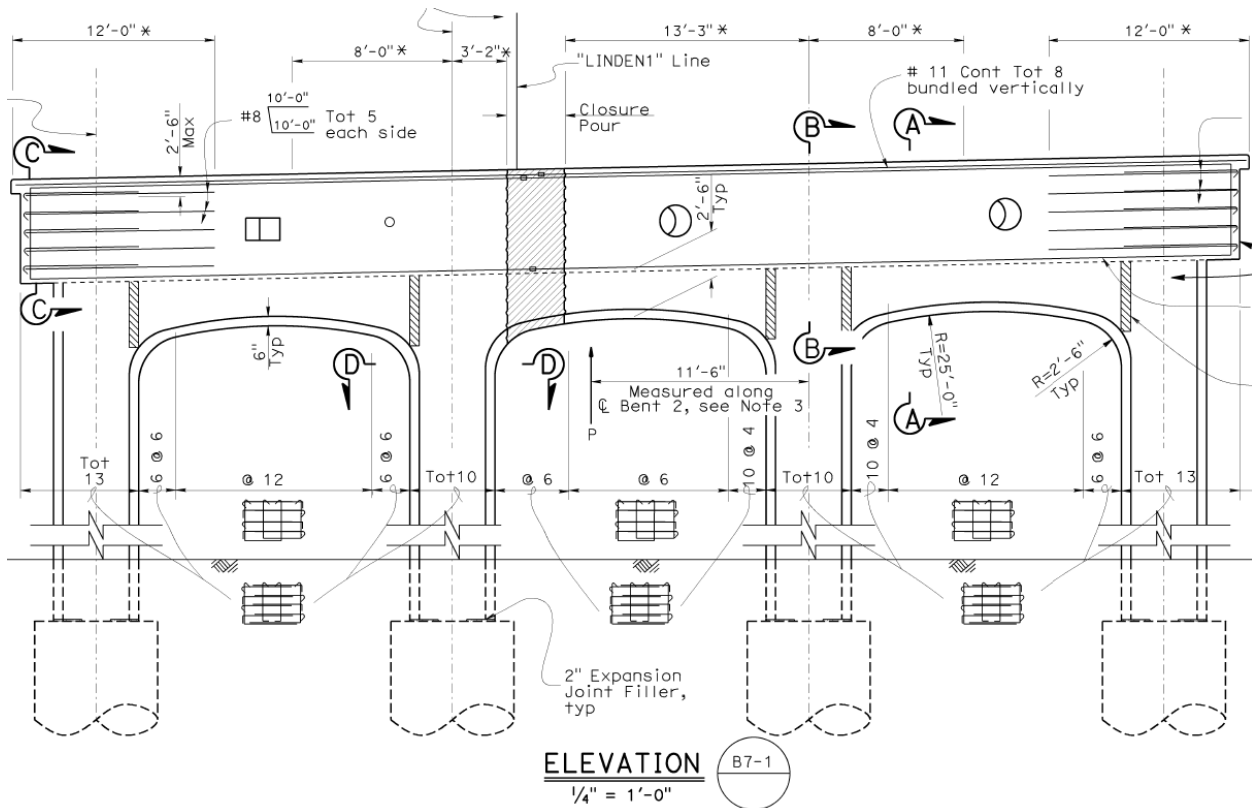


**Figure 6.9** Transverse elevation view of interior bent for proposed Linden Street Overcrossing replacement (after Caltrans [2016]).

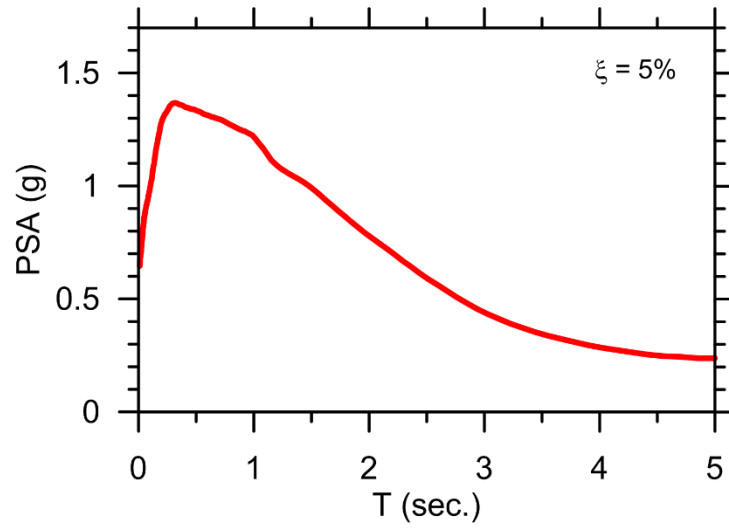


**Figure 6.10** Acceleration response spectrum used for proposed Linden Street Overcrossing replacement (after construction plans, Caltrans [2016]).

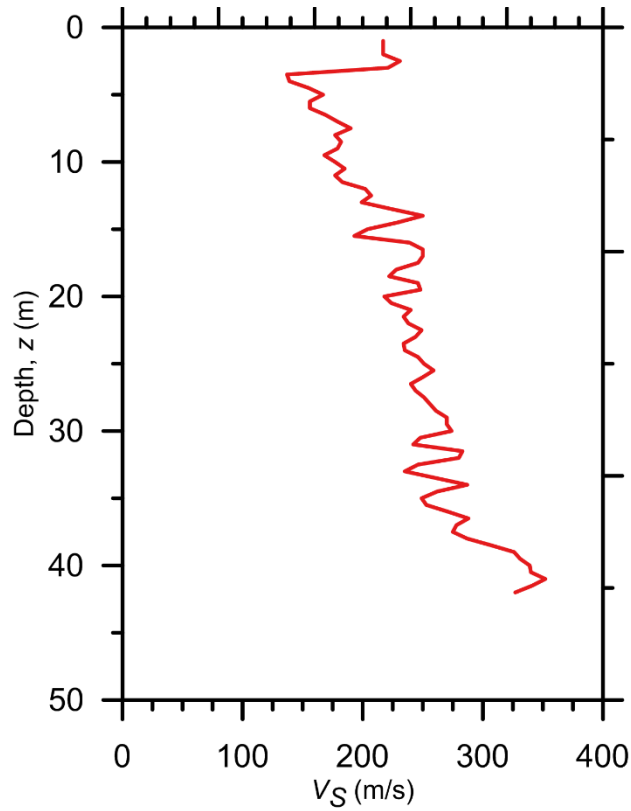


**Figure 6.11** Shear-wave velocity profile measured using P-S suspension logging (after Caltrans [2016]).

The following list summarizes how the parameters needed as inputs for the coefficient prediction models were defined based on information obtained from the construction plans and other references:

- The effective flexural rigidity (i.e., considering the reduced moment of inertia due to concrete cracking) was estimated from the following expression from AASHTO [2009] for concrete-filled steel structural members:

$$EI_{eff} = E_s I_s + 0.4 \left( \frac{E_c A_c}{A_s} \right) I_s \quad (6.1)$$

in which  $E$ ,  $I$ , and  $A$  are the Young's modulus, moment of inertia, and cross-sectional area, respectively, and the subscripts  $c$  and  $s$  denote concrete and steel. The steel shell has a wall thickness of 1 in. (25.4 mm) and an assumed Young's modulus of 29,000 ksi (200 GPa). The concrete has a design strength of 3.6 ksi and assumed modulus of 3420 ksi (23.6 GPa).  $EI_{eff}$  computed using these parameters and the appropriate values of  $I$  and  $A$  in the above equation is 28,100 MN·m<sup>2</sup>. This value was also checked with a moment-curvature analysis, which showed good agreement.

- Active length  $L_a$  was computed as 50 ft (15.4 m; about 8 times the pile diameter) using the iteration process described in §1.3.3. Based on this length,  $\lambda_{La}$  and  $V_{S,La}$  were computed as 0.079 ft<sup>-1</sup> (0.26 m<sup>-1</sup>) and 606 ft/sec (185 m/sec), respectively. The  $\lambda_{La}$  calculation was based on  $EI_{eff}$  and  $K_e$  computed from the shear-wave velocities and unit weights given above, an assumed Poisson's ratio of 0.35, and  $\delta = 3.0$  (for free-head piles) as described in §2.3.
- The frequency  $f_0$  as defined by Rathje et al. [2004] computed from the design acceleration response spectrum is 2.05 Hz. This parameter describes the frequency corresponding to the predominant energy of the spectrum as discussed in §4.5.2. In order to meet the period spacing criterion established by Rathje et al., the spectrum was resampled on a log-evenly spaced period axis.

- From the preceding terms,  $\left( \frac{f_0}{\lambda_{La} V_{S,La}} \right) = 0.043$

- Time-averaged shear-wave velocity over the full pile length is 656 ft/sec (200 m/sec), thus  $\left( \frac{V_{S,La}}{V_{S,L}} \right) = 0.93$

- The maximum spectral ordinate is  $\left( \frac{PSA_{max}}{g} \right) = 1.37$

The last three parameters in the above list are the inputs to the spectral ratio coefficient prediction models for free-head piles presented in §4.5.3. Using the coefficients predicted by Equations (4.27) through (4.32), the resulting spectral ratio curve defined by the Equation (4.21) functional form is presented in Figure 6.12.

The predicted spectral ratios in Figure 6.12 were multiplied by the design response spectrum to produce the modified spectrum shown in Figure 6.13. The modified spectral acceleration at the first mode period of the Linden Avenue Overcrossing (0.45 sec) is 1.34g, which is unchanged from the free-field spectrum value. For this example, the first-mode period of the bridge lies just beyond the range where kinematic pile–soil interaction is predicted to cause a significant modification to the free-field spectrum.

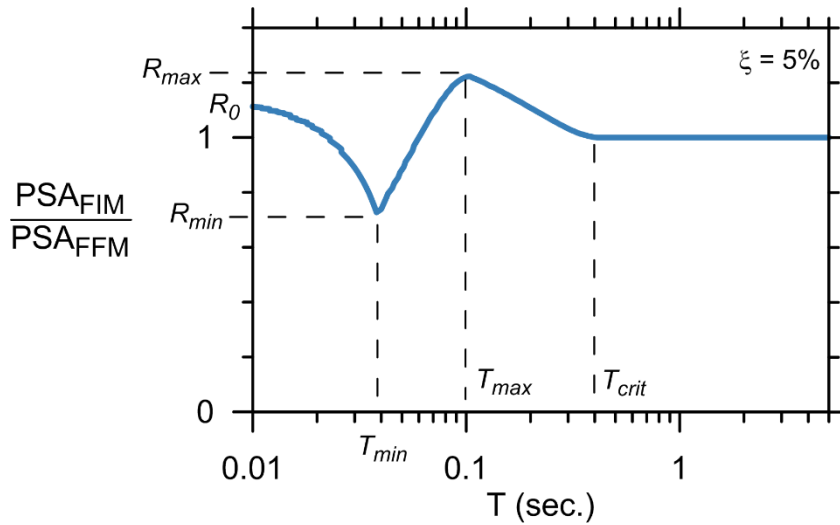


Figure 6.12 Predicted spectral ratios for Linden Street Overcrossing.

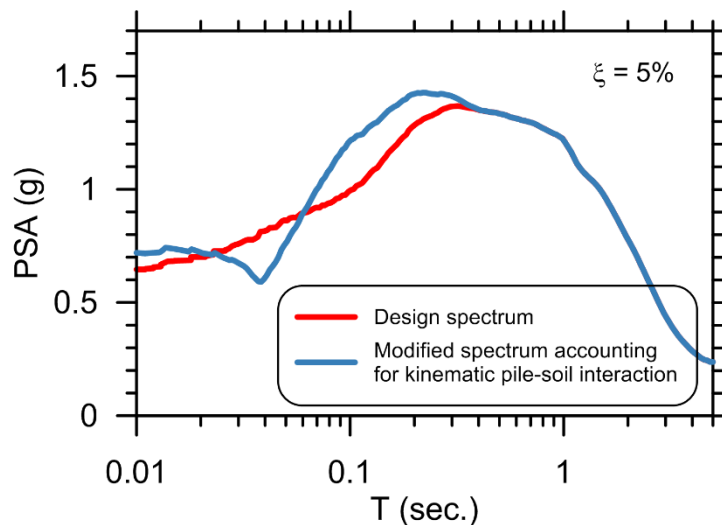


Figure 6.13 Kinematic pile–soil interaction effect on acceleration response spectrum.



## 7 Conclusions and Recommendations for Engineering Practice

A comprehensive parametric study of the influence of kinematic pile–soil interaction on foundation-input motions (FIM) by means of nonlinear numerical analysis has been presented. The analysis approach consisted of performing one-dimensional ground response analysis to define free-field motions, which were subsequently imposed on a beam-on-nonlinear-dynamic-Winkler-foundation model of a pile or pile group. The free-field ground surface motion (FFM) and top-of-pile “foundation-input motion” (FIM) computed from these results were then used to compute transfer functions and spectral ratios for use with the substructure method of seismic analysis. A total of 1920 parametric combinations of different pile sizes, soil profiles, and ground motions were analyzed.

Results of the study show significant reductions of the FFM due to kinematic pile–soil interaction occur for stiff, large-diameter piles in soft soil, which could result in a favorable reduction in design demands for short-period structures. Simulations of a  $3 \times 2$  pile group subjected to incoherent ground motions showed that group effects further reduce the FIM relative to the FFM in comparison to an equivalent single pile—but typically by less than 10%—and only over a limited frequency range. Still, the simulations performed for this study confirm this trend, and it is likely that consideration of ground-motion incoherence over a larger spatial extent, such as the footprint of a building supported on a piled-raft foundation, could be more significant. The tools for generating incoherent motions based on the work of Ancheta and Stewart [2015] described in §3.7.3 could be used for this purpose for future studies.

The key parameters controlling kinematic pile–soil interaction are:

- Pile head-fixity condition
- Pile-to-soil stiffness contrast
- Variations in soil stiffness over the pile length
- Nonlinear soil behavior due to pile–soil interaction, which depends on relative pile-to-soil stiffness contrast, and due to free-field ground response
- Radiation damping
- Variable frequency content of the free-field excitation, as opposed to harmonic excitation at a single frequency

The first three items in the above list have long been recognized from the results of elastic studies (e.g., Flores-Berrones and Whitman [1982], Fan et al. [1991], and Anoyatis et al. [2013]). The key differences between simplified elastic solutions and the nonlinear results computed for the more realistic conditions considered herein are caused by the latter three factors, including time-varying coupling and interference of these factors that is not captured when linear superposition is assumed.

The primary motivation for performing this study was to overcome the limitations of idealistic assumptions that have been employed in previous studies, such as linear-elastic material behavior, drastically simplified stratigraphy, and harmonic oscillations in lieu of real ground motions. In order to capture the important influence of more realistic conditions such as material nonlinearity, subsurface heterogeneity, and variable frequency-content ground motions, a set of models for predicting transfer functions and spectral ratios was developed through statistical regression of the results from this parametric study.

The results presented in Chapter 4 demonstrate that elastic solutions are approximately coincident with the average results of this study, but fail to capture the variability that is possible when more realistic subsurface conditions and ground motions are used along with explicit consideration of nonlinearity. While this suggests that elastic solutions provide a reasonable first-order approximation of behavior, it also means that they would *over*-predict the reduction in free-field ground motion due to kinematic pile–soil interaction roughly half of the time. A method that produces an erroneous prediction in the unsafe direction (i.e., an “un-conservative” estimate) half the time is generally unacceptable for engineering practice. A robust design approach should include measures for predicting the amount of variability that is anticipated due to realistic conditions.

Although a comparison to elastic analytical solutions provides a good means for checking that the results of this study fall within reasonable bounds (which has been confirmed), the importance of this comparison should not be weighted too heavily. Significant effort has been made to model realistic conditions for this study, which often represent a significant departure from the assumptions used in elastic analytical solutions; hence, it is expected that the results will differ. The large amount of variability exhibited by the results of this study should not be viewed as a negative outcome, but rather a reflection of the amount of variability that should be anticipated for real system behavior.

The results of the numerical analyses performed for this study are likely skewed slightly in the direction of under-predicting kinematic pile–soil interaction, which is to say that the computed transfer function ordinates are slightly above what may be anticipated for real behavior. Reductions in free-field motions computed in this study thus error slightly on the safe side in a design sense. This judgment is based on the effects of assumptions made when defining two of the modeling parameters as discussed subsequently: (i) radiation damping and (ii) using a value of  $\delta = 3.0$  for free-head piles.

Radiation damping manifests as an increase in stiffness for dynamic  $p$ - $y$  curves (see §3.4.4). Increases in soil stiffness, which correspond to a decrease in pile-to-soil stiffness contrast, result in less kinematic interaction. For example, Figure 4.18 showed that radiation damping effectively outweighed the effect of  $p$ - $y$  softening due to soil nonlinearity. The models used herein to define dashpot coefficients for radiation damping are from elasticity-based solutions that assume perfect radiation of stress waves to infinity through homogeneous elastic media. For more realistic

heterogeneous subsurface conditions, radiation damping may be a less efficient mechanism of energy dissipation than assumed by these models. Some portion of the energy due to stress waves generated at the pile–soil interface could be reflected back by other piles, adjacent structures, or geomaterial impedance contrasts. Hence, it is likely that the influence of radiation damping is over-predicted in this study, but because this results in a decrease in kinematic pile–soil interaction, it is considered acceptable. Experimental measurements of these effects could provide justification for reducing the magnitude of radiation damping employed in future studies.

It is worth noting that conventional deep foundation design based on static or pseudo-static methods does not take damping into consideration. Ignoring damping is usually a reasonable assumption for typical design applications in which soil is relied upon to provide resistance to loads generated in the superstructure and transmitted to the ground through foundations. For example, because ignoring the contribution of radiation damping to dynamic  $p$ - $y$  stiffness effectively results in a softer curve, estimates of lateral pile displacements due to superstructure lateral loads would be expected to exceed the real behavior. Thus a safe design can be developed by assuring that the predicted displacements are within tolerable limits.

For free-head piles, the assumption of zero rotational restraint at the pile head is an oversimplification. For a system that can be represented by a SDOF oscillator, such as a sign pole supported on a single pile, complete lack of rotational restraint may be a reasonable approximation. But for the case of piles supporting a bridge bent, the tendency for the pile head to rotate due to free-field kinematic demands would be resisted by other bridge components via the connection between the top of the bent and the superstructure. For example, consider rotations in the longitudinal direction of the bent foundations shown in Figure 6.8, which would be resisted by the bent-to-deck connection and the abutment stiffness. This connection was found to play an important role in resisting kinematic lateral spreading demands by Turner et al. [2016]. Likewise this factor could play an important role in influencing pile behavior during transient kinematic loading and affect the transfer of the foundation input motion to the superstructure. The most significant impact of this restraint would be to limit rotations of the pile near the ground surface, which should result in a smaller value of Winkler coefficient  $\delta$ . Recall that  $\delta = 3.0$  was used for free-head piles to account for the increases shear resistance mobilized in the soil due to pile rotation, while  $\delta = 1.0$  was used for the fixed-head piles, which undergo less rotation and thus exert predominantly compressive stresses in the direction of loading. Hence, the value of  $\delta = 3.0$  used in this study for free-head piles may result in an overestimate of  $p$ - $y$  stiffness and a corresponding underestimate of kinematic interaction for cases where significant restraint against rotation is provided by the superstructure, even if restraint is not provided at the ground surface elevation.

## 7.1 PREDICTIVE MODELS AND LIMITATIONS

Models for predicting transfer functions and spectral ratios were presented in §4.4 and §4.5. These models represent a means for predicting kinematic pile–soil interaction with consideration of nonlinear behavior, realistic subsurface condition, and real ground-motion characteristics without the need to perform dynamic analysis of a pile–soil system. Input parameters for the predictive models are computed from the type of information typically known for real projects, and are consistent with the type of seismic design that will be performed. For example, the spectral ratio

prediction equations use terms defined from the free-field response spectrum, while the transfer function prediction equations use terms defined from a free-field acceleration time series.

For design applications, a reasonable first-order approximation of pile-group behavior could be estimated by reducing transfer functions predicted using the single-pile prediction models by an additional 5% at frequencies beyond the corner frequency. Because of the idiosyncratic nature of the group results, for critical projects, modeling of the type used for this study would be more appropriate than this rough approximation. Alternatively, group effects could be ignored due to their relatively insignificant contribution to kinematic pile–soil interaction.

Caution should be exercised when applying the transfer function and spectral ratio prediction models to conditions falling outside the bounds considered in this study. In particular, the kinematic pile–soil interaction behavior predicted by the models may differ significantly from actual behavior for:

- Sites with a strong ground response effect caused by an abrupt impedance contrast occurring over the length of the pile or a stiff layer overlaying a significantly soft layer.
- Sites with time-averaged shear-wave velocity over the length of the pile ( $V_{s,L}$ ) significantly below 100 m/sec, which could result in soil nonlinearity during site response and due to pile–soil interaction that is beyond the amount of nonlinearity captured in this study.
- Cases of ground failure such as liquefaction, significant cyclic softening of cohesive soils, or permanent ground displacements.

For these cases, the nonlinear modeling approach used to generate the results for this study would be more appropriate than applying the generalized transfer function or spectral ratio predictions models.

## 7.2 REINTERPRETATION OF EMPIRICAL CASE STUDIES

Empirical transfer functions computed from pile-supported structures instrumented at the foundation level and adjacent free-field recordings were reported by Kim and Stewart [2003], Mikami et al. [2006], and Givens et al. [2012]. These studies found that elastic kinematic pile–soil interaction transfer function models (e.g., Fan et al. [1991]) did not provide a good match to empirical observations, while in some cases, base–slab averaging models considering ground-motion incoherence provided a better match (e.g., see Kim and Stewart [2003]). Based on these findings, the researchers posed questions as to whether consideration of ground-motion incoherence in combination with an improved kinematic interaction model would provide a better match to the empirical observations.

As shown in §6.1, the trends exhibited by the empirical transfer functions are dominated by inertial interaction. Simulations using the substructure modeling approach that included a SFOFO to represent the structure provided a close match to the observed behavior near the first-mode period of the system. The improved kinematic transfer function model developed herein produced a predicted kinematic transfer function that was not significantly different from previous kinematic models, suggesting that the ability or lack thereof to accurately capture kinematic

interaction was not critical for interpreting these cases; it was more important to consider the combination of inertial and kinematic effects. The original researchers recognized that inertial effects are present in the recorded foundation-level motions; therefore, they focused their efforts on interpreting kinematic effects at frequencies away from the fundamental frequency of the structures. Combined kinematic-inertial analysis methods or closed-form analytical methods give the opportunity to study both effects simultaneously, which can be particularly useful when evaluating case studies.

Further issues related to the combined effects of inertial and kinematic interaction were explored in Chapter 5. These findings, along with the lessons learned from revisiting the case studies, highlight the fact that when superstructure inertia is present, the foundation motion (FM) differs from the FIM corresponding to a pile that does not support a structure. To compute a FM/FFM transfer function for comparison to empirical transfer functions requires performing a dynamic analysis of a structural model (e.g., a SDOF oscillator) subjected to the FIM, e.g., using the substructure method. This requires knowing enough information to form a reasonably accurate structural model beyond just knowing the structure's period.

### 7.3 FUTURE RESEARCH NEEDS

In addition to the transfer function and spectral ratio models presented herein, the analytical framework that is used to generate the results can be used to investigate further complexities. Likewise, future improvements to numerical modeling methods such as improved  $p$ - $y$  curves can be incorporated.

The work performed for this study made it apparent that the following factors are important research topics in the field of pile dynamics that need further exploration:

- $P$ - $y$ - $\theta$  springs that explicitly consider pile rotation (applies to conventional static loading as well).
- Better quantification of  $\delta$  through theoretical and rigorous numerical modeling approaches as well as experimental measurements.
- Better quantification of the  $p$ - $y$  curve's ultimate resistance for sand based on rigorous theory and validated with experiments and rigorous three-dimensional numerical studies.
- Group analyses considering spatially-variable (incoherent) ground motions over the footprint of a typical building. Whereas group effects were relatively minor for the pile group layout considered here, which represents a typical bridge bent substructure, the larger footprint of a building could result in a greater group-averaging effect and further kinematic reduction of free-field motions.
- The analyses performed here decoupled free-field ground response from pile-soil interaction for computational efficiency. In a real system, because soil nonlinear behavior due to these two effects occurs simultaneously, it is difficult to predict their combined effects *a priori* without a coupled simulation. A limited number of couple numerical analyses and/or experimental data

specifically targeted at studying the combined effects of nonlinearity due to ground response and kinematic pile–soil interaction would be helpful for validating the results of this study.

- Experimental measurements of kinematic pile–soil interaction; especially measurements of radiation damping.
- Thorough recommendations on the combination of inertial and kinematic soil–structure interaction effects, especially as affected by system nonlinearity.

## REFERENCES

- AASHTO (2009). *Guide Specifications for LRFD Seismic Bridge Design*, 2<sup>nd</sup> ed., American Association of State Highway Transportation Officials, Washington D.C.
- Abrahamson N.A., Youngs R.R. (1992). A stable algorithm for regression analyses using the random effects model, *Bull. Seismol. Soc. Am.*, 82: 505–510.
- API (1993). *Recommended Practice for Planning, Design, and Constructing Fixed Offshore Platforms*, API RP 2A-WSD, 20th ed., American Petroleum Institute, API Publishing Services, Washington D.C.
- Ancheta T.D. (2010). *Engineering Characterization of Spatially Variable Earthquake Ground Motions*, PhD thesis, Department of Civil and Environmental Engineering, University of California at Los Angeles.
- Ancheta, T.D., Darragh R.B., Stewart J.P., Seyhan E., Silva W.J., Chiou B.S.-J., Wooddell K.E., Graves R.W., Kottke A.R., Boore D.M., Kishida T., Donahue J.L. (2014). NGA-West2 database, *Earthq. Spectra*, 30(3): 989–1005.
- Ancheta T.D., Stewart J.P. (2015). Conditional simulation of spatially variable motions on 2D grid, *Proceedings, 12th International Conference on Applications of Statistics and Probability in Civil Engineering ICASP12*, Vancouver, Canada.
- Anoyatis G., Di Laora R., Mandolini A., Mylonakis, G. (2013). Kinematic response of single piles for different boundary conditions: analytical solutions and normalization schemes, *Soil Dyn. Earthq. Eng.*, 44: 183–195.
- ASCE (2013). *Minimum Design Loads for Buildings And Other Structures*, ASCE 7-10, Reston, VA.
- Ashford S.A., Juirnarongrit T. (2003). Evaluation of pile diameter effect on initial modulus of subgrade reaction, *J. Geotech. Geoenviron. Eng.*, 129(3): 234–242.
- Ashlock J.C., Pak R.Y.S (2009). Experimental response of piles in sand under compound motion, *J. Geotech. Geoenviron. Eng.*, 135(6): 799–808.
- Badoni D., Makris N. (1996). Nonlinear response of single piles under lateral inertial and seismic loads, *Soil Dyn. Earthq. Eng.*, 15: 29–43.
- Baker J.W., Lin T., Shahi S.K., Jayaram N. (2011). New ground motion selection procedures and selected motions for the PEER Transportation Research Program, *Report No. 2011/03*, Pacific Earthquake Engineering Research Center, University of California, Berkeley, CA.
- Banerjee S, Stanton J.F., Hawkins N.M. (1987). Seismic performance of precast prestressed concrete piles, *J. Struct. Eng.*, 113(2): 381–396.
- Bentley K.J., El Naggar M.H. (2000). Dynamic analysis for laterally loaded piles and dynamic p–y curves, *Can. Geotech. J.*, 37: 1166–1183.
- Berger E., Mahin S.A., Pyke R. (1977). Simplified method for evaluating soil-pile structure interaction effects, *Proceedings, 9th Offshore Technology Conference*, OTC Paper 2954, Houston, TX., pp. 589–598.
- Blaney G.W., Kausel E., Roesset J.M. (1976). Dynamic stiffness of piles, *Proceedings, Numerical Methods in Geomechanics*, C.S Desai, ed., 2:1001–1012.
- Blaney G.W., O'Neill M.W. (1986). Measured lateral response of mass on single pile in clay, *J. Geotech. Eng.*, 112(4): 443–457.
- Bolton M.D. (1986). The strength and dilatancy of sands, *Geotechnique*, 36(1): 65–78.
- Boore D.M., Atkinson G. (2008). Ground-motion prediction equations for the average horizontal component of PGA, PGV, and 5%-damped PSA at spectral periods between 0.01 s and 10.0 s, *Earthq. Spectra*, 24: 99–138.
- Boulanger R.W., Curras C.J., Kutter B.L., Wilson D.W., Abghari A. (1999). Seismic soil-pile structure interaction experiments and analyses, *J. Geotech. Geoenviron. Eng.*, 125(9): 750–759.
- Boulanger R.W., Kutter B.L., Brandenberg S.J., Singh P., Chang D. (2003). Pile foundations in liquefied and laterally spreading ground during earthquakes: Centrifuge experiments and analyses, *Report No. Univ. of California Davis*

- (UCD)/Center for Geotechnical Modeling (CGM)-03/01, Department of Civil Engineering, University of California, Davis, CA.
- Bowles J.E. (1997). *Foundation Analysis and Design*, 5<sup>th</sup> ed., McGraw-Hill, New York.
- Box G.E.P., Cox D.R. (1964). An analysis of transformations, *J. Royal Statistical Soc.*, Series B(26), pp. 211–252.
- Brown D., Turner J.P., Castelli R. (2010) Drilled shafts: construction procedures and LRFD design methods, *FHWA/NHI Publication 10-016*, Reference Manual and Participants Guide for National Highway Inst. Course 132014, 972 pgs.
- Burr J.P., Pender M.J., Larkin T.J. (1997). Dynamic response of laterally excited pile groups, *J. Geotech. Geoenviron. Eng.*, 123(1): 1–8.
- Caltrans (2015). *Personal communication*.
- Caltrans (2016). Construction plans for Linden Street Overcrossing (Replacement), California Department of Transportation, Plans approval date 12-7-15. Last accessed 9 March 2016. Available: [http://www.dot.ca.gov/hq/esc/oe/project\\_ads\\_addenda/05/05-4482U4/plans/](http://www.dot.ca.gov/hq/esc/oe/project_ads_addenda/05/05-4482U4/plans/).
- Carter D.P. (1984). A non-linear soil model for predicting lateral pile response, *Report No. 359*, Civil Engineering Department, University of Auckland, New Zealand.
- Chau K.T., Yang X (2005). Nonlinear interaction of soil-pile in horizontal vibration, *J. Eng. Mech.*, 131(8): 847–858.
- Choi J.I., Kim M.M., Brandenberg S.J. (2015). Cyclic *p-y* plasticity model applied to pile foundations in sand, *J. Geotech. Geoenviron. Eng.*, 141(5): 04015013.
- Chopra A.K. (2007). *Dynamics of Structures, Theory and Applications to Earthquake Engineering*, 3<sup>rd</sup> ed., Prentice Hall, Upper Saddle River, NJ.
- Dafalias Y.F. (1986). Bounding surface plasticity. I: Mathematical foundation and hypoplasticity, *J. Eng. Mech.*, 112(9): 966–987.
- Darendeli M. (2001). *Development of a New Family of Normalized Modulus Reduction and Material Damping Curves*, Ph.D. thesis, Department of Civil Engineering, University of Texas, Austin, TX.
- Di Laora R., Mandolini A., Mylonakis G. (2012). Insight on kinematic bending of flexible piles in 610 layered soil, *Soil Dyn. Earthq. Eng.*, 43: 309–322.
- Di Laora R., Rovithis E. (2014). Kinematic bending of fixed-head piles in nonhomogeneous soil, *J. Geotech. Geoenviron. Eng.*, 141(4): 04014126-1-10.
- Di Laora R., Sanctis L. (2013). Piles-induced filtering effect on the foundation input motion, *Soil Dyn. Earthq. Eng.*, 46: 52–63.
- Dobry R.M., O’Rourke M.J., Roesset J.M. (1982). Horizontal stiffness and damping of single piles, ASCE, *J. Geotech. Div.*, 108(GT3): 439–459.
- Duncan J.M., Chang C.-Y. (1970), Nonlinear analysis of stress and strain in soils, ASCE, *J. Soil Mech. Foundation Div.*, 96 (SM5): 1629–1653.
- Durante M.G., Di Sarno L., Mylonakis G., Taylor C.A., Simonelli A.L. (2015). Soil-pile-structure interaction: experimental outcomes from shaking table tests, *Earthquake Eng Struct. Dyn.*, 45(7): 1041–1061.
- El-Marsafawi H., Han Y.C., Novak M. (1992). Dynamic experiments on two pile groups, *J. Geotech. Eng.*, 118(4): 576–592.
- Fan K., Gazetas G., Kaynia A., Kausal E., (1991). Kinematic seismic response of single piles and pile groups, *J. Geotech. Eng.*, 117(12): 1860–1879.
- Flores-Berrones, R. (1974). *Response of Pile Foundations to Earthquake Loading*, Ph.D. thesis, National University of Mexico.
- Flores-Berrones R., Whitman R.V. (1982) Seismic response of end-bearing piles, *J. Geotech. Eng. Div.*, 108(4): 554–569.
- Gaul R.D. (1958). Model study of a dynamically laterally loaded pile, ASCE, *J. Soil Mech. Foundations Div.*, 84(SM-1): 1–32.

- Gazetas G. (1983). Analysis of machine foundation vibrations: state of the art, *Soil Dyn. Earthq. Eng.*, 2(1): 2–42.
- Gazetas G. (1984). Seismic response of end-bearing single piles, *Soil Dyn. Earthq. Eng.*, 3(2): 82–93.
- Gazetas G. (1991). Foundation vibrations, in *Foundation Engineering Handbook*, H.Y. Fang, ed., Van Nostrand Reinholds, pp. 553–593.
- Gazetas G., Dobry R. (1984a). Horizontal response of piles in layered soils, *J. Geotech. Eng.*, 110(1): 20–40.
- Gazetas G., Dobry R. (1984b). Simple radiation damping model for piles and footings, *J. Eng. Mech.*, 110(6): 937–956.
- Giannakou A., Gerolymos N., Gazetas G., Tazoh T., Anastasopoulos I. (2010). Seismic behavior of batter piles: elastic response, *J. Geotech. Geoenviron. Eng.*, 136(9): 1187–1189.
- Givens M.J., Atsushi M., Toshihide K., Stewart J.P. (2012). Kinematic soil-structure interaction effects from building and free-field seismic arrays in Japan, *Proceedings, 9<sup>th</sup> International Conference on Urban Earthquake Engineering/4<sup>th</sup> Asia Conference on Earthquake Engineering*, Center for Urban Earthquake Engineering, Tokyo Inst. Of Technology, Tokyo, Japan. 11 pgs.
- Han Y., Novak M. (1988). Dynamic behavior of single piles under strong harmonic excitation, *Can. Geotech. J.*, 25: 523–534.
- Hardin B.O., Drnevich V.P. (1972). Shear modulus and damping in soils: Measurements and parameter effects, ASCE, *J. Soil Mech., Foundation Div.*, 98(SM6): 603–624.
- Hashash Y.M.A., Musgrove M.I., Harmon J.A., Groholski D.R., Phillips C.A., Park D. (2015) *DEEPSOIL 6.1, User Manual*. Urbana, IL, Board of Trustees of University of Illinois at Urbana-Champaign. Urbana-Champaign, IL.
- Hetenyi M. (1946). *Beams on elastic foundation*. University of Michigan Press, Ann Arbor Michigan.
- Hussein M.N., Karray M., Tobita T. Iai S. (2014). Effects of non-linear soil-structure interaction on dynamic characteristics of structures supported on piles, *Proceedings, GeoRegina 2014*, 67<sup>th</sup> Canadian Geotechnical Conference, Saskatchewan, Canada.
- Jaky J. (1948). Pressure in silos, *Proceedings, 2<sup>nd</sup> International Conference on Soil Mechanics and Foundation Engineering*, Rotterdam, 1: 103–107.
- Kachadoorian R. (1968). Effects of the earthquake of March 27, 1964, on the Alaska highway system, *United States Geological Survey Professional Paper 545-C*, United States Department of the Interior, Washington, D.C., 74 pgs.
- Kagawa T., Kraft L.M. (1980). Seismic *p-y* response of flexible piles, *J. Soil Mech. Foundation Div.*, 98(SM6): 603–624.
- Kagawa T., Kraft L.M. (1981). Lateral pile response during earthquakes, ASCE, *J. Geotech. Eng. Div.*, 107(GT12): 1713–1731.
- Kampitsis A.E., Sapountzakis E.J., Giannakos S.K., Geolymos N.A. (2013). Seismic soil-pile-structure kinematic and inertial interaction—A new beam approach, *Soil Dyn. Earthq. Eng.*, 55: 211–224.
- Kausel E. (2010). Early history of soil-structure interaction, *Soil Dyn. Earthq. Eng.*, 30(9): 822–832.
- Kavvadas M., Gazetas G. (1993). Kinematic seismic response and bending of free-head piles in layered soil, *Géotechnique*, 43(2): 207–222.
- Kaynia A.M., Kausel E. (1982). Dynamic behavior of pile groups, *Proceedings, 2nd International Conference on Numerical Methods in Offshore Piling*, Austin, TX, pp. 1–25.
- Kaynia A.M., Kausel E. (1991). Dynamics of piles and pile groups in layered soil media, *Soil Dyn. Earthq. Eng.*, 10(8): 386–401.
- Kaynia A.M., Mahzooni S. (1996). Forces in pile foundations under seismic loading, *J. Eng. Mech.*, 122(1): 46–53.
- Kaynia A.M., Novak M. (1992). Response of pile foundations to Rayleigh waves and to obliquely incident body waves, *Earthq. Eng. Struct. Dyn.*, 21(4): 303–318.

- Khalili-Tehrani P., Ahlberg E., Rha C., Lemnitzer A., Stewart J.P., Taciroglu E., Wallace J. (2014). Nonlinear load-deflection behavior of reinforced concrete drilled piles in stiff clay, *J. Geotech. Geoenviron. Eng.*, 140(3): 04013022.
- Kim S. (2001). *Calibration of Simple Models for Seismic Soil-Structure Interaction from Field Performance Data*, Ph.D. dissertation, Department of Civil and Environmental Engineering, University of California Los Angeles, 252 pgs.
- Kim S., Stewart J.P. (2003) Kinematic soil-structure interaction from strong motion recordings, *J. Geotech. Geoenviron. Eng.*, 129(4): 323–335.
- Klar A., Frydman S. (2002). Three-dimensional analysis of lateral pile response using two-dimensional explicit numerical scheme, *J. Geotech. Geoenviron. Eng.*, 128(9): 775–784.
- Kolozvari K., Orakcal K., Wallace J.W. (2015a). Modeling of cyclic shear-flexure interaction in reinforced concrete structural walls. I: Theory, ASCE, *J. Struct. Eng.*, 141(5): 04014135.
- Kolozvari K., Tran T., Orakcal K., Wallace J.W. (2015b). Modeling of cyclic shear-flexure interaction in reinforced concrete structural walls. II: Experimental validation, ASCE, *J. Struct. Eng.*, 141(5): 04014136.
- Kuhlemeyer R.L. (1979). Static and dynamic laterally loaded floating piles, ASCE, *J. Geotech. Eng. Div.*, 105(2): 289–304.
- Kutner M.H., Nachtsheim C.J., Neter J. (2004). *Applied Linear Statistical Models*, 5<sup>th</sup> ed., McGraw-Hill/Irwin, 1396 pgs.
- Lam I.P.O. (2009). Diameter effects on p-y curves, *Proceedings, Deep Marine Foundations—A Perspective on the Design and Construction of Deep Marine Foundations*, Deep Foundations Institute, Hawthorne, NJ, 15 pgs.
- Lewis, M.D. (1990). A laboratory study of the effect of stress state on the elastic moduli of sand, Ph.D. thesis, Air Force Institute of Technology, Wright-Patterson AFC, OH, 437 pgs.
- Lysmer J., Kuhlemeyer R.L. (1969). Finite dynamic model for infinite media, ASCE, *J. Eng. Mech. Div.*, 95(EM4): 859–877.
- Maheshwari B.K., Truman K.Z., El Naggar M.H., Gould P.L. (2004). Three-dimensional nonlinear analysis for seismic soil-pile-structure interaction, *Soil Dyn. Earthq. Eng.*, 24: 343–356.
- Maiorano R.M.S., de Sanctis L., Aversa S., Mandolini A. (2009). Kinematic response analysis of pile foundations under seismic loading, *Can. Geotech. J.*, 46: 571–584.
- Makris N. (1994). Soil-pile interaction during the passage of Rayleigh waves: An analytical solution. *Earthq. Eng. Struct. Dyn.*, 23: 153–167.
- Makris N., Gazetas G. (1992). Dynamic pile-soil-pile interaction. Part II: lateral and seismic response, *Earthq. Eng. Struct. Dyn.*, 21: 145–162.
- Makris N., Gazetas G., Delis E. (1996). Dynamic soil-pile-foundation-structure interaction: Records and predictions, *Géotechnique*, 46(1): 33–50.
- Mamoon S.M., Banerjee P.K. (1992). Time-domain analysis of dynamically loaded single piles, *J. Eng. Mech.*, 118(1): 140–160.
- Manna B., Baidya D.K. (2010). Nonlinear dynamic response of piles under horizontal excitation. *J. Geotech. Geoenviron. Eng.*, 136(12): 1600–1609.
- Marshall P.W., Gates W.E., Anagnostopoulos S. (1977). Inelastic dynamic analysis of tubular offshore structures. *Proceedings, 1977 Offshore Technology Conference*, Paper No. OTC 2908, Houston, TX.
- Massone L.M., Lemnitzer A. (2012). The influence of RC nonlinearity on p-y curves for CIDH bridge piers, *DFI Journal: J. Deep Foundations Inst.*, 6(1): 33–40.
- Massone L.M., Wallace J.W. (2004). Load–deformation responses of slender reinforced concrete walls. *ACI Struct. J.*, 101(1): 103–113.
- Matasovic N. (1993). *Seismic Response of Composite Horizontally-Layered Soil Deposits*, Ph.D. Thesis, University of California, Los Angeles. CA.

- Matlock H. (1970). Correlations for design of laterally loaded piles in soft clay, *Proceedings, 2<sup>nd</sup> Annual Offshore Technology Conference*, Houston, TX, pp. 577–594.
- Matlock H., Foo S.H.C., Bryant L.M. (1978). Simulation of lateral pile behavior under earthquake motion, ASCE, *Proceedings, Geotechnical Engineering Division Specialty Conference on Earthquake Engineering and Soil Dynamics, Vol. II*, Pasadena, CA, pp. 600–619.
- Mayne P.W., Coop M.R., Springman S.M., Huang A.B., Zornberg J.G. (2009). Geomaterial behavior and testing, *Proceedings, 17<sup>th</sup> Int. Conf. on Soil Mechanics and Geotechnical Engineering*, M. Hamza et al., eds., pp. 2777–2872.
- McClelland B., Focht J.A. (1958). Soil modulus for laterally loaded piles, ASCE, *Trans.*, Paper No. 2954, 1049–1086.
- McKenna F.T. (1997). *Object-Oriented Finite Element Programming: Frameworks for Analysis, Algorithms and Parallel Computing*, Ph.D. thesis, Department of Civil Engineering, University of California, Berkeley, CA.
- McKenna F.T., Scott M.H., Fenves G.L. (2010). Nonlinear finite-element analysis software architecture using object composition, ASCE, *J. Computing Civil Eng.*, 24(1): 95–107.
- McManus K.J., Alabaster D. (2004). Constant force shaking of a group of four drilled shafts, *J. Geotech. Geoenviron. Eng.*, 130(20): 123–128.
- Menq F.Y. (2003). *Dynamic Properties of Sandy and Gravelly Soils*, Ph.D. Dissertation, Department of Civil Engineering University of Texas, Austin, TX.
- Mikami A. (2015). *Personal communication*.
- Mikami A., Stewart J.P., Kamiyama M. (2008). Effects of time series analysis protocols on transfer functions calculated from earthquake accelerograms, *Soil Dyn. Earthq. Eng.*, 28: 695–706.
- Mikami A., Stewart J.P., Ostadan F., Crouse C.B. (2006). Representation of ground motion incoherence for the analysis of kinematic soil-structure interaction, *Proceedings, 8<sup>th</sup> U.S. National Conference on Earthquake Engineering*, Paper No. 1071, Earthquake Engineering Research Institute, Oakland, CA.
- Mizuno H. (1987). Pile damage during earthquake in Japan (1923-1983), *Proceedings, Dynamic Response of Pile Foundations—Experiment, Analysis and Observation*, ASCE Geotechnical Special Publication No. 11, pp. 53–78.
- Mylonakis G. (2001). Simplified model for seismic pile bending at soil layer interfaces, *Soils and Foundations*, 41(4): 47–58.
- Mylonakis, G., Gazetas, G. (1999). Lateral vibration and internal forces of grouped piles in layered soil. *J. Geotech. Geoenviron. Eng.*, 125(1), 16–25.
- Mylonakis G., Gazetas, G. (2002). Kinematic pile response to vertical p-wave seismic excitation. *J. Geotech. Geoenviron. Eng.*, 128(10), 860–867.
- Newmark N.M. (1967). Problems in wave propagation in soil and rocks, *Proceedings, International Symposium on Wave Propagation and Dynamic Properties of Earth Materials*, University of New Mexico Press, Albuquerque, pp 7–26.
- Nikolaou S., Mylonakis G., Gazetas G., Tazoh T. (2001). Kinematic pile bending during earthquakes: analysis and field measurements, *Géotechnique*, 51(5): 425–440.
- Nishizawa T., Tajiri S., Kawamura S. (1984). Excavation and response analysis of damaged RC piles by liquefaction, *Proceedings, Eighth World Conference on Earthquake Engineering*, Vol. III, San Francisco, CA.
- NIST (2012). Soil-structure interaction for building structures, *Report No. NIST GCR 12-917-21*, National Institute of Standards and Technology, U.S. Department of Commerce, Washington D.C. Project Technical Committee: Stewart, JP (Chair), CB Crouse, T Hutchinson, B Lizundia, F Naeim, and F Ostadan. 292 pgs.
- Nogami T., Konagai K. (1988). Time domain flexural response of dynamically loaded single piles, *J. Eng. Mech.*, 114(9): 1512–1525.
- Nogami T., Otani J., Konagai K., Chen H.L. (1992). Nonlinear soil-pile interaction model for dynamic lateral motion, *J. Geotech. Eng.*, 118(1): 89–106.

- Novak M. (1974). Dynamic stiffness and damping of piles, *Can. Geotech. J.*, 11: 574–598.
- Novak M., El Sharnouby B. (1984). Evaluation of dynamic experiments on pile group, *J. Geotech. Eng.*, 110(6): 738–756.
- Novak M., Grigg R.F. (1976). Dynamic experiments with small pile foundations, *Can. Geotech. J.*, 13: 372–385.
- Novak M., Nogami T., Aboul-Ella F. (1978). Dynamic soil reactions for plane strain case, ASCE, *J. Eng. Mech. Div.*, 104(EM4): 953–959.
- Novak M., Sheta, M., El-Sharnouby B., El-Hignawy L. (1983). *DYNA2, A Computer Program for Calculation of Response of Rigid Foundation to Dynamic Loads*, Systems Analysis Control and Design Activity, Faculty of Engineering Science, University of Western Ontario, London, Ont.
- O’Neill M.W., Murchison J.M. (1983). An evaluation of p-y relationships in sand, *American Petroleum Institute Report PRAC 82-41-1*, University of Houston, Department of Civil Engineering Research Report No. GT-DF02-83.
- Ostadan F. (2005). Soil-structure interaction analysis including ground motion incoherency effects, *Proceedings, 18th International Conference on Structural Mechanics in Reactor Technology (SMiRT 18)*, Beijing, China.
- OYO Corporation (2007). *PS logging at Tokoku Institute of Technology Campus in 2007*, Unpublished report, September 2007 (in Japanese<sup>8</sup>).
- Pak R.Y.S., Jennings P.C. (1987). Elastodynamic response of pile under transverse excitations, *J. Eng. Mech.*, 113(7): 1101–1116.
- Pandit S.M. (1991). *Modal and Spectrum Analysis*. Wiley, New York.
- Pecker A. (2014). Kinematic soil structure interaction for bridge piled foundations, *Inter. J. Bridge Eng.*, 2(3): 15-28.
- Pender M.J. (2004). Discussion of “Evaluation of pile diameter effect on initial modulus of subgrade reaction” by Scott A. Ashford and Terrawut Juirnarongrit, *J. Geotech. Geoenviron. Eng.*, 130(9): 981–982.
- Penzien J. (1970). Soil-pile foundation interaction. In *Earthquake Engineering*, R.L. Wiegell, ed.), Ch. 14. New York: Prentice Hall.
- Penzien J., Scheffey C., Parmelee R. (1964). Seismic analysis of bridges on long piles, ASCE, *J. Eng. Mech. Div.*, 90(EM3): 223–254.
- Prevost J.H., Romano J.D., Abdel-Ghaffar A.M., Rowland R. (1981). Dynamic response of laterally-loaded piles in centrifuge, *Proceedings, Second Specialty Conference on Dynamic Response of Structures: Experimentation, Observation, Prediction and Control*, ASCE, G. Hart ed., Atlanta, pp. 386–400.
- Randolph M.F. (1981). The response of flexible piles for lateral loading, *Geotechnique*, 31(2): 247–259.
- Rathje E.M., Faraj F, Russell S, Bray J.B. (2004). Empirical relationships for frequency content parameters of earthquake ground motions, *Earthq. Spectra*, 20(1): 119–144.
- R Core Team (2015). *R: A language and Environment for Statistical Computing*, R Foundation for Statistical Computing, Vienna, Austria. Available: <https://www.R-project.org/>.
- Reese L.C., Cox W.R., Koop F.D. (1974). Analysis of laterally loaded piles in sand, *Proceedings, 6<sup>th</sup> Annual Offshore Technology Conference*, Vol. 2, Paper No. OTC 2080, Houston, TX.
- Reese L.C., Cox W.R., Koop F.D. (1975). Field testing and analysis of laterally loaded piles in stiff clay. *Proceedings, 7<sup>th</sup> Offshore Technology Conf.*, Paper No. OTC 2321, Houston, Texas, pp. 671–690.
- Reese L.C., Isenhower W.M., Wang S.T. (2006). *Analysis and Design of Shallow and Deep Foundations*, John Wiley & Sons, Hoboken, NJ, 626 pgs.
- Reese L.C., Sullivan W.R. (1980). *Documentation of computer program COM624: Parts I and II, analysis of stresses and deflections for laterally-loaded piles including generation of p-y curves*. Geotechnical Engineering Software GS80-1, Geotechnical Engineering Center, Bureau of Engineering Research, University of Texas at Austin, TX.

---

<sup>8</sup> Data reported in Givens et al. [2012].

- Reese L.C., Wang S.T., Isenhower W.M., Arrelaga J.A., Hendrix J.A. (2005). *LPILE plus version 5.0*. Ensoft, Inc., Austin, TX.
- Reese L.C., Welch R.C. (1975). Lateral loading of deep foundation in stiff clay, ASCE, *J. Geotech. Eng. Div.*, 101(7): 633–649.
- Ridders C. (1979). A new algorithm for computing a single root of a real continuous function, *IEEE Trans. Circuits Systems*, 26: 979–980.
- Robertson P.K. (2012). Interpretation of in-situ tests—some insights, *Proceedings, 4<sup>th</sup> International Conference on Geotechnical and Geophysical Site Characterization (ISC-4)*, Pernambuco, Brazil, R.Q. Coutinho and P.W. Mayne, eds. 22 pgs.
- Rocscience (2013). *Phase 2, Version 8.016*, Rocscience Inc., Toronto, Canada.
- Roesset J.M. (1980a). Stiffness and damping coefficients of foundations, ASCE, *Special Technical Publication on Dynamic Response of Pile Foundations: Analytical Aspects*, O'Neill and Dobry, eds.
- Roesset J.M. (1994). Foreword in *Foundation Vibration Analysis Using Simple Physical Models* by J.P. Wolf, Prentice Hall, Upper Saddle River, NJ.
- Roesset J.M., Whitman R.V., Dobry R. (1973). Modal analysis for structures with foundation interaction, ASCE, *J. Struct. Div.*, 99(3): 399–416.
- Rovithis E.N., Pitilakis K.D., Mylonakis G.E. (2009). Seismic analysis of couple soil-pile-structure systems leading to the definition of a pseudo-natural SSI frequency, *Soil Dyn. Earthq. Eng.*, 29: 1005–1015.
- Saitoh M. (2005). Fixed-head pile bending by kinematic interaction and criteria for its minimization at optimal pile radius. *J. Geotech. Geoenviron. Eng.*, 131(10): 1243–1251.
- Scott M., Fenves G. (2010). Krylov subspace accelerated Newton algorithm: Application to dynamic progressive collapse simulation of frames, ASCE, *J. Struct. Eng.*, 136(5): 473–480.
- Sen R, Davies T.G., Banerjee P.K. (1985). Dynamic analysis of piles and pile groups embedded in homogeneous soils, *Earthq. Eng. Struct. Dyn.*, 13(1): 53–65.
- Sica S., Mylonakis G., Simonelli A.L. (2013). Strain effects on kinematic pile bending in layered soil, *Soil Dyn. Earthq. Eng.*, 49: 231–242.
- Simo J.C., Hughes T.J.R. (1998). *Computational Inelasticity*, Springer, New York.
- Skempton A.W. (1951). The bearing capacity of clays, *Proceedings of the Building Research Congress*, Division 1, Part 3, London, pp. 180–189.
- Stewart J.P. (1996). *An Empirical Evaluation of Soil-Structure Interaction Effects on the Seismic Response of Structures*, Ph.D. Dissertation, Department of Civil Engineering, University of California, Berkeley, CA.
- Stewart J.P., Fenves G.L., Seed R.B. (1999). Seismic soil-structure interaction in buildings. I: Analytical methods, *J. Geotech. Geoenviron. Eng.*, 125(1): 26–37.
- Stewart J.P., Fenves G.L., Seed R.B. (2000). Closure to discussion by MD Trifunac on seismic soil-structure interaction in buildings, I: Analytical methods, and II: Empirical findings, *J. Geotech. Geoenviron. Eng.*, 126(7): 671–672.
- Stewart J.P., Seed R.B., Fenves G.L. (1999). Seismic soil-structure interaction in buildings. II: Empirical findings, *J. Geotech. Geoenviron. Eng.*, 125(1): 38–48.
- Stewart J.P., Stewart A.F. (1997). Analysis of soil-structure interaction effects on building response from earthquake strong motion recordings at 58 sites, *Report. No. UCB/EERC 97/01*, Earthquake Engineering Research Center, University of California, Berkeley, Calif., 742 pgs.
- Syngros C. (2004). *Seismic Response of Piles and Pile-Supported Bridge Piers Evaluated Through Case Histories*, Ph.D. thesis, Civil Engineering Dept., City University of New York, NY.
- Tajimi H. (1969). Dynamic analysis of structure embedded in elastic stratum, *Proceedings, 4th World Conference on Earthquake Engineering*, Santiago, Chile, Vol. III, pp. A-6 53-69.

- Tazoh T., Shimizu K., Wakahara T. (1987). Seismic observations and analysis of grouped piles, *Proceedings, Dynamic Response of Pile Foundations—Experiment, Analysis and Observation*, ASCE Geotechnical Special Publication No. 11, pp. 1–21.
- Terzaghi K., Peck R.B. (1948). *Soil Mechanics in Engineering Practice*, John Wiley & Sons, Inc., New York, N.Y.
- Timoshenko S. (1948). *Strength of Materials, Part II, Advanced Theory and Problems*, 2<sup>nd</sup> ed.. Van Nostrand, New York.
- Tokimatsu K., Suzuki H., Sato M. (2005). Effects of inertial and kinematic interaction on seismic behavior of pile with embedded foundation. *Soil Dyn. Earthq. Eng.*, 25: 753–762.
- Trochanis A.M., Bielak J., Christiano P. (1991). Three-dimensional nonlinear study of piles, *J. Geotech. Eng.*, 117(3): 429–447.
- Turner B.J., Brandenberg S.J., Stewart J.P. (2016). Case study of parallel bridges affected by liquefaction and lateral spreading, *J. Geotech. Geoenviron. Eng.*, 142(7): 05016001-1-12.
- Vaziri H., Han Y. (1992). Dynamic response of pile groups under lateral loading, *Soil Dyn. Earthq. Eng.*, 11: 87–99.
- Veletsos A.S., Prasad A.M. (1988). Seismic interaction of structures and soils: Stochastic approach. *Technical Report NCEER-88-021*, State University of New York, Buffalo, N.Y.
- Veletsos A.S., Prasad A.M., Wu W.H. (1997). Transfer functions for rigid rectangular foundations, *Earthq. Eng. Struct. Dyn.*, 26(1): 87–102.
- Vesic A.S. (1961). Bending of beams resting on isotropic elastic solids, ASCE, *J. Eng. Mech. Div.*, 87(2): 35–53.
- Vesic A.S. (1977). *Design of Pile Foundations*. National Cooperative Highway Research Program Synthesis of Highway Practice NCHRP 42, Transportation Research Board, Washington, D.C.
- Vucetic M., Dobry R. (1991). Effect of soil plasticity on cyclic response, *J. Geotech. Eng.*, 117(1): 89–107.
- Wang S, Kutter B.L., Wilson D.W., Boulanger R.W., Abbas, A. (1998). Nonlinear seismic soil-pile structure interaction, *Earthq. Spectra*, 14(2): 377–396.
- White L.B., Boashash B. (1990). Cross spectral analysis of nonstationary processes, *IEEE Trans. Info. Theory*, 36(4): 830–835.
- Winkler E. (1867). *Die Lehre von der Elastizitat und Festigkeit*. Dominicus, Prague (in German).
- Wolf J.P. (1985). *Dynamic Soil-Structure Interaction*. Prentice-Hall, Inc., Englewood Cliffs, N.J.
- Wu G., Finn L. (1997a). Dynamic elastic analysis of pile foundations using finite element method in the frequency domain, *Can. Geotech. J.*, 34: 34–43.
- Wu G., Finn L. (1997b). Dynamic nonlinear analysis of pile foundations using finite element method in the time domain, *Can. Geotech. J.*, 34, 44–52.
- Yee E., Stewart J.P., Tokimatsu, K. (2013). Elastic and large-strain nonlinear seismic site response from analysis of vertical array recordings, *J. Geotech. Geoenviron. Eng.*, 139(10): 1789–1801.

# APPENDIX A SITE PROFILES FOR KINEMATIC PILE–SOIL INTERACTION ANALYSIS

## A.1 INTRODUCTION

Stratigraphy and soil properties for the six sites used for baseline pile kinematic soil–structure interaction analyses are presented below. Each of the six sites is based on CPT data, including seismic shear-wave velocity measurements obtained from the United States Geological Survey’s (USGS) CPT database website<sup>9</sup>. Note that several of the  $V_{S30}$  values presented on the USGS website are incorrect based on the data provided; the correct values are given in the site descriptions below. Soil properties presented in Appendix A were interpreted from CPT data in a manner consistent with routine practice following the methods of Mayne et al. [2009] and Robertson [2012] unless otherwise noted.

The stratigraphy has been slightly modified from conditions encountered during CPT as explained below in order to avoid significant impedance contrasts that would result in a strong site response effect. Analyses were also performed with these impedance contrasts left in the profiles to evaluate their influence on the pile kinematic response. Below the maximum depth of the CPT explorations, the profiles were extended such that they exceeded the maximum pile depth considered for the analyses ( $L = 60$  m) and reached a shear-wave velocity of 760 m/sec to be consistent with the input motions. The soil properties of these additional layers were computed based on stiffness versus depth scaling relationships as described in the main text.

The following sections briefly summarize the geologic setting and stratigraphy of each site.

## A.2 SITE 1

Site 1 is based on USGS CPT-ALC014, located on Alameda Island near the Alameda entrance to the Posey Tube tunnel that connects Alameda to Oakland, California. The original profile has been modified by removing the stiff layer at a depth of 22–23 m so that there is a relatively smooth increase in stiffness with depth. Layer properties of the idealized soil profile are presented the table below. Groundwater was estimated at a depth of 1.2 m below the surface during the CPT but is

---

<sup>9</sup> <http://earthquake.usgs.gov/research/cpt/>

considered to be at the ground surface for the idealized profile used for analyses. The  $V_{S30}$  of the idealized profile presented below is 111 m/sec. The  $V_{S30}$  computed using the actual data is 123 m/sec.

**Table A.1 Site 1 properties for DEEPSOIL analysis.**

Layer	Material type	Depth top	Thickness	Unit weight	V <sub>s</sub>	φ	OCR	K <sub>0</sub>	Shear strength	PI
-	-	m	m	kN/m <sup>3</sup>	m/sec	degrees	-	-	kPa	-
1	clay	0	2	16.5	90	N/A	1.5	0.54	12	15
2	clay	2	2	16.5	90	N/A	1.4	0.53	12	15
3	clay	4	2	16.5	95	N/A	1.3	0.52	15	15
4	clay	6	2	16.5	95	N/A	1.2	0.50	18	15
5	clay	8	2	16.5	100	N/A	1.1	0.49	20	15
6	clay	10	2	16.5	100	N/A	1.0	0.47	22	15
7	clay	12	2	16.5	105	N/A	1.0	0.47	25	15
8	clay	14	2	17	110	N/A	1.0	0.47	28	15
9	clay	16	2	17	115	N/A	1.0	0.47	32	15
10	clay	18	2	17	120	N/A	1.0	0.47	35	15
11	clay	20	2	17	125	N/A	1.0	0.47	39	15
12	clay	22	2	17.5	130	N/A	1.0	0.47	42	15
13	clay	24	2	17.5	140	N/A	1.0	0.47	46	15
14	clay	26	2	17.5	145	N/A	1.0	0.47	50	15
15	clay	28	2	17.5	160	N/A	1.0	0.47	53	15
16	clay	30	2	18	200	N/A	1.0	0.47	57	15
17	sand	32	2	19	220	38	1.0	0.38	201	0
18	sand	34	2	19	224	38	1.0	0.38	215	0
19	sand	36	2	19	228	38	1.0	0.38	230	0
20	sand	38	2	19	231	38	1.0	0.38	244	0
21	sand	40	2	19	234	38	1.0	0.38	258	0
22	sand	42	2	19	237	38	1.0	0.38	273	0
23	sand	44	2	19	241	38	1.0	0.38	287	0
24	sand	46	2	19	244	38	1.0	0.38	302	0
25	sand	48	2	19	246	38	1.0	0.38	316	0
26	sand	50	2	19	249	38	1.0	0.38	330	0
27	sand	52	2	19	252	38	1.0	0.38	345	0
28	sand	54	2	19	254	38	1.0	0.38	359	0
29	sand	56	2	19	257	38	1.0	0.38	373	0
30	sand	58	2	19	259	38	1.0	0.38	388	0
31	sand	60	2	19	262	38	1.0	0.38	402	0
32	sand	62	2	19	264	38	1.0	0.38	416	0
33	sand	64	2	19	266	38	1.0	0.38	431	0
34	sand	66	1	19	300	38	1.0	0.38	434	0
35	sand	67	1	19	350	38	1.0	0.38	441	0
36	sand	68	1	19	400	38	1.0	0.38	448	0
37	sand	69	1	19	450	38	1.0	0.38	456	0
38	sand	70	1	19	500	38	1.0	0.38	463	0
39	sand	71	1	19	550	38	1.0	0.38	470	0
40	sand	72	1	19	600	38	1.0	0.38	477	0
41	sand	73	1	19	650	38	1.0	0.38	484	0
42	sand	74	1	19	700	38	1.0	0.38	492	0
43	sand	75	1	19	760	38	1.0	0.38	499	0

### **A.3 SITE 2**

Site 2 is based on USGS CPT-SCC069, which is located on the southern margin of the San Francisco Bay near San Jose, California. The surficial materials are classified as fine-grained Holocene alluvial fan and overbank flood deposits. Deeper layers may be marine sediments. Groundwater is at a depth of 2 m. The  $V_{S30}$  of the idealized profile presented below is 192 m/sec. The  $V_{S30}$  computed using the actual data is 172 m/sec. The difference is a result of modifications made to the upper 14 m of the idealized profile to remove stiff layers overlying soft layers. The “stiff over soft” condition is considered in Site “2a” as described in the main text, which is closer to the conditions measured in the field.

**Table A.2 Site 2 properties for DEEPSOIL analysis.**

Layer	Material type	Depth top	Thickness	Unit weight	V <sub>s</sub>	Friction Angle	OCR	K <sub>0</sub>	Shear Atrength	PI
-	-	m	m	kN/m <sup>3</sup>	m/sec	degrees	-	-	kPa	-
1	clay	0	2	17	120	N/A	7.4	0.73	37	15
2	clay	2	1.5	17	130	N/A	5.3	0.60	44	15
3	clay	3.5	5.5	17	145	N/A	3.1	0.44	61	30
4	clay	9	3.5	17	165	N/A	3.4	0.45	73	15
5	clay	12.5	1.5	17	190	N/A	4.0	0.49	86	15
6	clay	14	2	18	206	N/A	3.9	0.48	96	15
7	clay	16	1.5	18	222	N/A	3.6	0.46	96	10
8	sand	17.5	1.5	18	251	37	3.4	0.40	127	0
9	clay	19	2.5	18	273	N/A	2.8	0.40	96	20
10	clay	21.5	2.5	18	276	N/A	2.6	0.38	101	15
11	clay	24	2	18	285	N/A	2.7	0.39	110	15
12	clay	26	2	18	302	N/A	3.4	0.43	143	15
13	clay	28	2	18	306	N/A	4.4	0.48	188	15
14	clay	30	2	18	315	N/A	4.3	0.47	197	15
15	clay	32	2	18	318	N/A	4.1	0.46	201	15
16	clay	34	2	18	321	N/A	4.0	0.45	205	15
17	clay	36	2	18	324	N/A	3.8	0.44	210	15
18	clay	38	2	18	328	N/A	3.7	0.43	214	15
19	clay	40	2	18	331	N/A	3.6	0.42	218	15
20	clay	42	2	18	334	N/A	3.4	0.42	223	15
21	clay	44	2	18	337	N/A	3.3	0.41	227	15
22	clay	46	2	18	340	N/A	3.3	0.40	231	15
23	clay	48	2	18	343	N/A	3.2	0.40	235	15
24	clay	50	2	18	346	N/A	3.1	0.39	239	15
25	clay	52	2	18	349	N/A	3.0	0.38	243	15
26	clay	54	2	19	343	N/A	2.9	0.38	248	15
27	clay	56	2	19	346	N/A	2.9	0.37	252	15
28	clay	58	2	19	349	N/A	2.8	0.37	257	15
29	clay	60	2	19	352	N/A	2.7	0.36	261	15
30	clay	62	2	19	355	N/A	2.7	0.36	266	15
31	sand	64	2	19	400	38	2.6	0.38	444	0
32	sand	66	2	19	450	38	2.6	0.38	458	0
33	sand	68	2	19	500	38	2.5	0.38	472	0
34	sand	70	2	19	550	38	2.5	0.38	487	0
35	sand	72	2	19	600	38	2.4	0.38	501	0
36	sand	74	2	19	650	38	2.4	0.38	516	0
37	sand	76	2	19	700	38	2.4	0.38	530	0
38	sand	78	2	19	760	38	2.3	0.38	544	0

### **A.3 SITE 3**

Site 3 is based off USGS CPT-MSC019, performed in point bar deposits in the Mississippi River Valley. Groundwater is at a depth of 4 m. The  $V_{S30}$  of the idealized profile presented below is 208 m/sec. The  $V_{S30}$  computed using the actual data is 217 m/sec.

**Table A.3 Site 3 properties for DEEPSOIL analysis.**

Layer	Material type	Depth top	Thickness	Unit weight	V <sub>s</sub>	Friction angle	OCR	K <sub>0</sub>	Shear strength	PI
-	-	m	m	kN/m <sup>3</sup>	m/sec	degrees	-	-	kPa	-
1	sand	0	3	17	150	34	N/A	0.44	34	0
2	sand	3	3	17	160	34	N/A	0.44	65	0
3	sand	6	2	17	170	34	N/A	0.44	72	0
4	sand	8	3	17	185	36	N/A	0.41	98	0
5	sand	11	2	17	205	40	N/A	0.36	118	0
6	sand	13	1	17	220	39	N/A	0.37	118	0
7	sand	14	2	18	235	40	N/A	0.35	141	0
8	sand	16	2	18	225	42	N/A	0.33	164	0
9	sand	18	2	18	233	42	N/A	0.32	182	0
10	sand	20	2	18	240	42	N/A	0.32	197	0
11	sand	22	2	18	280	42	N/A	0.33	209	0
12	sand	24	2	18	265	42	N/A	0.33	222	0
13	sand	26	2	18	285	42	N/A	0.34	235	0
14	sand	28	2	18	290	42	N/A	0.33	251	0
15	sand	30	2	19	295	42	N/A	0.33	269	0
16	sand	32	2	19	299	42	N/A	0.33	286	0
17	sand	34	2	19	303	42	N/A	0.33	302	0
18	sand	36	2	19	307	42	N/A	0.33	319	0
19	sand	38	2	19	311	42	N/A	0.33	336	0
20	sand	40	2	19	315	42	N/A	0.33	352	0
21	sand	42	2	19	319	42	N/A	0.33	369	0
22	sand	44	2	19	322	42	N/A	0.33	385	0
23	sand	46	2	19	326	42	N/A	0.33	402	0
24	sand	48	2	19	329	42	N/A	0.33	418	0
25	sand	50	2	19	332	42	N/A	0.33	435	0
26	sand	52	2	19	335	42	N/A	0.33	451	0
27	sand	54	2	19	338	42	N/A	0.33	468	0
28	sand	56	2	19	341	42	N/A	0.33	484	0
29	sand	58	2	19	344	42	N/A	0.33	501	0
30	sand	60	2	19	347	42	N/A	0.33	518	0
31	sand	62	2	19	350	42	N/A	0.33	534	0
32	sand	64	2	19	352	42	N/A	0.33	551	0
33	sand	66	2	19	400	42	N/A	0.33	567	0
34	sand	68	2	19	450	42	N/A	0.33	584	0
35	sand	70	2	19	500	42	N/A	0.33	600	0
36	sand	72	2	19	550	42	N/A	0.33	617	0
37	sand	74	2	19	600	42	N/A	0.33	633	0
38	sand	76	2	19	650	42	N/A	0.33	650	0
39	sand	78	2	19	700	42	N/A	0.33	667	0
40	sand	80	2	19	760	42	N/A	0.33	683	0

#### **A.4 SITE 4**

Site 4 is based off USGS CPT-CHN007, performed in Pleistocene barrier-beach ridge deposits near Charleston, South Carolina. Groundwater is estimated to be at a depth of 2.5 m. The  $V_{S30}$  of the idealized profile presented below is 253 m/sec. The  $V_{S30}$  computed using the actual data is 261 m/sec.

**Table A.5 Site 4 properties for DEEPSOIL analysis.**

Layer	Material type	Depth Top	Thickness	Unit weight	V <sub>s</sub>	Friction Angle	OCR	K <sub>0</sub>	Shear Strength	PI
-	-	m	m	kN/m <sup>3</sup>	m/sec	degrees	-	-	kPa	-
1	sand	0	2	17	170	35	1.0	0.43	24	0
2	sand	2	3	18	200	35	1.0	0.43	55	0
3	clay	5	1.5	17	170	N/A	3.1	0.45	44	15
4	sand	6.5	3.5	18	210	32	1.0	0.47	75	0
5	clay	10	1	18	215	N/A	3.4	0.46	68	15
6	sand	11	3	18	255	35	1.0	0.43	105	0
7	clay	14	1	18	210	N/A	2.7	0.40	73	15
8	sand	15	5	18	260	35	1.0	0.43	146	0
9	sand	20	2	18	335	32	1.0	0.47	131	0
10	sand	22	2	19	365	32	1.0	0.47	142	0
11	sand	24	2	19	380	33	1.0	0.46	158	0
12	sand	26	2	19	420	33	1.0	0.46	172	0
13	sand	28	2	19	440	34	1.0	0.44	190	0
14	sand	30	2	19	447	36	1.0	0.41	220	0
15	sand	32	2	19	453	36	1.0	0.41	233	0
16	sand	34	2	19	460	36	1.0	0.41	247	0
17	sand	36	2	19	466	36	1.0	0.41	260	0
18	sand	38	2	19	472	36	1.0	0.41	273	0
19	sand	40	2	19	477	36	1.0	0.41	287	0
20	sand	42	2	19	483	36	1.0	0.41	300	0
21	sand	44	2	19	488	36	1.0	0.41	314	0
22	sand	46	2	19	493	38	1.0	0.38	352	0
23	sand	48	2	19	498	38	1.0	0.38	366	0
24	sand	50	2	19	503	38	1.0	0.38	380	0
25	sand	52	2	19	508	38	1.0	0.38	395	0
26	sand	54	2	19	512	38	1.0	0.38	409	0
27	sand	56	2	19	517	38	1.0	0.38	423	0
28	sand	58	2	19	521	38	1.0	0.38	438	0
29	sand	60	2	19	525	38	1.0	0.38	452	0
30	sand	62	2	19	529	38	1.0	0.38	466	0
31	sand	64	2	19	533	38	1.0	0.38	481	0
32	sand	66	2	19	550	38	1.0	0.38	495	0
33	sand	68	2	19	600	38	1.0	0.38	510	0
34	sand	70	2	19	650	38	1.0	0.38	524	0
35	sand	72	2	19	700	38	1.0	0.38	538	0
36	sand	74	2	19	760	38	1.0	0.38	553	0

## A.5 SITE 5

Site 5 is based on USGS CPT-ALC046, which is located in the east San Francisco Bay in Albany, California, about 1 km from the Bay margin. The surficial materials are classified as Holocene alluvial fan and natural levee deposits. Groundwater is at a depth of 2.1 m. The profile generally consists of 18 m of soft to medium-stiff clay overlying stiff clay. The  $V_{S30}$  of the idealized profile presented below is 301 m/sec. The  $V_{S30}$  computed using the actual data is 305 m/sec.

**Table A.5 Site 5 properties for DEEPSOIL analysis.**

Layer	Material type	Depth top	Thickness	Unit weight	V <sub>s</sub>	Friction angle	OCR	K <sub>0</sub>	Shear strength	PI
-	-	m	m	kN/m <sup>3</sup>	m/sec	degrees	-	-	kPa	-
1	clay	0	2	17	205	N/A	48.2	1.81	166	15
2	clay	2	1	17	220	N/A	17.2	1.06	101	15
3	clay	3	2	17	250	N/A	24.4	1.22	188	15
4	clay	5	1	17	240	N/A	18.7	1.07	157	15
5	clay	6	2	18	245	N/A	54.5	1.76	485	15
6	clay	8	1.5	18	280	N/A	14.3	0.91	185	15
7	clay	9.5	2.5	18	300	N/A	17.9	1.00	277	15
8	clay	12	2.5	18	310	N/A	20.7	1.05	362	15
9	clay	14.5	3.5	18	320	N/A	6.6	0.60	178	15
10	clay	18	2	19	340	N/A	23.7	1.10	526	15
11	clay	20	3	19	360	N/A	23.1	1.07	604	15
12	clay	23	4	19	380	N/A	21.9	1.03	686	15
13	clay	27	3	19	400	N/A	22.4	1.03	759	15
14	clay	30	2	19	403	N/A	21.4	1.00	767	15
15	clay	32	2	19	406	N/A	20.2	0.97	778	15
16	clay	34	2	19	409	N/A	19.2	0.94	788	15
17	clay	36	2	19	411	N/A	18.2	0.92	799	15
18	clay	38	2	19	414	N/A	17.4	0.89	809	15
19	clay	40	2	19	416	N/A	16.6	0.87	818	15
20	clay	42	2	19	419	N/A	15.9	0.85	828	15
21	clay	44	2	19	421	N/A	15.3	0.83	837	15
22	clay	46	2	19	423	N/A	14.7	0.81	846	15
23	clay	48	2	19	425	N/A	14.2	0.79	854	15
24	clay	50	2	19	427	N/A	13.7	0.77	863	15
25	clay	52	2	19	429	N/A	13.2	0.76	871	15
26	clay	54	2	19	432	N/A	12.8	0.74	880	15
27	clay	56	2	19	433	N/A	12.4	0.73	888	15
28	clay	58	2	19	435	N/A	12.0	0.72	896	15
29	clay	60	2	19	437	N/A	11.6	0.71	903	15
30	clay	62	2	19	439	N/A	11.3	0.69	911	15
31	clay	64	2	19	486	N/A	14.1	0.77	1117	15
32	clay	66	2	19	488	N/A	13.7	0.76	1125	15
33	clay	68	2	19	512	N/A	14.9	0.79	1238	15
34	clay	70	2	19	534	N/A	16.0	0.81	1349	15
35	clay	72	2	19	556	N/A	17.0	0.83	1458	15
36	clay	74	2	19	576	N/A	18.0	0.86	1568	15
37	clay	76	2	19	645	N/A	23	1	1963	15
38	clay	78	2	19	704	N/A	28	1.1	2344	15

## A.6 SITE 6

Site 6 is based on USGS CPT-SBC109, performed in stiff granular alluvial fan deposits on the north side of the San Gabriel Mountains near Adelanto, California. Groundwater depth is assumed to be 4 m for analyses. The  $V_{S30}$  of the idealized profile presented below is 446 m/sec. The  $V_{S30}$  computed using the actual data to a depth of 18 m and then extrapolating to 30 m is 409 m/sec. The increase between the idealized and measured  $V_{S30}$  values is the result of replacing the soft layers encountered during the CPT in the upper 4 m of the profile with stiffer layers to prevent a strong impedance contrast. Site “6a” includes these softer layers as described in the main text such that their influence on the pile kinematic response can be considered.

**Table A.6 Site 6 properties for DEEPSOIL analysis.**

Layer	Material type	Depth top	Thickness	Unit weight	$V_s$	Friction angle	OCR	$K_0$	Shear strength	PI
-	-	m	m	kN/m <sup>3</sup>	m/sec	degrees	-	-	kPa	-
1	sand	0	2	18	320	43	N/A	0.32	17	0
2	sand	2	2	18	340	42	N/A	0.33	48	0
3	sand	4	3	18	360	41	N/A	0.34	74	0
4	sand	7	2	18	380	41	N/A	0.34	92	0
5	sand	9	1	18	480	43	N/A	0.32	107	0
6	sand	10	2	18	490	42	N/A	0.33	118	0
7	sand	12	3	19	500	41	N/A	0.34	133	0
8	sand	15	2	19	510	43	N/A	0.32	160	0
9	sand	17	3	19	510	43	N/A	0.32	185	0
10	sand	20	10	19	510	43	N/A	0.31	242	0
11	sand	30	2	19	535	41	N/A	0.34	271	0
12	sand	32	2	19	543	41	N/A	0.34	287	0
13	sand	34	2	19	551	41	N/A	0.34	303	0
14	sand	36	2	19	558	41	N/A	0.34	319	0
15	sand	38	2	19	565	41	N/A	0.34	335	0
16	sand	40	2	19	571	41	N/A	0.34	351	0
17	sand	42	2	19	577	41	N/A	0.34	367	0
18	sand	44	2	19	584	41	N/A	0.34	383	0
19	sand	46	2	19	590	41	N/A	0.34	399	0
20	sand	48	2	19	596	41	N/A	0.34	415	0
21	sand	50	2	19	601	41	N/A	0.34	431	0
22	sand	52	2	19	606	41	N/A	0.34	447	0
23	sand	54	2	19	612	41	N/A	0.34	463	0
24	sand	56	2	19	617	41	N/A	0.34	479	0
25	sand	58	2	19	622	41	N/A	0.34	495	0
26	sand	60	2	19	627	41	N/A	0.34	511	0
27	sand	62	2	19	632	41	N/A	0.34	527	0
28	sand	64	2	19	637	41	N/A	0.34	543	0
29	sand	66	2	19	650	41	N/A	0.34	559	0
30	sand	68	2	19	700	41	N/A	0.34	575	0
31	sand	70	2	19	760	41	N/A	0.34	591	0



## **APPENDIX B A FRAMEWORK FOR FULL-SCALE EXPERIMENTAL MEASUREMENTS OF KINEMATIC PILE–SOIL INTERACTION**

Experimental data for validating kinematic pile–soil transfer function models is scarce and often includes superstructure inertia, making it difficult to isolate the kinematic effects. The authors are not aware of any full-scale tests in which kinematic pile–soil transfer functions have been measured experimentally and without a superstructure supported on the pile(s).

In this appendix, a pilot experimental field test is briefly described. Although the results of the pilot test program do not necessarily provide a sufficiently accurate means for validating the models developed in Chapter 4, the approach is documented here in hopes that similar tests will be conducted in the future on a scale that does provide a means for validation.

The basic field test setup is depicted in Figure B.1. The goal is to replicate the modeling approach used for the numerical study described in the previous chapters in which a pile is subjected to free-field excitation, and the pile head and free-field ground surface responses are recorded; experimental transfer functions can then be computed from these recordings. Since most piles are built to support structures, executing an experiment like this requires either gaining access to a construction site during the brief window between completion of the piles but prior to the beginning of superstructure construction, or the costly alternative of building a sacrificial test pile solely for the purpose of the experiment.

Ideally, the vibration source should excite the free field to a level consistent with design earthquakes, but this would be difficult from a practical point of view. A more feasible approach is to measure small-strain soil behavior by exciting the ground with a shaker such as the type commonly used for geophysical testing methods like spectral analysis of surface waves (SASW). Ambient noise from traffic or other consistent sources could also provide enough energy to mobilize a small-strain response.

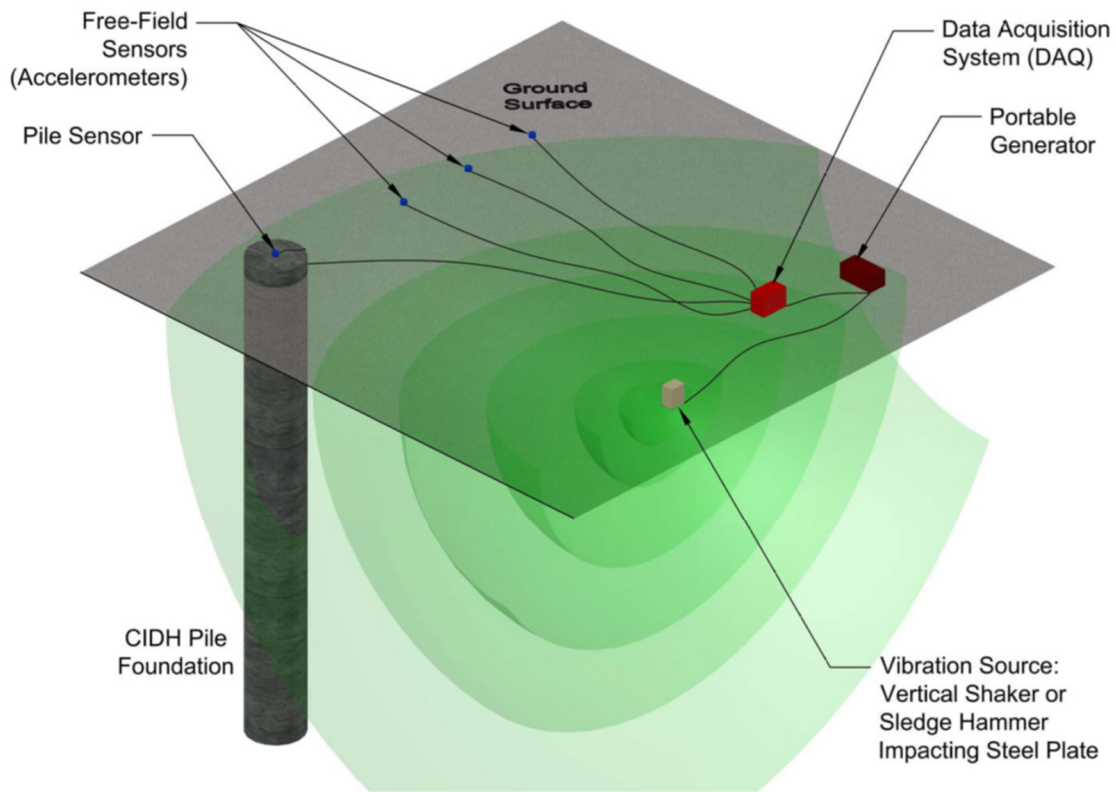


**Figure B.1 Instrumentation for full-scale measurements.**

## **B.1 PILOT STUDY**

The pilot field study program was conducted at a Caltrans culvert construction project site in Goleta, California. A row of 16-in. diameter,  $L = 60$  ft open pipe piles with 0.625-in. wall thickness had been driven to support the culvert wall as shown in Figure B.2, and a brief window of time was available to perform the experiment prior to beginning of the wall construction.

The pile to be tested and adjacent free field were instrumented with triaxial MEMS accelerometers<sup>10</sup> housed in PVC tubing. The pile accelerometer was epoxied to the pile head, and the instrumentation end of the free-field accelerometer was buried in surficial gravel to improve coupling with the ground surface as shown in Figure B.3. The accelerometers were connected to a portable data acquisition system that interfaced with a laptop computer.

---

<sup>10</sup> Model 4630 accelerometer manufactured by Measurement Specialties <http://meas-spec.com/>



**Figure B.2** Pilot study test site.



**Figure B.3** Pilot study test piles and free-field accelerometers.



**Figure B.4** Striking pile adjacent to test pile.

A number of vibration sources were used in combination with various spacings between the pile and free-field sensors as well as different spacings between the pile and the vibration source. The attempted vibration sources included striking a steel plate vertically with a sledge hammer, striking adjacent piles vertically and in multiple horizontal directions relative to the orientation of a line between the test pile and the pile being struck (Figure B.4), dropping a 75-lb bag of aggregate from a ladder, and recording ambient noise from traffic and other sources. For each attempted source, a series of at least ten recordings were made, which were later stacked to improve the quality of the signals. This was necessary in part because of the relatively low quality of the MEMS accelerometers that were used.

Spacing between the pile and free-field sensors corresponded to either two pile diameters or 6 pile diameters. For the sledge-hammer-on-steel-plate and aggregate sack sources, the spacing between the vibration source and the test pile either corresponded to a “near-field” spacing of approximately 3 pile diameters (steel plate visible in Figure B.3), or a “far-field” spacing of approximately 10 pile diameters.

## **B.2 RESULTS**

Recorded time signals of the pile-head and free-field response were stacked and used to compute transfer functions. A lower-bound coherence cutoff of 0.8 was applied, consistent with the procedures implemented in the numerical study and by Mikami et al. [2008]. The vibration sources that generated the strongest signals, and thus the most consistent trends in terms of their transfer functions, were striking the steel plate vertically and dropping the aggregate sack. Transfer functions for these sources are shown in Figure B.5. The figure also shows free-head pile elastic analytical transfer functions for vertically-propagating shear waves (derived in Chapter 2) and

Rayleigh waves (after Makris [1994]). The vertical  $S$ -wave analytical model significantly over-predicts the measured transfer functions, while the Rayleigh wave model appears to capture the underlying trends. This is likely due to the fact that the vibration sources primarily produced surface waves rather than vertically-propagating shear waves.

The measured transfer functions show significant fluctuations, and only have high coherence over a relatively high-frequency range; they do not constrain the underlying trend over the lower frequency range of zero to 10 Hz that is of greater foundation engineering interest. Hence, they are not very useful for validating the models developed for this study. An experimental program in which transfer functions are measured using high-quality instrumentation that exhibit significant deamplification of the free-field motion over this lower frequency range would be extremely valuable for validation purposes.

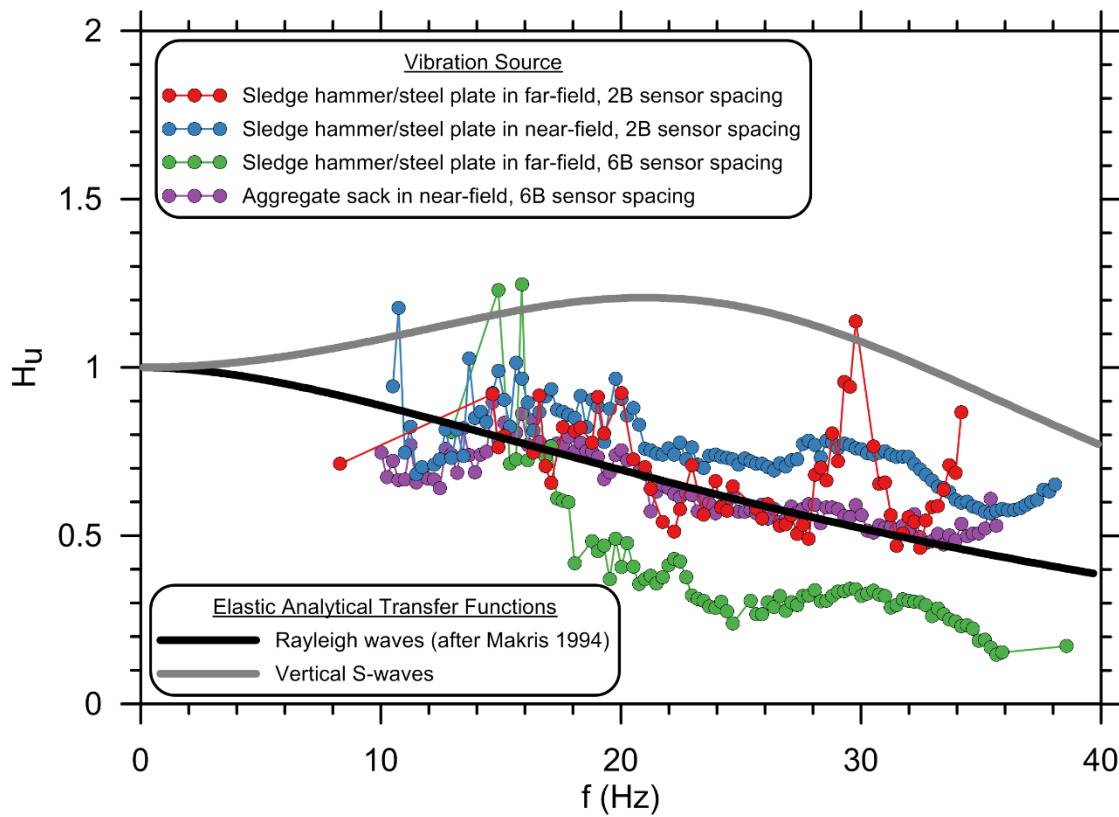


Figure B.5 Theoretical versus recorded transfer functions.



## PEER REPORTS

PEER reports are available as a free PDF download from <https://peer.berkeley.edu/peer-reports>. Printed hard copies of PEER reports can be ordered directly from our printer by following the instructions also available at <https://peer.berkeley.edu/peer-reports>. For other related questions about the PEER Report Series, contact the Pacific Earthquake Engineering Research Center, 325 Davis Hall; Mail Code 1792, Berkeley, CA 94720. Tel.: (510) 642-3437; and Email: [peer\\_center@berkeley.edu](mailto:peer_center@berkeley.edu).

- PEER 2017/07** *A Nonlinear Kinetic Model for Multi-Stage Friction Pendulum Systems*. Paul L. Drazin and Sanjay Govindjee, September 2017.
- PEER 2017/06** *Guidelines for Performance-Based Seismic Design of Tall Buildings, Version 2.02*. TBI Working Group led by co-chairs Ron Hamburger and Jack Moehle: Jack Baker, Jonathan Bray, C.B. Crouse, Greg Deierlein, John Hooper, Marshall Lew, Joe Maffei, Stephen Mahin, James Malley, Farzad Naeim, Jonathan Stewart, and John Wallace. May 2017.
- PEER 2017/05** *Recommendations for Ergodic Nonlinear Site Amplification in Central and Eastern North America*. Youssef M.A. Hashash, Joseph A. Harmon, Okan Ilhan, Grace A. Parker, and Jonathan P. Stewart. March 2017.
- PEER 2017/04** *Expert Panel Recommendations for Ergodic Site Amplification in Central and Eastern North America*. Jonathan P. Stewart, Grace A. Parker, Joseph P. Harmon, Gail M. Atkinson, David M. Boore, Robert B. Darragh, Walter J. Silva, and Youssef M.A. Hashash. March 2017.
- PEER 2017/03** *NGA-East Ground-Motion Models for the U.S. Geological Survey National Seismic Hazard Maps*. Christine A. Goulet, Yousef Bozorgnia, Nicolas Kuehn, Linda Al Atik, Robert R. Youngs, Robert W. Graves, and Gail M. Atkinson. March 2017.
- PEER 2017/02** *U.S.–New Zealand–Japan Workshop: Liquefaction-Induced Ground Movements Effects, University of California, Berkeley, California, 2–4 November 2016*. Jonathan D. Bray, Ross W. Boulanger, Misko Cubrinovski, Kohji Tokimatsu, Steven L. Kramer, Thomas O'Rourke, Ellen Rathje, Russell A. Green, Peter K. Robinson, and Christine Z. Beyzaei. March 2017.
- PEER 2017/01** *2016 PEER Annual Report*. Khalid Mosalam, Amarnath Kasalanati, and Grace Kang. March 2017.
- PEER 2016/10** *Performance-Based Robust Nonlinear Seismic Analysis with Application to Reinforced Concrete Bridge Systems*. Xiao Ling and Khalid M. Mosalam. December 2016.
- PEER 2016/08** *Resilience of Critical Structures, Infrastructure, and Communities*. Gian Paolo Cimellaro, Ali Zamani-Noori, Omar Kamouh, Vesna Terzic, and Stephen A. Mahin. December 2016.
- PEER 2016/07** *Hybrid Simulation Theory for a Classical Nonlinear Dynamical System*. Paul L. Drazin and Sanjay Govindjee. September 2016.
- PEER 2016/06** *California Earthquake Early Warning System Benefit Study*. Laurie A. Johnson, Sharyl Rabinovici, Grace S. Kang, and Stephen A. Mahin. July 2016.
- PEER 2016/05** *Ground-Motion Prediction Equations for Arias Intensity Consistent with the NGA-West2 Ground-Motion Models*. Charlotte Abrahamson, Hao-Jun Michael Shi, and Brian Yang. July 2016.
- PEER 2016/04** *The Mw 6.0 South Napa Earthquake of August 24, 2014: A Wake-Up Call for Renewed Investment in Seismic Resilience Across California*. Prepared for the California Seismic Safety Commission, Laurie A. Johnson and Stephen A. Mahin. May 2016.
- PEER 2016/03** *Simulation Confidence in Tsunami-Driven Overland Flow*. Patrick Lynett. May 2016.
- PEER 2016/02** *Semi-Automated Procedure for Windowing time Series and Computing Fourier Amplitude Spectra for the NGA-West2 Database*. Tadahiro Kishida, Olga-Joan Ktenidou, Robert B. Darragh, and Walter J. Silva. May 2016.
- PEER 2016/01** *A Methodology for the Estimation of Kappa ( $\kappa$ ) from Large Datasets: Example Application to Rock Sites in the NGA-East Database and Implications on Design Motions*. Olga-Joan Ktenidou, Norman A. Abrahamson, Robert B. Darragh, and Walter J. Silva. April 2016.
- PEER 2015/13** *Self-Centering Precast Concrete Dual-Steel-Shell Columns for Accelerated Bridge Construction: Seismic Performance, Analysis, and Design*. Gabriele Guerrini, José I. Restrepo, Athanassios Vervelidis, and Milena Massari. December 2015.
- PEER 2015/12** *Shear-Flexure Interaction Modeling for Reinforced Concrete Structural Walls and Columns under Reversed Cyclic Loading*. Kristijan Kolozvari, Kutay Orakcal, and John Wallace. December 2015.
- PEER 2015/11** *Selection and Scaling of Ground Motions for Nonlinear Response History Analysis of Buildings in Performance-Based Earthquake Engineering*. N. Simon Kwong and Anil K. Chopra. December 2015.

- PEER 2015/10** *Structural Behavior of Column-Bent Cap Beam-Box Girder Systems in Reinforced Concrete Bridges Subjected to Gravity and Seismic Loads. Part II: Hybrid Simulation and Post-Test Analysis.* Mohamed A. Moustafa and Khalid M. Mosalam. November 2015.
- PEER 2015/09** *Structural Behavior of Column-Bent Cap Beam-Box Girder Systems in Reinforced Concrete Bridges Subjected to Gravity and Seismic Loads. Part I: Pre-Test Analysis and Quasi-Static Experiments.* Mohamed A. Moustafa and Khalid M. Mosalam. September 2015.
- PEER 2015/08** *NGA-East: Adjustments to Median Ground-Motion Models for Center and Eastern North America.* August 2015.
- PEER 2015/07** *NGA-East: Ground-Motion Standard-Deviation Models for Central and Eastern North America.* Linda Al Atik. June 2015.
- PEER 2015/06** *Adjusting Ground-Motion Intensity Measures to a Reference Site for which  $V_{S30} = 3000$  m/sec.* David M. Boore. May 2015.
- PEER 2015/05** *Hybrid Simulation of Seismic Isolation Systems Applied to an APR-1400 Nuclear Power Plant.* Andreas H. Schellenberg, Alireza Sarebanha, Matthew J. Schoettler, Gilberto Mosqueda, Gianmario Benzoni, and Stephen A. Mahin. April 2015.
- PEER 2015/04** *NGA-East: Median Ground-Motion Models for the Central and Eastern North America Region.* April 2015.
- PEER 2015/03** *Single Series Solution for the Rectangular Fiber-Reinforced Elastomeric Isolator Compression Modulus.* James M. Kelly and Niel C. Van Engelen. March 2015.
- PEER 2015/02** *A Full-Scale, Single-Column Bridge Bent Tested by Shake-Table Excitation.* Matthew J. Schoettler, José I. Restrepo, Gabriele Guerrini, David E. Duck, and Francesco Carrea. March 2015.
- PEER 2015/01** *Concrete Column Blind Prediction Contest 2010: Outcomes and Observations.* Vesna Terzic, Matthew J. Schoettler, José I. Restrepo, and Stephen A Mahin. March 2015.
- PEER 2014/20** *Stochastic Modeling and Simulation of Near-Fault Ground Motions for Performance-Based Earthquake Engineering.* Mayssa Dabaghi and Armen Der Kiureghian. December 2014.
- PEER 2014/19** *Seismic Response of a Hybrid Fiber-Reinforced Concrete Bridge Column Detailed for Accelerated Bridge Construction.* Wilson Nguyen, William Trono, Marios Panagiotou, and Claudia P. Ostertag. December 2014.
- PEER 2014/18** *Three-Dimensional Beam-Truss Model for Reinforced Concrete Walls and Slabs Subjected to Cyclic Static or Dynamic Loading.* Yuan Lu, Marios Panagiotou, and Ioannis Koutromanos. December 2014.
- PEER 2014/17** *PEER NGA-East Database.* Christine A. Goulet, Tadahiro Kishida, Timothy D. Ancheta, Chris H. Cramer, Robert B. Darragh, Walter J. Silva, Youssef M.A. Hashash, Joseph Harmon, Jonathan P. Stewart, Katie E. Wooddell, and Robert R. Youngs. October 2014.
- PEER 2014/16** *Guidelines for Performing Hazard-Consistent One-Dimensional Ground Response Analysis for Ground Motion Prediction.* Jonathan P. Stewart, Kioumars Afshari, and Youssef M.A. Hashash. October 2014.
- PEER 2014/15** *NGA-East Regionalization Report: Comparison of Four Crustal Regions within Central and Eastern North America using Waveform Modeling and 5%-Damped Pseudo-Spectral Acceleration Response.* Jennifer Dreiling, Marius P. Isken, Walter D. Mooney, Martin C. Chapman, and Richard W. Godbee. October 2014.
- PEER 2014/14** *Scaling Relations between Seismic Moment and Rupture Area of Earthquakes in Stable Continental Regions.* Paul Somerville. August 2014.
- PEER 2014/13** *PEER Preliminary Notes and Observations on the August 24, 2014, South Napa Earthquake.* Grace S. Kang and Stephen A. Mahin, Editors. September 2014.
- PEER 2014/12** *Reference-Rock Site Conditions for Central and Eastern North America: Part II – Attenuation (Kappa) Definition.* Kenneth W. Campbell, Youssef M.A. Hashash, Byungmin Kim, Albert R. Kottke, Ellen M. Rathje, Walter J. Silva, and Jonathan P. Stewart. August 2014.
- PEER 2014/11** *Reference-Rock Site Conditions for Central and Eastern North America: Part I - Velocity Definition.* Youssef M.A. Hashash, Albert R. Kottke, Jonathan P. Stewart, Kenneth W. Campbell, Byungmin Kim, Ellen M. Rathje, Walter J. Silva, Sissy Nikolaou, and Cheryl Moss. August 2014.
- PEER 2014/10** *Evaluation of Collapse and Non-Collapse of Parallel Bridges Affected by Liquefaction and Lateral Spreading.* Benjamin Turner, Scott J. Brandenburg, and Jonathan P. Stewart. August 2014.
- PEER 2014/09** *PEER Arizona Strong-Motion Database and GMPEs Evaluation.* Tadahiro Kishida, Robert E. Kayen, Olga-Joan Ktenidou, Walter J. Silva, Robert B. Darragh, and Jennie Watson-Lamprey. June 2014.
- PEER 2014/08** *Unbonded Pretensioned Bridge Columns with Rocking Detail.* Jeffrey A. Schaefer, Bryan Kennedy, Marc O. Eberhard, and John F. Stanton. June 2014.

- PEER 2014/07** *Northridge 20 Symposium Summary Report: Impacts, Outcomes, and Next Steps.* May 2014.
- PEER 2014/06** *Report of the Tenth Planning Meeting of NEES/E-Defense Collaborative Research on Earthquake Engineering.* December 2013.
- PEER 2014/05** *Seismic Velocity Site Characterization of Thirty-One Chilean Seismometer Stations by Spectral Analysis of Surface Wave Dispersion.* Robert Kayen, Brad D. Carkin, Skye Corbet, Camilo Pinilla, Allan Ng, Edward Gorbis, and Christine Truong. April 2014.
- PEER 2014/04** *Effect of Vertical Acceleration on Shear Strength of Reinforced Concrete Columns.* Hyerin Lee and Khalid M. Mosalam. April 2014.
- PEER 2014/03** *Retest of Thirty-Year-Old Neoprene Isolation Bearings.* James M. Kelly and Niel C. Van Engelen. March 2014.
- PEER 2014/02** *Theoretical Development of Hybrid Simulation Applied to Plate Structures.* Ahmed A. Bakhaty, Khalid M. Mosalam, and Sanjay Govindjee. January 2014.
- PEER 2014/01** *Performance-Based Seismic Assessment of Skewed Bridges.* Peyman Kaviani, Farzin Zareian, and Ertugrul Taciroglu. January 2014.
- PEER 2013/26** *Urban Earthquake Engineering.* Proceedings of the U.S.-Iran Seismic Workshop. December 2013.
- PEER 2013/25** *Earthquake Engineering for Resilient Communities: 2013 PEER Internship Program Research Report Collection.* Heidi Tremayne (Editor), Stephen A. Mahin (Editor), Jorge Archbold Monterossa, Matt Brosman, Shelly Dean, Katherine deLaveaga, Curtis Fong, Donovan Holder, Rakeeb Khan, Elizabeth Jachens, David Lam, Daniela Martinez Lopez, Mara Minner, Geffen Oren, Julia Pavicic, Melissa Quinonez, Lorena Rodriguez, Sean Salazar, Kelli Slaven, Vivian Steyert, Jenny Taing, and Salvador Tena. December 2013.
- PEER 2013/24** *NGA-West2 Ground Motion Prediction Equations for Vertical Ground Motions.* September 2013.
- PEER 2013/23** *Coordinated Planning and Preparedness for Fire Following Major Earthquakes.* Charles Scawthorn. November 2013.
- PEER 2013/22** *GEM-PEER Task 3 Project: Selection of a Global Set of Ground Motion Prediction Equations.* Jonathan P. Stewart, John Douglas, Mohammad B. Javanbarg, Carola Di Alessandro, Yousef Bozorgnia, Norman A. Abrahamson, David M. Boore, Kenneth W. Campbell, Elise Delavaud, Mustafa Erdik, and Peter J. Stafford. December 2013.
- PEER 2013/21** *Seismic Design and Performance of Bridges with Columns on Rocking Foundations.* Grigorios Antonellis and Marios Panagiotou. September 2013.
- PEER 2013/20** *Experimental and Analytical Studies on the Seismic Behavior of Conventional and Hybrid Braced Frames.* Jiun-Wei Lai and Stephen A. Mahin. September 2013.
- PEER 2013/19** *Toward Resilient Communities: A Performance-Based Engineering Framework for Design and Evaluation of the Built Environment.* Michael William Mieler, Bozidar Stojadinovic, Robert J. Budnitz, Stephen A. Mahin, and Mary C. Comerio. September 2013.
- PEER 2013/18** *Identification of Site Parameters that Improve Predictions of Site Amplification.* Ellen M. Rathje and Sara Navidi. July 2013.
- PEER 2013/17** *Response Spectrum Analysis of Concrete Gravity Dams Including Dam-Water-Foundation Interaction.* Amkjell Løkke and Anil K. Chopra. July 2013.
- PEER 2013/16** *Effect of Hoop Reinforcement Spacing on the Cyclic Response of Large Reinforced Concrete Special Moment Frame Beams.* Marios Panagiotou, Tea Visnjic, Grigorios Antonellis, Panagiotis Galanis, and Jack P. Moehle. June 2013.
- PEER 2013/15** *A Probabilistic Framework to Include the Effects of Near-Fault Directivity in Seismic Hazard Assessment.* Shrey Kumar Shahi, Jack W. Baker. October 2013.
- PEER 2013/14** *Hanging-Wall Scaling using Finite-Fault Simulations.* Jennifer L. Donahue and Norman A. Abrahamson. September 2013.
- PEER 2013/13** *Semi-Empirical Nonlinear Site Amplification and its Application in NEHRP Site Factors.* Jonathan P. Stewart and Emel Seyhan. November 2013.
- PEER 2013/12** *Nonlinear Horizontal Site Response for the NGA-West2 Project.* Ronnie Kamai, Norman A. Abramson, Walter J. Silva. May 2013.
- PEER 2013/11** *Epistemic Uncertainty for NGA-West2 Models.* Linda Al Atik and Robert R. Youngs. May 2013.
- PEER 2013/10** *NGA-West 2 Models for Ground-Motion Directionality.* Shrey K. Shahi and Jack W. Baker. May 2013.

- PEER 2013/09** *Final Report of the NGA-West2 Directivity Working Group.* Paul Spudich, Jeffrey R. Bayless, Jack W. Baker, Brian S.J. Chiou, Badie Rowshandel, Shrey Shahi, and Paul Somerville. May 2013.
- PEER 2013/08** *NGA-West2 Model for Estimating Average Horizontal Values of Pseudo-Absolute Spectral Accelerations Generated by Crustal Earthquakes.* I. M. Idriss. May 2013.
- PEER 2013/07** *Update of the Chiou and Youngs NGA Ground Motion Model for Average Horizontal Component of Peak Ground Motion and Response Spectra.* Brian Chiou and Robert Youngs. May 2013.
- PEER 2013/06** *NGA-West2 Campbell-Bozorgnia Ground Motion Model for the Horizontal Components of PGA, PGV, and 5%-Damped Elastic Pseudo-Acceleration Response Spectra for Periods Ranging from 0.01 to 10 sec.* Kenneth W. Campbell and Yousef Bozorgnia. May 2013.
- PEER 2013/05** *NGA-West 2 Equations for Predicting Response Spectral Accelerations for Shallow Crustal Earthquakes.* David M. Boore, Jonathan P. Stewart, Emel Seyhan, and Gail M. Atkinson. May 2013.
- PEER 2013/04** *Update of the AS08 Ground-Motion Prediction Equations Based on the NGA-West2 Data Set.* Norman Abrahamson, Walter Silva, and Ronnie Kamai. May 2013.
- PEER 2013/03** *PEER NGA-West2 Database.* Timothy D. Ancheta, Robert B. Darragh, Jonathan P. Stewart, Emel Seyhan, Walter J. Silva, Brian S.J. Chiou, Katie E. Wooddell, Robert W. Graves, Albert R. Kottke, David M. Boore, Tadahi Kishida, and Jennifer L. Donahue. May 2013.
- PEER 2013/02** *Hybrid Simulation of the Seismic Response of Squat Reinforced Concrete Shear Walls.* Catherine A. Whyte and Bozidar Stojadinovic. May 2013.
- PEER 2013/01** *Housing Recovery in Chile: A Qualitative Mid-program Review.* Mary C. Comerio. February 2013.
- PEER 2012/08** *Guidelines for Estimation of Shear Wave Velocity.* Bernard R. Wair, Jason T. DeJong, and Thomas Shantz. December 2012.
- PEER 2012/07** *Earthquake Engineering for Resilient Communities: 2012 PEER Internship Program Research Report Collection.* Heidi Tremayne (Editor), Stephen A. Mahin (Editor), Collin Anderson, Dustin Cook, Michael Erceg, Carlos Esparza, Jose Jimenez, Dorian Krausz, Andrew Lo, Stephanie Lopez, Nicole McCurdy, Paul Shipman, Alexander Strum, Eduardo Vega. December 2012.
- PEER 2012/06** *Fragilities for Precarious Rocks at Yucca Mountain.* Matthew D. Purvance, Rasool Anooshehpour, and James N. Brune. December 2012.
- PEER 2012/05** *Development of Simplified Analysis Procedure for Piles in Laterally Spreading Layered Soils.* Christopher R. McGann, Pedro Arduino, and Peter Mackenzie-Helnwein. December 2012.
- PEER 2012/04** *Unbonded Pre-Tensioned Columns for Bridges in Seismic Regions.* Phillip M. Davis, Todd M. Janes, Marc O. Eberhard, and John F. Stanton. December 2012.
- PEER 2012/03** *Experimental and Analytical Studies on Reinforced Concrete Buildings with Seismically Vulnerable Beam-Column Joints.* Sangjoon Park and Khalid M. Mosalam. October 2012.
- PEER 2012/02** *Seismic Performance of Reinforced Concrete Bridges Allowed to Uplift during Multi-Directional Excitation.* Andres Oscar Espinoza and Stephen A. Mahin. July 2012.
- PEER 2012/01** *Spectral Damping Scaling Factors for Shallow Crustal Earthquakes in Active Tectonic Regions.* Sanaz Rezaeian, Yousef Bozorgnia, I. M. Idriss, Kenneth Campbell, Norman Abrahamson, and Walter Silva. July 2012.
- PEER 2011/10** *Earthquake Engineering for Resilient Communities: 2011 PEER Internship Program Research Report Collection.* Heidi Faison and Stephen A. Mahin, Editors. December 2011.
- PEER 2011/09** *Calibration of Semi-Stochastic Procedure for Simulating High-Frequency Ground Motions.* Jonathan P. Stewart, Emel Seyhan, and Robert W. Graves. December 2011.
- PEER 2011/08** *Water Supply in regard to Fire Following Earthquake.* Charles Scawthorn. November 2011.
- PEER 2011/07** *Seismic Risk Management in Urban Areas.* Proceedings of a U.S.-Iran-Turkey Seismic Workshop. September 2011.
- PEER 2011/06** *The Use of Base Isolation Systems to Achieve Complex Seismic Performance Objectives.* Troy A. Morgan and Stephen A. Mahin. July 2011.
- PEER 2011/05** *Case Studies of the Seismic Performance of Tall Buildings Designed by Alternative Means.* Task 12 Report for the Tall Buildings Initiative. Jack Moehle, Yousef Bozorgnia, Nirmal Jayaram, Pierson Jones, Mohsen Rahnama, Nilesh Shome, Zeynep Tuna, John Wallace, Tony Yang, and Farzin Zareian. July 2011.
- PEER 2011/04** *Recommended Design Practice for Pile Foundations in Laterally Spreading Ground.* Scott A. Ashford, Ross W. Boulanger, and Scott J. Brandenberg. June 2011.

- PEER 2011/03** *New Ground Motion Selection Procedures and Selected Motions for the PEER Transportation Research Program.* Jack W. Baker, Ting Lin, Shrey K. Shahi, and Nirmal Jayaram. March 2011.
- PEER 2011/02** *A Bayesian Network Methodology for Infrastructure Seismic Risk Assessment and Decision Support.* Michelle T. Bensi, Armen Der Kiureghian, and Daniel Straub. March 2011.
- PEER 2011/01** *Demand Fragility Surfaces for Bridges in Liquefied and Laterally Spreading Ground.* Scott J. Brandenburg, Jian Zhang, Pirooz Kashighandi, Yili Huo, and Minxing Zhao. March 2011.
- PEER 2010/05** *Guidelines for Performance-Based Seismic Design of Tall Buildings.* Developed by the Tall Buildings Initiative. November 2010.
- PEER 2010/04** *Application Guide for the Design of Flexible and Rigid Bus Connections between Substation Equipment Subjected to Earthquakes.* Jean-Bernard Dastous and Armen Der Kiureghian. September 2010.
- PEER 2010/03** *Shear Wave Velocity as a Statistical Function of Standard Penetration Test Resistance and Vertical Effective Stress at Caltrans Bridge Sites.* Scott J. Brandenburg, Naresh Bellana, and Thomas Shantz. June 2010.
- PEER 2010/02** *Stochastic Modeling and Simulation of Ground Motions for Performance-Based Earthquake Engineering.* Sanaz Rezaeian and Armen Der Kiureghian. June 2010.
- PEER 2010/01** *Structural Response and Cost Characterization of Bridge Construction Using Seismic Performance Enhancement Strategies.* Ady Aviram, Božidar Stojadinović, Gustavo J. Parra-Montesinos, and Kevin R. Mackie. March 2010.
- PEER 2009/03** *The Integration of Experimental and Simulation Data in the Study of Reinforced Concrete Bridge Systems Including Soil-Foundation-Structure Interaction.* Matthew Dryden and Gregory L. Fenves. November 2009.
- PEER 2009/02** *Improving Earthquake Mitigation through Innovations and Applications in Seismic Science, Engineering, Communication, and Response.* Proceedings of a U.S.-Iran Seismic Workshop. October 2009.
- PEER 2009/01** *Evaluation of Ground Motion Selection and Modification Methods: Predicting Median Interstory Drift Response of Buildings.* Curt B. Haselton, Editor. June 2009.
- PEER 2008/10** *Technical Manual for Strata.* Albert R. Kottke and Ellen M. Rathje. February 2009.
- PEER 2008/09** *NGA Model for Average Horizontal Component of Peak Ground Motion and Response Spectra.* Brian S.-J. Chiou and Robert R. Youngs. November 2008.
- PEER 2008/08** *Toward Earthquake-Resistant Design of Concentrically Braced Steel Structures.* Patxi Uriz and Stephen A. Mahin. November 2008.
- PEER 2008/07** *Using OpenSees for Performance-Based Evaluation of Bridges on Liquefiable Soils.* Stephen L. Kramer, Pedro Arduino, and HyungSuk Shin. November 2008.
- PEER 2008/06** *Shaking Table Tests and Numerical Investigation of Self-Centering Reinforced Concrete Bridge Columns.* Hyung IL Jeong, Junichi Sakai, and Stephen A. Mahin. September 2008.
- PEER 2008/05** *Performance-Based Earthquake Engineering Design Evaluation Procedure for Bridge Foundations Undergoing Liquefaction-Induced Lateral Ground Displacement.* Christian A. Ledezma and Jonathan D. Bray. August 2008.
- PEER 2008/04** *Benchmarking of Nonlinear Geotechnical Ground Response Analysis Procedures.* Jonathan P. Stewart, Annie On-Lei Kwok, Youssef M. A. Hashash, Neven Matasovic, Robert Pyke, Zhiliang Wang, and Zhaohui Yang. August 2008.
- PEER 2008/03** *Guidelines for Nonlinear Analysis of Bridge Structures in California.* Ady Aviram, Kevin R. Mackie, and Božidar Stojadinović. August 2008.
- PEER 2008/02** *Treatment of Uncertainties in Seismic-Risk Analysis of Transportation Systems.* Evangelos Stergiou and Anne S. Kiremidjian. July 2008.
- PEER 2008/01** *Seismic Performance Objectives for Tall Buildings.* William T. Holmes, Charles Kircher, William Petak, and Nabih Youssef. August 2008.
- PEER 2007/12** *An Assessment to Benchmark the Seismic Performance of a Code-Conforming Reinforced Concrete Moment-Frame Building.* Curt Haselton, Christine A. Goulet, Judith Mitrani-Reiser, James L. Beck, Gregory G. Deierlein, Keith A. Porter, Jonathan P. Stewart, and Ertugrul Taciroglu. August 2008.
- PEER 2007/11** *Bar Buckling in Reinforced Concrete Bridge Columns.* Wayne A. Brown, Dawn E. Lehman, and John F. Stanton. February 2008.
- PEER 2007/10** *Computational Modeling of Progressive Collapse in Reinforced Concrete Frame Structures.* Mohamed M. Talaat and Khalid M. Mosalam. May 2008.

- PEER 2007/09** *Integrated Probabilistic Performance-Based Evaluation of Benchmark Reinforced Concrete Bridges.* Kevin R. Mackie, John-Michael Wong, and Božidar Stojadinović. January 2008.
- PEER 2007/08** *Assessing Seismic Collapse Safety of Modern Reinforced Concrete Moment-Frame Buildings.* Curt B. Haselton and Gregory G. Deierlein. February 2008.
- PEER 2007/07** *Performance Modeling Strategies for Modern Reinforced Concrete Bridge Columns.* Michael P. Berry and Marc O. Eberhard. April 2008.
- PEER 2007/06** *Development of Improved Procedures for Seismic Design of Buried and Partially Buried Structures.* Linda Al Atik and Nicholas Sitar. June 2007.
- PEER 2007/05** *Uncertainty and Correlation in Seismic Risk Assessment of Transportation Systems.* Renee G. Lee and Anne S. Kiremidjian. July 2007.
- PEER 2007/04** *Numerical Models for Analysis and Performance-Based Design of Shallow Foundations Subjected to Seismic Loading.* Sivapalan Gajan, Tara C. Hutchinson, Bruce L. Kutter, Prishati Raychowdhury, José A. Ugalde, and Jonathan P. Stewart. May 2008.
- PEER 2007/03** *Beam-Column Element Model Calibrated for Predicting Flexural Response Leading to Global Collapse of RC Frame Buildings.* Curt B. Haselton, Abbie B. Liel, Sarah Taylor Lange, and Gregory G. Deierlein. May 2008.
- PEER 2007/02** *Campbell-Bozorgnia NGA Ground Motion Relations for the Geometric Mean Horizontal Component of Peak and Spectral Ground Motion Parameters.* Kenneth W. Campbell and Yousef Bozorgnia. May 2007.
- PEER 2007/01** *Boore-Atkinson NGA Ground Motion Relations for the Geometric Mean Horizontal Component of Peak and Spectral Ground Motion Parameters.* David M. Boore and Gail M. Atkinson. May 2007.
- PEER 2006/12** *Societal Implications of Performance-Based Earthquake Engineering.* Peter J. May. May 2007.
- PEER 2006/11** *Probabilistic Seismic Demand Analysis Using Advanced Ground Motion Intensity Measures, Attenuation Relationships, and Near-Fault Effects.* Polsak Tothong and C. Allin Cornell. March 2007.
- PEER 2006/10** *Application of the PEER PBEE Methodology to the I-880 Viaduct.* Sashi Kunnath. February 2007.
- PEER 2006/09** *Quantifying Economic Losses from Travel Forgone Following a Large Metropolitan Earthquake.* James Moore, Sungbin Cho, Yue Yue Fan, and Stuart Werner. November 2006.
- PEER 2006/08** *Vector-Valued Ground Motion Intensity Measures for Probabilistic Seismic Demand Analysis.* Jack W. Baker and C. Allin Cornell. October 2006.
- PEER 2006/07** *Analytical Modeling of Reinforced Concrete Walls for Predicting Flexural and Coupled-Shear-Flexural Responses.* Kutay Orakcal, Leonardo M. Massone, and John W. Wallace. October 2006.
- PEER 2006/06** *Nonlinear Analysis of a Soil-Drilled Pier System under Static and Dynamic Axial Loading.* Gang Wang and Nicholas Sitar. November 2006.
- PEER 2006/05** *Advanced Seismic Assessment Guidelines.* Paolo Bazzurro, C. Allin Cornell, Charles Menun, Maziar Motahari, and Nicolas Luco. September 2006.
- PEER 2006/04** *Probabilistic Seismic Evaluation of Reinforced Concrete Structural Components and Systems.* Tae Hyung Lee and Khalid M. Mosalam. August 2006.
- PEER 2006/03** *Performance of Lifelines Subjected to Lateral Spreading.* Scott A. Ashford and Teerawat Juirnarongrit. July 2006.
- PEER 2006/02** *Pacific Earthquake Engineering Research Center Highway Demonstration Project.* Anne Kiremidjian, James Moore, Yue Yue Fan, Nesrin Basoz, Ozgur Yazali, and Meredith Williams. April 2006.
- PEER 2006/01** *Bracing Berkeley. A Guide to Seismic Safety on the UC Berkeley Campus.* Mary C. Comerio, Stephen Tobriner, and Ariane Fehrenkamp. January 2006.
- PEER 2005/16** *Seismic Response and Reliability of Electrical Substation Equipment and Systems.* Junho Song, Armen Der Kiureghian, and Jerome L. Sackman. April 2006.
- PEER 2005/15** *CPT-Based Probabilistic Assessment of Seismic Soil Liquefaction Initiation.* R. E. S. Moss, R. B. Seed, R. E. Kayen, J. P. Stewart, and A. Der Kiureghian. April 2006.
- PEER 2005/14** *Workshop on Modeling of Nonlinear Cyclic Load-Deformation Behavior of Shallow Foundations.* Bruce L. Kutter, Geoffrey Martin, Tara Hutchinson, Chad Harden, Sivapalan Gajan, and Justin Phalen. March 2006.
- PEER 2005/13** *Stochastic Characterization and Decision Bases under Time-Dependent Aftershock Risk in Performance-Based Earthquake Engineering.* Gee Liek Yeo and C. Allin Cornell. July 2005.

- PEER 2005/12** *PEER Testbed Study on a Laboratory Building: Exercising Seismic Performance Assessment.* Mary C. Comerio, Editor. November 2005.
- PEER 2005/11** *Van Nuys Hotel Building Testbed Report: Exercising Seismic Performance Assessment.* Helmut Krawinkler, Editor. October 2005.
- PEER 2005/10** *First NEES/E-Defense Workshop on Collapse Simulation of Reinforced Concrete Building Structures.* September 2005.
- PEER 2005/09** *Test Applications of Advanced Seismic Assessment Guidelines.* Joe Maffei, Karl Telleen, Danya Mohr, William Holmes, and Yuki Nakayama. August 2006.
- PEER 2005/08** *Damage Accumulation in Lightly Confined Reinforced Concrete Bridge Columns.* R. Tyler Ranf, Jared M. Nelson, Zach Price, Marc O. Eberhard, and John F. Stanton. April 2006.
- PEER 2005/07** *Experimental and Analytical Studies on the Seismic Response of Freestanding and Anchored Laboratory Equipment.* Dimitrios Konstantinidis and Nicos Makris. January 2005.
- PEER 2005/06** *Global Collapse of Frame Structures under Seismic Excitations.* Luis F. Ibarra and Helmut Krawinkler. September 2005.
- PEER 2005/05** *Performance Characterization of Bench- and Shelf-Mounted Equipment.* Samit Ray Chaudhuri and Tara C. Hutchinson. May 2006.
- PEER 2005/04** *Numerical Modeling of the Nonlinear Cyclic Response of Shallow Foundations.* Chad Harden, Tara Hutchinson, Geoffrey R. Martin, and Bruce L. Kutter. August 2005.
- PEER 2005/03** *A Taxonomy of Building Components for Performance-Based Earthquake Engineering.* Keith A. Porter. September 2005.
- PEER 2005/02** *Fragility Basis for California Highway Overpass Bridge Seismic Decision Making.* Kevin R. Mackie and Božidar Stojadinović. June 2005.
- PEER 2005/01** *Empirical Characterization of Site Conditions on Strong Ground Motion.* Jonathan P. Stewart, Yoojoong Choi, and Robert W. Graves. June 2005.
- PEER 2004/09** *Electrical Substation Equipment Interaction: Experimental Rigid Conductor Studies.* Christopher Stearns and André Filiatrault. February 2005.
- PEER 2004/08** *Seismic Qualification and Fragility Testing of Line Break 550-kV Disconnect Switches.* Shakhzod M. Takhirov, Gregory L. Fenves, and Eric Fujisaki. January 2005.
- PEER 2004/07** *Ground Motions for Earthquake Simulator Qualification of Electrical Substation Equipment.* Shakhzod M. Takhirov, Gregory L. Fenves, Eric Fujisaki, and Don Clyde. January 2005.
- PEER 2004/06** *Performance-Based Regulation and Regulatory Regimes.* Peter J. May and Chris Koski. September 2004.
- PEER 2004/05** *Performance-Based Seismic Design Concepts and Implementation: Proceedings of an International Workshop.* Peter Fajfar and Helmut Krawinkler, Editors. September 2004.
- PEER 2004/04** *Seismic Performance of an Instrumented Tilt-up Wall Building.* James C. Anderson and Vitelmo V. Bertero. July 2004.
- PEER 2004/03** *Evaluation and Application of Concrete Tilt-up Assessment Methodologies.* Timothy Graf and James O. Malley. October 2004.
- PEER 2004/02** *Analytical Investigations of New Methods for Reducing Residual Displacements of Reinforced Concrete Bridge Columns.* Junichi Sakai and Stephen A. Mahin. August 2004.
- PEER 2004/01** *Seismic Performance of Masonry Buildings and Design Implications.* Kerri Anne Taeko Tokoro, James C. Anderson, and Vitelmo V. Bertero. February 2004.
- PEER 2003/18** *Performance Models for Flexural Damage in Reinforced Concrete Columns.* Michael Berry and Marc Eberhard. August 2003.
- PEER 2003/17** *Predicting Earthquake Damage in Older Reinforced Concrete Beam-Column Joints.* Catherine Pagni and Laura Lowes. October 2004.
- PEER 2003/16** *Seismic Demands for Performance-Based Design of Bridges.* Kevin Mackie and Božidar Stojadinović. August 2003.
- PEER 2003/15** *Seismic Demands for Nondeteriorating Frame Structures and Their Dependence on Ground Motions.* Ricardo Antonio Medina and Helmut Krawinkler. May 2004.

- PEER 2003/14** *Finite Element Reliability and Sensitivity Methods for Performance-Based Earthquake Engineering*. Terje Haukaas and Armen Der Kiureghian. April 2004.
- PEER 2003/13** *Effects of Connection Hysteretic Degradation on the Seismic Behavior of Steel Moment-Resisting Frames*. Janise E. Rodgers and Stephen A. Mahin. March 2004.
- PEER 2003/12** *Implementation Manual for the Seismic Protection of Laboratory Contents: Format and Case Studies*. William T. Holmes and Mary C. Comerio. October 2003.
- PEER 2003/11** *Fifth U.S.-Japan Workshop on Performance-Based Earthquake Engineering Methodology for Reinforced Concrete Building Structures*. February 2004.
- PEER 2003/10** *A Beam-Column Joint Model for Simulating the Earthquake Response of Reinforced Concrete Frames*. Laura N. Lowes, Nilanjan Mitra, and Arash Altoontash. February 2004.
- PEER 2003/09** *Sequencing Repairs after an Earthquake: An Economic Approach*. Marco Casari and Simon J. Wilkie. April 2004.
- PEER 2003/08** *A Technical Framework for Probability-Based Demand and Capacity Factor Design (DCFD) Seismic Formats*. Fatemeh Jalayer and C. Allin Cornell. November 2003.
- PEER 2003/07** *Uncertainty Specification and Propagation for Loss Estimation Using FOSM Methods*. Jack W. Baker and C. Allin Cornell. September 2003.
- PEER 2003/06** *Performance of Circular Reinforced Concrete Bridge Columns under Bidirectional Earthquake Loading*. Mahmoud M. Hachem, Stephen A. Mahin, and Jack P. Moehle. February 2003.
- PEER 2003/05** *Response Assessment for Building-Specific Loss Estimation*. Eduardo Miranda and Shahram Taghavi. September 2003.
- PEER 2003/04** *Experimental Assessment of Columns with Short Lap Splices Subjected to Cyclic Loads*. Murat Melek, John W. Wallace, and Joel Conte. April 2003.
- PEER 2003/03** *Probabilistic Response Assessment for Building-Specific Loss Estimation*. Eduardo Miranda and Hesameddin Aslani. September 2003.
- PEER 2003/02** *Software Framework for Collaborative Development of Nonlinear Dynamic Analysis Program*. Jun Peng and Kincho H. Law. September 2003.
- PEER 2003/01** *Shake Table Tests and Analytical Studies on the Gravity Load Collapse of Reinforced Concrete Frames*. Kenneth John Elwood and Jack P. Moehle. November 2003.
- PEER 2002/24** *Performance of Beam to Column Bridge Joints Subjected to a Large Velocity Pulse*. Natalie Gibson, André Filiatrault, and Scott A. Ashford. April 2002.
- PEER 2002/23** *Effects of Large Velocity Pulses on Reinforced Concrete Bridge Columns*. Greg L. Orozco and Scott A. Ashford. April 2002.
- PEER 2002/22** *Characterization of Large Velocity Pulses for Laboratory Testing*. Kenneth E. Cox and Scott A. Ashford. April 2002.
- PEER 2002/21** *Fourth U.S.-Japan Workshop on Performance-Based Earthquake Engineering Methodology for Reinforced Concrete Building Structures*. December 2002.
- PEER 2002/20** *Barriers to Adoption and Implementation of PBEE Innovations*. Peter J. May. August 2002.
- PEER 2002/19** *Economic-Engineered Integrated Models for Earthquakes: Socioeconomic Impacts*. Peter Gordon, James E. Moore II, and Harry W. Richardson. July 2002.
- PEER 2002/18** *Assessment of Reinforced Concrete Building Exterior Joints with Substandard Details*. Chris P. Pantelides, Jon Hansen, Justin Nadauld, and Lawrence D. Reaveley. May 2002.
- PEER 2002/17** *Structural Characterization and Seismic Response Analysis of a Highway Overcrossing Equipped with Elastomeric Bearings and Fluid Dampers: A Case Study*. Nicos Makris and Jian Zhang. November 2002.
- PEER 2002/16** *Estimation of Uncertainty in Geotechnical Properties for Performance-Based Earthquake Engineering*. Allen L. Jones, Steven L. Kramer, and Pedro Arduino. December 2002.
- PEER 2002/15** *Seismic Behavior of Bridge Columns Subjected to Various Loading Patterns*. Asadollah Esmaeily-Gh. and Yan Xiao. December 2002.
- PEER 2002/14** *Inelastic Seismic Response of Extended Pile Shaft Supported Bridge Structures*. T.C. Hutchinson, R.W. Boulanger, Y.H. Chai, and I.M. Idriss. December 2002.
- PEER 2002/13** *Probabilistic Models and Fragility Estimates for Bridge Components and Systems*. Paolo Gardoni, Armen Der Kiureghian, and Khalid M. Mosalam. June 2002.

- PEER 2002/12** *Effects of Fault Dip and Slip Rake on Near-Source Ground Motions: Why Chi-Chi Was a Relatively Mild M7.6 Earthquake.* Brad T. Aagaard, John F. Hall, and Thomas H. Heaton. December 2002.
- PEER 2002/11** *Analytical and Experimental Study of Fiber-Reinforced Strip Isolators.* James M. Kelly and Shakhzod M. Takhirov. September 2002.
- PEER 2002/10** *Centrifuge Modeling of Settlement and Lateral Spreading with Comparisons to Numerical Analyses.* Sivapalan Gajan and Bruce L. Kutter. January 2003.
- PEER 2002/09** *Documentation and Analysis of Field Case Histories of Seismic Compression during the 1994 Northridge, California, Earthquake.* Jonathan P. Stewart, Patrick M. Smith, Daniel H. Whang, and Jonathan D. Bray. October 2002.
- PEER 2002/08** *Component Testing, Stability Analysis and Characterization of Buckling-Restrained Unbonded Braces<sup>TM</sup>.* Cameron Black, Nicos Makris, and Ian Aiken. September 2002.
- PEER 2002/07** *Seismic Performance of Pile-Wharf Connections.* Charles W. Roeder, Robert Graff, Jennifer Soderstrom, and Jun Han Yoo. December 2001.
- PEER 2002/06** *The Use of Benefit-Cost Analysis for Evaluation of Performance-Based Earthquake Engineering Decisions.* Richard O. Zerbe and Anthony Falit-Baiamonte. September 2001.
- PEER 2002/05** *Guidelines, Specifications, and Seismic Performance Characterization of Nonstructural Building Components and Equipment.* André Filiatrault, Constantin Christopoulos, and Christopher Stearns. September 2001.
- PEER 2002/04** *Consortium of Organizations for Strong-Motion Observation Systems and the Pacific Earthquake Engineering Research Center Lifelines Program: Invited Workshop on Archiving and Web Dissemination of Geotechnical Data, 4–5 October 2001.* September 2002.
- PEER 2002/03** *Investigation of Sensitivity of Building Loss Estimates to Major Uncertain Variables for the Van Nuys Testbed.* Keith A. Porter, James L. Beck, and Rustem V. Shaikhutdinov. August 2002.
- PEER 2002/02** *The Third U.S.-Japan Workshop on Performance-Based Earthquake Engineering Methodology for Reinforced Concrete Building Structures.* July 2002.
- PEER 2002/01** *Nonstructural Loss Estimation: The UC Berkeley Case Study.* Mary C. Comerio and John C. Stallmeyer. December 2001.
- PEER 2001/16** *Statistics of SDF-System Estimate of Roof Displacement for Pushover Analysis of Buildings.* Anil K. Chopra, Rakesh K. Goel, and Chatpan Chintanapakdee. December 2001.
- PEER 2001/15** *Damage to Bridges during the 2001 Nisqually Earthquake.* R. Tyler Ranf, Marc O. Eberhard, and Michael P. Berry. November 2001.
- PEER 2001/14** *Rocking Response of Equipment Anchored to a Base Foundation.* Nicos Makris and Cameron J. Black. September 2001.
- PEER 2001/13** *Modeling Soil Liquefaction Hazards for Performance-Based Earthquake Engineering.* Steven L. Kramer and Ahmed-W. Elgamal. February 2001.
- PEER 2001/12** *Development of Geotechnical Capabilities in OpenSees.* Boris Jeremić. September 2001.
- PEER 2001/11** *Analytical and Experimental Study of Fiber-Reinforced Elastomeric Isolators.* James M. Kelly and Shakhzod M. Takhirov. September 2001.
- PEER 2001/10** *Amplification Factors for Spectral Acceleration in Active Regions.* Jonathan P. Stewart, Andrew H. Liu, Yoojoong Choi, and Mehmet B. Baturay. December 2001.
- PEER 2001/09** *Ground Motion Evaluation Procedures for Performance-Based Design.* Jonathan P. Stewart, Shyh-Jeng Chiou, Jonathan D. Bray, Robert W. Graves, Paul G. Somerville, and Norman A. Abrahamson. September 2001.
- PEER 2001/08** *Experimental and Computational Evaluation of Reinforced Concrete Bridge Beam-Column Connections for Seismic Performance.* Clay J. Naito, Jack P. Moehle, and Khalid M. Mosalam. November 2001.
- PEER 2001/07** *The Rocking Spectrum and the Shortcomings of Design Guidelines.* Nicos Makris and Dimitrios Konstantinidis. August 2001.
- PEER 2001/06** *Development of an Electrical Substation Equipment Performance Database for Evaluation of Equipment Fragilities.* Thalia Agnanos. April 1999.
- PEER 2001/05** *Stiffness Analysis of Fiber-Reinforced Elastomeric Isolators.* Hsiang-Chuan Tsai and James M. Kelly. May 2001.
- PEER 2001/04** *Organizational and Societal Considerations for Performance-Based Earthquake Engineering.* Peter J. May. April 2001.

- PEER 2001/03** *A Modal Pushover Analysis Procedure to Estimate Seismic Demands for Buildings: Theory and Preliminary Evaluation.* Anil K. Chopra and Rakesh K. Goel. January 2001.
- PEER 2001/02** *Seismic Response Analysis of Highway Overcrossings Including Soil-Structure Interaction.* Jian Zhang and Nicos Makris. March 2001.
- PEER 2001/01** *Experimental Study of Large Seismic Steel Beam-to-Column Connections.* Egor P. Popov and Shakhzod M. Takhirov. November 2000.
- PEER 2000/10** *The Second U.S.-Japan Workshop on Performance-Based Earthquake Engineering Methodology for Reinforced Concrete Building Structures.* March 2000.
- PEER 2000/09** *Structural Engineering Reconnaissance of the August 17, 1999 Earthquake: Kocaeli (Izmit), Turkey.* Halil Sezen, Kenneth J. Elwood, Andrew S. Whittaker, Khalid Mosalam, John J. Wallace, and John F. Stanton. December 2000.
- PEER 2000/08** *Behavior of Reinforced Concrete Bridge Columns Having Varying Aspect Ratios and Varying Lengths of Confinement.* Anthony J. Calderone, Dawn E. Lehman, and Jack P. Moehle. January 2001.
- PEER 2000/07** *Cover-Plate and Flange-Plate Reinforced Steel Moment-Resisting Connections.* Taejin Kim, Andrew S. Whittaker, Amir S. Gilani, Vitelmo V. Bertero, and Shakhzod M. Takhirov. September 2000.
- PEER 2000/06** *Seismic Evaluation and Analysis of 230-kV Disconnect Switches.* Amir S. J. Gilani, Andrew S. Whittaker, Gregory L. Fenves, Chun-Hao Chen, Henry Ho, and Eric Fujisaki. July 2000.
- PEER 2000/05** *Performance-Based Evaluation of Exterior Reinforced Concrete Building Joints for Seismic Excitation.* Chandra Clyde, Chris P. Pantelides, and Lawrence D. Reaveley. July 2000.
- PEER 2000/04** *An Evaluation of Seismic Energy Demand: An Attenuation Approach.* Chung-Che Chou and Chia-Ming Uang. July 1999.
- PEER 2000/03** *Framing Earthquake Retrofitting Decisions: The Case of Hillside Homes in Los Angeles.* Detlof von Winterfeldt, Nels Roselund, and Alicia Kitsuse. March 2000.
- PEER 2000/02** *U.S.-Japan Workshop on the Effects of Near-Field Earthquake Shaking.* Andrew Whittaker, Editor. July 2000.
- PEER 2000/01** *Further Studies on Seismic Interaction in Interconnected Electrical Substation Equipment.* Armen Der Kiureghian, Kee-Jeung Hong, and Jerome L. Sackman. November 1999.
- PEER 1999/14** *Seismic Evaluation and Retrofit of 230-kV Porcelain Transformer Bushings.* Amir S. Gilani, Andrew S. Whittaker, Gregory L. Fenves, and Eric Fujisaki. December 1999.
- PEER 1999/13** *Building Vulnerability Studies: Modeling and Evaluation of Tilt-up and Steel Reinforced Concrete Buildings.* John W. Wallace, Jonathan P. Stewart, and Andrew S. Whittaker, Editors. December 1999.
- PEER 1999/12** *Rehabilitation of Nonductile RC Frame Building Using Encasement Plates and Energy-Dissipating Devices.* Mehrdad Sasani, Vitelmo V. Bertero, James C. Anderson. December 1999.
- PEER 1999/11** *Performance Evaluation Database for Concrete Bridge Components and Systems under Simulated Seismic Loads.* Yael D. Hose and Frieder Seible. November 1999.
- PEER 1999/10** *U.S.-Japan Workshop on Performance-Based Earthquake Engineering Methodology for Reinforced Concrete Building Structures.* December 1999.
- PEER 1999/09** *Performance Improvement of Long Period Building Structures Subjected to Severe Pulse-Type Ground Motions.* James C. Anderson, Vitelmo V. Bertero, and Raul Bertero. October 1999.
- PEER 1999/08** *Envelopes for Seismic Response Vectors.* Charles Menun and Armen Der Kiureghian. July 1999.
- PEER 1999/07** *Documentation of Strengths and Weaknesses of Current Computer Analysis Methods for Seismic Performance of Reinforced Concrete Members.* William F. Cofer. November 1999.
- PEER 1999/06** *Rocking Response and Overturning of Anchored Equipment under Seismic Excitations.* Nicos Makris and Jian Zhang. November 1999.
- PEER 1999/05** *Seismic Evaluation of 550 kV Porcelain Transformer Bushings.* Amir S. Gilani, Andrew S. Whittaker, Gregory L. Fenves, and Eric Fujisaki. October 1999.
- PEER 1999/04** *Adoption and Enforcement of Earthquake Risk-Reduction Measures.* Peter J. May, Raymond J. Burby, T. Jens Feeley, and Robert Wood. August 1999.
- PEER 1999/03** *Task 3 Characterization of Site Response General Site Categories.* Adrian Rodriguez-Marek, Jonathan D. Bray and Norman Abrahamson. February 1999.

- PEER 1999/02** *Capacity-Demand-Diagram Methods for Estimating Seismic Deformation of Inelastic Structures: SDF Systems.* Anil K. Chopra and Rakesh Goel. April 1999.
- PEER 1999/01** *Interaction in Interconnected Electrical Substation Equipment Subjected to Earthquake Ground Motions.* Armen Der Kiureghian, Jerome L. Sackman, and Kee-Jeung Hong. February 1999.
- PEER 1998/08** *Behavior and Failure Analysis of a Multiple-Frame Highway Bridge in the 1994 Northridge Earthquake.* Gregory L. Fenves and Michael Ellery. December 1998.
- PEER 1998/07** *Empirical Evaluation of Inertial Soil-Structure Interaction Effects.* Jonathan P. Stewart, Raymond B. Seed, and Gregory L. Fenves. November 1998.
- PEER 1998/06** *Effect of Damping Mechanisms on the Response of Seismic Isolated Structures.* Nicos Makris and Shih-Po Chang. November 1998.
- PEER 1998/05** *Rocking Response and Overturning of Equipment under Horizontal Pulse-Type Motions.* Nicos Makris and Yiannis Roussos. October 1998.
- PEER 1998/04** *Pacific Earthquake Engineering Research Invitational Workshop Proceedings, May 14–15, 1998: Defining the Links between Planning, Policy Analysis, Economics and Earthquake Engineering.* Mary Comerio and Peter Gordon. September 1998.
- PEER 1998/03** *Repair/Upgrade Procedures for Welded Beam to Column Connections.* James C. Anderson and Xiaojing Duan. May 1998.
- PEER 1998/02** *Seismic Evaluation of 196 kV Porcelain Transformer Bushings.* Amir S. Gilani, Juan W. Chavez, Gregory L. Fenves, and Andrew S. Whittaker. May 1998.
- PEER 1998/01** *Seismic Performance of Well-Confined Concrete Bridge Columns.* Dawn E. Lehman and Jack P. Moehle. December 2000.

## PEER REPORTS: ONE HUNDRED SERIES

The following PEER reports are available by Internet only at [http://peer.berkeley.edu/publications/peer\\_reports\\_complete.html](http://peer.berkeley.edu/publications/peer_reports_complete.html).

- PEER 2012/103** *Performance-Based Seismic Demand Assessment of Concentrically Braced Steel Frame Buildings*. Chui-Hsin Chen and Stephen A. Mahin. December 2012.
- PEER 2012/102** *Procedure to Restart an Interrupted Hybrid Simulation: Addendum to PEER Report 2010/103*. Vesna Terzic and Božidar Stojadinovic. October 2012.
- PEER 2012/101** *Mechanics of Fiber Reinforced Bearings*. James M. Kelly and Andrea Calabrese. February 2012.
- PEER 2011/107** *Nonlinear Site Response and Seismic Compression at Vertical Array Strongly Shaken by 2007 Niigata-ken Chuetsu-oki Earthquake*. Eric Yee, Jonathan P. Stewart, and Kohji Tokimatsu. December 2011.
- PEER 2011/106** *Self Compacting Hybrid Fiber Reinforced Concrete Composites for Bridge Columns*. Pardeep Kumar, Gabriel Jen, William Trono, Marios Panagiotou, and Claudia Ostertag. September 2011.
- PEER 2011/105** *Stochastic Dynamic Analysis of Bridges Subjected to Spatially Varying Ground Motions*. Katerina Konakli and Armen Der Kiureghian. August 2011.
- PEER 2011/104** *Design and Instrumentation of the 2010 E-Defense Four-Story Reinforced Concrete and Post-Tensioned Concrete Buildings*. Takuya Nagae, Kenichi Tahara, Taizo Matsumori, Hitoshi Shiohara, Toshimi Kabeyasawa, Susumu Kono, Minehiro Nishiyama (Japanese Research Team) and John Wallace, Wassim Ghannoum, Jack Moehle, Richard Sause, Wesley Keller, Zeynep Tuna (U.S. Research Team). June 2011.
- PEER 2011/103** *In-Situ Monitoring of the Force Output of Fluid Dampers: Experimental Investigation*. Dimitrios Konstantinidis, James M. Kelly, and Nicos Makris. April 2011.
- PEER 2011/102** *Ground-Motion Prediction Equations 1964–2010*. John Douglas. April 2011.
- PEER 2011/101** *Report of the Eighth Planning Meeting of NEES/E-Defense Collaborative Research on Earthquake Engineering*. Convened by the Hyogo Earthquake Engineering Research Center (NIED), NEES Consortium, Inc. February 2011.
- PEER 2010/111** *Modeling and Acceptance Criteria for Seismic Design and Analysis of Tall Buildings*. Task 7 Report for the Tall Buildings Initiative - Published jointly by the Applied Technology Council. October 2010.
- PEER 2010/110** *Seismic Performance Assessment and Probabilistic Repair Cost Analysis of Precast Concrete Cladding Systems for Multistory Buildings*. Jeffrey P. Hunt and Božidar Stojadinovic. November 2010.
- PEER 2010/109** *Report of the Seventh Joint Planning Meeting of NEES/E-Defense Collaboration on Earthquake Engineering. Held at the E-Defense, Miki, and Shin-Kobe, Japan, September 18–19, 2009*. August 2010.
- PEER 2010/108** *Probabilistic Tsunami Hazard in California*. Hong Kie Thio, Paul Somerville, and Jascha Polet, preparers. October 2010.
- PEER 2010/107** *Performance and Reliability of Exposed Column Base Plate Connections for Steel Moment-Resisting Frames*. Ady Aviram, Božidar Stojadinovic, and Armen Der Kiureghian. August 2010.
- PEER 2010/106** *Verification of Probabilistic Seismic Hazard Analysis Computer Programs*. Patricia Thomas, Ivan Wong, and Norman Abrahamson. May 2010.
- PEER 2010/105** *Structural Engineering Reconnaissance of the April 6, 2009, Abruzzo, Italy, Earthquake, and Lessons Learned*. M. Selim Günay and Khalid M. Mosalam. April 2010.
- PEER 2010/104** *Simulating the Inelastic Seismic Behavior of Steel Braced Frames, Including the Effects of Low-Cycle Fatigue*. Yuli Huang and Stephen A. Mahin. April 2010.
- PEER 2010/103** *Post-Earthquake Traffic Capacity of Modern Bridges in California*. Vesna Terzic and Božidar Stojadinović. March 2010.
- PEER 2010/102** *Analysis of Cumulative Absolute Velocity (CAV) and JMA Instrumental Seismic Intensity ( $I_{JMA}$ ) Using the PEER–NGA Strong Motion Database*. Kenneth W. Campbell and Yousef Bozorgnia. February 2010.
- PEER 2010/101** *Rocking Response of Bridges on Shallow Foundations*. Jose A. Ugalde, Bruce L. Kutter, and Boris Jeremic. April 2010.
- PEER 2009/109** *Simulation and Performance-Based Earthquake Engineering Assessment of Self-Centering Post-Tensioned Concrete Bridge Systems*. Won K. Lee and Sarah L. Billington. December 2009.
- PEER 2009/108** *PEER Lifelines Geotechnical Virtual Data Center*. J. Carl Stepp, Daniel J. Ponti, Loren L. Turner, Jennifer N. Swift, Sean Devlin, Yang Zhu, Jean Benoit, and John Bobbitt. September 2009.

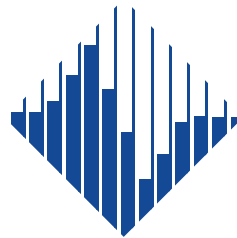
- PEER 2009/107** *Experimental and Computational Evaluation of Current and Innovative In-Span Hinge Details in Reinforced Concrete Box-Girder Bridges: Part 2: Post-Test Analysis and Design Recommendations.* Matias A. Hube and Khalid M. Mosalam. December 2009.
- PEER 2009/106** *Shear Strength Models of Exterior Beam-Column Joints without Transverse Reinforcement.* Sangjoon Park and Khalid M. Mosalam. November 2009.
- PEER 2009/105** *Reduced Uncertainty of Ground Motion Prediction Equations through Bayesian Variance Analysis.* Robb Eric S. Moss. November 2009.
- PEER 2009/104** *Advanced Implementation of Hybrid Simulation.* Andreas H. Schellenberg, Stephen A. Mahin, Gregory L. Fenves. November 2009.
- PEER 2009/103** *Performance Evaluation of Innovative Steel Braced Frames.* T. Y. Yang, Jack P. Moehle, and Božidar Stojadinovic. August 2009.
- PEER 2009/102** *Reinvestigation of Liquefaction and Nonliquefaction Case Histories from the 1976 Tangshan Earthquake.* Robb Eric Moss, Robert E. Kayen, Liyuan Tong, Songyu Liu, Guojun Cai, and Jiaer Wu. August 2009.
- PEER 2009/101** *Report of the First Joint Planning Meeting for the Second Phase of NEES/E-Defense Collaborative Research on Earthquake Engineering.* Stephen A. Mahin et al. July 2009.
- PEER 2008/104** *Experimental and Analytical Study of the Seismic Performance of Retaining Structures.* Linda Al Atik and Nicholas Sitar. January 2009.
- PEER 2008/103** *Experimental and Computational Evaluation of Current and Innovative In-Span Hinge Details in Reinforced Concrete Box-Girder Bridges. Part 1: Experimental Findings and Pre-Test Analysis.* Matias A. Hube and Khalid M. Mosalam. January 2009.
- PEER 2008/102** *Modeling of Unreinforced Masonry Infill Walls Considering In-Plane and Out-of-Plane Interaction.* Stephen Kadsiewicz and Khalid M. Mosalam. January 2009.
- PEER 2008/101** *Seismic Performance Objectives for Tall Buildings.* William T. Holmes, Charles Kircher, William Petak, and Nabih Youssef. August 2008.
- PEER 2007/101** *Generalized Hybrid Simulation Framework for Structural Systems Subjected to Seismic Loading.* Tarek Elkhoraibi and Khalid M. Mosalam. July 2007.
- PEER 2007/100** *Seismic Evaluation of Reinforced Concrete Buildings Including Effects of Masonry Infill Walls.* Alidad Hashemi and Khalid M. Mosalam. July 2007.



The Pacific Earthquake Engineering Research Center (PEER) is a multi-institutional research and education center with headquarters at the University of California, Berkeley. Investigators from over 20 universities, several consulting companies, and researchers at various state and federal government agencies contribute to research programs focused on performance-based earthquake engineering.

These research programs aim to identify and reduce the risks from major earthquakes to life safety and to the economy by including research in a wide variety of disciplines including structural and geotechnical engineering, geology/seismology, lifelines, transportation, architecture, economics, risk management, and public policy.

PEER is supported by federal, state, local, and regional agencies, together with industry partners.



#### **PEER Core Institutions**

University of California, Berkeley (Lead Institution)  
California Institute of Technology  
Oregon State University  
Stanford University  
University of California, Davis  
University of California, Irvine  
University of California, Los Angeles  
University of California, San Diego  
University of Nevada, Reno  
University of Southern California  
University of Washington

PEER reports can be ordered at <https://peer.berkeley.edu/peer-reports> or by contacting

Pacific Earthquake Engineering Research Center  
University of California, Berkeley  
325 Davis Hall, Mail Code 1792  
Berkeley, CA 94720-1792  
Tel: 510-642-3437  
Email: [peer\\_center@berkeley.edu](mailto:peer_center@berkeley.edu)

ISSN 1547-0587X